

3 Study of Vector-Boson Scattering with
4 the ATLAS detector and design of the
5 High Granularity Timing Detector for
6 HL-HLC

7 *Etude des diffusions de bosons vecteurs avec le*
8 *détecteur ATLAS et conception du High Granularity*
9 *Timing Detector pour HL-HLC*

10 Thèse de doctorat de l'université Paris-Saclay

11 École doctorale n° 576 Particules, Hadrons, Energie et noyau : instrumentation,
12 imagerie, cosmos et simulation (PHENIICS)
13 Spécialité de doctorat : Physique des Particules
14 Graduate School : Physique. Référent : Faculté des sciences d'Orsay

15 Thèse préparée dans la unité de recherche **IJCLab** (Université Paris-Saclay, CNRS) et
16 **CERN**, sous la direction de **Nikola MAKOVEC**, Chargé de recherche

17 Thèse soutenue à Paris-Saclay, le 27 Septembre 2024, par

18 Oleksii KURDYSH

19 Composition du jury

Fabien CAVALIER	Président
Directeur de recherche, IJCLab	
Emmanuel MONNIER	Rapporteur & Examinateur
Directeur de recherche, CPPM	
Christophe OCHANDO	Rapporteur & Examinateur
Chargé de recherche, LLR	
Reina CAMACHO TORO	Examinateuse
Chargée de recherche, LPNHE	
Caroline COLLARD	Examinateuse
Directrice de recherche, IPHC	
Nikola MAKOVEC	Directeur
Chargé de recherche, IJCLab	

ÉCOLE DOCTORALE

Particules, hadrons, énergie et noyau:
instrumentation, imagerie, cosmos
et simulation (PHENIICS)

Titre : Etude des diffusions de bosons vecteurs avec le détecteur ATLAS et conception du High Granularity Timing Detector pour HL-HLC

Mots clés : Front-end electronique, High Granularity Timing Detector, Rejection de l'empilement, Interaction électrofaible, Au-delà du Modèle Standard

Title : Study of Vector-Boson Scattering with the ATLAS detector and design of the High Granularity Timing Detector for HL-HLC

Keywords : Front-end Electronics, High Granularity Timing Detector, Pile-up rejection, Electroweak interaction, Beyond the Standard Model

²² Table des matières

23 1 Theoretical context	7
24 1.1 The Standard Model	7
25 1.1.1 Particle content	7
26 1.1.2 Lagrangian and underlying symmetries	8
27 1.1.3 EWK symmetry breaking	9
28 1.1.4 Experimental results	9
29 1.2 Vector Boson Scattering within the SM	10
30 1.2.1 Process definition	10
31 1.2.2 Vertices	10
32 1.2.3 Diagrams	12
33 1.2.4 Unitarity restoration	14
34 1.3 VBS measurements at the LHC	15
35 1.3.1 Motivation	15
36 1.3.2 Experimental features	16
37 1.3.3 Experimental status	17
38 1.4 Beyond the Standard Model motivation	18
39 1.5 Effective Field Theory	20
40 2 Experimental context	21
41 2.1 Historical overview	21
42 2.2 Accelerator complex	21
43 2.2.1 Overview	21
44 2.2.2 Injector chain	21
45 2.2.3 LHC	23
46 2.2.4 Luminosity	24
47 2.3 ATLAS	24
48 2.3.1 From proto-collaborations to Higgs discovery	24
49 2.3.2 Run-3 detector configuration	26
50 2.3.3 Object reconstruction	30
51 3 aQGC EFT VBS Run-2 combination	37
52 3.1 Analyses involved	37
53 3.2 Eboli operators	37
54 3.3 Expectation from the combination	39
55 3.4 EFT samples generation	39
56 3.5 EFT cross-sections	40
57 3.6 SM and EFT distributions	41
58 3.7 Unitarity bound	41

59	3.8 Clipping	42
60	3.9 Cross-term size	46
61	3.10 Operator replacement	50
62	3.10.1 $Z(\rightarrow \bar{\nu}\nu)\gamma$ analysis	51
63	3.10.2 $W^\pm Z$ analysis	54
64	3.10.3 Other analyses	55
65	3.11 Preliminary results	58
66	3.11.1 1-D limits	58
67	3.11.2 2-D limits	58
68	3.12 Outlook	58
69	3.12.1 Inputs	61
70	3.12.2 1-D limits	61
71	3.12.3 n-D limits	61
72	3.13 Conclusion	62
73	4 Forward Jet Vertex Tagger	69
74	4.1 Principle of operation	69
75	4.2 Release 22 update	72
76	4.3 fJVT calibration	74
77	4.3.1 Methodology	74
78	4.3.2 Binning and working points	75
79	4.3.3 Uncertainties	75
80	4.3.4 $Z \rightarrow \ell\bar{\ell} + jets$ samples and validation	76
81	4.3.5 Run-2 R22 calibration	78
82	4.3.6 Run-3 R22 calibration	78
83	4.4 Potential improvement	83
84	4.4.1 Shape information	83
85	4.4.2 Targeting specific type of pile-up	83
86	4.4.3 Adding timing information	84
87	4.5 Conclusion	85
88	5 HL-LHC	87
89	5.1 Project overview	87
90	5.2 Accelerator upgrades	87
91	5.3 ATLAS Phase-II upgrades	89
92	5.3.1 Trigger and Data Acquisition	90
93	5.3.2 Inner Tracker	90
94	5.3.3 Calorimeters	90
95	5.3.4 Muon	91
96	5.3.5 Higg Granularity Timing Detector	91
97	5.3.6 Computing	91
98	5.4 Physics case - VBS	93
99	5.4.1 $W^\pm W^\pm$ analysis	93

100	5.4.2 ZZ analysis	93
101	5.4.3 $W^\pm Z$ analysis	95
102	5.5 HGTD	97
103	5.5.1 Detector overview	98
104	5.5.2 Sensor	101
105	5.5.3 Time resolution components	101
106	5.5.4 Front-end electronics	103
107	5.5.5 ASIC characterization aspects	107
108	6 ALTIROC1 testbeam	111
109	6.1 Campaign overview	111
110	6.2 Method of time resolution extraction	113
111	6.3 SiPM time reconstruction and it's matching with hybrid	114
112	6.4 Resolution obtained with TZ preamplifier	115
113	6.4.1 TOA-TOT coupling caveat	115
114	6.4.2 Event selections	115
115	6.4.3 Uncorrected resolution	117
116	6.4.4 Timewalk correction variables	117
117	6.4.5 Amplitude dependence	126
118	6.4.6 Impact of TDC DNL	128
119	6.5 Resolution obtained with VPA preamplifier	128
120	7 ALTIROC2 testbench	131
121	7.1 LSB calibration	131
122	7.1.1 Methodology	131
123	7.1.2 General trends observed	132
124	7.1.3 More on LSB dependence on injection	133
125	7.2 Lowest detectable charge and associated jitter	138
126	7.3 TID test	142
127	7.4 Low temperature test	146
128	8 ALTIROC2/3 testbeam	149
129	8.1 Setup	149
130	8.2 ALTIROC2 timing	151
131	8.3 Tracking, efficiency and interpad	154
132	8.4 ALTIROC3 timing	157
133	8.4.1 LSBs from resolution minimization	157
134	8.4.2 LSBs from $t_{MCP} : TOA$ fit	159
135	8.4.3 Correction for DNL	160
136	8.4.4 TOT-inclusive timewalk correction	161
137	8.4.5 Summary of different configurations	165
138	A $Z \rightarrow \ell\bar{\ell} + \text{jets}$ basic distributions	167

¹³⁹	B ε_{HS} , SF, σ_{SF} for Tighter WP	171
¹⁴⁰	C ε_{HS} , SF, σ_{SF} for Loose WP	173
¹⁴¹	D $Z(\rightarrow \bar{\nu}\nu)\gamma$ replacements	175
¹⁴²	E $Z(\rightarrow \bar{\nu}\nu)\gamma$ replacements validation fits	183

¹⁴³ 1 - Theoretical context

¹⁴⁴ 1.1 The Standard Model

¹⁴⁵ The Standard Model (SM) embodies particles with no known (at the time) substructure, called
¹⁴⁶ fundamental particles, and interactions between them : strong, weak and electromagnetic force. The
¹⁴⁷ SM is founded on principles of QFT, developed in early 1970's and withstood all the experimental
¹⁴⁸ tests done since then, including, notably, Higgs boson discovery in 2012.

¹⁴⁹ 1.1.1 Particle content

¹⁵⁰ Fundamental particles included in the SM are summarized on Fig. 1.1. Depending on the spin
¹⁵¹ there are two types of particles in the SM : bosons (integer spin) and fermions (half-integer spin).
¹⁵² All "matter" particles are fermions, further divided into quarks and leptons where only quarks are
¹⁵³ participating in strong interactions. Both quarks and leptons are organized into three generations
¹⁵⁴ where each generation properties are the same except the mass (third generation has the highest
¹⁵⁵ mass). Each generation includes two pairs of particles. For quarks, each pair members has electric
¹⁵⁶ charges $+2/3$ (in units of e) and $-1/3$, for leptons pair includes particle with charge -1 and un-
¹⁵⁷ charged one. All force carriers are bosons : in the SM there are four vector bosons (spin-1) and
¹⁵⁸ one scalar (spin-0) boson. Names, masses, charges, spins can be read-off from the figure. For each
¹⁵⁹ particle, there is an anti-particle with opposite quantum numbers and same mass.

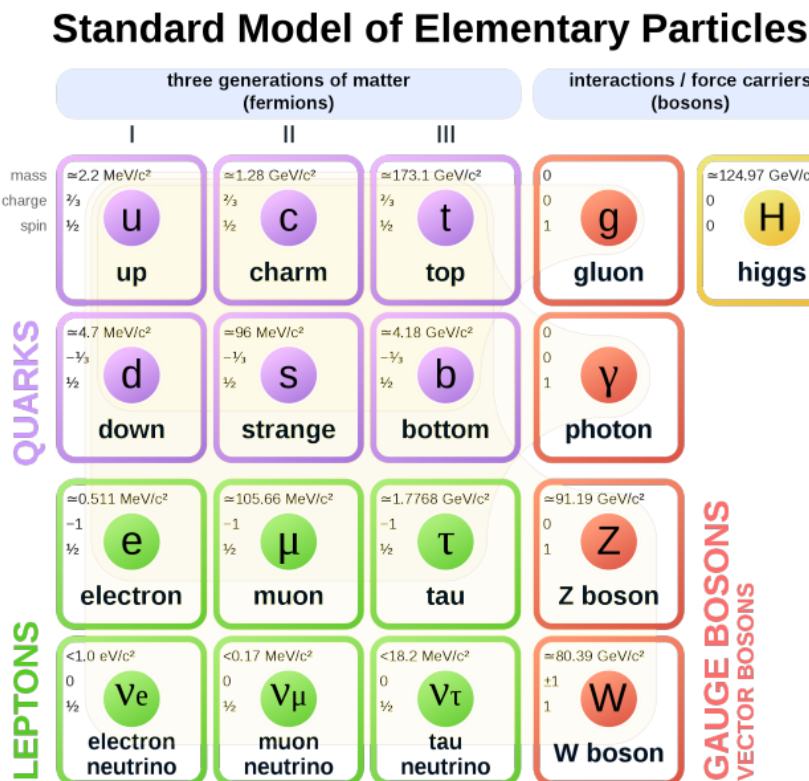


FIGURE 1.1 – Particle content of the Standard Model

¹⁶⁰ 1.1.2 Lagrangian and underlying symmetries

161 The main model building tool in SM is the Lagrangian density (word density is often drop-
 162 ped) \mathcal{L} . Equations of motion follows from Lagrangian via the least action principle. In SM \mathcal{L} is
 163 designed to be invariant under local symmetries of $SU(3)_C \times SU(2)_{I(Left)} \times U(1)_Y$ group. Conser-
 164 vation of corresponding charges follow from symmetry : color C, weak isospin I and hypercharge
 165 Y. The SM Lagrangian can be separated into Quantum Choromodynamics (QCD) and electro-
 166 weak (EWK) non-broken parts, described in two following subsubsections. Another contribution,
 167 subject of Sec. 1.1.3, is from EWK symmetry breaking.

168 QCD Lagrangian

169 QCD part of the Lagrangian is given by

$$\mathcal{L}_{QCD} = \bar{\psi}_i \left(i(\gamma^\mu D_\mu)_{i,j} - m\delta_{i,j} \right) \psi_j - \frac{1}{4} G_{\mu\nu}^a G_a^{\mu\nu} \quad (1.1)$$

170 where

$$D_\mu = \partial_\mu - \frac{1}{2} ig_s \sum_{a=1}^8 \lambda_a G_\mu^a \quad (1.2)$$

$$G_{\mu\nu}^a = \partial_\mu G_\nu^a - \partial_\nu G_\mu^a + g_s f^{abc} G_\mu^b G_\nu^c \quad (1.3)$$

172 in which D_μ is a covariant derivative and index a runs over 8 gluon fields G_μ . λ are the Gell-Mann
 173 matrices. g_s is the coupling constant of $SU(3)$ color group. f^{abc} are the structure constants of
 174 $SU(3)_C$ group.

175 Consequences of such Lagrangian is that all interactions are given in terms of a single strong
 176 coupling constant. Strength of coupling depends on energy and at low energy it becomes too large
 177 bringing QCD into non-perturbative regime. There are self-interactions among the gauge fields
 178 and these self-interactions give rise to color confinement (starting point to formation of jets, see
 179 Sec. 2.3.3).

180 EWK Lagrangian

181 Gluons was mentioned above. Other vector bosons mentioned in Fig. 1.1 are obtained from the
 182 $B_\mu, W_\mu^1, W_\mu^2, W_\mu^3$ fields of $SU(2)_L \times U(1)_Y$ symmetry by

$$W_\mu^\pm = \frac{1}{\sqrt{2}} (W_\mu^1 \mp iW_\mu^2) \quad (1.4)$$

$$\begin{pmatrix} A_\mu \\ Z_\mu \end{pmatrix} = \begin{pmatrix} \cos \theta_W & \sin \theta_W \\ -\sin \theta_W & \cos \theta_W \end{pmatrix} \begin{pmatrix} B_\mu \\ W_\mu^3 \end{pmatrix} \quad (1.5)$$

184 where θ_W is Weinberg angle.

185 Three lepton families under EWK group are organized as doublets, e.g. left-handed electron
 186 together with electron neutrino. For quarks up- and down-type form doublets. Right-handed fields
 187 are singlets : quarks and leptons, except that there no right-handed neutrino is SM. Description of
 188 interactions between fermions and fields of Eq. 1.5 and Eq. 1.4 lies in

$$\mathcal{L}_{EWK}^{non-broken} = i\bar{\psi}_L \gamma^\mu D_\mu \psi_L + i\bar{\psi}_R \gamma^\mu D_\mu \psi_R - \frac{1}{4} W_{\mu\nu}^a W_a^{\mu\nu} - \frac{1}{4} B_{\mu\nu}^a B_a^{\mu\nu} \quad (1.6)$$

189 where covariant derivative contains both W and B fields.

190 In above considerations, masses of W and Z bosons are not allowed¹. This is resolved by EWK
 191 symmetry breaking.

1. Also fermion masses are forbidden

192 1.1.3 EWK symmetry breaking

193 To explain the missing masses, following François Englert, Robert Brout and Peter Higgs one
 194 might add the following term to SM Lagrangian

$$195 \quad \mathcal{L}_{\text{Higgs}} = (D^\mu \phi)^\dagger (D_\mu \phi) - V(\phi) \quad (1.7)$$

with ϕ being complex scalar doublet and

$$V(\phi) = \mu^2 \phi^\dagger \phi + \lambda (\phi^\dagger \phi)^2 \quad (1.8)$$

being the Higgs potential that depends on two parameters Λ, μ , and it's shape is illustrated on Fig. 1.2 for the case $\mu^2 < 0$. It's visible that there is not one but multiple possible minima of potential but multiple of them, choosing one of them breaks EW symmetry spontaneously. One can arbitrarily choose minimum

$$\phi_0 = \frac{1}{\sqrt{2}} \begin{pmatrix} 0 \\ v \end{pmatrix} \quad (1.9)$$

with v being vacuum expectation and expand $\phi(x)$ around the that minimum

$$\phi(x) = \frac{1}{\sqrt{2}} \begin{pmatrix} 0 \\ v + h(x) \end{pmatrix} \quad (1.10)$$

It will lead to $(D^\mu \phi)^\dagger (D_\mu \phi)$ term in Eq. 1.7 containing desired mass terms for W, Z² with masses

$$\begin{aligned} M_W &= \frac{1}{2} g v \\ M_Z &= \frac{1}{2} (g^2 + g'^2) v \end{aligned} \quad (1.11)$$

photons, as desired, are massless and mass of newly-appeared particle, Higgs boson, should have mass $M_H = \sqrt{2\lambda v^2}$. Coupling of Higgs to W pair at vertex should be $i g^2 / 2$ and $i(g^2 + g'^2) / 2$ between Higgs and Z pair.

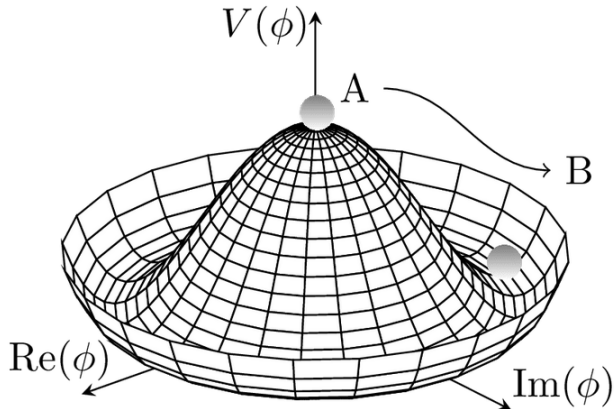


FIGURE 1.2 – Illustration of Higgs potential

205 1.1.4 Experimental results

206 Extensive experimental test of the Standard Model were performed and one facet of them is
 207 shown on Fig. 1.3 : ATLAS “dinosaur“ plot displaying production cross-sections, measured and
 208 predicted by SM. For a wide array of different processes spanning 14 orders of magnitude in cross-
 209 section, data is consistent with the Standard Model which is a remarkable achievement ! Electroweak
 210 Vector Boson Scattering processes, subject of Sec. 1.2 and Chapter 3, are denoted as “ $V\gamma jj$ “ and
 211 “ $VVjj$ “.

2. Mechanism also generates masses for fermions

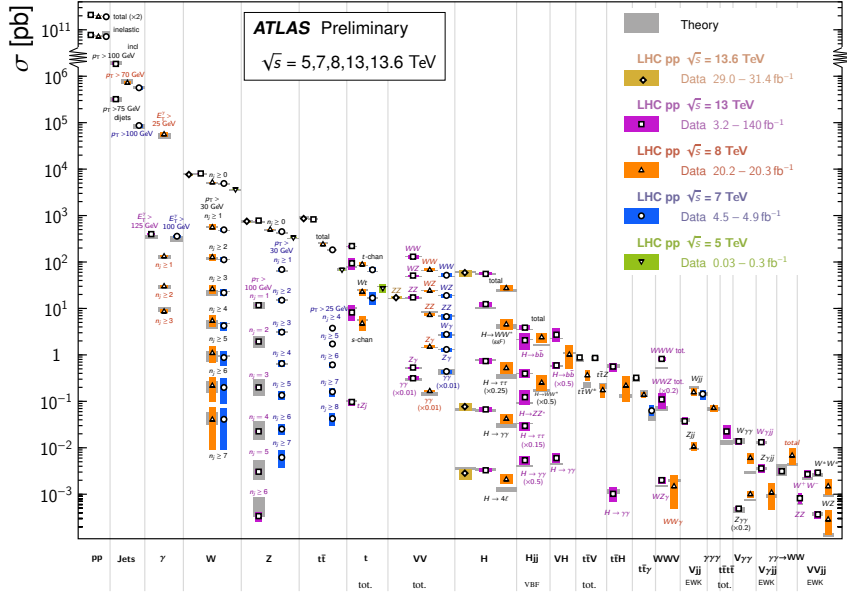


FIGURE 1.3 – Summary of several Standard Model total and fiducial production cross-section measurements where total cross sections are reported, the measurements are corrected for branching fractions and compared to the corresponding theoretical expectations. In some cases, the fiducial selection is different between measurements in the same final state for different centre-of-mass energies \sqrt{s} , resulting in lower cross section values at higher \sqrt{s} [28].

1.2 Vector Boson Scattering within the SM

1.2.1 Process definition

Example of what is referred by “Electroweak VBS“, as shown on Fig. 1.4, is a process where two incoming partons each radiate a vector boson $V \equiv W/Z/\gamma$ (not necessary the same from each parton) that scatter of each other. Scattering options (not all of them are available to all di-boson combinations) are shown on Fig. 1.5, from left to right : quartic self-interaction, s-channel with intermediate V , t-channel with intermediate V (u is not drawn), s- and t-channel(u is not drawn) involving Higgs.

Including the decays of V , if both V are not photons, one arrives at a process (at tree-level) of type

$$qq' \rightarrow f_V \bar{f}'_V f''_V \bar{f}'''_V q'' q''' \quad (1.12)$$

or if a photon is involved

$$qq' \rightarrow f_V \bar{f}'_V \gamma q'' q''' \quad (1.13)$$

where q denote initial (anti)quark, f_V is (anti)fermion appeared from decay of scattered vector boson and γ is a photon.

1.2.2 Vertices

Let’s see how vertices participating in Fig. 1.5 arise within SM. Pure kinetic term of gauge fields B_μ , \vec{W}_μ can be separated from Eq. 1.6

$$\mathcal{L}_G = -\frac{1}{4} F_{\mu\nu} F^{\mu\nu} - \frac{1}{4} \vec{W}_{\mu\nu} \cdot \vec{W}^{\mu\nu} \quad (1.14)$$

where

$$F_{\mu\nu} \equiv \partial_\mu B_\nu - \partial_\nu B_\mu \quad (1.15)$$

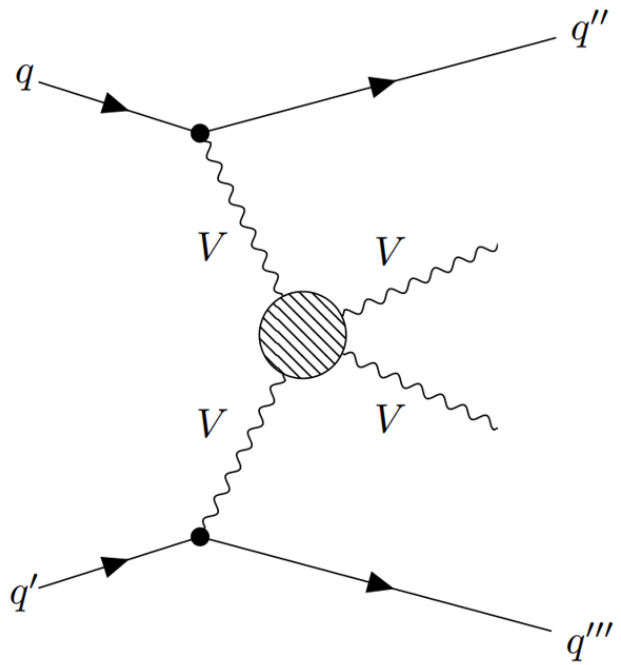


FIGURE 1.4 – Feynman diagram illustrating collection of VBS processes allowed by SM. Content of “blob“ is shown on Fig. 1.5

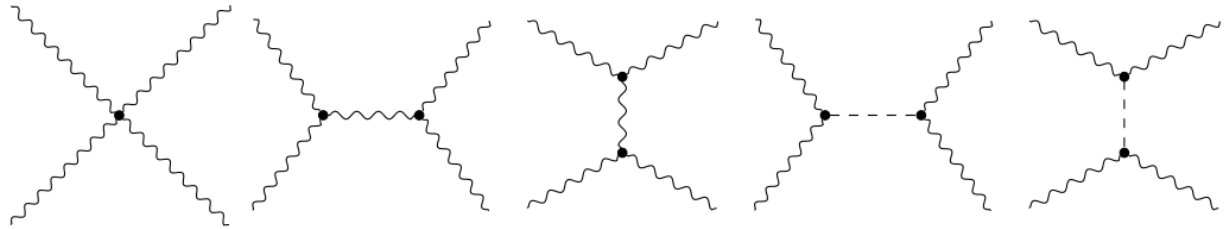


FIGURE 1.5 – Feynman diagrams contributing to “blob“ of Fig. 1.4 at Leading Order

229

$$\vec{W}_{\mu\nu} \equiv \partial_\mu \vec{W}_\nu - \partial_\nu \vec{W}_\mu - g_2 \vec{W}_\mu \times \vec{W}_\nu \quad (1.16)$$

230 Then quadrilinear gauge bosons vertices (main interest for VBS) can be obtained from the
 231 Lagrangian Eq. 1.14 . Substituting definitions Eq. 1.15, Eq. 1.16 resulting expression one would get
 232 will contain

$$\begin{aligned} \mathcal{L}_4 = & -\frac{g_2^2}{4} [2W_\mu^+ W^{-\mu} W_\nu^+ W^{-\nu} - 2W_\mu^+ W^{+\mu} W_\nu^- W^{-\nu} \\ & + 4W_\mu^+ W^{-\mu} W_{3\nu} W^{3\nu} - 4W_\mu^+ W_3^\mu W_\nu^- W^{3\nu}] \end{aligned} \quad (1.17)$$

233 Inverting Eq. 1.5 to eliminate B, W^3 in favour of A, Z one would obtain expression in terms of
 234 W^-, W^+, Z, A leading vertices allowed by SM with four gauge bosons participating

$$W^+ W^- W^+ W^-, W^+ W^- ZZ, W^+ W^- Z\gamma, W^+ W^- \gamma\gamma \quad (1.18)$$

235 Similarly one would obtain allowed tri-linear vertices(which will constitute a background for aQGC),
 236 there are only two

$$W^+ W^- \gamma, W^+ W^- Z \quad (1.19)$$

237 1.2.3 Diagrams

238 Currently NLO simulations for VBS are available only for Standard Model processes and not
 239 for aQGC EFT which is the subject of Chapter 3. Therefore, discussion will be focused on LO.

240 There are different ways to transition from initial to final states mentioned in Eq. 1.12 and
 241 Eq. 1.13, they can be classified into

- 242 1. Pure electroweak vector boson scattering diagrams with quartic gauge (named EW VBS for
 243 brevity), in turn divided into cases with quartic or triple gauge couplings
- 244 2. Pure EW diagrams with Higgs
- 245 3. Pure EW non-VBS case
- 246 4. QCD-induced production - gluon or quark initiated

247 Specific examples of diagrams of each case are shown below.

248 LO EW

249 EW diagrams contributing to $WZjj$ process is as a concrete example of case where both bosons
 250 are massive. EW QGC VBS diagram at LO is shown on Fig. 1.6, it is of order α_{EW}^6 . EW TGC VBS
 251 diagrams without Higgs are shown on Fig. 1.7. Higgs exchange diagram, of particular importance
 252 for the reasons that will be mentioned in Sec. 1.2.4 , is shown on Fig. 1.8. Both Fig. 1.7 and Fig. 1.8
 253 are also of order α_{EW}^6 .

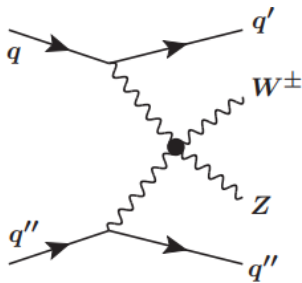


FIGURE 1.6 – EW quartic gauge coupling VBS WZ

254 For a class of EW diagrams where photons are involved, one can consider $Z\gamma jj$ case. Here at
 255 LO, there are no diagrams with Higgs. EW VBS, QGC and TGC are shown on Fig. 1.9. QGC is

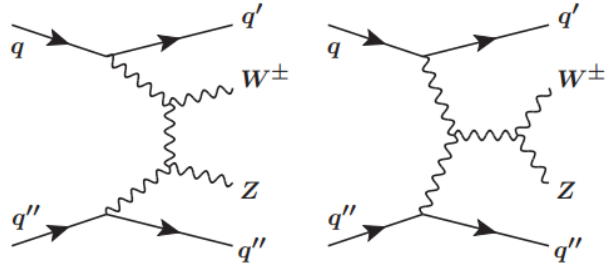


FIGURE 1.7 – EW VBS triple gauge coupling WZ

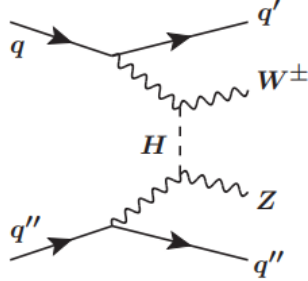


FIGURE 1.8 – EW VBS with Higgs exchange WZ

256 forbidden in the SM but can be induced by BSM physics, for example aQGC EFT (see Sec. 3.2).
 257 EW non-VBS diagram is shown on Fig. 1.9. Both Fig. 1.9 and Fig. 1.10 are of order α_{EW}^4 .

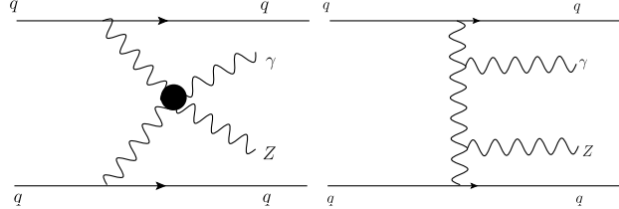


FIGURE 1.9 – EW VBS quartic and triple gauge coupling $Z\gamma$

258 LO QCD diagrams

259 Major background to EW VBS is QCD-induced $VVjj$ production mode. There are kinematic
 260 differences between the two, allowing to separate EW and QCD, as will be discussed in Sec. 1.3.2.
 261 Examples of such diagrams are shown for $W^\pm Z$ on Fig. 1.11a (quark-initiated) and on Fig. 1.11b (gluon-
 262 initiated) - they are of order $\alpha_{EW}^4 \alpha_S^2$. Similarly, for $Z\gamma$ QCD diagrams are shown on Fig. 1.12, they
 263 are of order $\alpha_{EW}^2 \alpha_S^2$

264 Comparison of EW and QCD effects

265 For the case where all bosons are massive, like $W^\pm Z$ above, cross-section (being proportional
 266 to squared amplitude) receives contributions from both pure EW (power 6 in α_{EW} and denoted as
 267 $VVjj$ -EW6) and EW-QCD components (power 4 in α_{EW} and denoted as $VVjj$ -EW4) as follows

$$\begin{aligned}\sigma_{VVjj} &\sim |\mathcal{M}_{VVjj-EW6} + \mathcal{M}_{VVjj-EW4}|^2, \\ &\sim |\mathcal{M}_{VVjj-EW6}|^2 + |\mathcal{M}_{VVjj-EW4}|^2 + 2 \operatorname{Re} (\mathcal{M}_{VVjj-EW6} \mathcal{M}_{VVjj-EW4}^*) \\ &\equiv \sigma_{EW6} + \sigma_{EW4} + \sigma_{INT}\end{aligned}\quad (1.20)$$

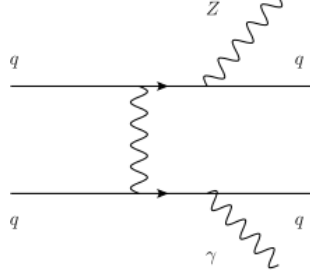


FIGURE 1.10 – EW non-VBS $Z\gamma$

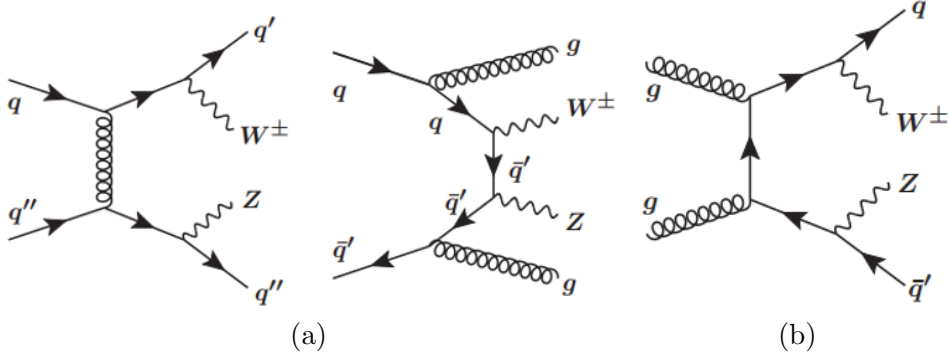


FIGURE 1.11 – QCD WZ (a) quark-initiated (b) gluon-initiated

giving, apart from pure $VVjj$ -EW6 and $VVjj$ -EW4 terms, rise also to the interference term, denoted as σ_{INT} , of order $\alpha_{EW}^5 \alpha_S$. Interference contribution is color suppressed. For example in the case of W^+W^+ , as shown in [23], it's contribution at LO is within few percent.

Depending on process, contributions from $VVjj$ -EW6 and $VVjj$ -EW4 may be different. Summary of cross-sections, for the case where all bosons are massive and are decaying leptonically, is given in Table 1.1. It can be seen that contribution from QCD differs per process but never dominating (this would mean $\frac{\sigma_{EW6}}{\sigma_{EW4}} \ll 1$). Among three cases shown ($W^\pm W^\pm$, $W^\pm Z$, ZZ) a special place is taken by $W^\pm W^\pm$ where QCD background is small, but for the other two processes QCD is a major background.

1.2.4 Unitarity restoration

Diagrams with Higgs, like the one that was shown on Fig. 1.8 for $W^\pm Z$ case, are the ones without which VBS cross-section would diverge at high energy. This can be demonstrated, following [98], via $W^\pm W^\pm$ example. All the LO diagrams contributing are shown on Fig. 1.13, involving quartic and triple gauge vertex (the ones with Z, γ) and Higgs exchange diagrams. Then amplitude

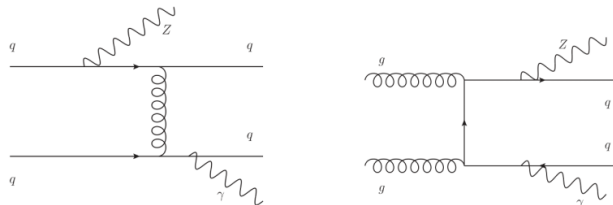


FIGURE 1.12 – QCD $Z\gamma$ (left) quark-initiated (right) gluon-initiated

TABLE 1.1 – Pure EW and EW with contributions from QCD cross-sections for different processes, predicted by SHERPA [75]

Process	$\sigma_{EW6}[\text{fb}]$	$\sigma_{EW4}[\text{fb}]$	$\frac{\sigma_{EW6}}{\sigma_{EW4}}$
$W^\pm W^\pm jj$	3.97	0.346	11.5
$W^\pm Z jj$	2.34	4.38	0.53
$ZZ jj$	0.098	0.100	0.98

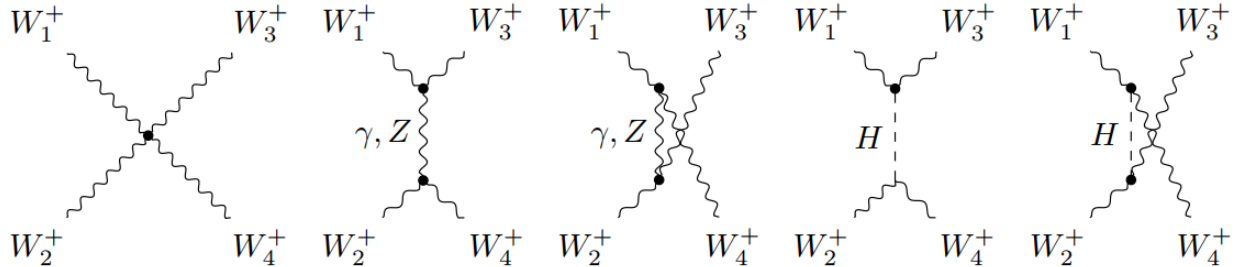


FIGURE 1.13 – $W^\pm W^\pm$ LO diagrams

282 is

$$\mathcal{M} = \mathcal{M}^{QGC} + \mathcal{M}^{TGC} + \mathcal{M}^H \quad (1.21)$$

283 Calculation shows, making an assumption that energies involved are much higher than bosons mass,
284 that

$$\begin{aligned} i \mathcal{M}^{QGC} &= g_W^2 \left[\frac{E^4}{m_W^4} (6 - 2 \cos^4 \theta^*) - 4 \frac{E^2}{m_W^2} \right] \\ i \mathcal{M}^{TGC} &= g_W^2 \left[-\frac{E^4}{m_W^4} (6 - 2 \cos^4 \theta^*) + 3 \frac{E^2}{m_W^2} \right] \\ i \mathcal{M}^H &= g_W^2 \left[\frac{E^2}{m_W^2} \right] \end{aligned} \quad (1.22)$$

285 individually all (QGC,TGC,H) cross-sections grow $\propto E^4$, however adding them all together cancels
286 exactly such dependence.

287 Behaviour of cross-section depending on energy, this for W^+W^- process gives the dependence
288 shown on Fig. 1.14 - only the inclusion of Higgs prevents the divergence with energy. Similar results
289 for more boson pairs are shown on Fig. 1.15 with same conclusion. It thus said that Higgs boson
290 restores unitarity in VBS : more specifically tree unitarity, stating that for any given $2 \rightarrow 2$ process
291 its amplitude with respect to increasing energy cannot grow indefinitely.

292 1.3 VBS measurements at the LHC

293 1.3.1 Motivation

294 Interest to VBS experimental test is two-fold. On one hand, process provide unique opportunity
295 to test self-couplings of gauge bosons via QGC and TGC couplings. Couplings arise from underlying
296 EW symmetry group $SU(2)_L \times U(1)_Y$. Particularly some vertices are forbidden in SM, like neutral
297 Quartic Gauge Couplings (nQGC), and provide a stringent test of the SM. On the other hand,
298 W and Z bosons acquire masses through Higgs mechanism and therefore longitudinal polarisation
299 mode. $V_L V_L$ cross-section is not diverging due to a delicate cancellation mechanism necessarily
300 involving QGC, TGC, Higgs diagrams together. It would only work if Higgs boson's coupling to
301 weak bosons doesn't deviate from SM prediction. Thus, VBS is an indirect probe of Electroweak

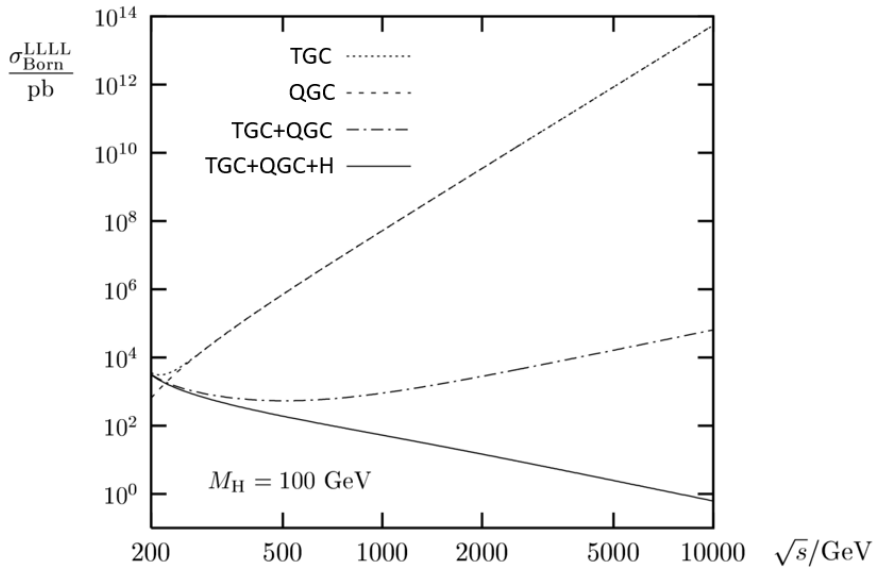


FIGURE 1.14 – Te cross-sections for longitudinal W^+W^- gauge-boson scattering resulting from subsets of the tree-level diagrams. Adapted from [63]

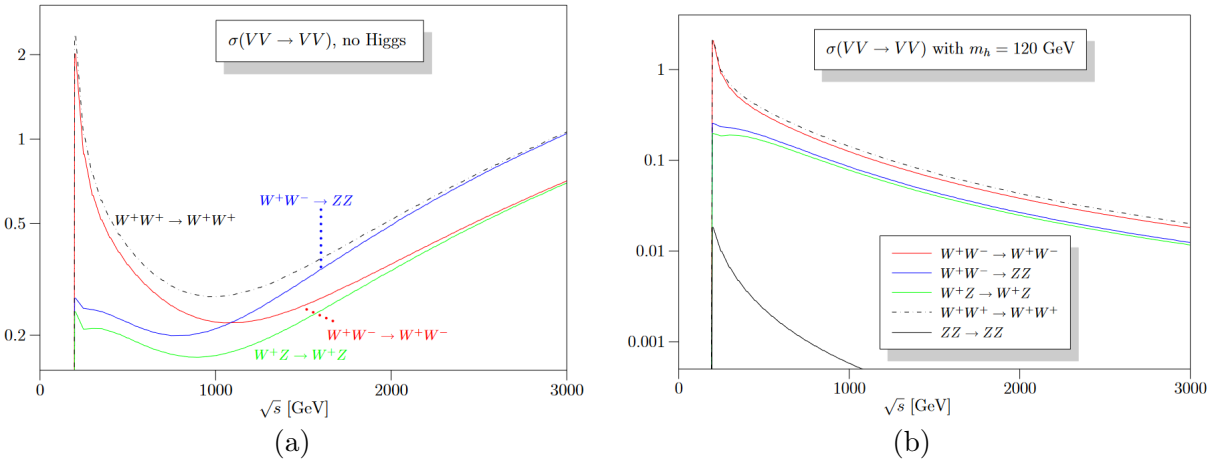


FIGURE 1.15 – Cross-sections for longitudinal component of the electroweak $VVjj$ production depending on energy [17] (a) without Higgs (b) with Higgs

302 Symmetry breaking.

303 **1.3.2 Experimental features**

304 First of all EW VBS process is very rare, as already can be seen from powers of coupling
 305 constant counting giving α_{EW}^6 for $VVjj$ where $V=W,Z$ and α_{EW}^4 for $V\gamma jj$. Also process has a
 306 specific topology that one might want to target :

- 307 • Two jets that radiated vector bosons (called tagging jets) are expected to have large m_{jj}
 308 and large rapidity separation. m_{jj} selection is often used to reduce contamination from TGC
 309 processes
- 310 • Bosons are expected to be emitted centrally and jet activity in central is expected to be small

311 and this is often quantified by Zeppenfeld variable³

$$\xi_X = \left| \left(y_X - \frac{(y_{j_1} + y_{j_2})}{2} \right) / (y_{j_1} - y_{j_2}) \right| \quad (1.23)$$

312 where X is an object or collection of objects centrality of which, with respect to VBS tagging
 313 jets, one wants to define, for example third-leading jet in $p_T \ell\gamma$ system. Smaller values
 314 correspond to more centrality and selection is often applied to obtain separation from QCD
 315 VBS

316 As a concrete example of two points above, Fig. 1.16 shows illustration of an expected EW
 317 $W^\pm Z$ event if both bosons are decaying leptonically.

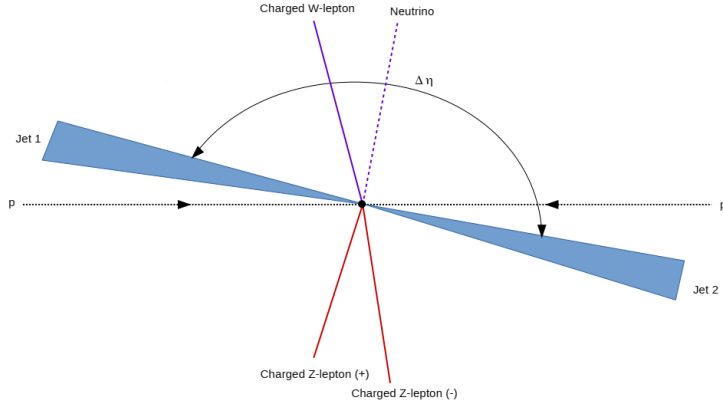


FIGURE 1.16 – Schematic representation of a WZjj-EW event from a pp collision [93]

318 Depending on how massive bosons decay, one might obtain final states which are fully hadro-
 319 nomic (when both bosons are decaying into quarks), semileptonic (when one boson decays leptonically
 320 and second one - into quarks) or fully leptonic. Branching fraction of leptonic decay is smaller
 321 however configuration is “cleaner” to measure - multiple of the analyses that will be shown below
 322 are of this type. On the other hand, fully hadronic final state is dominated by multi-jet background
 323 and was never measured. There are also analyses with photon, their final state is photon together
 324 with either lepton or neutrino pair.

325 1.3.3 Experimental status

326 Despite long-standing interest (first experimental projections for not-cancelled -yet SSC were
 327 published in 80s), because of small cross-sections and rather challenging background of other di-
 328 boson processes, searches for VBS only started with Run-1 LHC data, that would typically result
 329 in seeing 5σ later with Run-2 data . Particularly, ATLAS⁴ reported

- 330 • Evidence [35] and later observation [9] of $W^\pm W^\pm$
- 331 • $Z\gamma$ significance of 2σ [36] and later observation in [12]
- 332 • Observation of $W^\pm Z$ in [10]
- 333 • ZZ observation in [50]

334 With observation being made, people started to measure cross-sections, particularly differen-
 335 tially. Resulting analyses are summarized in Table 1.2 and they constitute inputs to EFT aQGC
 336 combination discussed in Chapter 3.

337 In light of Sec. 1.3.2, Table 1.3 summarizes “common VBS“ selections applied by those analysis.
 338 On top of them, depending on background specific per analysis, listed in “major non-EW4 bkg“

3. Sometimes also confusingly called centrality

4. There are CMS counter-parts to most analyses

TABLE 1.2 – Summary of non-hadronic input analyses to combination

Production	Boson Decay	Ref.	σ_{EW}^{fid} [fb]
$Z\gamma$	$\nu\nu\gamma$	[48]	$0.77^{+0.34}_{-0.3}$
ZZ	$\ell\ell\ell\ell$	[50],[52]	1.27 ± 0.14
same-sign WW	$\ell\nu\ell\nu$	[55]	2.92 ± 0.29
$W^\pm Z$	$\ell\nu\ell\ell$	[56]	0.368 ± 0.07 per lep. mode
$W\gamma$	$\ell\nu\gamma$	[31]	13.2 ± 2.5

339 column (QDC is background for everyone so removed from this list), each team optimizes the
340 selection specifically. Major systematic uncertainties, listed in “major syst” column, often involve
341 theoretical and jet (experimental) ones.

342 In tables there is no analysis with hadronic or semi-leptonic final state. ATLAS VV semileptonic
343 analysis⁵ is not yet published (team is close though) and I’m not able to discuss internal results
344 here. However, VV semileptonic is also an input to combination.

345 Measurements discussed is already a part of ATLAS Standard Model compilation previously
346 shown on Fig. 1.3 - they occupy the right-bottom corner of plot as one of rarest processes measured
347 thus far at the LHC. Additionally, VBS measurements together with Vector Boson Fusion and tri-
348 boson fiducial production cross-sections are compared to SM prediction in Fig. 1.17. Unfortunately,
349 no deviation from the Standard Model is seen. However, motivation for Beyond the Standard Model
350 physics arises elsewhere.

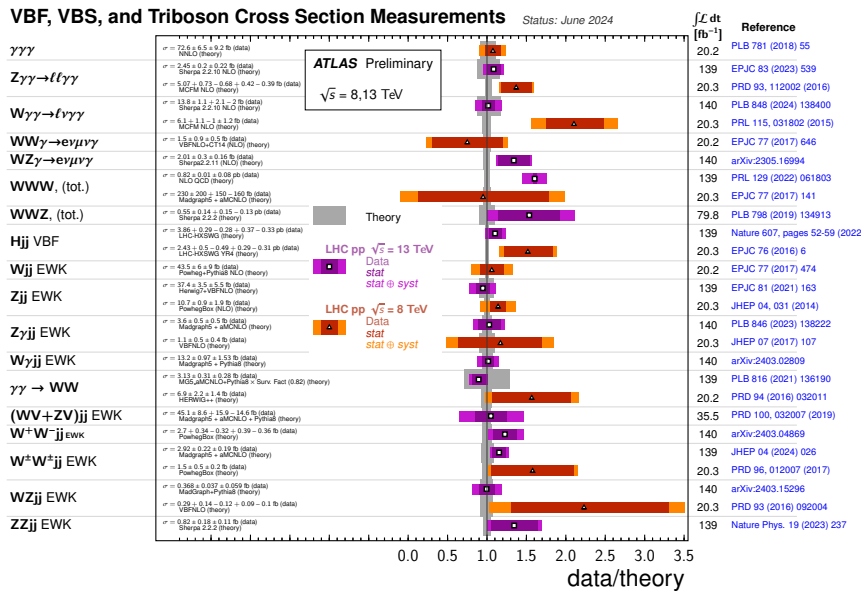


FIGURE 1.17 – The data/theory ratio for several vector boson fusion, vector boson scattering, and triboson fiducial production cross-section measurements. [28].

1.4 Beyond the Standard Model motivation

Thus far no deviations from the Standard Model were seen in VBS measurements (Fig. 1.17), but also in other SM tests (Fig. 1.3). Nevertheless, it’s clear that SM is not a complete theory of

5. ATLAS internal code ANA-STDM-2018-27 : https://atlas-glance.cern.ch/atlas/analyses/analyses/details.php?ref_code=ANA-STDM-2018-27

TABLE 1.3 – Summary of SR selections, backgrounds and systematics of Table 1.2 analyses

Analysis	m_{ij} sel.	ΔY sel.	Zeppenfeld sel.	major non-EW4 bkg.	major syst.
$Z\gamma \rightarrow \nu\nu\gamma$	> 300	-	$\xi_{4\ell} < 0.4$	$W(\ell\nu)\gamma jj$ QCD and EWK $t\bar{t}\gamma jj$ w/ semilep., lep. dec.	$Z(\rightarrow \bar{\nu}\nu)\gamma jj$ EWK, QCD model. exp. jet, E_T^{miss}
$ZZ \rightarrow \ell\ell\ell\ell$	> 300	$\Delta\eta_{jj} > 2.0$	$\xi_{4\ell} < 0.4$	Non-prompt leptons $t\bar{t}Z, WWZ, WZZ$	Jets Unfolding Backgrounds
$W^\pm W^\pm \rightarrow \ell\nu\ell\nu$	> 500	$\Delta y_{jj} > 2.0$	-	$WZ/\gamma^* jj$	bkg. misid. leptons QCD $W^\pm W^\pm$ theor. model. EW $W^\pm W^\pm$, QCD corrections JES&JER, Luminosity
$W^\pm Z \rightarrow \ell\nu\ell\ell$	> 500	$\eta_{j1} \cdot \eta_{j2} < 0$	-	$ZZ, t\bar{t}Z, t\bar{t}W$	EW theor. model QCD theor. model. PDFs
$W\gamma \rightarrow \ell\nu\gamma$	> 1000	$\Delta y_{jj} > 2.0$	$\xi_{W\gamma} < 0.35$	$W\gamma jj, t(1+)\gamma$ misid. W+jet	exp. jets exp. lepton, photon, pile-up Strong, EW $W\gamma jj$ model.

- 354 Nature :
- 355 • Gravity, which is fourth fundamental force, is not included in the SM
- 356 • Neutrino masses (much smaller than other ones but non-zero), following from observation of
- 357 neutrino oscillations, are not included
- 358 • Dark Matter, evidence for which is provided from astronomical and cosmological data, is not
- 359 included in the SM
- 360 • Asymmetry between matter and anti-matter is not following from the SM

361 **1.5 Effective Field Theory**

362 We know that SM is not complete, however there is no one particularly striking theory to start

363 searching for at the LHC, like it was with SM before Higgs discovery. At the same time, there are way

364 too many other models published on arXiv and searching for each of them is practically undoable.

365 Therefore, it is desirable to formulate a model-independent approach which gives “complete set of

366 possibilities“. Working within such framework allows to find a “direction“ where New Physics more

367 likely lies.

368 One such model-independent approach is an Effective Field Theory (EFT). EFT also allows to

369 probe energy scales currently unreachable : underlying assumption that SM is low energy limit of

370 some other theory that we don't know yet and typical scale Λ of this theory is well above the EW

371 scale. Higher-scale theory should have symmetries and field content as the SM. In this case one

372 organizes NP is Taylor series of form

$$\mathcal{L}_{\text{EFT}} = \mathcal{L}_{\text{SM}} + \sum_i \frac{c_i}{\Lambda^2} \mathcal{O}_i^{(d=6)} + \sum_i \frac{c_i}{\Lambda^4} \mathcal{O}_i^{(d=8)} + \dots \quad (1.24)$$

373 i.e. SM Lagrangian is extended with new non-SM operators \mathcal{O}_i entering together with coeffi-

374 cients (called Wilson coefficients) c_i . Each next term is suppressed by $1/\Lambda^{d-4}$. Dimension-5 and

375 dimension-7 are excluded as they violate lepton number conservation. Dimension-6 and dimension-

376 8 are the largest terms left. Here series is truncated at dimension-8 as it's the smallest dimension

377 exclusively modifying quartic gauge couplings. The corresponding operators will be introduced in

378 Sec. 3.2

³⁷⁹ 2 - Experimental context

³⁸⁰ 2.1 Historical overview

³⁸¹ LHC as we know it today is a result of decades of work by many people - key events and dates
³⁸² are summarized in Table 2.1. Already in 1979 (before LEP approval), its construction was foreseen,
³⁸³ as discussed in LEP White Book [101] : “Tunnel with 27 km circumference and a diameter of 5
³⁸⁴ m, with a view to the replacement of LEP at the end of its activities by a proton-proton Collider
³⁸⁵ using cryogenic magnets“ .

³⁸⁶ 2.2 Accelerator complex

³⁸⁷ 2.2.1 Overview

³⁸⁸ For ATLAS, colliding beams are provided by the Large Hadron Collider (LHC). Beams are
³⁸⁹ colliding instead of one beam impinging on a fixed target as it allows to reach a higher center-of-
³⁹⁰ mass (CM) energy. The LHC is the largest particle accelerator in the world (27 km ring), at the
³⁹¹ moment of writing, operating at $\sqrt{s} = 13.6 \text{ TeV}$ CM energy (another category where LHC is the
³⁹² most powerful in the world). To reach that energy, a whole chain of accelerators is used, partially
³⁹³ re-using pre-LHC components. Proton-proton specific part of the accelerator chain is shown on
³⁹⁴ Fig. 2.1.

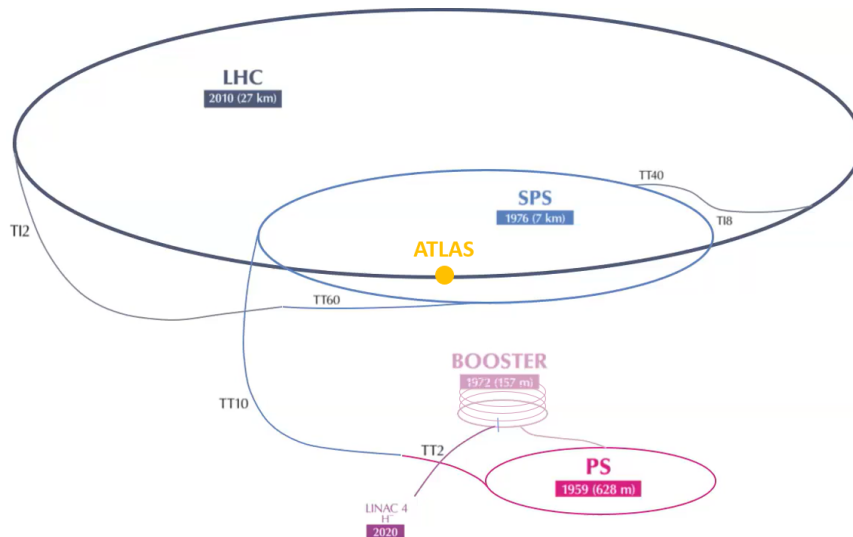


FIGURE 2.1 – LHC chain, proton-proton injector path only. Adapted from [90]. Only the ATLAS experiment is located.

³⁹⁵ 2.2.2 Injector chain

³⁹⁶ It all starts with a hydrogen bottle, a clone of which one can buy in a CERN souvenir shop.
³⁹⁷ H^- ions then enter the LINAC4¹ which accelerates them up to 160 MeV energy and forms
³⁹⁸ bunches thanks to Radio Frequency (RF) cavities, as illustrated on Fig. 2.2a. They feature an
³⁹⁹ alternating voltage, and particles passing through them will gain different amounts of energy de-
⁴⁰⁰ pending on their phase : particles falling behind will be accelerated more, and the ones leading can
⁴⁰¹ be decelerated. RF cavities are used in all parts of the whole chain.

1. LINAC3 is a starting point for heavy ions

1984	Workshop on a Large Hadron Collider in the LEP tunnel, Lausanne, Switzerland where the feasibility of hadron collider in future LEP tunnel was discussed
1987	Workshop on the Physics at Future Accelerators, La Thuile, Italy. The Rubbia “Long-Range Planning Committee“ recommends the Large Hadron Collider as the right choice for CERN’s future.
1990	LHC Workshop, Aachen, Germany (discussion of physics, technologies, and detector design concepts, including the first realistic MC studies).
1992	General Meeting on LHC Physics and Detectors, Evian-les-Bains, France (with four general-purpose experiment Expressions of Interest presented).
1993	Three Letters of Intent were evaluated by the CERN peer review committee LHCC. ATLAS and CMS were selected to proceed to a detailed technical proposal.
1994	The LHC accelerator was approved for construction, initially in two stages.
1995	LHC Conceptual Design Report.
1996	ATLAS and CMS Technical Proposals approved.
1996	Approval for the construction of the 14 TeV LHC , to be completed in 2005.
1997	Formal approval for ATLAS and CMS to move to construction.
1997	Construction of the experiments commences (after approval of detailed Technical Design Reports of detector subsystems).
2000	Assembly of experiments commences at CERN. The LEP accelerator is closed down to make way for the LHC .
2008	LHC experiments ready for pp collisions. LHC starts operation. An incident stops the LHC operation.
2009	LHC restarts operation, first pp collisions at 900 GeV recorded by the LHC detectors.
2010	LHC collides protons at high energy (center of mass energy of 7 TeV).
2012	LHC operates at 8 TeV : announcement of the discovery of a Higgs-like boson.
2015	After a shutdown in 2013-2014, the LHC operates at 13 TeV for Run-2 until 2018.
2022	Start of Run-3

TABLE 2.1 – Some key dates of the LHC project. Adapted from [8]

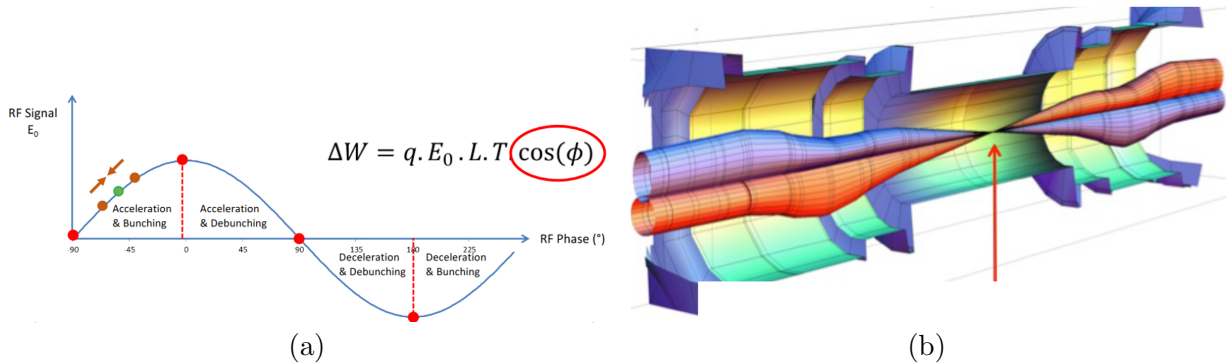


FIGURE 2.2 – (a) RF cavity principle of operation illustration [99] (b) beam squeezing at IP illustration

402 The next stage after LINAC4 is the Proton Synchrotron Booster (PSB), which is, in fact, not a
 403 single ring but four independent rings, each with a circumference of 157 m. PSB is the place where
 404 H^- gets converted to protons. The output of the PSB is a proton beam with 2 GeV energy. Some
 405 experiments use this beam already, e.g., ISOLDE studies atomic nuclei, including the most exotic
 406 species.

407 The next stage after the PSB is the Proton Synchrotron (PS) - the oldest operating synchrotron
 408 at CERN with a circumference of 628 m. The PS raises the proton energy to 26 GeV . The PS
 409 is the most flexible regarding “RF gymnastics“. Particularly, it’s the only stage in the accelerator
 410 chain that has combined-function magnets : not just dipoles bending the trajectory followed by the
 411 quadrupoles for focusing but a hybrid of the two. Among notable experiments happening at the
 412 PS is AD-ELENA, anti-proton deceleration facility, where recently measurement was done showing
 413 that antihydrogen atoms, released from magnetic confinement in the ALPHA-g apparatus, behave
 414 in a way consistent with gravitational attraction to the Earth [66].

415 Last pre-LHC stage is the Super Proton Synchrotron (having a ring of 6.9 km length), acce-
 416 lering the protons from the PS up to 450 GeV. It’s the first CERN accelerator underground.
 417 Separate dipole and quadrupole magnets are used (unlike PS). In the 80s it was operated as a
 418 proton-antiproton collider ($S\bar{p}S$ project), leading to the Nobel Prize for the discovery of the W
 419 and Z bosons² by the UA1³ and UA2⁴ experiments [68, 70]. The SPS is particularly relevant for
 420 this thesis as it delivers the beam to the test area (H6A) where ALTIROC tests were performed (see
 421 Chapter 6, Chapter 8).

422 2.2.3 LHC

423 The LHC is the first and only accelerator in the chain with two beams circulating in it (in oppo-
 424 site directions, going through cold mass 19.4 cm apart) before collision. Each beam is accelerated up
 425 to 6.8 TeV energy through a series of RF cavities. Keeping those beams on the trajectory requires
 426 usage of innovative, at the time of construction, superconducting magnets. The main magnets are
 427 immersed in superfluid helium and operate at a temperature of 1.9 K (RF cavities are also super-
 428 conducting and operated at 4.5 K). LHC magnets are not only dipoles (main dipoles having a field
 429 of 8.33 T, 1232 of them) and quadrupoles (833 used) but also corrector magnets (6000 are used)
 430 for beam quality. Once LHC beams reach their top energy, they are focused to four Interaction
 431 Points (IP), ATLAS being one of them. At the IP beam size reaches transverse size of $\approx 10\mu m$.

-
2. Providing, among other things, belief that a “dirty“ hadron collider can do great discoveries
 3. First hermetic hadron collider detector, like ATLAS
 4. Fine (by its time) calorimeter cells, operated in phases - like ATLAS

432 Squeezing is illustrated on Fig. 2.2b. However, one cannot squeeze at IP infinitely as β^* will then
 433 explode away from the IP and the beam may hit the accelerator.

434 LHC nominal cycle is shown on Fig. 2.3. By design, LHC can collide up to 2800 bunches. There
 435 are 1.6×10^{11} protons in each bunch. Spacing between bunches is 25 ns, coming from the extraction
 436 from the PS - injection to SPS, done via kicker whose rise-time is not instantaneous but 25 ns.
 437 Similarly, the SPS-LHC interface is done via another kicker, which also introduces spacing between
 438 groups of batches.

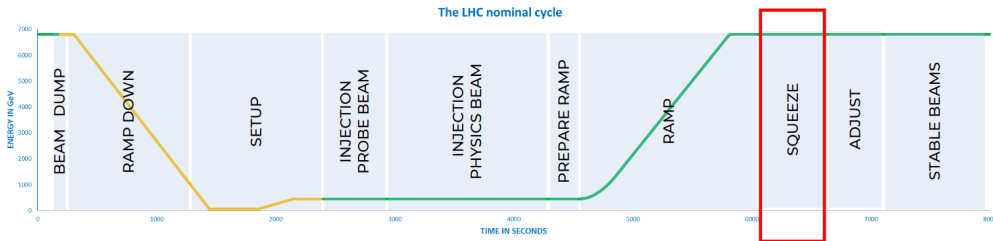


FIGURE 2.3 – The LHC nominal cycle [99]

439 2.2.4 Luminosity

440 The instantaneous luminosity can be written as

$$L = \frac{N_b^2 n_b f_{rev} \gamma}{4\pi \varepsilon_n \beta^*} F = \underbrace{\frac{c}{4\pi} \times \frac{\gamma}{l}}_{\text{accelerator features}} \times \underbrace{\frac{N_b^2 n_b}{\varepsilon_n \beta^*}}_{\substack{\text{beam intensity features}}} \times \underbrace{\frac{F}{l}}_{\text{beam geometry features}} \quad (2.1)$$

441 where γ and l are, respectively, the “energy” and length of the machine, n_b and N_b are, respectively,
 442 the number of bunches and particles in a bunch. The size of the beam at IP is controlled by
 443 ε_n (normalized emittance) and β^* (beta function) and a geometry reduction factor (0.55) taking
 444 into account that beams are rotated and not head-on at IP .

445 The integrated delivered by the LHC and collected per day in 2024 (year of writing) is shown
 446 on Fig. 2.4

447 2.3 ATLAS

448 2.3.1 From proto-collaborations to Higgs discovery

449 In Evian meeting (see Table 2.1) four general-purpose experiment concepts were presented -
 450 too many for the budget. Two of them, toroid proto-experiments ASCOT and EAGLE (whose
 451 sketches are shown on Fig. 2.5) then merged to form the ATLAS⁵ (A Toroidal LHC ApparatuS)
 452 collaboration.

453 ATLAS then submitted a Letter of Intent [3] in 1992, where some key decisions about the
 454 detector were made and later refined for the ATLAS Technical Proposal (TP) [4]⁶. According to
 455 TP, detector optimization is guided by physics issues such as the sensitivity to the largest possible
 456 Higgs mass range, the searches for heavy W- and Z-like objects, the searches for supersymmetric
 457 particles, the searches for compositeness of the fundamental fermions, the investigation of CP

5. A vote decided the name, and funnily, the second-leading option in the vote was ALICE, but it has nothing to do with today’s ALICE (one of four big LHC experiments)

6. In the LHCC open session, the TDR presentation consisted of four major talks. One of them is about the Calorimeter, notably for IJCLab, was given by Daniel Fournier, who received La Prix Lagarrigue in 2023 for his Calorimeter contributions

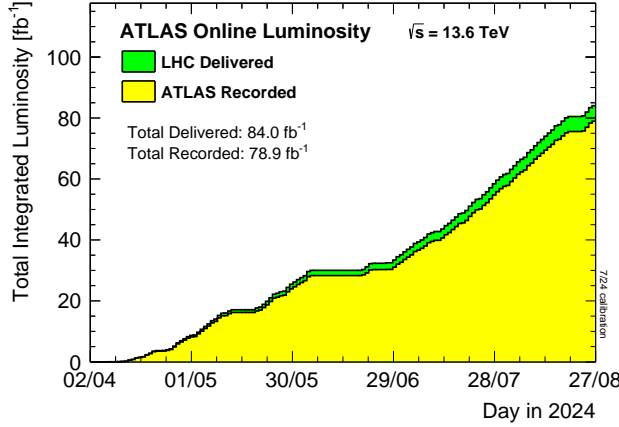


FIGURE 2.4 – Cumulative luminosity versus time delivered to (green) and recorded by ATLAS (yellow) during stable beams for p-p collisions at 13.6 TeV center-of-mass energy in 2024. The delivered luminosity accounts for luminosity delivered from the start of stable beams until the LHC requests ATLAS to put the detector in a safe standby mode to allow for a beam dump or beam studies. The recorded luminosity reflects the DAQ inefficiency, as well as the inefficiency of the so-called “warm start” [27]

458 violation in B-decays, the detailed studies of the top quark - so a rich physics program was foreseen
 459 from the beginning. The Higgs search was particularly important, and the detector had to cover
 460 the mass range $m_H > 80 \text{ GeV}$ (lower masses were already excluded by LEP experiments) by being
 461 sensitive to the following processes

462 $80 < m_H < 100 \text{ GeV}$: $H \rightarrow b\bar{b}$ from WH, ZH and $t\bar{t}H$ using a ℓ^\pm tag and b-tagging

463 $90 < m_H < 150 \text{ GeV}$: $H \rightarrow \gamma\gamma$

464 $130 < m_H < 2m_Z \text{ GeV}$: $H \rightarrow ZZ^* \rightarrow 4\ell^\pm$

465 $2m_Z < m_H$: $H \rightarrow ZZ \rightarrow 4\ell^\pm, 2\ell^\pm 2\nu$

466 $m_H < 1000 \text{ GeV}$: $H \rightarrow WW, ZZ \rightarrow \ell^\pm \nu jj, 2\ell^\pm jj$ from WW, ZZ using tagging of forward jets

467 Therefore, the detector should be able to provide as many signatures as possible using electrons,
 468 photons, muons, jets, missing transverse energy measurements, and b-quark tagging. Large $|\eta|$
 469 acceptance is desired together with the capability of triggering on and measurements of particles at
 470 low- p_T thresholds. Also, the cross-sections for most of these processes are small, and the detector
 471 should be able to cope with high instantaneous luminosities.

472 Taking into account the requirements from the physics program, the technologies available at
 473 the time and the budget constraints, the basic detector concepts were settled by the end of 1995⁷
 474 and led to the following configuration

- 475 • A cylindrical, as hermetic as possible (for) detector
- 476 • The usage of a toroidal magnet with eight superconducting coils in an air-core configuration⁸
- 477 • A configuration with a barrel (taken by innovative “accordion” lead-LAr sampling EM calorimeter and pre-sampler) and two extended barrel cylinders (for iron-scintillator tile hadronic calorimeters)
- 478 • A muon spectrometer employing separate precision and trigger chambers
- 479 • An inner detector with pixel detectors for the innermost parts, followed by a Silicon strip detectors, followed by straw-tube tracker

7. Some important decisions were made later ; for example, TDAQ TDR was written only in 2003

8. Initially 12, but this was too expensive

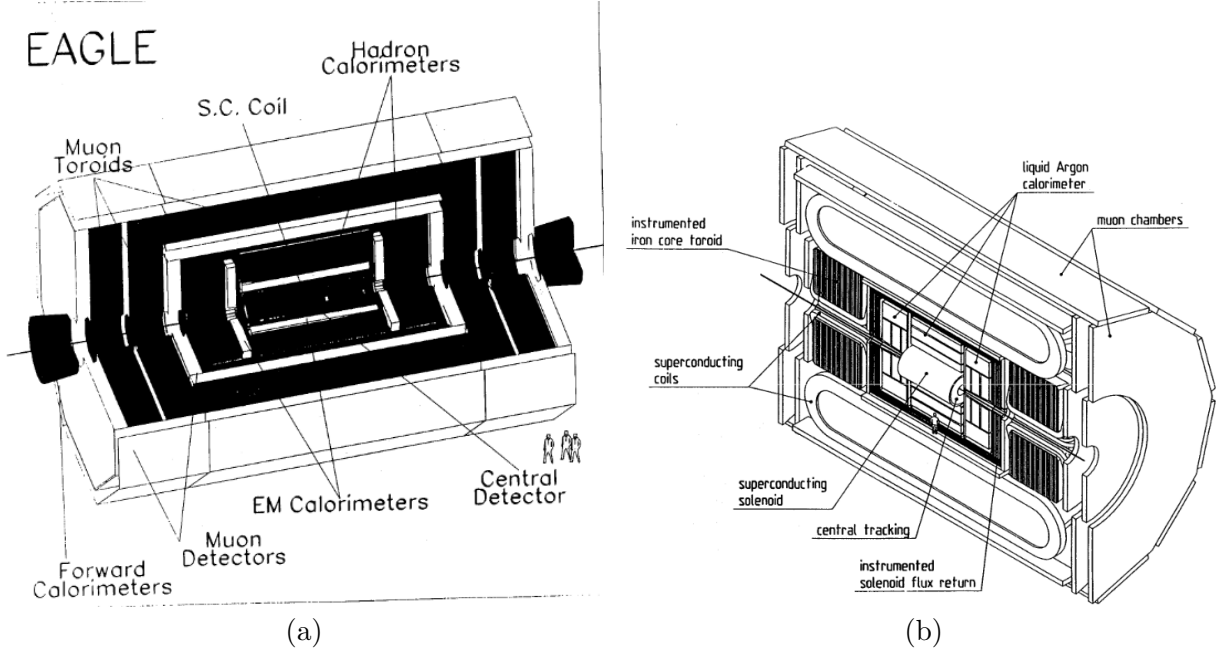


FIGURE 2.5 – (a) EAGLE with warm iron barrel and end cap toroids [80] (b) ASCOT with a superconducting air-core barrel and warm iron end cap toroids [91]

483 Requirements for the sub-detectors are summarized in Table 2.2. After extensive R&D, sub-
 484 detectors reached the testbeam stage happening in 2002-2006, followed by two years of installation
 485 in the cavern. Once installed, cosmic ray tests were done in 2008-2009. The first stable colliding
 486 beams were recorded on December 5, 2009 ; the rest of the year was devoted to 900 GeV collisions.
 487 Run-1 happened in 2010-2012, collecting data for the Higgs discovery announced in 2012 [29]⁹ for
 488 which the Nobel Prize was awarded : a significant design goal was reached. .

489 2.3.2 Run-3 detector configuration

490 ATLAS evolved from the TP to Run-3, and the schematic view of the current detector is shown
 491 on Fig. 2.6. It consists of an inner tracking detector (ID) surrounded by a thin superconducting
 492 solenoid, electromagnetic and hadronic calorimeters, and a muon spectrometer incorporating three
 493 large superconducting air-core toroidal magnets - most of this was foreseen in the TP . The dimen-
 494 sions of the detector are 25 m in height and 44 m in length, the overall weight of the detector is
 495 approximately 7000 T : it is the largest experiment at the LHC.

496 Among the detector sub-systems, the ID and forward sub-detectors will be shown in a bit more
 497 detail. The performance of the ID is strongly linked to and motivate the construction of the HGTD
 498 for the HL-LHC, which is discussed in Chapter 6, Chapter 7, Chapter 8. The timing information
 499 is complementary to the spatial information of the ID. The forward detectors are at the core of
 500 the work on fJVT described in Chapter 4 and crucial to tag forward jets in the VBS analyses,
 501 combination of which is discussed in Chapter 3.

502 Inner detector

503 The ID schematic view is shown on Fig. 2.7. It is immersed in a 2 T magnetic field (which bends
 504 the particles track) generated by the central solenoid, which extends over a length of 5.3 m with a
 505 diameter of 2.5 m. The overall radial extension of ID is $0 < r < 1150 \text{ mm}$, and length covers the
 506 region $0 < |z| < 3512 \text{ mm}$. The ID covers $|\eta| \leq 2.5$ and is intended to reconstruct the trajectory,

9. Also discovered by the CMS collaboration [32]

Detector component	Minimally required resolution, characteristics	η coverage	
		Measurement	Trigger
EM calorimetry	$10\%/\sqrt{E} \oplus 0.7\%$	± 3	± 2.5
Pre-shower detection	Enhanced $\gamma - \pi^0$ and γ -jet separation, direction measurements	± 2.4	
Jet and missing E_T Calorimetry barrel and end-cap forward	$50\%/\sqrt{E} \oplus 3\%$ $100\%/\sqrt{E} \oplus 10\%$	± 3 $3 < \eta < 5$	± 3 $3 < \eta < 5$
Inner detector	30% at $p_T = 500\text{GeV}$ Enhanced electron identification τ - and b-tagging Secondary vertex detection at initial luminosities	± 2.5 ± 2.5 ± 2.5 ± 2.5	
Muon detection	10% at $p_T = 1\text{TeV}$ in stand-alone mode at highest luminosity	± 3	± 2.2

TABLE 2.2 – General detector performance goals [4]

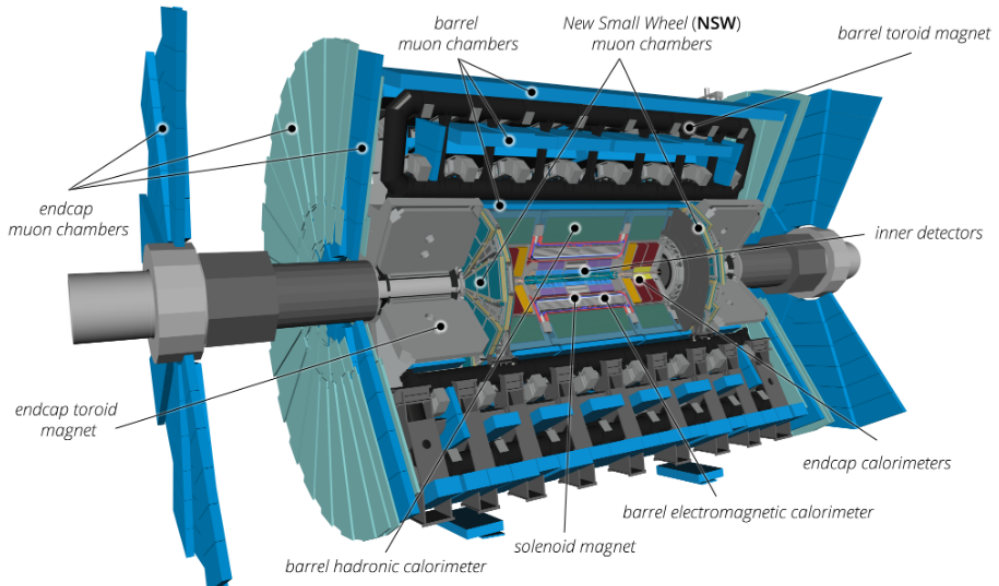


FIGURE 2.6 – Cut-away view of the Run 3 configuration of the ATLAS detector indicating the locations of the larger detector sub-systems [51]

measure momentum, charge, and contribute to the PID of charged particles by detecting their interactions with the material at several points along the path. Another ID function is the location of the primary vertex of the events, which is done by extrapolating tracks to the beam axis.

The ID is composed of Pixel, SCT, and TRT sub-systems.

- The Pixel detector consists of the IBL (12 million channels), three barrel layers, and three discs on each side, and has approximately 80 million readout channels. IBL whose sensors have $50 \mu\text{m} \times 250 \mu\text{m}$ ($r\phi, z$) pixels at an average radius of 33.4 mm. The pixel layers are segmented in $r\phi$ and z . Typically, a track crosses three pixel layers. For these three outer layers, all pixel sensors are identical, with a pixel size of $50 \mu\text{m} \times 400 \mu\text{m}$
- The SCT (having ≈ 6.3 million readout channels) has four strip layers(each is double-sided). In the barrel region, this detector uses small-angle (40 mrad) stereo strips to measure both $r\phi$ and z , with one set of strips in each layer parallel to the beam direction, measuring $r\phi$. They comprise two 6.4 cm long daisy-chained sensors with a strip pitch of $80 \mu\text{m}$. In the endcap region, the detectors have a set of strips running radially and a set of stereo strips at an angle of 40 mrad. The mean pitch of the strips is also approximately $80 \mu\text{m}$
- The TRT is located furthest away and intended to provide continuous tracking and electron identification capability by detecting transition radiation X-ray photons. TRT is built from several layers of gas-filled straw tubes interleaved with transition radiation material. The 300000 thin-walled proportional-mode drift tubes provide on average 30 (r, ϕ) points with a $130 \mu\text{m}$ resolution for charged particle tracks with $|\eta| < 2$ and $p_T > 0.5 \text{ GeV}$

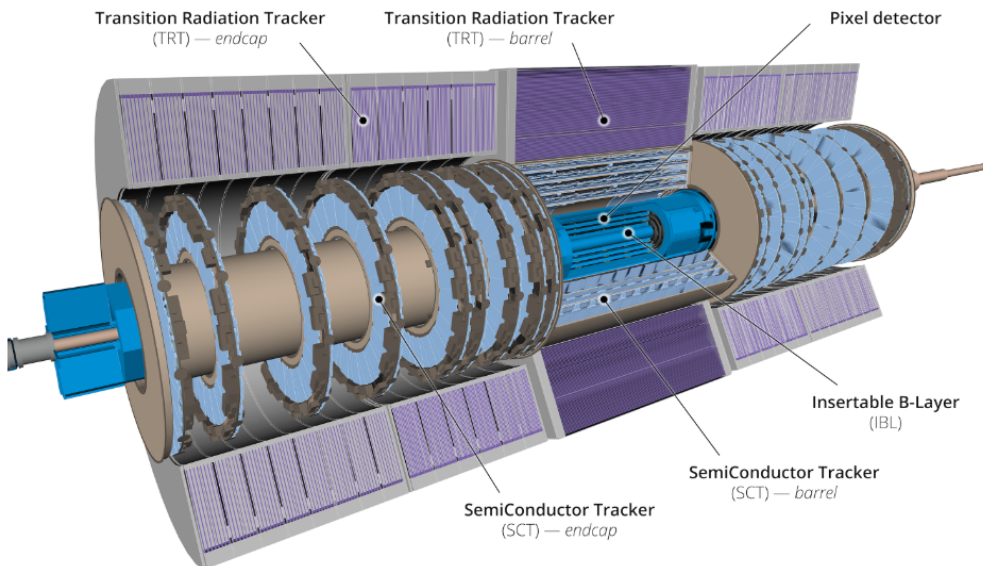


FIGURE 2.7 – Cut-away view of the ATLAS ID [51]

The transverse momentum resolution is expressed as

$$\frac{\sigma_{p_T}}{p_T} = a \cdot p_T[\text{GeV}] \oplus b \quad (2.2)$$

with $a=0.05\%$ and $b=1.6\%$ for cosmic ray muons measurement.

Forward calorimeters

The purpose of the calorimeters is to measure the energies and positions of charged and neutral particles that interact electromagnetically or strongly by absorbing as much particle energy as possible. ATLAS used sampling calorimeters built from alternating layers of absorbing layers (intended

533 to stop incoming particles, thickness depends on $|\eta|$) and active layers (intended to measure the
 534 deposits). A schematic view of all calorimeters is shown on Fig. 2.8 ; they are located outside of the
 535 ID.

536 The calorimeters in the forward $|\eta|$ region are LAr calorimeters and there are two systems
 537 covering different $|\eta|$ ranges : most-forward region $3.1 < |\eta| \leq 4.9$ is covered by FCal(has electro-
 538 magnetic and hadronic part) and $1.5 < |\eta| \leq 3.2$ is covered by electromagnetic endcap(EMEC) and
 539 hadronic endcap (HEC).

- 540 • FCal has 3542 readout channels and comprises three layers : FCal1, FCal2, and FCal3, where
 541 the granularity is different in each, per $|\eta|$. For example FCal1 covers $3.15 < |\eta| \leq 4.83$ and
 542 $\Delta x \times \Delta y$ (cm) is 3.0×2.6 for $3.15 < |\eta| \leq 4.3$ but $\Delta x \times \Delta y$ is about four times finer for
 543 $3.10 < |\eta| \leq 3.15$ and $4.3 < |\eta| \leq 4.83$
- 544 • HEC has 5632 readout channels and four layers. The granularity in $\Delta\eta \times \Delta\phi$ is 0.1×0.1 for
 545 $1.5 < |\eta| \leq 2.5$ and 0.2×0.2 for $2.5 < |\eta| \leq 3.2$
- 546 • EMEC has 62208 readout channels and three layers. Organization of segmentation can be
 547 shown with 2nd layer, which has $\Delta\eta \times \Delta\phi$ is 0.025×0.025 for $1.425 < |\eta| \leq 2.5$ and larger
 548 for $1.375 < |\eta| \leq 1.425$ (0.05×0.025) and $2.5 < |\eta| \leq 3.2$ (0.1×0.1)

549 The energy resolution of the calorimeter is often expressed as

$$\frac{\sigma_E}{E} = \frac{a}{\sqrt{E}} \oplus \frac{b}{E} \oplus c \quad (2.3)$$

550 $\frac{b}{E}$ is typically negligible. Overall for electromagnetic showers performance is better compared to
 551 hadronic. For EMEC (HEC) $a \approx 10\%$, $c \approx 1\%$ ($a \approx 50\%$, $c \approx 4\%$). For FCAL $a \approx 100\%$, $c \approx 10\%$.

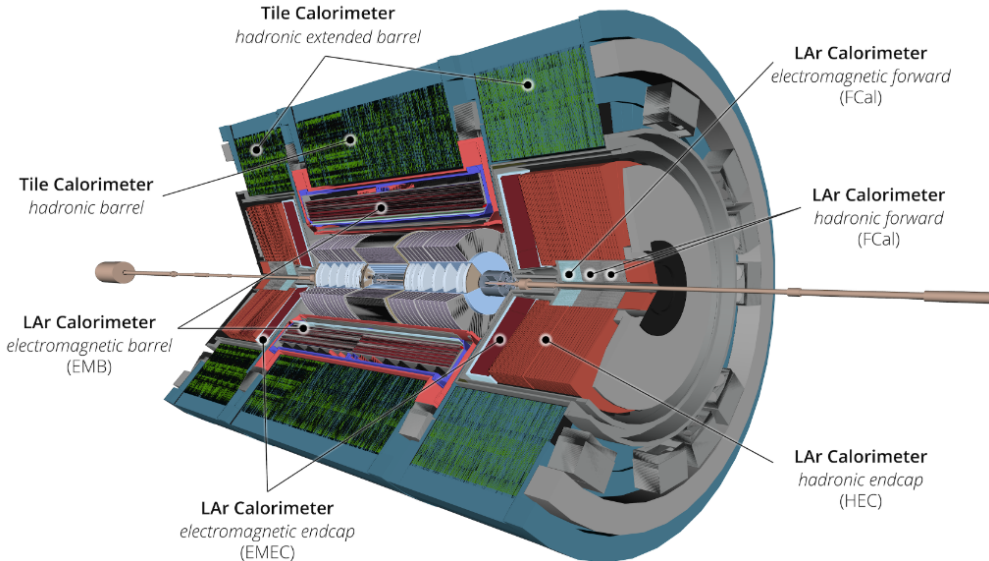


FIGURE 2.8 – Cut-away view of the ATLAS calorimeters [51]

552 Other calorimeters, muon systems, TDAQ

553 Non-forward calorimeters include electromagnetic barrel (EMB, just outside of ID) and hadronic
 554 barrel Tile (concentric and outside of EMB), hadronic extended barrel Tile (located in the “corner”).
 555 EMB is an LAr calorimeter like the ones in the forward region. Tile(s) is the only ATLAS non-LAr
 556 calorimeter made of a plastic scintillator as an active material and a low-carbon steel absorber
 557 plate.

558 The Muon Spectrometer (MS) is a sub-system located at the largest radius (at $r=11$ m), behind
 559 the ID and the calorimeters for the reason that muons lose only a tiny fraction of their energy
 560 interacting with more inner-lying sub-detectors. A separate from ID magnetic field is used. As MS
 561 is large, one needs to use a detector technology “easily“ scalable in size but not in price - various
 562 kinds of gaseous detectors are used. MS covers $|\eta| < 2.7$ and can be used independently of other
 563 sub-detectors, however, combining its information with ID is beneficial.

564 The trigger and Data Acquisition (TDAQ) system is based on a two-level trigger system served
 565 by the Data Acquisition (DAQ) system. The trigger is responsible for the event selection. Given
 566 the rate of collisions, it’s impossible to both record and store all of them, so one needs to decide
 567 on what to keep. Two levels of triggers are implemented : a Level-1 Trigger (L1, based on custom-
 568 built electronics) and High-Level Trigger (HLT, based on software implemented on commodity
 569 computers) After the trigger decision, DAQ transports data from custom sub-detector electronics
 570 to offline processing.

571 2.3.3 Object reconstruction

572 Most analyses rely on reconstructed jets and at least one another type of object : electron,
 573 photon, muon or MET. However, on object reconstruction, I only worked on jets (see Chapter 4)
 574 and therefore other types of objects would only be briefly mentioned, for completeness.

575 Jets

576 Isolated quarks or gluon cannot be observed due to color confinement, instead multiple of them
 577 hadronize together to form color singlets. As a result of chain of hadronizations occurring while
 578 particles are propagating from IP through detector, so-called “jet“ is formed. Illustration of such
 579 process is shown on Fig. 2.9. Experimental task, then, is to reconstruct the jet according to certain
 580 algorithm : cluster tracks (reconstructed from tracker hits, giving track jets), cluster calorimeter
 581 clusters (giving calorimeter jets) or combination of the two. In simulation, it’s possible to build
 582 so-called truth jets, which typically means inputs are particle-level (giving particle jets). Algorithm
 583 maps set of final state 4-momenta to jet 4-momenta. It’s desirable that algorithm has the following
 584 properties (called IRC safety requirements)

- 585 • Infrared safety : addition of soft particles among jet components does not affect the outcome
 of the clustering
- 587 • Collinear safety : splitting of one particle into two collinear ones does not affect the outcome
 of the clustering

589 Algorithm should work without taking too much computer resources.

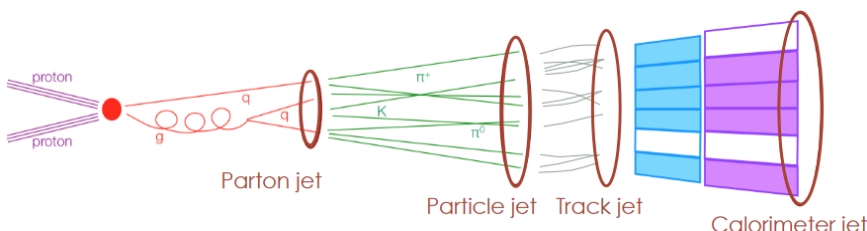


FIGURE 2.9 – Illustration of jet formation [94].

590 anti- k_t is a sequential pair-wise algorithm [24] chosen to be used at the LHC. Following strategy
 591 is employed : inputs are combined according to metric defined as

$$d_{ij} = \frac{1}{\max(p_{Ti}^2, p_{Tj}^2)} \frac{\Delta R_{ij}^2}{R^2} \quad (2.4)$$

$$d_{iB} = \frac{1}{p_{Ti}^2} \quad (2.5)$$

592 where p_{Ti}, p_{Tj} are transverse momentums of the input pair and $\Delta R_{ij} = \sqrt{(y_i - y_j)^2 + (\phi_i - \phi_j)^2}$
 593 is a distance between them in $y - \phi$ space. Inputs should have $p_T > p_T^{min}$ where p_T^{min} a parameter
 594 user defines. R is another a free parameter that user defines. At each step, minimum between d_{ij}
 595 and d_{iB} is computed. If d_{iB} turns out to be smaller than i is declared to be a jet a removed from
 596 the list of inputs, otherwise if d_{ij} is smaller than i,j are combined into one single input by taking
 597 the sum of their 4-momenta. Most energetic inputs would be clustered first.

598 There are two main reasons why anti- k_t became the default jet algorithm (apart from IRC
 599 safety). One is that resulting jets have circular shape, as shown in Fig. 2.10a. Also resulting jet p_T
 600 is linear as function of transverse momentum of one of the inputs.

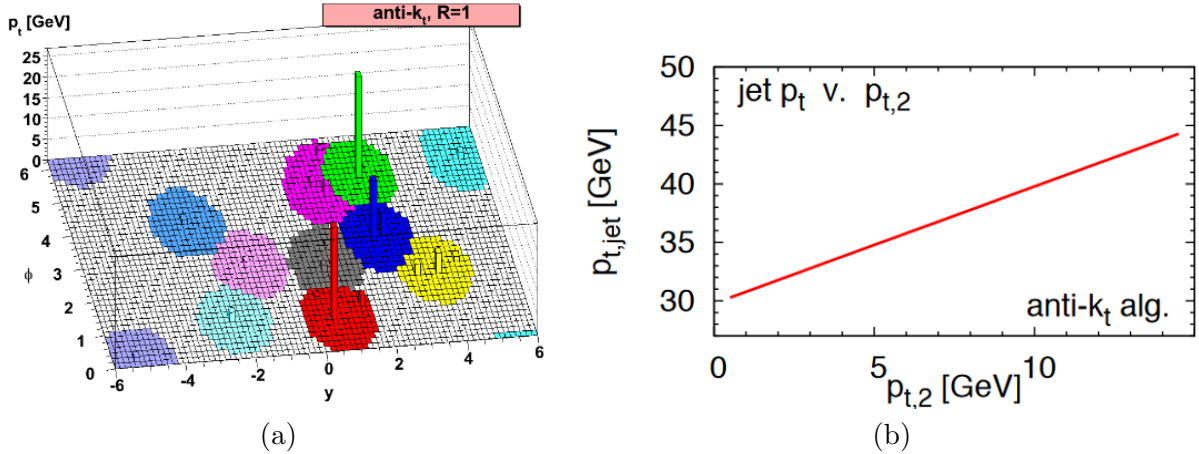


FIGURE 2.10 – (a) A sample parton-level event together with many random soft “ghosts“, clustered with anti- k_t algorithm [24] (b) anti- k_t jets as function of transverse momentum of one of the inputs [96]

601 Typical values for R currently used in ATLAS range from 0.4 to 1. In what follows focus will
 602 be on R=0.4 jets, also called small-R jets, because that's a most common type of jet used through
 603 the thesis - for fJVT calibration (see Chapter 4) and in all analyses in VBS combination (see
 604 Chapter 3).

605 Currently, default ATLAS algorithm to prepare inputs to clustering algorithm is particle flow (PFlow) [6]
 606 and resulting jets are named “PFlow jets“. PFlow utilized information from both the tracker and
 607 the calorimeter which are combined to form the signals. In chronologically previous approach jets
 608 were built from topological cluster of calorimeter cells (topo-clusters)[7] only and resulting jets are
 609 referred to as “EMtopo jets“. Motivations to use PFlow instead of EMtopo jets are that for low- p_T
 610 charged particles, tracker has (compared to calorimeter) significantly better momentum resolution,
 611 lower p_T threshold (400 MeV) for reconstruction and better angular resolution. On the other hand,
 612 at high energies calorimeter’s energy resolution is superior to that of tracker. Therefore, it is advan-
 613 tageous to combine the two types of information. Key steps of PFlow algorithm are summarized on
 614 Fig. 2.11 - major goal is to avoid double-counting of energy in the reconstruction. Either tracker or
 615 calorimeter measurement is used. If a particle’s track measurement is to be used, the corresponding
 616 energy must be subtracted from the calorimeter measurement. Care is taken to accurately subtract
 617 all of a single particle’s energy, without removing any energy deposited by any other particle. One
 618 example of benefits from utilization of PFlow is shown on Fig. 2.12a - p_T resolution is improved at
 619 low p_T up to 15%.

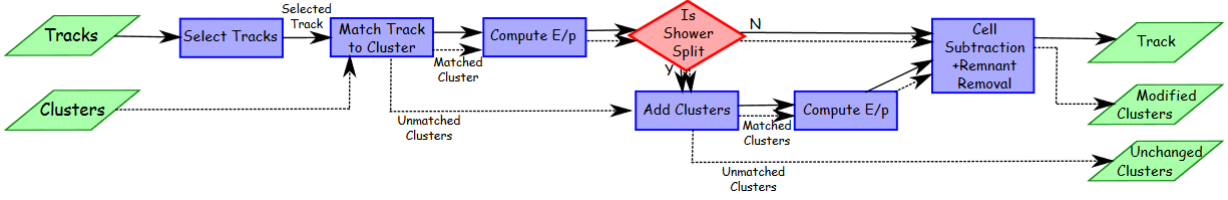


FIGURE 2.11 – A flow chart of how the particle flow algorithm proceeds, starting with track selection and continuing until the energy associated with the selected tracks has been removed from the calorimeter. At the end, charged particles, topo-clusters which have not been modified by the algorithm, and remnants of topo-clusters which have had part of their energy removed remain [6].

620 In each bunch crossing, it's not just one proton colliding with another proton but multiple of
 621 them. During Run-3 in ATLAS typically around 50 collision are happening simultaneously and
 622 therefore different objects would originate from different collisions. Different kinds of jets can be
 623 distinguished. Typically, there is an interest in only interaction vertex called hard-scatter (HS) and
 624 jets coming from it HS jets. Jet is labelled as HS jet if truth HS jet with $p_T > 10 \text{ GeV}$ is found
 625 within $\Delta R < 0.3$ and if there are several matches, jet with highest p_T^{truth} among them is taken. All
 626 the other collisions are referred to as pile-up ¹⁰. Jets originating from pile-up interaction are called
 627 pile-up (PU) jets. Different types of jets are illustrated on Fig. 2.13 where one might see two types
 628 of PU jets :

- 629 1. QDC PU jets : the majority of constituents come from single vertex, but not the HS vertex
 630 of interest. At truth level historical ATLAS definition [34] of such jet is the one for which
 631 no truth-particle hard-scatter jet with $p_T > 4\text{GeV}$ is found within $\Delta R < 0.6$ but there is a
 632 pile-up truth jet within $\Delta R < 0.3$
- 633 2. Stochastic PU jets : typically not having contribution from single prevalent vertex but do
 634 often contain out-of-time pile-up. Not a jet in a sense of “energetic spray of hadronic showers”
 635 but instead clustered accidentally. With truth stochastic PU jet is identified as the one for
 636 which no truth-particle hard-scatter jet with $p_T > 4\text{GeV}$ is found within $\Delta R < 0.6$ (this part
 637 of definition is same as for QCD PU) but there is no pile-up truth jet within $\Delta R < 0.6$

638 One might see truth PU definitions are not exhaustive in p_T and ΔR , rest cannot be unambiguously matched. Benefit of using PFlow for removal undesirable pile-up is shown on Fig. 2.12b
 639 in comparison to calorimeter jets. “Fake jets” are stochastic jets, and they are almost absent in
 640 central region, but QCD PU still needs to be removed which is the purpose of NNJVT, considered
 641 below. There is no gain in forward region because there is no tracker there.

642 Jets needs to be calibrated, it's described in [11],[14] done via steps summarized on Fig. 2.14.
 643 Goal of “Pile-up correction” steps is to remove the dependence of p_T^{reco} on pile-up. Both in-time,
 644 out-of time types and correlation between them is addressed. It's achieved by correcting measured
 645 jet transverse momentum as follows

$$p_T^{\text{corr}} = p_T^{\text{reco}} - \rho \times A - \alpha \times (N_{\text{PV}} - 1) - \beta \times \mu \quad (2.6)$$

647 where ρ is median pile-up momentum density (derived from central region) weighted to the jet
 648 area. α (β) are coefficients derived per $|\eta|$ bin sensitive to N_{PV} (μ) residual dependence.

649 Calibration proceeds with absolute MC-based calibration (jet energy scale and $|\eta|$), where
 650 the goal is to correct p_T^{reco} (both energy and direction) by taking into account for energy losses in

10. Actually in-time pile-up. There is also out-of-time pile-up formed from energy leftovers in calorimeter from previous or following bunch crossing

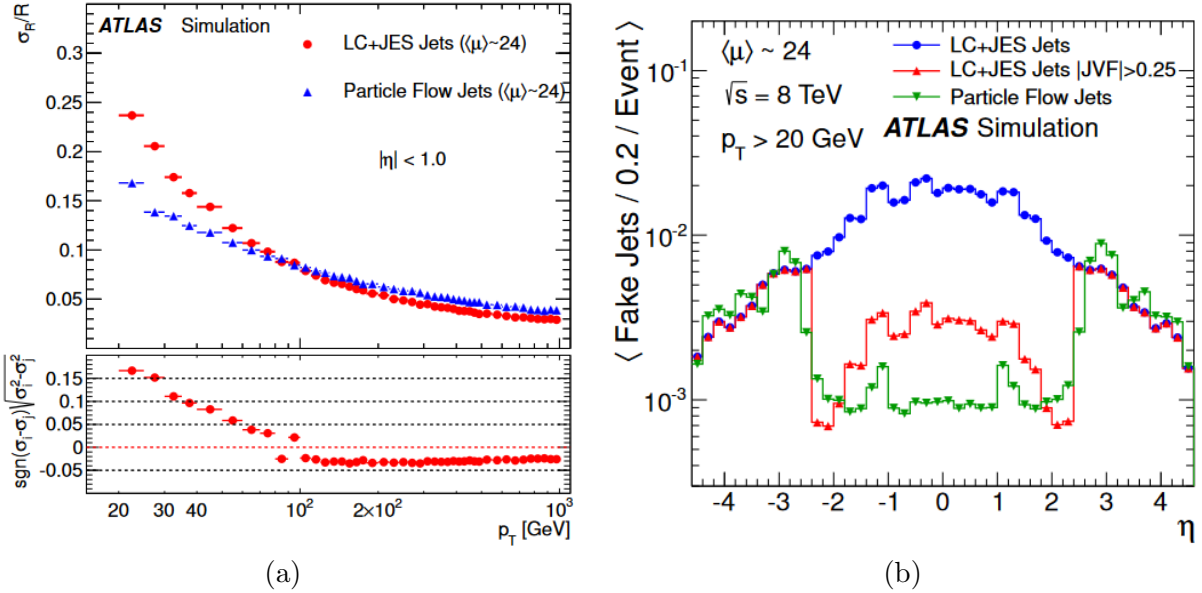


FIGURE 2.12 – (a) The jet transverse momentum resolution as a function of p_T for jets with $|\eta| < 1.0$, determined in dijet MC events for calorimeter jets and particle flow jets. Simulated pile-up conditions are similar to the data-taking in 2012. To quantify the difference in resolution between particle flow and calorimeter jets, the lower figure shows the square root of the difference of the squares of the resolution for the two classes of jets. (b) The number of pile-up “fake jets” in dijet MC events. Simulated pile-up conditions are similar to the data-taking in 2012

passive material, out-of-cone effects and non-compensating calorimeter response, $|\eta|$ biases primarily caused by the transition between different calorimeter technologies and granularities. The next step is the Global Neural Network Calibration (GNNC) which is a recent addition superseedring Global Sequential Calibration (GSC), corrects for differences between the calorimeter response to different types of jets, which improves the jet resolution without changing the jet energy response. GNNC is a DNN trained to predict p_T based on calorimeter, jet kinematics, tracking, muon segments, pile-up informations and taking into account correlations between variables. After all those steps, there still would be differences arising from MC mismodelling of detector material, detector response, EM and hadronic showers etc. - discrepancy between data and the MC simulation are accounted for.

Subject of Chapter 4 is an algorithm designed to rejection of PU jets in forward region. It’s instructive to see how this is done in the central region, where Neural Network Jet Vertex Tag-

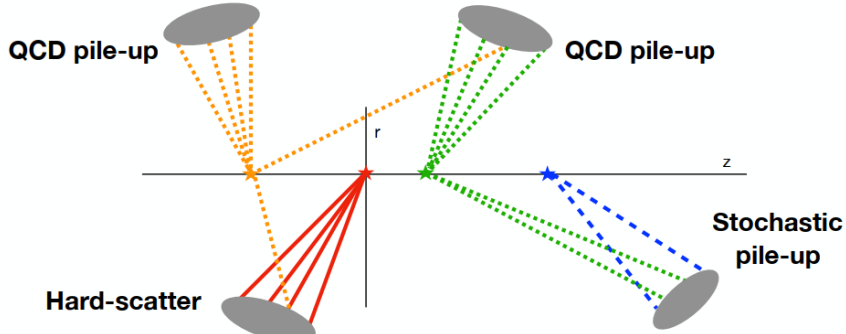


FIGURE 2.13 – Schematic example of different jet types[84]

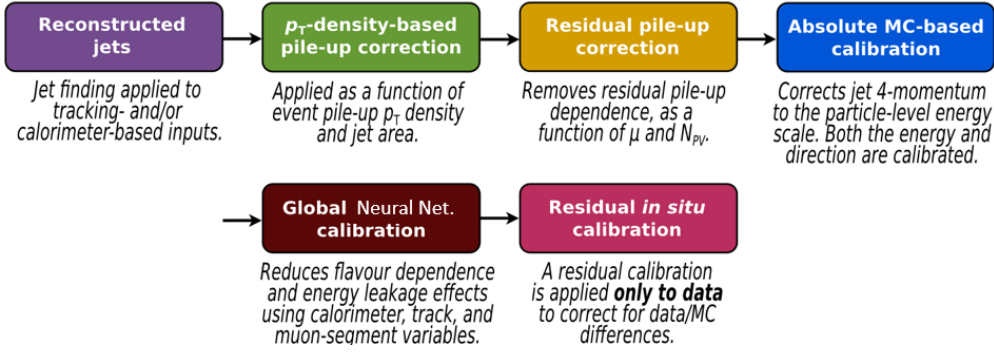


FIGURE 2.14 – Stages of jet energy scale calibrations. Each one is applied to the four-momentum of the jet. Adapted from [11]

663 ging (NNJVT) algorithm is utilized. NNJVT is a Neural Network continuation of JVT [5], providing
664 fixed efficiency to select hard-scatter jet over $|\eta|$ in each p_T bin. JVT, in turn, is also a neural net :
665 derived using simulated dijet events and based on a k-nearest neighbour (kNN) from $R_{pT,corrJVF}$
666 defined as

$$R_{pT} = \frac{\sum_k p_{T,k}^{\text{track}}(\text{PV}_0)}{p_T^{\text{jet}}} \quad (2.7)$$

$$\text{corrJVF} = \frac{\sum_m p_{T,m}^{\text{track}}(\text{PV}_0)}{\sum_l p_{T,l}^{\text{track}}(\text{PV}_0) + \frac{\sum_{n \geq 1} \sum_l p_{T,l}^{\text{track}}(\text{PV}_n)}{(k \cdot n_{\text{track}}^{\text{PU}})}} \quad (2.8)$$

668 Both variables are relying on track information. R_{pT} , shown on Fig. 2.15a, is estimating fraction of
669 jet p_T carried by tracks originating from the HS vertex. corrJVF is shown on Fig. 2.15b, and it's a
670 measure of jet's tracks fraction associated to HS vertex, including correction for number for NPV.

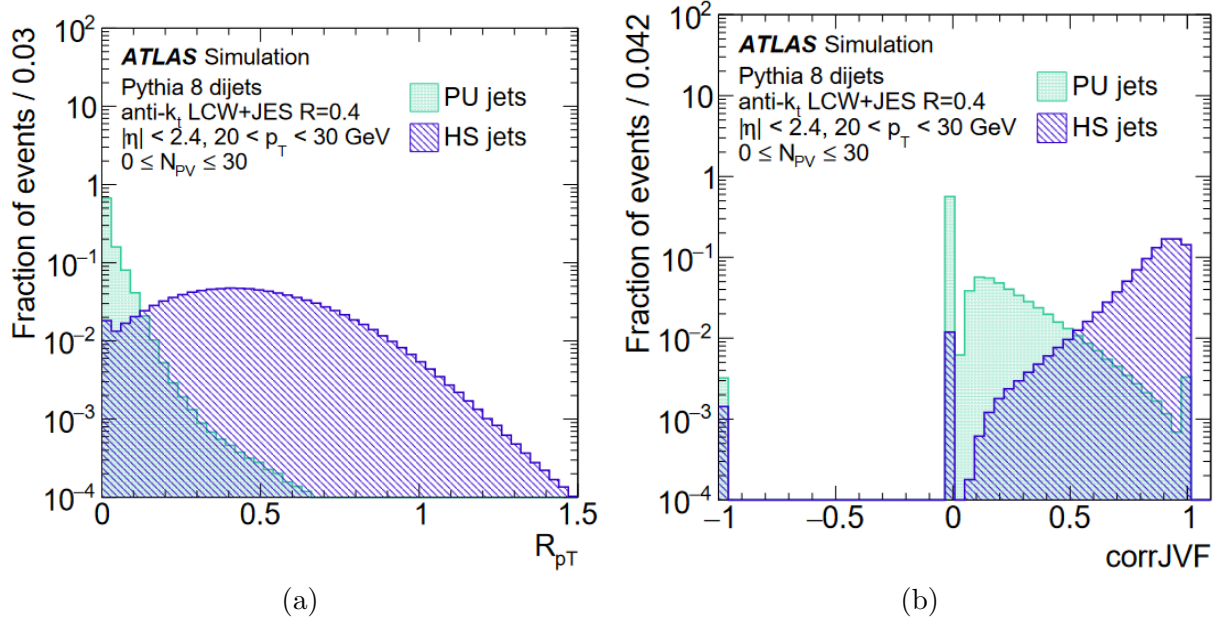


FIGURE 2.15 – Distribution for pile-up (PU) and hard-scatter (HS) jets with $20 < p_T \leq 30$ 30 GeV [5] of (a) R_{pT} (b) corrJVF

671 **Electrons and photons, Muons, MET**

672 To reconstruct electrons and photons one mostly relies on EM calorimeters since those particles
673 initiate EM showers. Also ID information is useful to distinguish between electron (charged particle,
674 expected to leave track) and photon (doesn't have charge, should not be in ID hits). However,
675 photon can be converted to electron-positron pair while propagating to calorimeter. In that case
676 pair of tracks originating away from IP expected to be visible via tracker. Starting point for electron
677 reconstruction is clustering of deposits in calorimeter result of which matched to tracks. If matching
678 is not possible electron is tagged as converted photon. Correction for energy lost during interactions
679 with material is done. Prompt electron is required to be identified as the originating from HS vertex.
680 For the identification likelihood-based discriminant is used, relying on typical shape variables of
681 EM showers to reduce misidentification with other objects. Three working points : loose, medium,
682 tight are utilized for electron and two for photon identification : loose, tight.

683 Muon, being a stable charged particle typically undergoing a little amount of interactions reaches
684 furthest-away layers of detector. It thus may leave hits in both tracker and MS. MIP-compatible
685 calorimeter hits also may be used for reconstruction. As MS from the beginning of ATLAS were
686 designed to be able to work stand-alone if needed (it's only used as last resort) this regime can be
687 utilized. For muon to be classified as prompt, various requirements are applied, such as compatibility
688 between momentum ID and MS measurements, number of hits in each sub-detector, quality of χ^2 fit
689 (hits from segments in different layers are fitted together). Three working points for $20 < p_T \leq 100$
690 muons are defined with selection efficiency ranging between 98.1% to 91.8%.

691 If there are neutrinos (or some other exotic non-interacting particle) in final state they will not
692 be detected by any detector sub-system. Workaround can be utilized relying on detector hermeticity,
693 detector design decision made in the very beginning. Because initial $\sum p_T$ in event is zero, if one
694 measured everything else except neutrinos, resulting non-zero $\sum p_T$ would mean presence of neutrinos.
695 One then defines Missing Transverse Energy (MET, confusingly not called Missing Transverse
696 Momentum) as $\overrightarrow{E_T^{\text{miss}}} = \sum_i \overrightarrow{p_T^i}$ where sum runs over both hard final state objects (reviewed above)
697 and soft objects (un-associated to hard objects tracks), as everything should be included. Special
698 care is taken to avoid double counting (e.g. same energy deposit should not be included in both
699 jet and calorimeter), for which overlap removal procedure excludes hits from the list in particular
700 order : electrons are prioritized, then photons, other leptons, jets and finally, tracks.

701 3 - aQGC EFT VBS Run-2 combination

702 3.1 Analyses involved

703 Many ATLAS Run-2 VBS analyses are already published or close to be published

- 704 • $Z\gamma$ with Z decaying leptonically [49] or into MET [48],
- 705 • ZZ decaying into four leptons [52] or into $\ell\ell\nu\nu$ [92] final states
- 706 • VBS semileptonic analysis [89]
- 707 • With at least one W : $W^\pm W^\pm$ [55], WZ [56], $W\gamma$ [31]

708 covering different di-boson pairs and final states involving various couplings. All of them are Stan-
 709 dard Model analyses aiming at observing the process, measuring cross-sections, and various dif-
 710 fferential cross-sections. In addition, the results of these analyses are used to constraint anomalous
 711 Quartic Gauge Couplings (aQGC) even though they were not necessarily optimized for that pur-
 712 pose¹.

713 3.2 Eboli operators

714 VBS process contains QGC, and therefore, one might study those couplings in the hunt for
 715 potential deviation from the SM. One needs dimension-8 EFT operators to act only on QGC
 716 without affecting triple gauge coupling. A complete set of those dimension-8 operators was derived
 717 in [102]; however, as it turned out later, it was not complete as it was missing two operators added
 718 in [62]. Twenty operators from [62] in the community are referred to as “Eboli operators” and
 719 constitute a basis for C-even and P-even aQGC operators² and include all possible modifications
 720 to VVVV, VVWH, and VVHH vertices compatible with conservation of C, P, electric charge.
 721 Eboli operators are grouped into three families : scalar, mixed, and tensor, depending on the
 722 content. Scalar (S) operators are built only from covariant derivatives of the Higgs field $D_\mu \Phi =$
 723 $\left(\partial_\mu + igW_\mu^j \frac{\sigma^j}{2} + ig'B_\mu \frac{1}{2}\right) \Phi$, where Φ is a Higgs doublet and $\sigma^j = \sigma^1, \sigma^2, \sigma^3$ are the Pauli matrices

$$\begin{aligned} \mathcal{O}_{S0} &= \left[(D_\mu \Phi)^\dagger D_\nu \Phi \right] \times \left[(D^\mu \Phi)^\dagger D^\nu \Phi \right] \\ \mathcal{O}_{S1} &= \left[(D_\mu \Phi)^\dagger D^\mu \Phi \right] \times \left[(D_\nu \Phi)^\dagger D^\nu \Phi \right] \\ \mathcal{O}_{S2} &= \left[(D_\mu \Phi)^\dagger D_\nu \Phi \right] \times \left[(D^\nu \Phi)^\dagger D^\mu \Phi \right] \end{aligned} \quad (3.1)$$

724 Mixed (M) operators, in addition to covariant derivatives of the Higgs field, contain field

1. This will be the program for some follow-up analyses

2. Currently under discussion is the CP-even basis, which, in addition to Eboli operators, includes two C-odd and P-odd operators, making them even under combined CP [69]

TABLE 3.1 – Vertices affected by aQGC operators

Operators	SM				Not SM				
	WWWW	WWZZ	WW $\gamma\gamma$	WW γZ	ZZZZ	ZZZ γ	ZZ $\gamma\gamma$	Z $\gamma\gamma\gamma$	$\gamma\gamma\gamma\gamma$
S0, S1	✓	✓			✓				
M0, M1, M7	✓	✓	✓	✓	✓	✓	✓		
M2, M3, M4, M5		✓	✓	✓	✓	✓	✓		
T0, T1, T2	✓	✓	✓	✓	✓	✓	✓	✓	✓
T3, T4, T5, T6, T7		✓	✓	✓	✓	✓	✓	✓	✓
T8, T9					✓	✓	✓	✓	✓

strengths $\widehat{W}_{\mu\nu} \equiv W_{\mu\nu}^j \frac{\sigma^j}{2}$ (for $SU(2)_L$) and $B_{\mu\nu}$ (for $U(1)_Y$) :

$$\begin{aligned}
 \mathcal{O}_{M0} &= \text{Tr} \left[\hat{W}_{\mu\nu} \hat{W}^{\mu\nu} \right] \times \left[(D_\beta \Phi)^\dagger D^\beta \Phi \right] \\
 \mathcal{O}_{M1} &= \text{Tr} \left[\hat{W}_{\mu\nu} \hat{W}^{\nu\beta} \right] \times \left[(D_\beta \Phi)^\dagger D^\mu \Phi \right] \\
 \mathcal{O}_{M2} &= [B_{\mu\nu} B^{\mu\nu}] \times \left[(D_\beta \Phi)^\dagger D^\beta \Phi \right] \\
 \mathcal{O}_{M3} &= \left[B_{\mu\nu} B^{\nu\beta} \right] \times \left[(D_\beta \Phi)^\dagger D^\mu \Phi \right] \\
 \mathcal{O}_{M4} &= \left[(D_\mu \Phi)^\dagger \hat{W}_{\beta\nu} D^\mu \Phi \right] \times B^{\beta\nu} \\
 \mathcal{O}_{M5} &= \left[(D_\mu \Phi)^\dagger \hat{W}_{\beta\nu} D^\nu \Phi \right] \times B^{\beta\mu} + \text{h.c.} \\
 \mathcal{O}_{M7} &= \left[(D_\mu \Phi)^\dagger \hat{W}_{\beta\nu} \hat{W}^{\beta\mu} D^\nu \Phi \right]
 \end{aligned} \tag{3.2}$$

Finally, tensor (T) operators only contain field strengths

$$\begin{aligned}
 \mathcal{O}_{T0} &= \text{Tr} \left[\hat{W}_{\mu\nu} \hat{W}^{\mu\nu} \right] \times \text{Tr} \left[\hat{W}_{\alpha\beta} \hat{W}^{\alpha\beta} \right] \\
 \mathcal{O}_{T1} &= \text{Tr} \left[\hat{W}_{\alpha\nu} \hat{W}^{\mu\beta} \right] \times \text{Tr} \left[\hat{W}_{\mu\beta} \hat{W}^{\alpha\nu} \right] \\
 \mathcal{O}_{T2} &= \text{Tr} \left[\hat{W}_{\alpha\mu} \hat{W}^{\mu\beta} \right] \times \text{Tr} \left[\hat{W}_{\beta\nu} \hat{W}^{\nu\alpha} \right] \\
 \mathcal{O}_{T5} &= \text{Tr} \left[\hat{W}_{\mu\nu} \hat{W}^{\mu\nu} \right] \times B_{\alpha\beta} B^{\alpha\beta} \\
 \mathcal{O}_{T6} &= \text{Tr} \left[\hat{W}_{\alpha\nu} \hat{W}^{\mu\beta} \right] \times B_{\mu\beta} B^{\alpha\nu} \\
 \mathcal{O}_{T7} &= \text{Tr} \left[\hat{W}_{\alpha\mu} \hat{W}^{\mu\beta} \right] \times B_{\beta\nu} B^{\nu\alpha} \\
 \mathcal{O}_{T8} &= B_{\mu\nu} B^{\mu\nu} B_{\alpha\beta} B^{\alpha\beta} \\
 \mathcal{O}_{T9} &= B_{\alpha\mu} B^{\mu\beta} B_{\beta\nu} B^{\nu\alpha}
 \end{aligned} \tag{3.3}$$

The sum of a number of operators in Eq. 3.1, Eq. 3.2, Eq. 3.3, contrary to what was said above, is not 20. From Eq. 3.2 \mathcal{O}_{M6} was omitted as it is proportional to \mathcal{O}_{M1} . From Eq. 3.3 $\mathcal{O}_{T3}, \mathcal{O}_{T4}$ were omitted as they vanish identically. Moreover, $\mathcal{O}_{S0}, \mathcal{O}_{S2}$ from Eq. 3.1 are often merged in practice (only difference being $\mu \leftrightarrow \nu$ in second term of product). In the end, there are only 17 independent dimension-8 operators containing only SM fields.

Some of those operators modify existing SM couplings, and some add new ones, as summarized in Table 3.1

3.3 Expectation from the combination

Analyses listed in Sec. 3.1 all individually derived limits on Wilson coefficients associated with operators shown in Eq. 3.1, Eq. 3.2, Eq. 3.3. From Table 3.1 not all the analyses are sensitive to all the operators - for example \mathcal{O}_{T8} , \mathcal{O}_{T9} are only appearing in electrically neutral vertices and can be probed by $Z(\rightarrow \bar{\nu}\nu)\gamma$, $Z(\rightarrow \bar{\ell}\ell)\gamma$, $ZZ \rightarrow \bar{\ell}\bar{\ell}\nu\bar{\nu}$, $ZZ \rightarrow 4\ell$ and semileptonic VV (which contains all the pairs) but not $W^\pm Z$, $W^\pm W^\pm$. S family operators are unavailable in all analyses with photons : $W\gamma$, $Z(\rightarrow \bar{\ell}\ell)\gamma$, $Z(\rightarrow \bar{\nu}\nu)\gamma$, etc. By combining the analyses, one can put constraints on all the operators, opening the road for multi-dimensional constraints on the complete set.

When several analysis are sensitive to the same operator like \mathcal{O}_{M2} (just for concreteness) which can be probed by all the analyses ; one might hope that the combined limit is more stringent than the best individual limits. It can be illustrated by results of previous aQGC ATLAS combination [13] done with Early-Run-2 data and including only early $W^\pm W^\pm$ and $W^\pm Z$ analyses. As seen on Fig. 3.1 combined \mathcal{O}_{T0} , \mathcal{O}_{T2} limits are more stringent than the best individual limit (which for those two cases turns out to be given by $W^\pm W^\pm$)

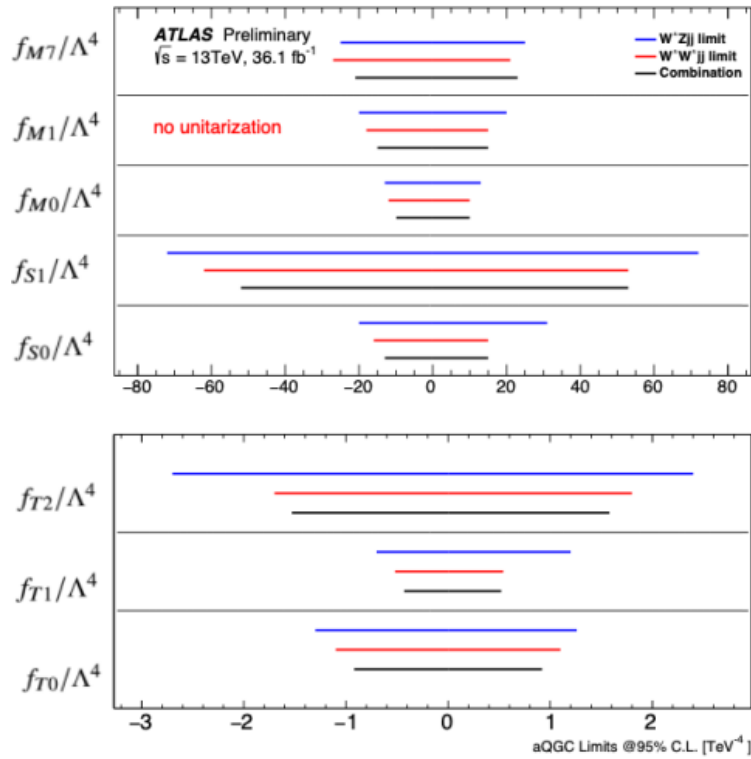


FIGURE 3.1 – Observed lower and upper 95% confidence level limits on the parameters of the quartic operators M0, M1, M7, S0, S1, T0, T1 and T2 in $W^\pm Z$ jj and $W^\pm W^\pm$ jj individual channels and combination [13].

3.4 EFT samples generation

Inclusion of EFT into amplitude will give, compared to SM-only case

$$A_{SM} \rightarrow A_{SM} + \sum_{operator \equiv o} c_o A_o \quad (3.4)$$

Where A_{SM} is SM amplitude, A_o is the contribution from each of Eboli operators (like $\mathcal{O}_{T0}, \mathcal{O}_{T1}$ etc) with a corresponding Wilson coefficient c_o . Squaring this amplitude to obtain the cross-section

752 will give, focusing only on one operator with label i

$$\sigma_{SM+i} \propto |A_{SM} + A_i|^2 = |A_{SM}|^2 + c_i \cdot 2 \operatorname{Re} (A_{SM} A_i^\dagger) + c_i^2 |A_i|^2 \quad (3.5)$$

753 Among the three terms, the first one corresponds to SM-only contribution for cross-section, which
 754 one would observe in absence of New Physics(NP), the second term is the interference term between
 755 the SM and aQGC operator i, and the last term is a pure EFT contribution (also known as quadratic
 756 term).

757 Considering two operators i,j $A_{SM} + A_i + A_j$ and squaring to obtain the cross-section for this
 758 case gives now

$$\sigma_{SM+i+j} \propto |A_{SM}|^2 + \underbrace{c_i \cdot 2 \operatorname{Re} (A_{SM} A_i^\dagger)}_{\text{SM interference with EFT i}} + \underbrace{c_j \cdot 2 \operatorname{Re} (A_{SM} A_j^\dagger)}_{\text{SM interference EFT j}} + \underbrace{c_i^2 |A_1|^2 + c_j^2 |A_2|^2}_{\text{EFT quadratic terms}} + \underbrace{c_i c_j \cdot 2 \operatorname{Re} (A_i A_j^\dagger)}_{\text{EFT cross-term}} \quad (3.6)$$

759 where there is still the SM term but also two interference terms (one per operator) and two quadratic
 760 terms. A new addition is a cross-term between two aQGC operators, sometimes confusingly can be
 761 called an interference term, but this one has nothing to do with SM. $\sigma_{SM+i+j+k+\dots}$ with three or
 762 more operators will get decomposed into a corresponding number of interference, quadratic terms,
 763 and cross-terms from all the pairs of operators considered on top of the SM cross-section.

764 MC generation is done separately for SM, each interference, quadratic, and cross-term terms.
 765 Our end goal is to derive Confidence Limits (CL) driven by cross-sections/events obtained $\sigma_{operator(pair)}^{order}$,
 766 entering with a corresponding operator(s) coefficient(s) that we want to fit. For EFT generation,
 767 a Wilson coefficient equal to 1 is typically used. Whatever the value, it should be consistent bet-
 768 ween different samples. In this section and for analyses considered, EFT generation is done with
 769 **MadGraph5** [19] and UFO model used is QA11_5_Aug21v2³, coming from **FeynRules** 2.3.47 [18]
 770 and integrated into ATLAS software⁴. The current (published reasonably recently) version of
 771 the model allows us to obtain predictions for T3 T4 operators, however, they were not part of the
 772 original Eboli model **MadGraph** implementation and not used by most of the analyses (many started
 773 5+ years ago) who used older implementation.

774 When deriving limits for one coefficient c_i at the time, all the others coefficients $c_{j \neq i}$ are set to
 775 zero and one is back at the configuration of Eq. 3.5, where there is no EFT cross-term. However,
 776 one should consider the cross-term(s) when fitting two or more coefficients simultaneously.

777 3.5 EFT cross-sections

778 Table 3.2 is showing a summary of the production cross-section of quadratic terms, all operators,
 779 for four di-boson pairs. Dashes correspond to cases where operators are not accessible by boson
 780 pair. The cross-section for the T operators family is typically larger than for S and M operators.

781 Table 3.3 is similar to Table 3.2 but for interference terms - showing (in comparison to the table
 782 above) characteristic feature of aQGC EFT : interference terms are mostly much smaller. Also, it
 783 can be seen that apart from quadratic terms, interference can be negative.

784 A representative example of the relationship between interference and quadratic terms depen-
 785 ding on di-boson mass is shown on Fig. 3.2 (T6 operator of $W\gamma$ analysis) where both distributions
 786 are normalized to their corresponding cross-section. The interference term is negative, sharper,
 787 peaks at smaller $m_{W\gamma}$ and there is no slice of $m_{W\gamma}$ where quadratic terms would not dominate (apart
 788 from very low values). The cumulative distribution function of interference and quadratic terms sum

3. <https://feynrules.irmp.ucl.ac.be/wiki/AnomalousGaugeCoupling>

4. https://gitlab.cern.ch/atlas-generators-team/MadGraphModels/-/tree/main/EFT/QA11_5_Aug21v2?ref_type=heads

TABLE 3.2 – Production cross-sections (in femtobarns) for quadratic EFT terms

	ZZ	Zy	WZ	Wy
T0	75.33	42.08	35.26	9.65
T1	47.58	26.45	79.54	22.27
T2	11.42	6.41	9.43	2.63
T5	12.19	39.32	5.80	19.35
T6	5.01	8.50	6.34	21.61
T7	1.08	2.83	1.05	3.58
T8	18.03	122.80	-	-
T9	3.92	26.79	-	-
S02	0.08	-	0.11	-
S1	0.03	-	0.01	-
M0	2.85	0.04	0.49	0.06
M1	0.22	0.01	0.20	0.02
M2	1.44	0.29	0.15	0.52
M3	0.12	0.10	0.06	0.21
M4	0.20	0.08	0.61	0.15
M5	0.10	0.13	0.34	0.21
M7	0.06	0.01	0.12	0.01

⁷⁸⁹ shows no features of interference term basically follows quadratic term di-boson mass - interference
⁷⁹⁰ term is small.

⁷⁹¹ 3.6 SM and EFT distributions

⁷⁹² Effect of aQGC on various spectrums is shown on Fig. 3.3, Fig. 3.4, Fig. 3.5 together with SM
⁷⁹³ distribution (for reference) for the distributions that differ the most. For aQGC T1 quadratic term
⁷⁹⁴ is shown as a representative example, because all T operators turn out to have similar shapes and
⁷⁹⁵ this is utilized later in Sec. 3.10 to replace missing operators.

⁷⁹⁶ As was seen in Table 3.2 quadratic terms dominate the cross-section, and from from Fig. 3.2
⁷⁹⁷ example m_{VV} (proxy for Q^2 of the process) is peaking at around 2.5 TeV so quadratic effects are
⁷⁹⁸ taking place at much larger Q^2 compared to the Standard Model. Then m_{4l} of $ZZ \rightarrow 4\ell$ analysis
⁷⁹⁹ which is m_{VV} seen by detector also behaving in the similar way (Fig. 3.3). If m_{4l} , built from
⁸⁰⁰ transverse momentums of four leptons, is different, one would expect to see some of the individual
⁸⁰¹ lepton distribution tails enhanced compared to the SM, and this is shown on Fig. 3.4. Tagging jets
⁸⁰² also may receive an enhancement, although not as dramatic, as shown on Fig. 3.5.

⁸⁰³ 3.7 Unitarity bound

⁸⁰⁴ Within the Standard Model, VBS diagrams considered alone would diverge at high Q^2 and
⁸⁰⁵ violate unitarity. The same applies to tri-linear gauge coupling diagrams and Higgs boson pro-
⁸⁰⁶ cesses. However, considering all those three types together, unitarity is restored. This statement
⁸⁰⁷ was important for ATLAS from the beginning at constituted a “no-loose theorem“ : there should
⁸⁰⁸ either be a Higgs boson no heavier than approximately 1 TeV or otherwise, NP should occur near
⁸⁰⁹ or below that energy scale. The ATLAS and LHC are sensitive to both cases. As we know after
⁸¹⁰ 2012, the Higgs boson exists.

TABLE 3.3 – Production cross-sections (in femtobarns) for SM-interference EFT terms

	ZZ	Zy	WZ	Wy
T0	3.97	2.25	-1.43	-0.28
T1	0.96	0.52	-5.59	-1.52
T2	1.41	0.78	-3.04	-0.79
T5	1.13	-2.16	0.57	-0.30
T6	0.23	-0.32	1.11	-0.97
T7	0.37	-0.67	0.68	-0.55
T8	0.01	0.08	-	-
T9	0.01	0.05	-	-
S02	-0.03	-	-0.10	-
S1	-0.00	-	-0.03	-
M0	-0.21	-0.04	0.16	0.02
M1	0.09	0.01	-0.06	-0.02
M2	-0.03	0.07	-0.02	0.01
M3	0.01	-0.02	0.02	-0.06
M4	-0.01	-0.01	-0.02	-0.04
M5	-0.02	0.03	-0.01	0.01
M7	-0.04	-0.01	-0.01	0.01

aQGC considered in this chapter may violate unitarity, too, as EFT is not a complete model.
 When Wilson coefficients are small, unitarity can be violated at very high energies, but we know
 Higgs restores it there. In the case with more significant coefficients, unitarity may be violated
 even at lower energies, where we might hope to see signs of NP. Luckily, there is a benchmark
 provided by unitarity bounds depending on energy, derived in [62] that allows us to judge whether
 the derived Wilson coefficients are meaningful. Bounds for the case of 1 operator at the time are
 given in Table 3.4.

3.8 Clipping

Limits obtained in combination will be compared with unitarity bounds above, per energy.
 To check if results make sense, clipping technique [67] is used as it is simple and reproducible :
 clipping is a cut-off scale beyond which the Wilson coefficient is set to 0. In practice, fitted variable
 distribution is build for $m_{VV} \leq C$, where m_{VV} is taken from the truth information, particle before
 showering. An example of such distribution, obtained from $Z(\rightarrow \bar{\nu}\nu)\gamma$ events with corresponding
 analysis selections, is shown on Fig. 3.6 for $m_{Z\gamma}$ (Hard-Scatter level particles) and corresponding
 change of p_T^γ shape is shown on Fig. 3.7 for $C = 3000, 2000, 1500, 1000 \text{ GeV}$ together with reference
 distribution without clipping (aka clipping infinity point). Apart from shape change, cross-section
 is decreasing according to fraction of $m_{Z\gamma}$ selected. Taking $m_{Z\gamma} \leq C$ shifts p_T^γ shape toward lower
 values and cross-section decreases by a fraction contained in $m_{Z\gamma} > C$.

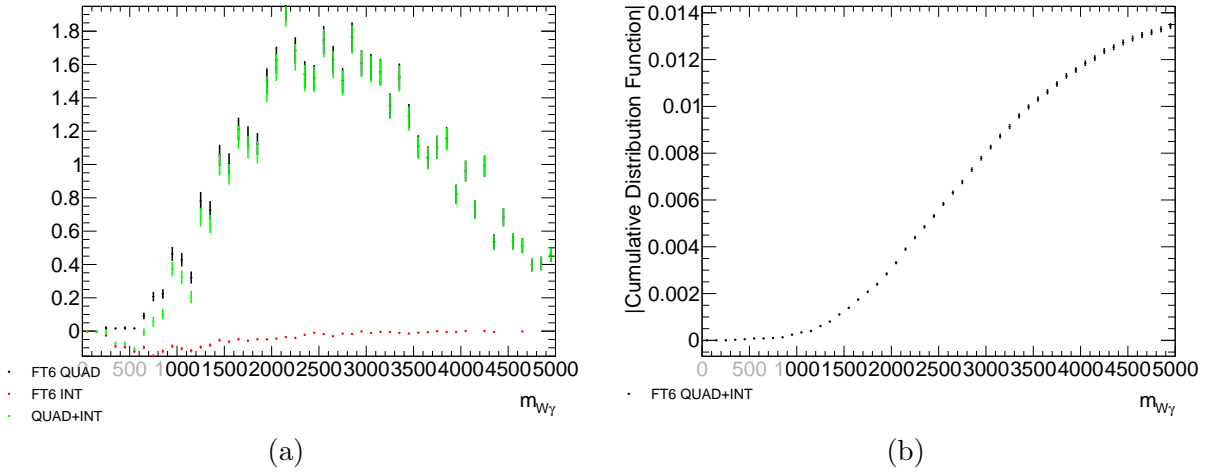


FIGURE 3.2 – $W\gamma$ FT6 (a) m_{VV} INT, QUAD and their sum (b) Cumulative Distribution of absolute of INT+QUAD

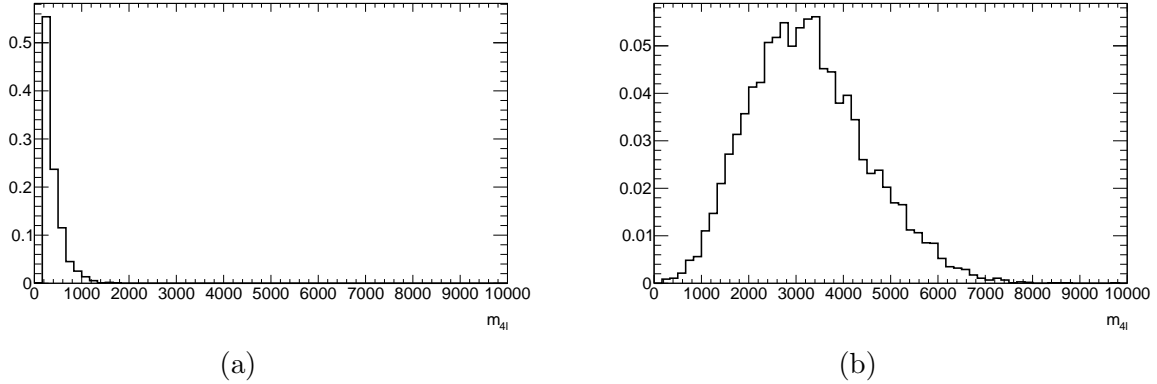


FIGURE 3.3 – Particle-level $ZZ \rightarrow 4\ell$ events generated with **MadGraph** and with $ZZ \rightarrow 4\ell$ analysis selections applied : comparison of mass of four-lepton system (GeV) obtained in (a) SM (b) aQGC T1 quadratic term

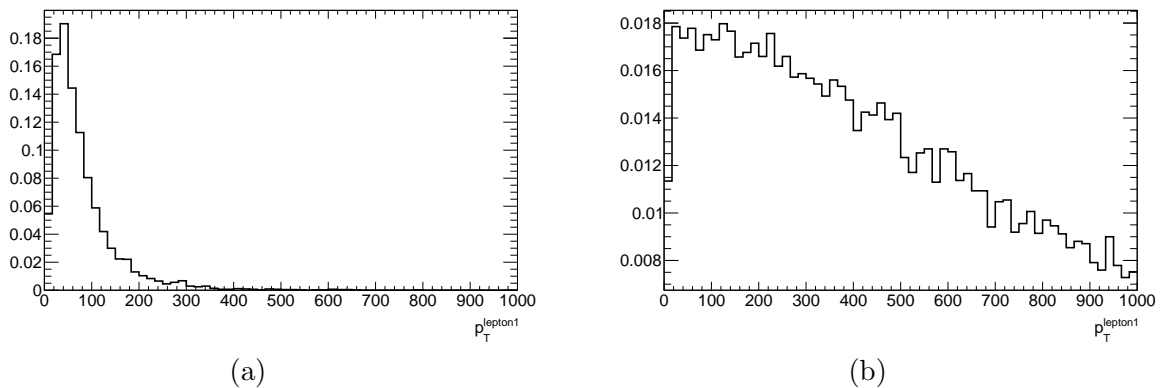


FIGURE 3.4 – Particle-level $ZZ \rightarrow 4\ell$ events generated with **MadGraph** and with $ZZ \rightarrow 4\ell$ analysis selections applied : comparison of leading lepton p_T (GeV) obtained in (a) SM (b) aQGC T1 quadratic term

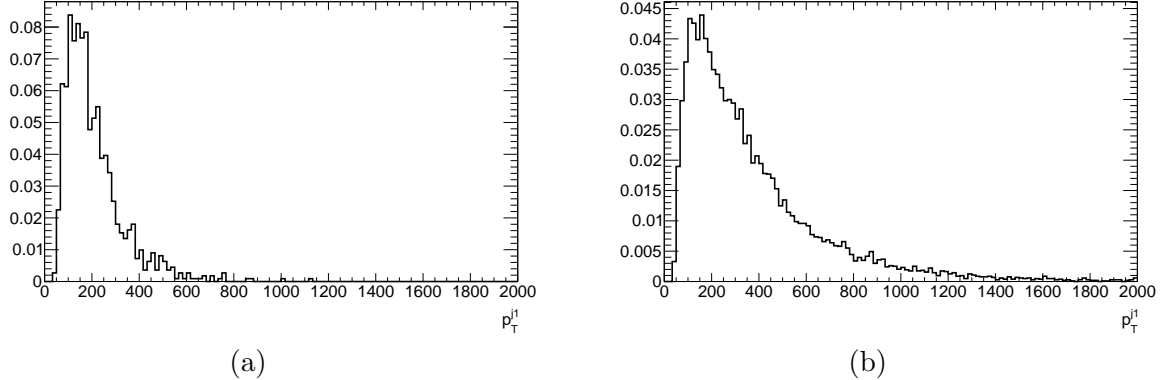


FIGURE 3.5 – Particle-level $ZZ \rightarrow 4\ell$ events generated with `MadGraph` and with $ZZ \rightarrow 4\ell$ analysis selections applied : comparison of leading jet p_T (GeV) obtained in (a) SM (b) aQGC T1 quadratic term

TABLE 3.4 – 1D unitarity bounds for aQGC operators [62]

Wilson coefficient	Bound
$\left \frac{f_{T0}}{\Lambda^4} \right $	$\frac{12/5\pi}{s^2}$
$\left \frac{f_{T1}}{\Lambda^4} \right $	$\frac{4/5\pi}{s^2}$
$\left \frac{f_{T2}}{\Lambda^4} \right $	$\frac{96/13\pi}{s^2}$
$\left \frac{f_{T5}}{\Lambda^4} \right $	$\frac{8/\sqrt{3}\pi}{s^2}$
$\left \frac{f_{T6}}{\Lambda^4} \right $	$\frac{48/7\pi}{s^2}$
$\left \frac{f_{T7}}{\Lambda^4} \right $	$\frac{32/\sqrt{3}\pi}{s^2}$
$\left \frac{f_{T8}}{\Lambda^4} \right $	$\frac{2/3\pi}{s^2}$
$\left \frac{f_{T9}}{\Lambda^4} \right $	$\frac{24/7\pi}{s^2}$
$\left \frac{f_{M0}}{\Lambda^4} \right $	$\frac{32/\sqrt{6}\pi}{s^2}$
$\left \frac{f_{M1}}{\Lambda^4} \right $	$\frac{127/\sqrt{6}\pi}{s^2}$
$\left \frac{f_{M2}}{\Lambda^4} \right $	$\frac{16/\sqrt{2}\pi}{s^2}$
$\left \frac{f_{M3}}{\Lambda^4} \right $	$\frac{64/\sqrt{2}\pi}{s^2}$
$\left \frac{f_{M4}}{\Lambda^4} \right $	$\frac{32\pi}{s^2}$
$\left \frac{f_{M5}}{\Lambda^4} \right $	$\frac{64\pi}{s^2}$
$\left \frac{f_{M7}}{\Lambda^4} \right $	$\frac{256/\sqrt{6}\pi}{s^2}$
$\left \frac{f_{M7}}{\Lambda^4} \right $	$\frac{256/\sqrt{6}\pi}{s^2}$
$\left \frac{f_{S02}}{\Lambda^4} \right $	$\frac{32\pi}{s^2}$
$\left \frac{f_{S1}}{\Lambda^4} \right $	$\frac{96/7\pi}{s^2}$

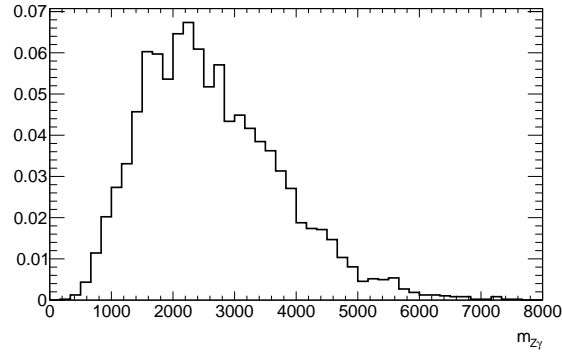


FIGURE 3.6 – $Z(\rightarrow \bar{\nu}\nu)\gamma$ M3 quadratic term $m_{Z\gamma}$

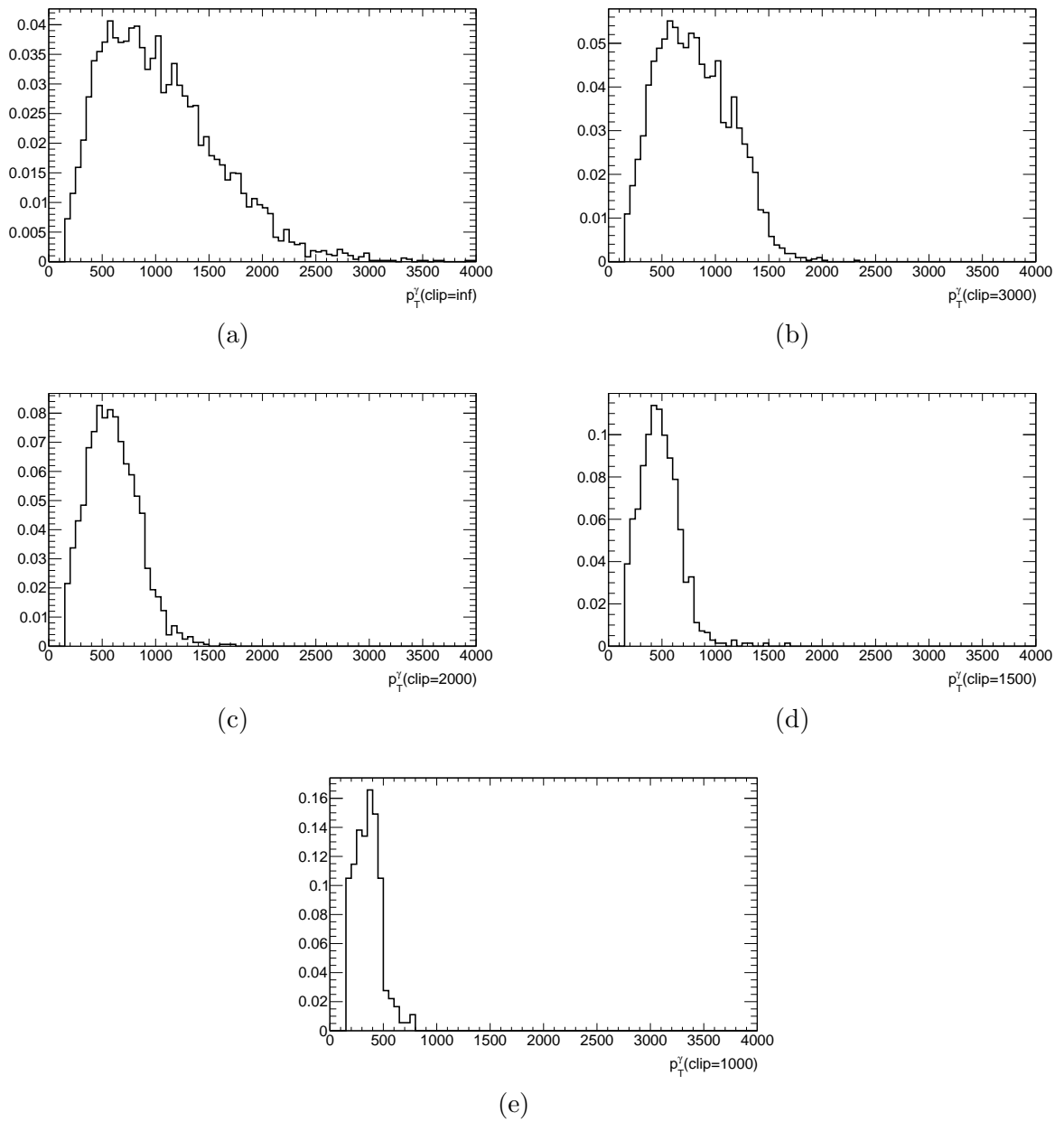


FIGURE 3.7 – Change of p_T^γ shape with clipping ($Z(\rightarrow \bar{\nu}\nu)\gamma$ FM3 QUAD)

829 3.9 Cross-term size

830 Most analyses didn't generate cross-terms (Eq. 3.6), but as we want to make 2D limits, the
 831 impact of their absence should be evaluated.

832 A custom metric was chosen to quantify the importance of cross-terms. Typically $\sigma_{INT} \ll$
 833 σ_{QUAD} therefore one can compare σ_{CROSS} to $(\sigma_{QUAD1}, \sigma_{QUAD2})$: dealing with part of expression
 834 above where c_1, c_2 are unknown

$$835 c_1^2 |A_1|^2 + c_2^2 |A_2|^2 + c_1 c_2 \cdot 2 \operatorname{Re} (A_1 A_2^\dagger) \quad (3.7)$$

835 We want to build a metric that somewhat resembles the 2D limit curves we will obtain, and we
 836 know from some individual analyses who made 2D limits that curve very likely will be an ellipse.
 837 For this, we will choose the area excluded in the 2D plane, assuming we observed no events in
 838 Run-2. One can obtain the ellipse only considering the quadratic terms with area $S_{no-cross}$ and
 839 ellipse with cross-term taken into account with area S_{cross} . The metric chosen to quantify how
 840 important cross-term can be is ratio of two areas $S_{cross}/S_{no-cross}$ obtained from

$$841 S_{no-cross} : 140 \cdot (c_1^2 \sigma_{Q1}^{gen} \epsilon_{Q1}^{evt.sel} + c_2^2 \sigma_{Q2}^{gen} \epsilon_{Q2}^{evt.sel}) \leq 3 \\ 842 S_{cross} : 140 \cdot (c_1^2 \sigma_{Q1}^{gen} \epsilon_{Q1}^{evt.sel} + c_2^2 \sigma_{Q2}^{gen} \epsilon_{Q2}^{evt.sel} + c_1 c_2 \sigma_{CROSS12}^{gen} \epsilon_{CROSS12}^{evt.sel}) \leq 3 \quad (3.8)$$

841 where $\sigma_{Q1}^{gen}, \sigma_{Q2}^{gen}$ are cross-sections of quadratic terms for the pair of operators in question and
 842 $\sigma_{CROSS12}^{gen}$ is cross-section of pair cross-term. Each term is generated separately with **MadGraph** to
 843 obtain corresponding $\sigma, \epsilon_{Q1}^{evt.sel}, \epsilon_{Q2}^{evt.sel}, \epsilon_{CROSS12}^{evt.sel}$ are the selection efficiencies obtained from replicating
 844 analysis fiducial selections on the corresponding sample with Rivet. Number 140 (fb) is there
 845 to convert cross-section to counts. Number 3 is on the RHS as 3 is upper 95% CL on Poisson μ if
 846 nothing was observed and zero counts for BSM during Run-2 is a good approximation.

847 Fig. 3.8 shows possible relationships between ellipses with or without cross-terms. Each plot is
 848 taken from a different pair of operators with a corresponding set of $\sigma_{Q1}^{gen}, \sigma_{Q2}^{gen}, \sigma_{CROSS12}^{gen}$. Two things
 849 may happen : cross-term does modify the ellipse or not. If cross-term is relevant, the magnitude of
 850 area enlargement may be different. Depending on the sign of the cross-term (positive or negative
 851 cross-section), an ellipse is inclined in one way or another.

852 The importance of cross-terms is given by the ratio of areas of two ellipses $S_{cross}/S_{no-cross}$ - it
 853 is 1 when cross-term is negligible and above 1 when not. The higher the value, the more important
 854 it is. The ratio is taken between all pairs of operators available per analysis.

855 The resulting matrix for $Z(\rightarrow \bar{\nu}\nu)\gamma$ analysis is shown in Fig. 3.9. It can be seen that between
 856 families (T/M) ratio is always close to 1, and therefore, cross-term can be neglected. Within the
 857 same family (T/T, M/M), the ratio is often above one - it often happens within the pairs taken from
 858 sub-families (groups of operators that "look similarly") $(\mathcal{O}_{S0}, \mathcal{O}_{S1}, \mathcal{O}_{S2}), (\mathcal{O}_{M0}, \mathcal{O}_{M1}), (\mathcal{O}_{M2}, \mathcal{O}_{M3}),$
 $(\mathcal{O}_{M4}, \mathcal{O}_{M5}), (\mathcal{O}_{T0}, \mathcal{O}_{T1}, \mathcal{O}_{T2}), (\mathcal{O}_{T5}, \mathcal{O}_{T6}, \mathcal{O}_{T7}), (\mathcal{O}_{T8}, \mathcal{O}_{T9})$,

856 Similar matrices were produced for $W^\pm Z$ and $W\gamma$ analyses, shown on Fig. 3.10, Fig. 3.11,
 857 respectively, with the same conclusion as for $Z(\rightarrow \bar{\nu}\nu)\gamma$. Comparison between three analyses also
 858 shows that for the same pair of the operator when $S_{cross}/S_{no-cross} \neq 1$, the value can be different.
 859 Also, there are cases when for given pair $S_{cross}/S_{no-cross}$ is 1 for one analysis and above 1 for the
 860 other analysis - for example $(\mathcal{O}_{M1}, \mathcal{O}_{M5})$ in $Z(\rightarrow \bar{\nu}\nu)\gamma$ (Fig. 3.9) and $W^\pm Z$ (Fig. 3.10).

861 Given the above, cross-terms can be ignored between different families. This seems reasonable,
 862 given the varying structures within the families. Within a family (T/T), (M/M), (S/S), cross-
 863 terms can be significant, particularly within sub-families, and are expected to influence the limits.
 864 However, the extent of this impact depends on the specific case analysis Therefore, they have to be
 865 studied individually for each analysis.

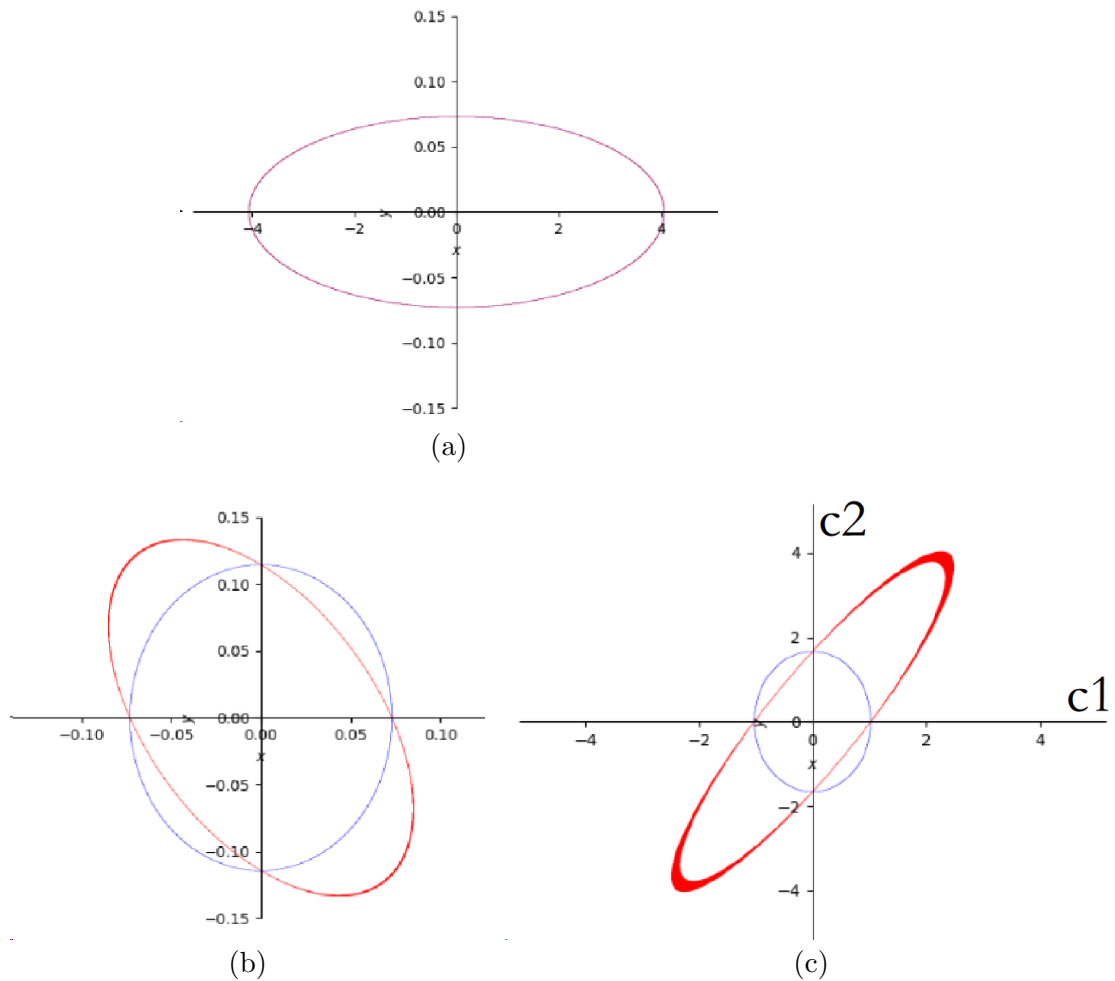


FIGURE 3.8 – Possible cases for c_1, c_2 values based on templates cross-section when including (in red) or neglecting (in blue) cross-terms

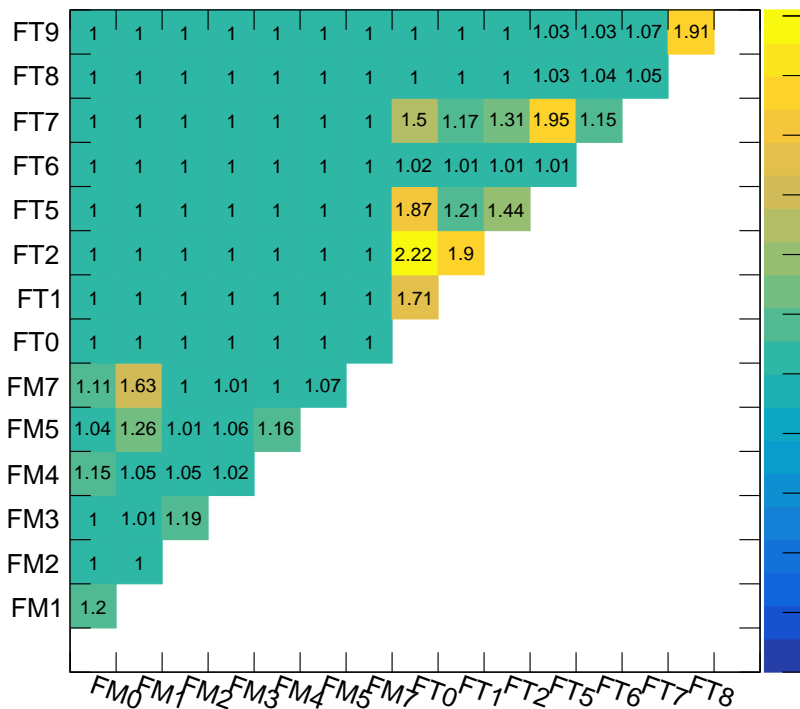


FIGURE 3.9 – $Z(\rightarrow \bar{\nu}\nu)\gamma$ analysis $S_{cross}/S_{no-cross}$ matrix

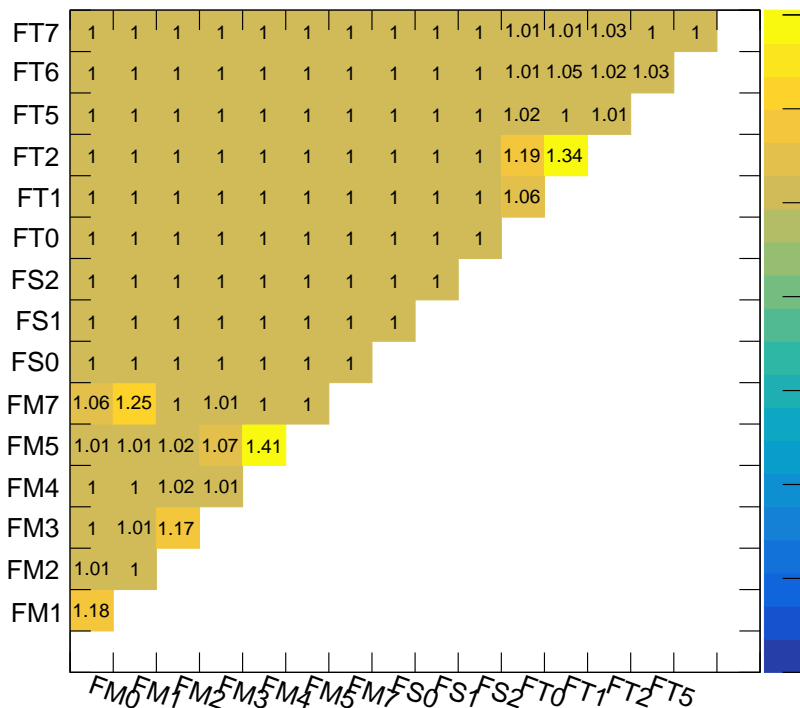


FIGURE 3.10 – $W^\pm Z$ analysis $S_{cross}/S_{no-cross}$ matrix

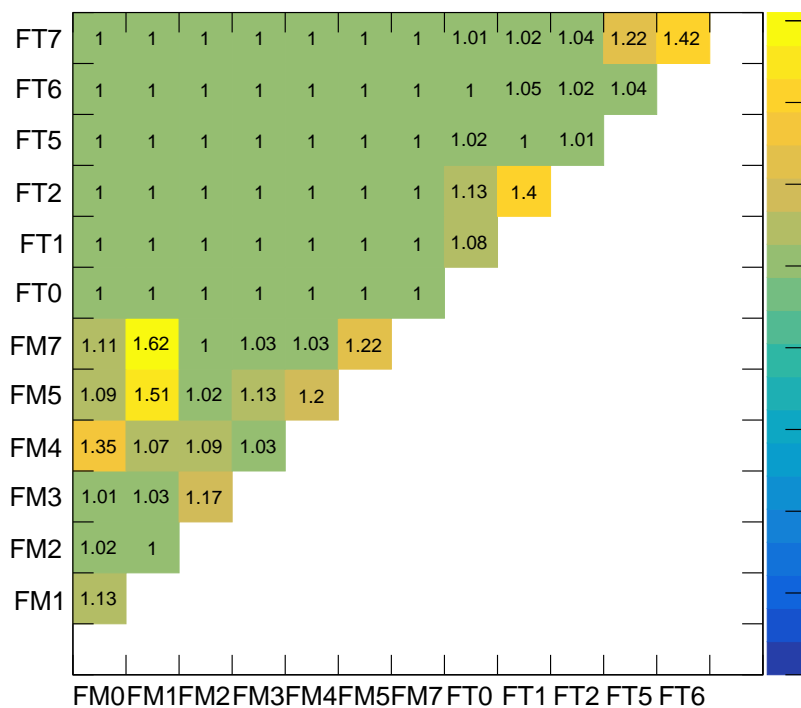


FIGURE 3.11 – $W\gamma$ analysis $S_{cross}/S_{no-cross}$ matrix

870 **3.10 Operator replacement**

871 For combination, it's beneficial that all analyses have all operators, including cross-terms, even
872 if individual analysis does not provide a competitive limit for specific operators. All analyses are
873 missing one piece or another, sometimes because of technical limitations at the time and sometimes
874 because no combination was foreseen. The following subsections describe what is missing for each
875 analysis.

876 Combination includes both reco-level and unfolded fits. Since getting all the missing samples
877 with the full ATLAS simulation would be very time-consuming, an alternative method has been
878 developed to achieve adequate results using only generator-level samples. This method, which
879 modifies existing workspace has the additional benefit of being applicable even when the original
880 analysis team does not exist any longer to make modifications to their workspaces. Its main goal
881 is to insert missing operators and cross-terms by re-using existing workspace contents.

882 In each analysis, limits are obtained by fitting distributions where aQGC have some shape
883 different from backgrounds and Standard Model VBS (also a special kind of background for aQGC
884 fit), e.g., p_T^γ in $Z(\rightarrow \bar{\nu}\nu)\gamma$. Generator-level comparisons show that many operators have similar
885 shapes (normalized to unity, quantified by χ^2) in each signal region, and that also the change with
886 clipping is similar. Therefore, one can use existing shapes in the workspaces, but they need to be
887 re-scaled appropriately to match the cross-section of the original operator.

888 First, TRUTH EFT samples are generated with MadGraph. The typical size of the sample
889 is 100000 events. They are passed through RIVET, where analysis selections are replicated, and
890 distributions are built.

891 To insert the missing operator, one needs to add quadratic and interference terms of the missing
892 operator to the workspace. Replacements are derived based on QUAD shape agreement using
893 clipping points $\infty, 3000, 2000$ because they are the ones where statistics are high. Replacement
894 chosen is an operator whose $\chi_{\infty}^2 + \chi_{3000}^2 + \chi_{2000}^2$ is the lowest. The decision is based only on quadratic
895 terms, without looking at interference terms because they are often negligible (see Sec. 3.5). Instead,
896 a decision based on QUAD terms is applied to INT terms. The same applies to other clippings
897 points - the decision is based on three of them, then the same operator is applied on rest of clipping
898 points (1500,1000). In that way, one operator is substituted with another at all clipping points.
899 With the shape match found, it needs to be re-scaled. For this, the ratio of normalization at the
900 generator level is applied in the workspace.

901 The addition of the missing CROSS term is similar and based on existing QUAD terms.

902 Thus, this proxy solution, despite being based on TRUTH samples, also allows the modification
903 of reco-level workspaces. The idea is that when replicating the analysis cuts at the generator level
904 if you get the same shape, it's very likely that the shape will also be the same at the reco level.
905 The reason is that the experimental acceptance $\varepsilon_{evt.sel.}$ is probably very similar if the shapes (and
906 therefore the important kinematics) are the same.

907 When replacements are found, they need to be added to the original workspace. How this is
908 done depends on what kind of workspace it is - all of the combination analysis provided RooFit
909 workspaces but built with different software; there are two types : EFTFun⁵ (e.g. $Z(\rightarrow \bar{\nu}\nu)\gamma$,
910 $W^\pm Z$) and HistFactory [81] (e.g. $W^\pm W^\pm$, semileptonic VV). We'll return to HistFactory in
911 Sec. 3.10.3. Both $Z(\rightarrow \bar{\nu}\nu)\gamma$ and $W^\pm Z$ analyses, replacements for which are shown below, are
912 EFTFun workspaces, where each bin contains the sum of EFT terms, and a string represents each
913 EFT term depending on order

914 **INT term** $[C_O] * N_{bin}^{INT} * unc^{INT}$
915 **QUAD term** $[C_O] * N_{bin}^{QUAD} * unc^{QUAD}$

5. <https://gitlab.cern.ch/eft-tools/eft-fun>

916 **CROSS term** $[C_{O1}] * [C_{O2}] * N_{bin}^{CROSS} * unc^{CROSS}$

917 Where C_O is a coefficient being fitted and N_{bin}^{order} for reco-level analysis, N is a number of observed
 918 counts in a particular bin over Run-2. To add another missing EFT term, N_b^{order} are replaced by the
 919 ones obtained from re-scaling appropriate shape matches and systematic uncertainties (unc^{order})
 920 of the base operator are copied.

921 To validate the method, “closure test“ is done as follows. For any operator A in the workspace,
 922 one can use instead the shape of another operator also present in the workspace, A' , with a re-scaling
 923 coefficient obtained in the truth study. Then one obtains CL_A , $CL_{A'}$, hoping they are similar. To
 924 quantify the similarity ratio of CL width (most CLs are parabolas centered at 0) is taken given by

$$\frac{CL95_{A'}^{max} - CL95_{A'}^{min}}{CL95_A^{max} - CL95_A^{min}} \quad (3.9)$$

925 More details about each specific analysis are given below.

3.10.1 $Z(\rightarrow \bar{\nu}\nu)\gamma$ analysis

927 Operators already present in the workspace (interference and quadratic terms) are \mathcal{O}_{T0} , \mathcal{O}_{T5} ,
 928 \mathcal{O}_{T8} , \mathcal{O}_{T9} , \mathcal{O}_{M0} , \mathcal{O}_{M1} , \mathcal{O}_{M2} - from each family there are representatives (scalar operators are not
 929 accessible by the topology). Then we want to include \mathcal{O}_{M3} , \mathcal{O}_{M4} , \mathcal{O}_{M5} , \mathcal{O}_{M7} and \mathcal{O}_{T1} , \mathcal{O}_{T2} , \mathcal{O}_{T6} ,
 930 \mathcal{O}_{T7} based on available operators. Also, the analysis is missing the cross-terms.

931 Before injecting anything into the workspace, it's good to check that the truth samples gene-
 932 rated with `MadGraph` and processed with `RIVET` routine can reproduce the shapes already in the
 933 workspace. For this comparison, histograms from truth histograms are normalized to

$$\sigma_{gen} \times \epsilon_{ev.sel} \times L_{Run-2} \quad (3.10)$$

934 and workspace shapes are untouched. Overall, good agreement is seen in shape.

935 The starting point of looking for replacements is a matrix of χ^2 between all pairs of operators.
 936 One of them is partially shown for QUAD terms, clipping ∞ on Table 3.5. The table is symmetric
 937 across the diagonal, and both sides are kept for easier reading by column and row shape matching
 938 quality. For example, looking at the FM0 column, it can be seen that the lower value is 0.28 given
 939 by FM2 - meaning that the best replacement at clipping ∞ for FM0 is FM2, on which cross-section
 940 difference should be taken into account. As both \mathcal{O}_{M0} and \mathcal{O}_{M2} are available, this replacement is
 941 used during reshuffling for validation. Looking at one of the missing operators, for example, FM3,
 942 it can be seen that the best replacement for it is FM7 with $\chi^2 = 6.48$; however, \mathcal{O}_{M7} is also not in
 943 the workspace, and some other base for replacement should be used. Among available operators,
 944 \mathcal{O}_{M1} turns out to have the best (lowest) χ^2 .

945 The matrix shown above is used for each clipping point, and the decision is made based on the
 946 sum across the three highest clipping points. Results for missing operators are shown in Table 3.6
 947 and Table 3.7 shows a similar Table obtained for the closure of the method. It turns out, as it should
 948 be, that if X is a good replacement for Y, then the inverse is also true - e.g., FM0/FM2, showing the
 949 stability of the procedure for generated sample size of 100000 events. Reshuffling matched shapes
 950 will not be shown for brevity, but one example of shape comparison of replacement pair is shown
 951 in Fig. 3.12- rest can be found in Appendix D

952 Once a base for replacement is chosen, its cross-section is scaled with $RN^{clip} = \sigma_{missing}^{fid} / \sigma_{available}^{fid}$
 953 where each σ^{fid} is obtained from the product of cross-section and analysis cuts selection efficiency.
 954 For missing operators, the table of RN^{clip} is shown in Table 3.8 for QUAD terms and in Table 3.9
 955 for INT terms.

956 With the replacement for the missing operator and its renormalization found for each clipping,
 957 missing templates can be inserted into the workspace by first reading the base sample counts from

TABLE 3.5 – $Z(\rightarrow \bar{\nu}\nu)\gamma$ χ^2 matrix, clipping ∞ , for part of QUAD operators

	FM0	FM1	FM2	FM3	FM4	FM5	FM7	FT0	FT1	FT2
FM0		74.1	0.3	107.9	1.3	77.7	109.9	856.7	771.5	786.5
FM1	74.1		73.9	8.6	82.1	2.4	6.7	435.0	379.2	385.8
FM2	0.3	73.9		107.0	1.5	76.2	107.6	846.2	761.9	776.9
FM3	107.9	8.6	107.0		119.1	7.7	6.3	313.0	267.5	273.8
FM4	1.3	82.1	1.5	119.1		85.0	117.5	871.8	787.7	802.1
FM5	77.7	2.4	76.2	7.7	85.0		3.1	390.8	339.7	346.6
FM7	109.9	6.7	107.6	6.3	117.5	3.1		345.5	296.4	302.7
FT0	856.7	435.0	846.2	313.0	871.8	390.8	345.5		4.1	2.0
FT1	771.5	379.2	761.9	267.5	787.7	339.7	296.4	4.1		1.0
FT2	786.5	385.8	776.9	273.8	802.1	346.6	302.7	2.0		1.0
FT5	843.7	433.8	832.9	309.6	860.1	388.2	343.7	3.4		4.7
FT6	259.3	56.8	256.1	27.7	272.4	48.6	30.7	199.9		159.6
FT7	683.8	317.4	674.7	219.3	700.1	282.9	241.8	13.8		6.0
FT8	630.4	297.3	621.7	208.8	644.4	264.1	226.2	10.2		4.3
FT9	617.5	287.8	609.8	198.3	633.2	258.9	221.0	11.9		5.4

 TABLE 3.6 – χ^2 shape agreement results obtained for replacement of $Z(\rightarrow \bar{\nu}\nu)\gamma$ missing operators

missing	replacement	$\chi^2_\infty + \chi^2_{3000} + \chi^2_{2000}$
FM7	FM1	24.5
FM3	FM1	17.2
FM4	FM2	22.4
FM5	FM1	22.9
FT1	FT5	8.6
FT2	FT0	4.6
FT6	FM1	90.0
FT7	FT9	6.1

 TABLE 3.7 – χ^2 shape agreement results obtained for replacement of in-workspace $Z(\rightarrow \bar{\nu}\nu)\gamma$ operators among themselves

available	reshuffling	$\chi^2_\infty + \chi^2_{3000} + \chi^2_{2000}$
FM0	FM2	2.7
FM1	FM0	131.4
FM2	FM0	2.7
FT0	FT5	7.3
FT5	FT0	7.3
FT8	FT9	6.6
FT9	FT8	6.6

TABLE 3.8 – $Z(\rightarrow \bar{\nu}\nu)\gamma$ QUAD terms replacements renormalization applied on base sample to obtain cross-section matching the missing sample

missing	replacement	RN_{∞}	RN_{3000}	RN_{2000}	RN_{1500}	RN_{1000}
FM7	FM1	0.38	0.39	0.40	0.41	0.46
FM3	FM1	6.67	6.4	6.34	5.97	5.87
FM4	FM2	0.31	0.32	0.33	0.34	0.41
FM5	FM1	9.59	9.7	9.92	10.2	10.88
FT1	FT5	0.66	0.65	0.64	0.6	0.59
FT2	FT0	0.14	0.15	0.15	0.16	0.16
FT6	FM1	819.5	687.13	590.09	527.18	538.61
FT7	FT9	0.14	0.14	0.14	0.15	0.14

TABLE 3.9 – $Z(\rightarrow \bar{\nu}\nu)\gamma$ INT terms replacements renormalization applied on base sample to obtain cross-section matching the missing sample

missing	replacement	RN_{∞}	RN_{3000}	RN_{2000}	RN_{1500}	RN_{1000}
FM7	FM1	-0.41	-0.41	-0.40	-0.40	-0.43
FM3	FM1	-2.00	-1.99	-1.97	-1.99	-2.08
FM4	FM2	-0.12	-0.13	-0.13	-0.13	-0.12
FM5	FM1	3.55	3.3	3.31	2.87	2.12
FT1	FT5	-0.14	-0.14	-0.15	-0.15	-0.16
FT2	FT0	0.31	0.31	0.31	0.31	0.29
FT6	FM1	-46.0	-45.13	-41.83	-34.23	-23.82
FT7	FT9	-32.99	-31.51	-30.54	-29.77	-29.84

TABLE 3.10 – $Z(\rightarrow \bar{\nu}\nu)\gamma$ replacement closure with INT+QUAD

operator	c=∞	c=3000	c=2000	c=1500	c=1000
T0r	0.99	1.01	0.98	0.98	0.96
T5r	1.01	1.0	0.93	1.02	1.02
T8r	1.0	1.0	0.92	0.92	0.99
T9r	1.0	1.0	1.09	1.08	1.0
M0r	1.02	1.04	1.0	1.05	1.0
M1r	1.06	1.09	1.2	1.06	1.01
M2r	0.98	0.97	1.0	0.95	1.0

the workspace, then scaling them by RN, and adding the resulting counts back to the workspace. No tool on the market can do that⁶. Therefore, custom software was developed to edit the workspace, relying on **WSFactory** in **ROOT**.

One can then move to closure, the results of which are shown in Table 3.10 for observed Data. Overall, non-closure is below 10% and degrades when going to lower clipping values - this is expected because of larger statistical uncertainties in the signal templates.

Also Fig. 3.13 shows one example (\mathcal{O}_{M0} replacement validation) of NLL scan that gives the ratio in the table for clipping point 1500. According to Eq. 3.9 this case gives closure of $\frac{30.33 - (-29.89)}{28.91 - (-28.30)} = 1.05$ so non-closure is 5%. Other cases are shown in Appendix E.

Augmented workspaces were produced at all clipping points selected, containing in addition to the original operators, the ones previously missing, together with missing cross-terms.

3.10.2 $W^\pm Z$ analysis

Similarly to $Z(\rightarrow \bar{\nu}\nu)\gamma$, from M and T families, some operator shapes are available, and some are missing. Scalar $W^\pm Z$ operators are already in the workspace. Already present in the workspace (interference and quadratic terms) are $\mathcal{O}_{M0}, \mathcal{O}_{M1}, \mathcal{O}_{M7}, \mathcal{O}_{T0}, \mathcal{O}_{T1}, \mathcal{O}_{T2}, \mathcal{O}_{S1}, \mathcal{O}_{S02}$ and we want to include by relying on available ones $\mathcal{O}_{M2}, \mathcal{O}_{M3}, \mathcal{O}_{M4}, \mathcal{O}_{M5}$ from M family and $\mathcal{O}_{T5}, \mathcal{O}_{T6}, \mathcal{O}_{T7}, \mathcal{O}_{T8}, \mathcal{O}_{T9}$ from tensor family. Also missing the cross-terms.

Procedure for replacement was described for $Z(\rightarrow \bar{\nu}\nu)\gamma$ case, and here only $W^\pm Z$ specific details are highlighted.

The analysis uses a boosted decision tree that provides a score based on several kinematic variables. What is fitted to obtain the limit is detector-level one-dimension distribution of the two-dimensional combination of BDT score and M_T^{WZ} , example of which is shown on Fig. 3.14 At generator level with **MadGraph** and **RIVET** we can easily only check shapes similarity on M_T^{WZ} , but we expect other aQGC kinematics (entering the BDT) will be similar, too.

Replacements were derived based on M_T^{WZ} and re-normalizations are taken from appropriate pair of cross-sections. A closure test similar to what was done for $Z(\rightarrow \bar{\nu}\nu)\gamma$ was performed, and results are shown in Table 3.11. One finds that replacement based on M_T^{WZ} alone gives good closure for workspace using BDT. As the analysis team provided, for one of the clipping points, the workspace without BDT (where only M_T^{WZ} is used), validation was done twice : replacements were applied on workspace with and without the BDT and limit agreement was the same.

Missing operators and cross-terms were added, and now a complete workspace is available.

3.10.3 Other analyses

6. Particularly **workspaceCombiner** doesn't allow independent manipulation of interference, quadratic, and cross-terms terms

TABLE 3.11 – $W^\pm Z$ replacement closure with INT+QUAD

operator	c=∞	c=3000	c=1500	c=1000
T0r	1.12	0.99	0.89	0.78
T1r	1.03	1.03	1.0	0.98
T2r	0.97	0.97	1.0	1.02
M0r	0.92	0.94	1.0	1.25
M1r	1.1	0.99	1.0	1.03
M7r	0.91	1.02	1.0	0.95
S02r	1.02	1.01	1.03	1.01
S1r	1.1	1.06	1.0	0.8

- $W^\pm W^\pm$ analysis only lacks cross-terms and only at some clipping points. They can be added similarly to $Z(\rightarrow \bar{\nu}\nu)\gamma$, $W^\pm Z$ cases with two differences. One is that $W^\pm W^\pm$ workspace is not built with `EFTFun` but with `HistFactory` (HF). To modify HF workspace, it is exported to `JSON`, where each EFT term is one entry that contains an array of bin counts and separately minus sign for negative cross-section if needed, modified in this format, and then imported back to `HistFactory`. Another difference is that in the $W^\pm W^\pm$ analysis, EFT is not only in the Signal Region but also in the WZ Control Region. Therefore, there are more samples to track for replacements, and replacement should be done twice
- For VV semileptonic analysis, cross-terms were not generated, but INT+QUAD terms for all operators are available. The analysis is detector-level, so one can't just insert a truth sample into the workspace. The overall idea is the same as the one used in Sec. 3.10.1 and Sec. 3.10.2, but there are two difficulties. One is just the amount of samples to track, as this analysis is a combination in itself of ZZ, WW, and WZ topologies. Second is that the RNN score is fitted, which cannot be obtained easily from simple kinematic distributions. However, the network is available, and one can feed information into it to get the RNN distributions. The χ^2 search can be applied to that distribution. VV semileptonic workspace was made with `HistFactory`, and technical implementation will rely on `JSON` similarly to $W^\pm W^\pm$ analysis case
- $W\gamma$ analysis (unfolded) originally was missing cross-terms. I generated MC EFT samples, based on which the analysis team produced an updated workspace, now containing cross-terms
- $ZZ \rightarrow 4\ell$ analysis (also unfolded) originally was missing cross-terms and only had quadratic and interference terms for T family operators. I generated MC EFT samples for cross-terms and M, S family operators, based on which the analysis team produced an updated workspace, now containing all operators and cross-terms

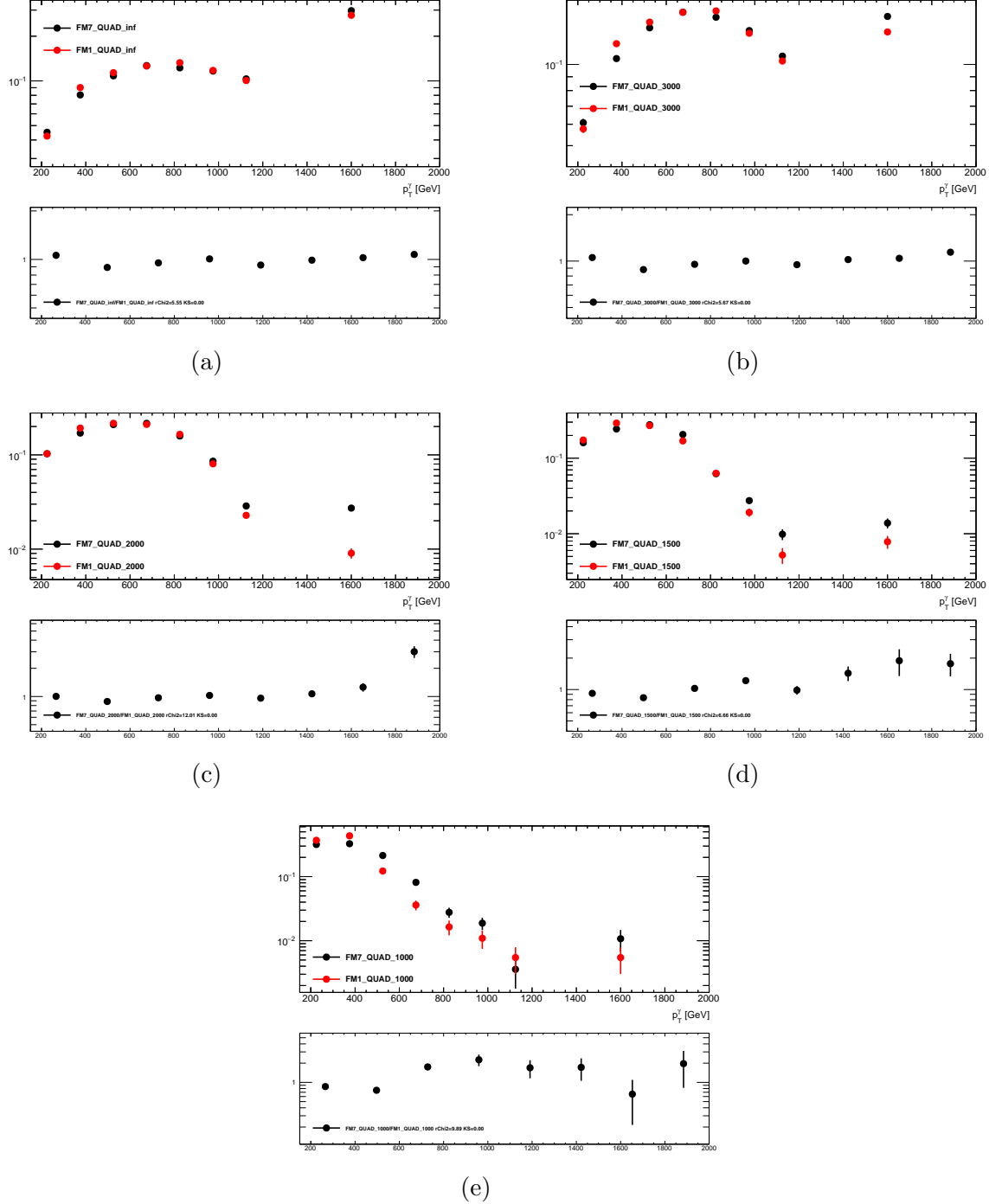


FIGURE 3.12 – FM7vsFM1 shape comparison obtained in $Z(\rightarrow \bar{\nu}\nu)\gamma$ sample, replicating analysis selections. Bins match those used in the analysis. The bottom pad is the ratio between two operator shapes (a) without clipping (b) clipping=3000 (c) clipping=2000 (d) clipping=1500 (e) clipping=1000

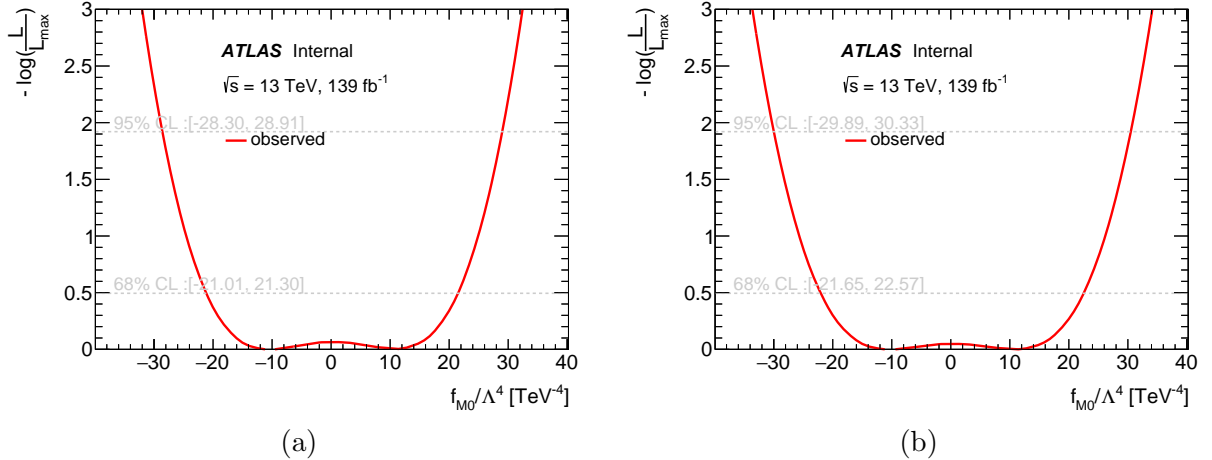


FIGURE 3.13 – $Z(\rightarrow \bar{\nu}\nu)\gamma$ analysis replacement validation : comparison between M0 (a) original limit (b) replaced limit

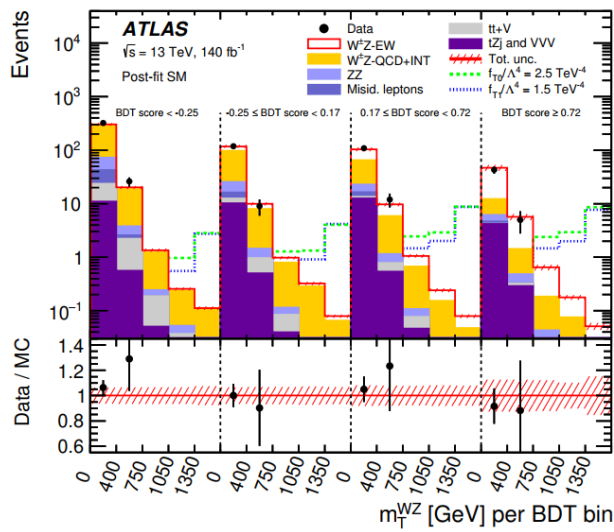


FIGURE 3.14 – Detector-level one-dimension distribution of the two-dimensional combination of BDT score and M_T^{WZ} T observables used to obtain limits on EFT coefficients [56].

1015 **3.11 Preliminary results**

1016 The combination means that we want to do a simultaneous fit to all the workspaces to derive
1017 limits on Wilson coefficients for all the operators. We do so [86] by combining workspaces into
1018 one “combined“ using `workspaceCombiner`⁷ and working with several combined workspaces, one
1019 per clipping point. In combination, we want to correlate the systematic uncertainties as much as
1020 possible between the various analyses to have a consistent treatment - a summary of correlations
1021 is shown in Table 3.12.

1022 At the moment of writing, not all the building blocks are available to do the full combination

- Missing cross-terms in VV semileptonic, $W^\pm W^\pm$ analyses
- Missing clipping points 1000, 700 in VV semileptonic analysis
- We don't want certain data events to be selected by multiple analyses to avoid the time-consuming task of evaluating and correcting for potentially arising statistical correlations. Unfortunately, it happens because individual analyses' selections are not orthogonal to each other. Most overlapping events in our case, are expected to be between the Control Region in one analysis and Signal Region in another analysis, so no large impact on the final results is expected, but still requires careful treatment. Orthogonality studies are ongoing

1023 Cross-terms are not involved for 1D limits; therefore, one can obtain them for the time being,
1024 ignoring the overlap. As shown in Table 3.13, without clipping, $Z(\rightarrow \bar{\nu}\nu)\gamma$ analysis leads the
1025 combination. For M, S typically, VV semileptonic analysis is leading.

1026 **3.11.1 1-D limits**

1027 Expanding the combination machinery to cover all the clippings points and considering for the
1028 time being only four analysis : $Z(\rightarrow \bar{\nu}\nu)\gamma$, $W^\pm Z$, $W\gamma$, $ZZ \rightarrow 4\ell$ one can already obtain limits
1029 that should be close to the final ones for T operators. Results are shown Fig. 3.15 for clipping
1030 points up to 1000. It can be seen that $Z(\rightarrow \bar{\nu}\nu)\gamma$ is leading the combination at higher clippings
1031 as expected, however, at lower clippings for some operators, it becomes comparable with other
1032 analyses - likely because here SM background is coming into play. As was shown in Fig. 3.7, without
1033 clipping, distribution is peaking at high values which are greatly separated from the Standard Model
1034 background. At lower clipping, this is not the case anymore, and one may have a Standard Model
1035 “pedestal“ underneath the aQGC signal - degrading the limit. Also, gain from the combination is
1036 visible when there are several comparable analyses, for example at clipping=1000 \mathcal{O}_{T2} individual
1037 $Z(\rightarrow \bar{\nu}\nu)\gamma$ and $W^\pm Z$ limits are the same and worse than the combined limit.

1038 On Fig. 3.16, the combined limits are compared with unitarity bounds (see Sec. 3.7). At clipping
1039 3000, unitarity is often violated (when limits are larger than the unitarity bound) as expected, but
1040 at clipping 2000, all the operators except T8 are better than the unitarity bound.

1041 **3.11.2 2-D limits**

1042 The main interest in 2D limits is the correlation between limits (as magnitude will follow 1D
1043 results). An example of several analyses for one pair is shown on Fig. 3.17 - there is a gain from the
1044 combination, but mostly, the combined limit follows the $Z(\rightarrow \bar{\nu}\nu)\gamma$ one. This is a typical situation
1045 for all T-T 2D limits obtained. A summary of limit correlations is shown on Fig. 3.18 - each cell is a
1046 correlation of two-dimensional limits obtained in combination. Cross-terms drive those correlations
1047 - just like ellipses considered in Sec. 3.9.

1048 **3.12 Outlook**

1049 **3.12.1 Inputs**

7. https://gitlab.cern.ch/atlas_higgs_combination/software/workspaceCombiner/

TABLE 3.12 – Correlations of systematic uncertainties in combination. Adapted from [87]

	VV Semileptonic	$W^\pm W^\pm$	$W^\pm Z$	$W\gamma$	$Z(\rightarrow \bar{\nu}\nu)\gamma$	$ZZ \rightarrow 4\ell$	Correlated
Luminosity	x	x	x	x	x	x	x
Pile-up reweighting	x	x	x	x	x	x	x
EMPFflow jets	x	x	x	x	x	x	x
E_T^{miss}	x	x	x	x	x	x	x
Electrons	x	x	x	x	x	x	x
Muons	x	x	x	x	x	x	x
Photons				x	x	x	x
b -tagging extrapolation	x	x	x	x	x	x	x
Other b -tagging systematics	x	x	x	x	x	x	x
Background modelling	x	x	x	x	x	x	x
Parton shower	x	x	x	x	x	x	x
QCD scale on VBS signal	x	x	x	x	x	x	x
PDF/ α_s on VBS signal	x	x	x	x	x	x	x
QCD scale on aQGC signal	x	x	x	x	x	x	x
PDF/ α_s on aQGC signal	x	x	x	x	x	x	x

TABLE 3.13 – Individual and combined observed limits without clipping [88]

Operator	VV Semileptonic	$W^\pm W^\pm$	$W^\pm Z$	$W\gamma$	$Z(\rightarrow \bar{\nu}\nu)\gamma$	$ZZ \rightarrow 4\ell$	Combined
FS02/ Λ^4	[−3.72, 3.73]	[−5.88, 5.93]	[−10.0, 10.0]	Absent	Absent	[−26.6, 26.8]	[−3.41, 3.40]
FS1/ Λ^4	[−7.62, 7.63]	[−23.5, 23.6]	[−30.0, 29.6]	Absent	Absent	[−41.8, 42.0]	[−7.17, 7.14]
FM0/ Λ^4	[−1.20, 1.19]	[−4.11, 4.13]	[−5.56, 5.55]	[−24.0, 23.8]	[−4.57, 4.65]	[−4.85, 4.88]	[−1.10, 1.07]
FM1/ Λ^4	[−3.77, 3.77]	[−6.73, 6.98]	[−8.49, 8.41]	[−36.7, 37.8]	[−7.66, 7.65]	[−17.9, 17.8]	[−3.18, 3.18]
FM2/ Λ^4	[−1.76, 1.76]	Absent	[−10.5, 10.6]	[−8.60, 8.57]	[−1.89, 1.89]	[−7.38, 7.41]	[−1.35, 1.35]
FM3/ Λ^4	[−5.43, 5.44]	Absent	[−15.9, 16.0]	[−13.4, 13.7]	[−2.96, 2.97]	[−25.9, 25.9]	[−2.71, 2.72]
FM4/ Λ^4	[−2.82, 2.83]	Absent	[−4.43, 4.44]	[−15.4, 15.5]	[−3.31, 3.33]	[−19.4, 19.4]	[−2.10, 2.11]
FM5/ Λ^4	[−4.20, 4.21]	Absent	[−6.27, 6.29]	[−14.0, 12.3]	[−2.35, 2.35]	[−27.5, 27.6]	[−2.18, 2.19]
FM7/ Λ^4	[−6.32, 6.15]	[−9.70, 9.47]	[−11.3, 11.4]	[−66.0, 65.2]	[−12.2, 12.3]	[−33.9, 34.2]	[−5.20, 5.22]
FT0/ Λ^4	[−0.24, 0.21]	[−0.36, 0.36]	[−0.56, 0.55]	[−2.11, 2.22]	[−0.093, 0.084]	[−0.97, 0.92]	[−0.095, 0.083]
FT1/ Λ^4	[−0.23, 0.23]	[−0.17, 0.19]	[−0.40, 0.35]	[−1.32, 1.44]	[−0.12, 0.11]	[−1.22, 1.21]	[−0.10, 0.10]
FT2/ Λ^4	[−0.53, 0.53]	[−0.63, 0.74]	[−1.20, 1.00]	[−3.44, 3.90]	[−0.24, 0.22]	[−2.50, 2.41]	[−0.24, 0.22]
FT5/ Λ^4	[−0.61, 0.55]	Absent	[−1.43, 1.45]	[−1.52, 1.55]	[−0.088, 0.099]	[−2.50, 2.41]	[−0.088, 0.097]
FT6/ Λ^4	[−0.71, 0.68]	Absent	[−1.33, 1.41]	[−1.19, 1.23]	[−0.26, 0.26]	[−3.88, 3.84]	[−0.25, 0.25]
FT7/ Λ^4	[−1.86, 1.61]	Absent	[−3.87, 3.87]	[−3.03, 3.16]	[−0.27, 0.31]	[−8.44, 8.12]	[−0.32, 0.35]
FT8/ Λ^4	[−0.47, 0.47]	Absent	Absent	[−0.060, 0.060]	[−2.11, 2.11]	[−0.059, 0.059]	
FT9/ Λ^4	[−1.01, 1.01]	Absent	Absent	[−0.13, 0.13]	[−4.52, 4.52]	[−0.13, 0.13]	

TABLE 3.14 – $ZZ \rightarrow \ell\bar{\ell}\nu\bar{\nu}$ expected limits without clipping and at clipping=1000 GeV

operator	no clip	clip=1000
T0	[-0.66, 0.63]	[-5.63, 5.57]
T1	[-0.72, 0.71]	[-5.17, 5.12]
T2	[-1.50, 1.46]	[-10.88, 10.84]
T5	[-1.16, 1.11]	[-9.01, 8.96]
T6	[-1.72, 1.71]	[-9.52, 9.54]
T7	[-5.23, 4.88]	[-27.78, 27.34]
T8	[-0.91, 0.91]	[-8.9, 8.92]
T9	[-1.98, 1.98]	[-18.93, 18.90]

There is a hope to add more analyses, for example, $ZZ \rightarrow \ell\bar{\ell}\nu\bar{\nu}$ and $Z(\rightarrow \ell\bar{\ell})\gamma$.

$ZZ \rightarrow \ell\bar{\ell}\nu\bar{\nu}$ analysis is blinded at the moment of writing; however, with Asimov, EFT limits are finalized. Currently, only T limits are considered. Results are shown on Table 3.14 - it will not be a leading analysis, but valuable input to cover all the VBS processes.

$Z(\rightarrow \ell\bar{\ell})\gamma$ analysis was published but lacks the EFT part - it will be added. Naively one may expect limits to be the ones of $Z(\rightarrow \bar{\nu}\nu)\gamma$ but worse by branching fraction.

3.12.2 1-D limits

Limits on T family Wilson coefficients were shown with four analyses combined in the clipping region where one is competitive with unitarity bound, there are several comparable analyses, despite the expectation that $Z(\rightarrow \bar{\nu}\nu)\gamma$ analysis would dominate because this is the case without clipping. It's interesting to see if VV semileptonic, $W^\pm W^\pm$ and potentially $ZZ \rightarrow \ell\bar{\ell}\nu\bar{\nu}$, $Z(\rightarrow \ell\bar{\ell})\gamma$ would also contribute.

For scalar and mixed operator families, the expectation is that VV semileptonic would lead, but given experience with T, it may not be the case. The goal is to check that by combining all the analyses at all clipping points (at the moment, this is not possible because of missing VV semileptonic workspaces).

With that, one wants to obtain unitarized limits : at energy where unitarity bound and measured limits cross. Need to compare continuous (in m_{VV}) unitarized bound with limits obtained at discrete m_{VV} points (1000, 1500, 2000, 3000, inf were shown). Some well-motivated interpolation clippings points should be chosen.

Also, non-orthogonality removal will be done ; potentially, some studies on systematics correlation are missing.

3.12.3 n-D limits

Once missing crosses are added to VV Semileptonic and $W^\pm W^\pm$ analyses, one can obtain a two-operator limit correlation. As was shown, at lower clippings, 1D limits become comparable between two analyses - then one can expect for this case and also when correlations are in opposite directions, like for Fig. 3.19 case, that resulting combined shape will be the one more complicated than just ellipse.

Going further to n-D limits, one can look at collective deviations of operator limits.

Limits obtained by simultaneous fit to two operators, some of which were shown on Fig. 3.17 and Fig. 3.19 are described by an ellipse. While fitting three operators at the time, the resulting shape will likely be an ellipsoid. Continuing along the same lines, one might obtain an 18-dimensional ellipsoid (for all the operators) showing how all the Wilson coefficients are related to each other.

1091 The shape obtained and projected into the original Eboli coordinates should give something re-
1092 sembling one-dimensional limits. But projection also can be made into some other, non-rectangular
1093 coordinates and with this mapping, one might indirectly test concrete models of anomalous gauge
1094 couplings.

1095 **3.13 Conclusion**

1096 I've worked on both inputs to combination (without complete inputs, there is nothing to com-
1097 bine) and the combination itself.

1098 The operator content of published analyses is non-homogeneous, which doesn't allow us to really
1099 probe the full Eboli model. At the moment of writing, I contributed in one way or another to four
1100 out of six ($W^\pm Z$, $W^\pm W^\pm$, $W\gamma$, $Z(\rightarrow \bar{\nu}\nu)\gamma$, $ZZ \rightarrow 4\ell$, VV semileptonic) analyses that are
1101 available for combination. The method was developed to add missing operators to an analysis. The
1102 method was implemented on $Z(\rightarrow \bar{\nu}\nu)\gamma$ and $W^\pm Z$ analyses, and non-closure of replacement was
1103 evaluated, typically giving CL agreement within 10%. The method will be applied on $W^\pm W^\pm$ and
1104 VV Semileptonic analyses but with different technical implementations. Two analyses, $ZZ \rightarrow 4\ell$
1105 and $W\gamma$, now also have full operator content by relying on Monte Carlo samples I generated.
1106 Additionally, I participated in the derivation of $ZZ \rightarrow \ell\bar{\ell}\nu\bar{\nu}$ analysis expected limits, currently
1107 finished.

1108 In combination itself, studies were done on reduced set (T family) of one-dimensional operator
1109 limits, already showing at times the power of combination at lower clipping values, despite the
1110 opposite expectation because of one clearly leading unclipped analysis. EFT cross-terms added
1111 to analyses are essential to multi-dimensional limits - two-dimensional limits were evaluated and
1112 correlation of limits was studied between T family operators individually and in combination.

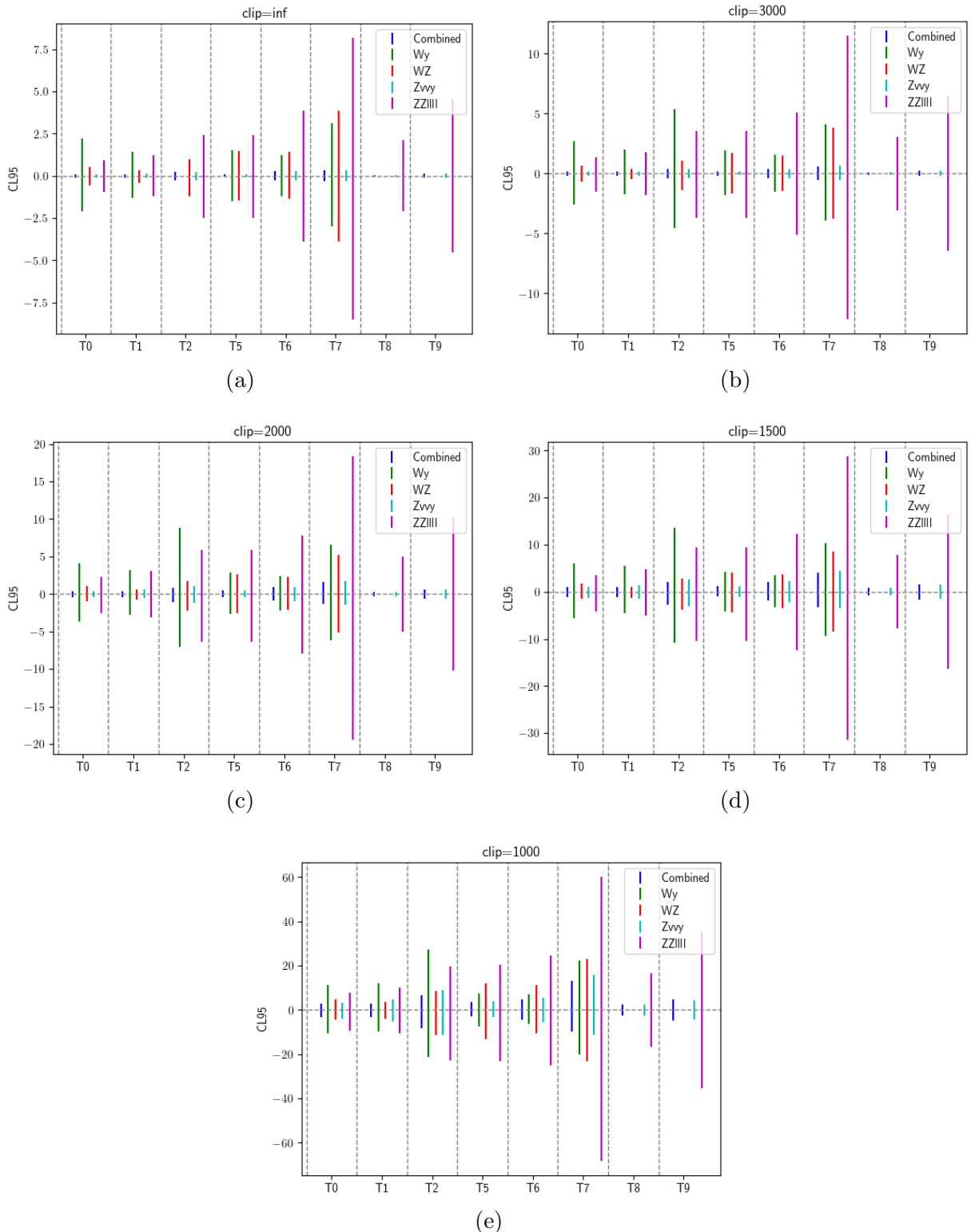


FIGURE 3.15 – Individual $Z(\rightarrow \bar{\nu}\nu)\gamma$, $W^\pm Z$, $W\gamma$, $ZZ \rightarrow 4\ell$ and combined one-dimensional T family limits for (a) without clipping (b) clipping=3000 (c) clipping=2000 (d) clipping=1500 (e) clipping=1000

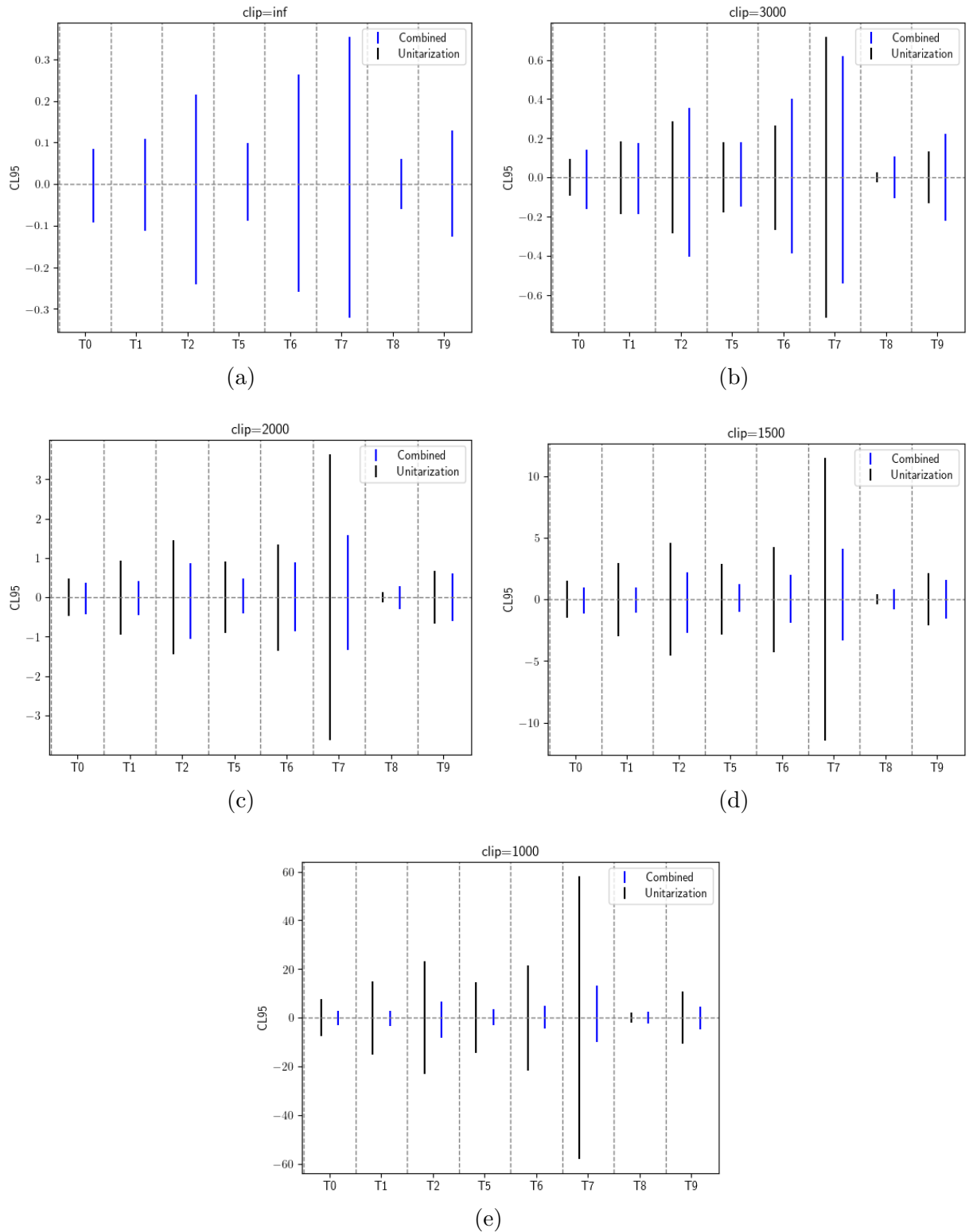


FIGURE 3.16 – Combined $Z(\rightarrow \bar{\nu}\nu)\gamma$, $W^\pm Z$, $W\gamma$, $ZZ \rightarrow 4\ell$ one-dimensional T family limits and unitarity bounds (a) without clipping (b) clipping=3000 (c) clipping=2000 (d) clipping=1500 (e) clipping=1000

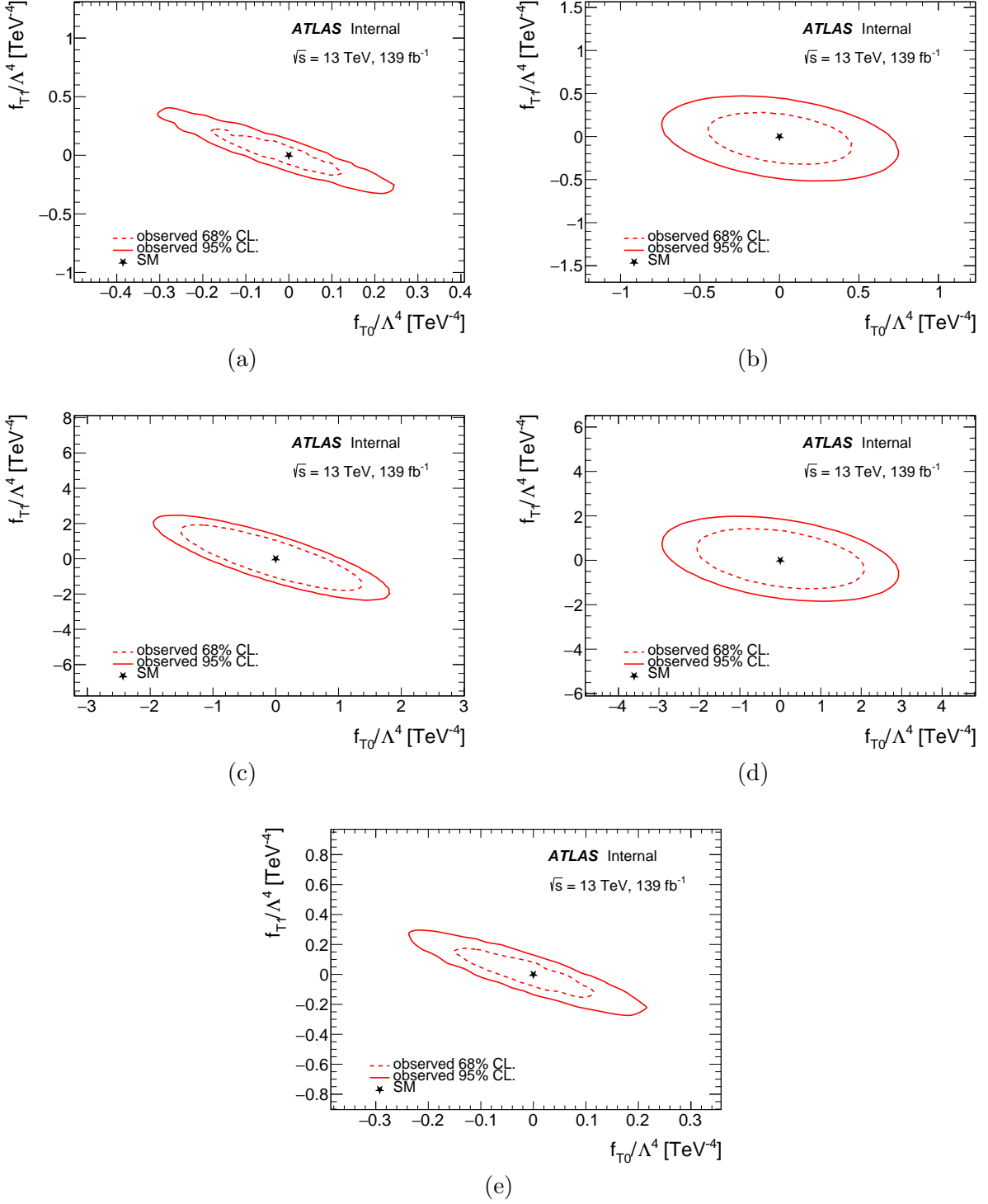


FIGURE 3.17 – T0vsT1 two-dimensional limit for (a) $Z(\rightarrow \bar{\nu}\nu)\gamma$ (b) $W^\pm Z$ (c) $ZZ \rightarrow 4\ell$ (d) $W\gamma$ (e) combined

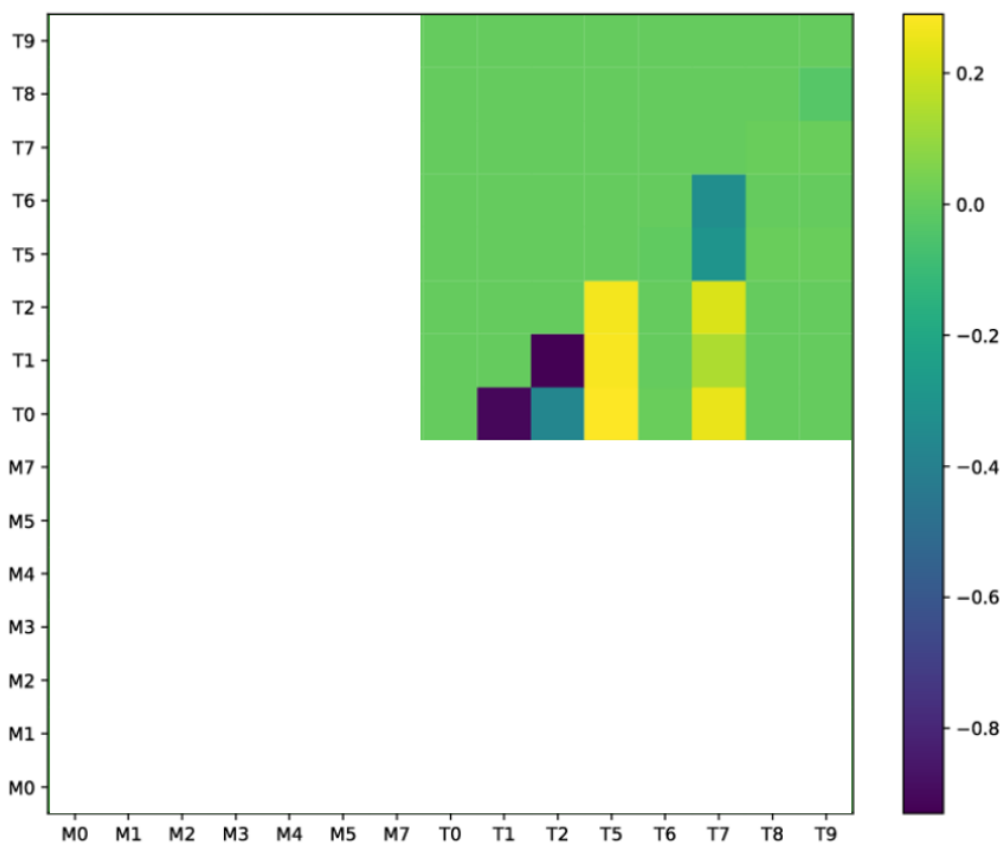


FIGURE 3.18 – Summary of 2D T pairs limit correlations (combined)

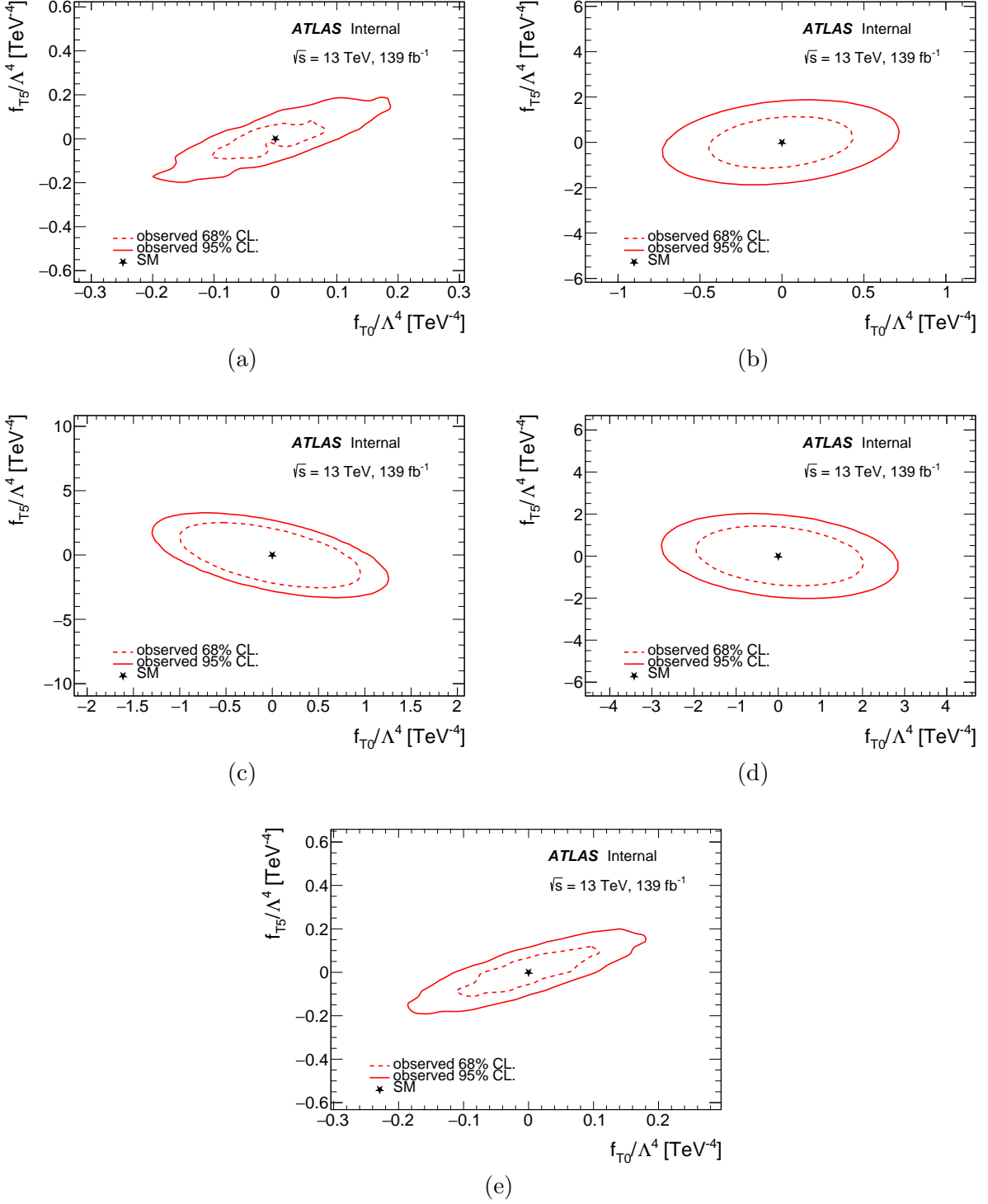


FIGURE 3.19 – T0vsT5 two-dimensional limit for (a) $Z(\rightarrow \bar{\nu}\nu)\gamma$ (b) $W^\pm Z$ (c) $ZZ \rightarrow 4\ell$ (d) $W\gamma$ (e) combined

1113 4 - Forward Jet Vertex Tagger

1114 ATLAS detector doesn't have a tracker for $|\eta| \geq 2.5$ and in this region, a separate pile-up tagging
 1115 method is used (as opposed to barrel region with Jet Vertex Tagger), called forward Jet Vertex
 1116 Tagger¹ (fJVT). fJVT was introduced in EMTopo times[34], then ported to PFlow jets [44, 84]
 1117 and calibrated [93] in Release 21 (R21) ATLAS software for Run-2. Release 22 (R22) is a major
 1118 update to ATLAS software intended for Run-3 and above.

1119 The need for pile-up rejection for $|\eta| \geq 2.5$ is shown on Fig. 4.1, where the fraction (out of a
 1120 total number of forward jets) of HS, QCD PU, and stochastic PU jets is shown depending on the
 1121 number of p-p interactions in the event. Dependencies are obtained from MC Sherpa $Z \rightarrow \ell\bar{\ell} + jets$
 1122 sample. It can be seen that especially at μ values close to Run-3 conditions, HS jets constitute about
 1123 10% of all forward jets - the rest is pile-up, roughly equally divided between QCD and stochastic
 1124 pile-up.

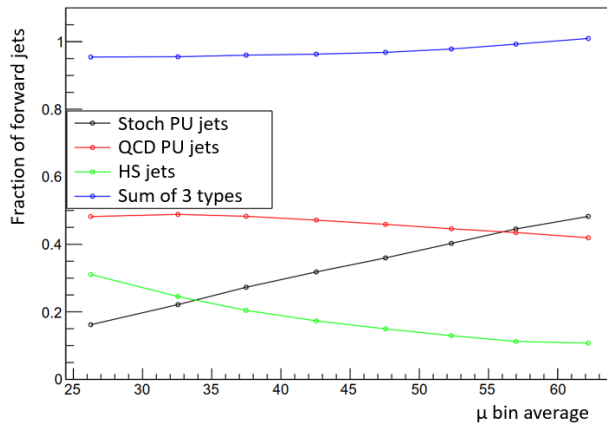


FIGURE 4.1 – Fraction of HS, QCD PU, stochastic PU forward jets depending on number of p-p interactions

1125 4.1 Principle of operation

1126 Key steps of the algorithm are summarized in Fig. 4.2. The goal of the method is to find the
 1127 vertex v (out of ≈ 40 in Run-2) whose \overrightarrow{MET}_v balances forward jet j with a transverse momentum
 1128 \vec{p}_T^{vj} under consideration where the first index corresponds to the vertex with respect to which
 1129 momentum is calculated and the second index is for the jet. For this, all the objects in the event,
 1130 including jets, are re-build with respect to each vertex except Hard Scatter (HS) vertex. \overrightarrow{MET}_v is
 1131 computed excluding objects associated to HS vertex, as identified with NNJVT and R_{p_T} . Metric
 1132 for \overrightarrow{MET}_v and \vec{p}_T^{vj} balance is the normalized scalar product of them - as illustrated on Fig. 4.3.
 1133 Then, fJVT for jet j is defined as

$$fJVT^{vj} = \max_v \left(\frac{\overrightarrow{MET}_v \cdot \vec{p}_T^{vj}}{|\vec{p}_T^{vj}|^2} \right) \quad (4.1)$$

1134

$$fJVT_j = \max_v (fJVT^{vj}) \quad (4.2)$$

1. Name can be misleading as algorithm working principle has nothing to do with JVT

1135 The resulting example fJVT distribution is shown in Fig. 4.4 for Hard-Scatter (HS) jets and Pile-
 1136 up (PU) jets (inclusive, no difference between QCD and Stochastic PU made) jets (labeled with
 1137 truth² MC information) - degree of separation visible. HS jets tend to be closer to 0, as they do not
 1138 balance PU vertices' momentum. Also, the long tail of high fJVT values is visible - from looking
 1139 at Eq. 4.2, it can be expected to be coming from events where the MET of the selected vertex was
 1140 large. Dependence is shown on Fig. 4.5 and supports the intuition. For this distribution custom
 1141 derivation³ format was developed⁴ because information on fJVT MET of vertex typically gets
 1142 rejected.

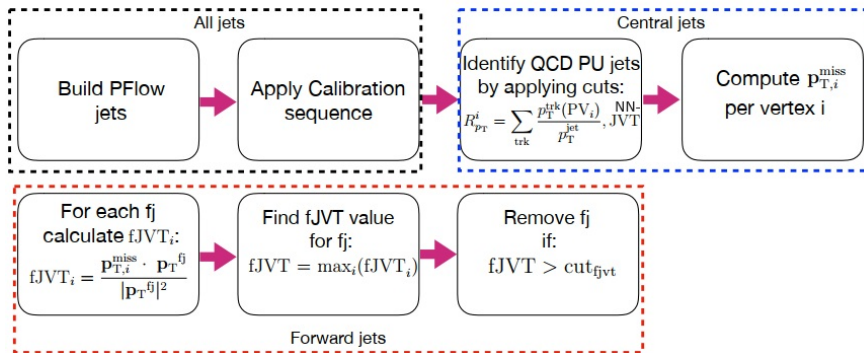


FIGURE 4.2 – fJVT algorithm. Adapted from [84]

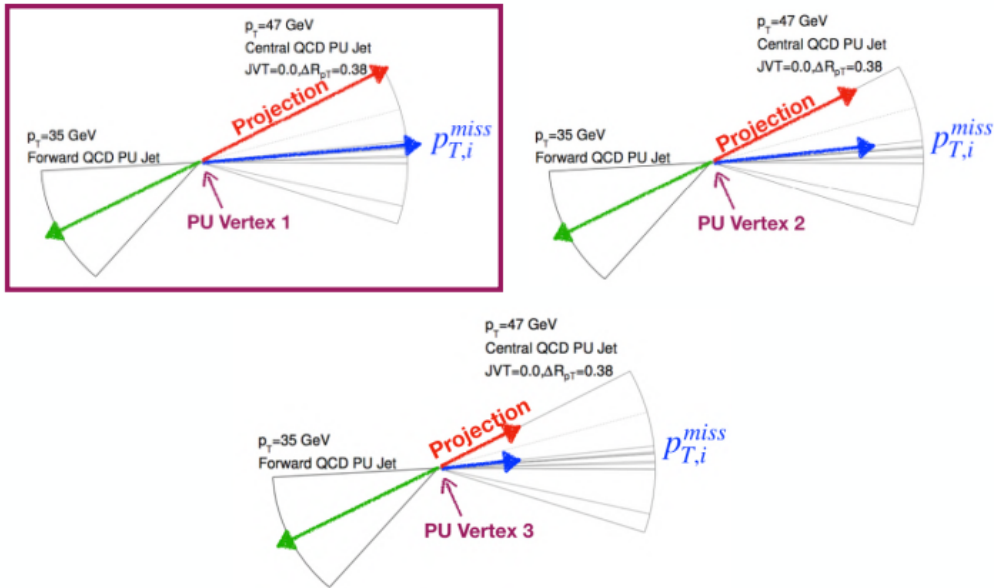


FIGURE 4.3 – fJVT algorithm illustration [84]

1143 The performance of the algorithm is quantified with a receiver operating characteristic (ROC)

2. For the typical philosopher of science, particularly for Age Of Enlightenment (particularly French) authors, the term is nonsense, as in physics, being an experimental science, truth is given by the measurement and not by whatever thought or computer simulation one might do

3. One of the data processing stages in ATLAS

4. Instead of DAOD_PHYS used elsewhere

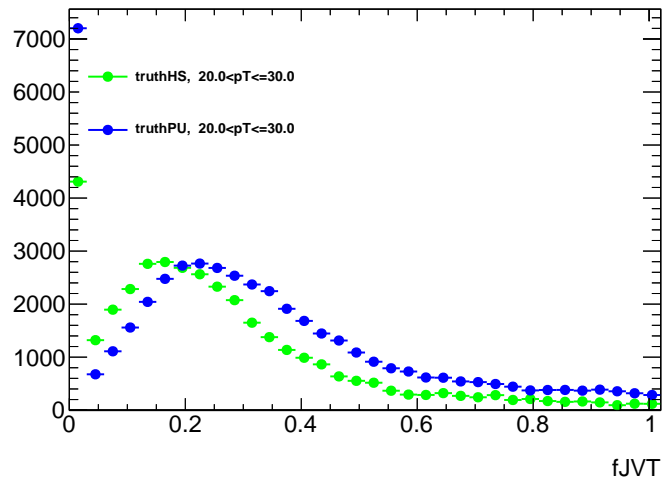


FIGURE 4.4 – fJVT distribution for truth HS and inclusive PU jets, $20 < p_T \leq 30$ GeV, $35 < \bar{\mu} \leq 45$, fJVT calibration fiducial region

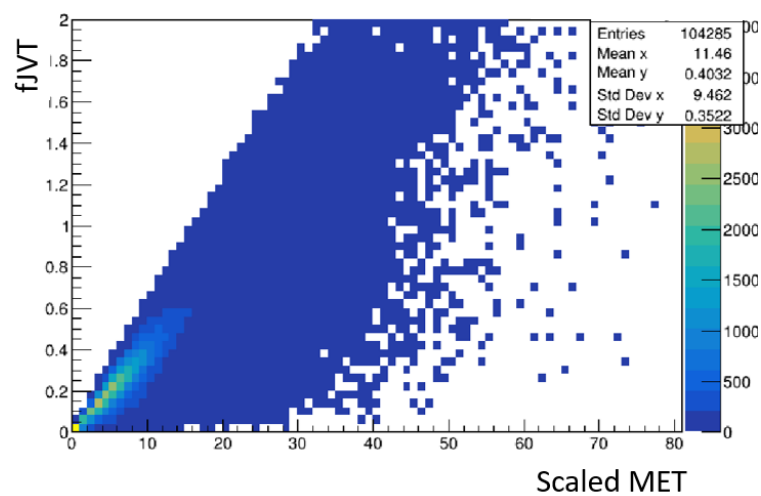


FIGURE 4.5 – fJVT depending on MET of vertex where it's taken from

1144 curve, which in MC (with truth selection) is built from ε_{HS} , ε_{PU} , defined according to Eq. 4.3.

$$\begin{cases} \varepsilon_{HS} = \frac{\int_0^{cut(WP)} fJVT_{HS}}{\int_0^{\infty} fJVT_{HS}} \\ \varepsilon_{PU} = \frac{\int_0^{cut(WP)} fJVT_{PU}}{\int_0^{\infty} fJVT_{PU}} \end{cases} \quad (4.3)$$

1145 Scanning over fJVT cuts values, each cut gives (ε_{HS} , ε_{PU}) point. Resulting curves for four p_T
 1146 bins in $0 < \bar{\mu} \leq 35$ are shown on Fig. 4.6a and for $45 < \bar{\mu} \leq 55$ on Fig. 4.6b. In both cases
 1147 $cut_{fJVT} \in [0.05, 0.1, 0.15 \dots 1.5]$, where perfect performance is in the right-bottom corner, as
 1148 one wants to obtain ε_{HS} as high as possible and ε_{PU} as low as possible. Degradation of perfor-
 1149 mance (shift of ε_{PU} towards higher values) is visible with increasing average number of proton-
 1150 proton interactions per collision (denoted as $\bar{\mu}$). This is intuitively expected for algorithm relying
 1151 on balance that it gets more challenging in a busier environment.

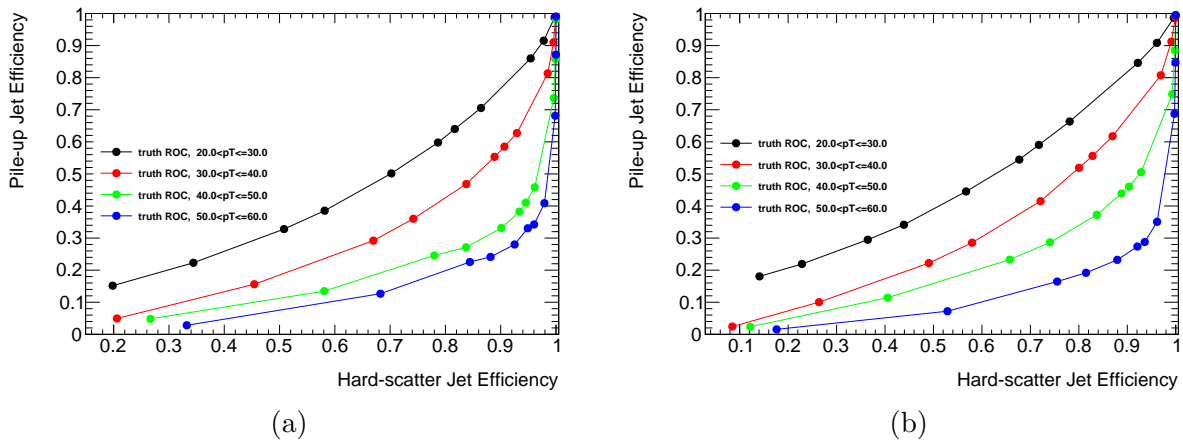


FIGURE 4.6 – (a) fJVT truth ROC curve for $0 < \bar{\mu} \leq 35$ (b) fJVT truth ROC curve for $45 < \bar{\mu} \leq 55$

1152 4.2 Release 22 update

1153 Both HS and PU distributions in Fig. 4.4 display peak in the first bin, which dominantly consists
 1154 of cases where fJVT value is exactly zero. Zero is a fJVT default value that gets overwritten once the
 1155 calculation is done, but the calculation is done only for forward jets⁵ with transverse momentum is
 1156 above the user-defined threshold T ($p_T \geq T$). p_T value attached to jet depends on calibration used
 1157 and in a processing chain p_T value changes several times for the same jet - sometimes resulting
 1158 in a situation where jet seen by fJVT had $p_T < T$ and moment was not calculated, but at the
 1159 end of full processing, the user sees a jet with different $p_T \geq T$ and fJVT=0. The amplitude of
 1160 the peak at fJVT=0 is bigger if the larger value for T is used⁶. In R22, a value of 18 GeV is
 1161 chosen as a compromise between suppression of peak and CPU cost (because of steeply falling
 1162 jet p_T spectrum). Despite being ugly, there is no problem as the effect has minimal effect on the
 1163 algorithm performance (seen by comparison of obtained ε_{HS} to R21).

1164 The crucial step of the algorithm is excluding HS objects (the ones geometrically close to
 1165 JVT-identified HS jet in the event, if any) from each PU vertex's MET calculation. Because of
 1166 misconfiguration, this was not done in R22 initially, and the resulting ROC curves are shown in
 1167 Fig. 4.7 (no $\bar{\mu}$ selection is applied but as this is Run-2 data the peak of the distribution can be

5. For central jets with $|\eta| \leq 2.5$ fJVT is always 0 as the algorithm is not executed on them

6. In R21 peak was absent and the threshold was set at 20 GeV]

assumed to be ≈ 30 [26]). They are to be compared with Fig. 4.6a - while excluding HS vertex objects⁷ much better performance and different behavior are seen.

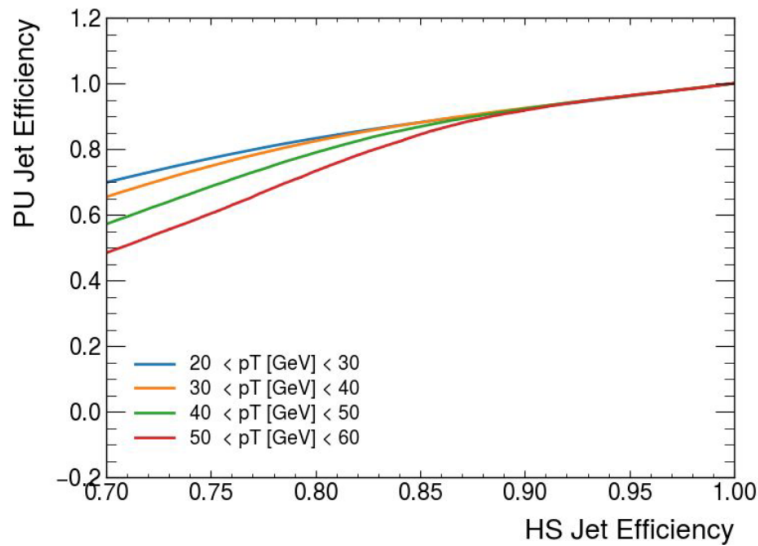


FIGURE 4.7 – fJVT ROC curves if HS objects are not rejected in MET calculation [77]

Another update to the algorithm is migration to NNJVT instead of JVT for the identification of HS objects to be rejected. For NNJVT “FixedEffPt” working point⁸ is used corresponding to fixed efficiency across $|\eta|$ in each p_T bin (88% to 99% HS jet efficiency for jets with p_T between 20 GeV and 60 GeV). A slight change of logic is done for this : JVT recommendation was a flat cut value, and therefore, if a specific jet had a value above the recommended one, it was rejected - with NNJVT, there are many values depending on the bin in question to be compared with, and therefore, only the NNJVT pass/not flag is used.

7. Regulated by `m_includePV` parameter of fJVT algorithm [83] - it is now set to `False` [85]

8. <https://twiki.cern.ch/twiki/bin/viewauth/AtlasProtected/PileupJetRecommendations>

1177 **4.3 fJVT calibration**

1178 For the algorithm to be used in actual analysis with real data, it should be calibrated, as MC
 1179 doesn't reproduce real life perfectly. This time, truth information is unavailable, and the procedure
 1180 described above cannot be used to characterize performance. This section describes Run-2 and
 1181 Run-3 fJVT data/MC calibration - using R22+ software (see Sec. 4.2).

1182 **4.3.1 Methodology**

1183 Method from [93] with modifications is used to quantify data/MC disagreement. Instead of
 1184 selecting HS or PU jet using truth MC variable, one relies on $\Delta\phi(Z, jet)$ selection in $Z \rightarrow \ell\bar{\ell} + jets$
 1185 events to measure ε_{HS} .

1186 One looks at $Z \rightarrow \ell\bar{\ell} + jets$ events and uses a variation of the “tag-and-probe” method. Both
 1187 $Z \rightarrow e\bar{e}$ and $Z \rightarrow \mu\bar{\mu}$ are included. Jets from HS are expected to be balanced by Z (reconstructed
 1188 from two leptons). The measure of balance is how back-to-back it is in $\Delta\phi(Z, jet)$. Events with
 1189 only one jet, which is the forward jet, are selected. The number of central HS jets is required to be
 1190 zero. One then defines CR (Control Region) enriched in pile-up and SR (Signal Region) enriched
 1191 in HS by looking at Fig. 4.8a. Method is inspired by Monte-Carlo, but truth information is not
 1192 used for calibration. Pileup is flat as a function of $\Delta\phi(Z, jet)$, and Hard-scatter is peaking around
 1193 $\Delta\phi(Z, jet) = \pi$. Pileup, being flat, gives a pedestal for HS jets. Then, in the case of real data, one
 1194 defines pileup CR to be $\Delta\phi(Z, jet) < 1.2$ (based on this plot, anything until ≈ 1.8 will also do
 1195 the job). SR is defined to be $\Delta\phi(Z, jet) > 2.8$ to contain the HS peak. In SR to obtain actual HS
 1196 contribution, CR contribution takes into account the difference in width of SR and CR given by

$$c_w = \frac{\pi - 2.8}{1.2} \quad (4.4)$$

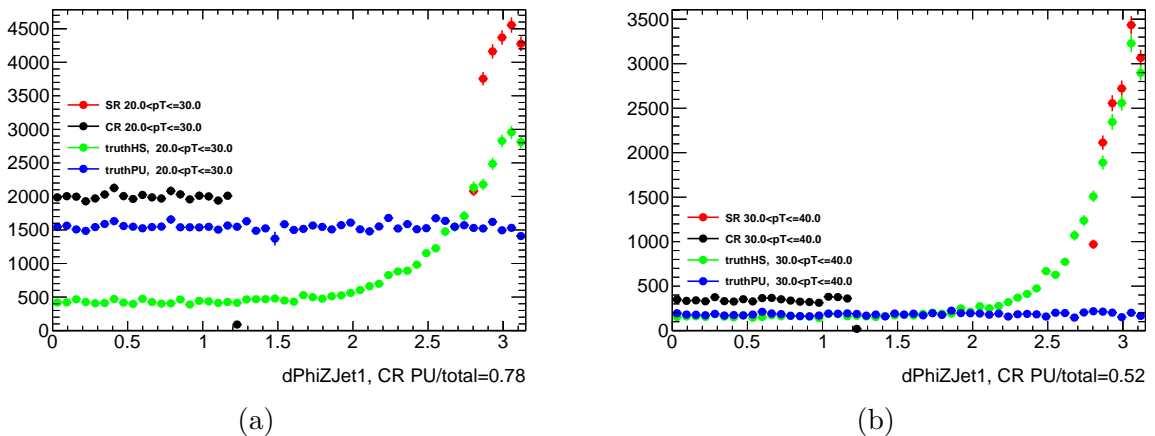


FIGURE 4.8 – (a) $\Delta\phi(Z, jet)$ used to select SR and CR for fJVT calibration, $20 < p_T \leq 30$ (b)
 (b) $\Delta\phi(Z, jet)$ used to select SR and CR for fJVT calibration, $30 < p_T \leq 40$

1197 CR and SR events are used together to get ε_{HS} from fJVT distribution

$$\varepsilon_{HS}^{WP} = \frac{N_{SR}^{WP} - c_w N_{CR}^{WP}}{N_{SR}^{total} - c_w N_{CR}^{total}} = \frac{\int_0^{\text{cut}(WP)} fJVT^{SR} - c_w \int_0^{\text{cut}(WP)} fJVT^{CR}}{\int_0^{\infty} fJVT^{SR} - c_w \int_0^{\infty} fJVT^{CR}} \quad (4.5)$$

1198 ε_{HS} is derived in this way twice : for MC and real data, and the goal of the calibration is to
 1199 derive Scale Factors (SF) that give corrections to MC necessary to reproduce algorithm behavior
 1200 in data :

$$SF = \frac{\varepsilon_{HS}^{data, WP}}{\varepsilon_{HS}^{MC, WP}} \quad (4.6)$$

4.3.2 Binning and working points

SF is derived in $p_T \times \bar{\mu}$ bins because, as we saw above with truth, performance changes as a function of them. p_T bins considered are within range $20 < p_T \leq 60$. The contribution above 60 GeV pile-up is small, and there is likely no need for the algorithm, as can already be seen on truth curves. In addition because $20 < p_T \leq 60$ is the range for which NNJVT is calibrated, and it's used inside of fJVT. Therefore, it is better for NNJVT and fJVT to have consistent p_T binning.

The working points defined are $fJVT \leq 0.2$ (named Tighter), $fJVT \leq 0.4$ (named Tight), and $fJVT \leq 0.5$ (named Loose).

4.3.3 Uncertainties

Uncertainties are one statistical and five systematic ones : MC generator dependence, data-taking campaign dependence, calibration final state, CR PU misestimation, forward sub-detector.

Statistical uncertainty on efficiency is computed as

$$\sigma_{\varepsilon_{HS}} = \sqrt{\frac{\varepsilon_{HS}(1 - \varepsilon_{HS})}{N_{SR}^{total} - c_w N_{CR}^{total}}} \quad (4.7)$$

where ε_{HS} is taken from Eq. 4.5 and denominator under square root gives PU-subtracted SR content before application of certain fJVT cut - see Eq. 4.5 denominator. $\sigma_{\varepsilon_{HS}^{data}}, \sigma_{\varepsilon_{HS}^{MC}}$ are then propagated to obtain $\sigma_{SF_{stat}}$

MC modeling dependence is taken into account through the generator envelope - depending on the list of generators considered, which is different for Run-2 and Run-3. The nominal generator in both cases is Sherpa. Correction for possible differences between jets reconstructed in different forward sub-detectors is done. Nominal case is inclusive $2.5 \leq |\eta| \leq 4.9$. In addition scale factors are derived for $2.5 \leq |\eta| \leq 3.2$ and $3.2 \leq |\eta| \leq 4.9$. Envelope over three cases is then taken.

The potential difference between different years of data-taking - this includes, for example different $\bar{\mu}$ shape or detector configuration is removed by considering the envelope over the years within each $\bar{\mu}$ bin. For example, in Run-3, ε_{HS} and SFs are calculated separately for nominal, 2022, and 2023, and an envelope is taken separately in each $\bar{\mu}$ bin. The total per Run-2 or Run-3 is a nominal case ; other contributions are each campaign year separately. In some $\bar{\mu}$ bins (like in Run-3) this is not possible, for example in $\bar{\mu} > 55$ there is only data taken in 2023 and in 2022 $\bar{\mu}$ has lower values. For those cases, when one doesn't have at least two years, the year envelope is 0.

As both $Z \rightarrow e\bar{e}$ and $Z \rightarrow \mu\bar{\mu}$ events are used, the difference in results between them is checked. Nominal case is $Z \rightarrow e\bar{e} + Z \rightarrow \mu\bar{\mu}$ combined. $Z \rightarrow \mu\bar{\mu}$ SF and $Z \rightarrow e\bar{e}$ SFs are derived separately, and 3 cases are put into an envelope.

The last uncertainty is coming from possible PU misestimation. As already seen on Fig. 4.8a for $20 < p_T \leq 30$ pile-up constitutes most of CR but not all of it (78%). This can be compared to Fig. 4.8b for $30 < p_T \leq 40$ where CR PU purity is lower (52%) . However, CR itself shrinks compared to SR. To take into account CR PU non-purity, SFs are derived in the nominal case and also in up, down PU variation cases where the amount of non-purity gives variation magnitude. Rewriting more compactly Eq. 4.5 together with variation factor V gives

$$\varepsilon_{HS}^{WP} = \frac{N_{SR}^{WP} - c_w N_{CR}^{WP} \times V}{N_{SR}^{total} - c_w N_{CR}^{total} \times V} \quad (4.8)$$

Nominal case gives V=1, for particular case shown on Fig. 4.8b for up and down variations V=0.52

1238 and $V=1/0.52$. This is repeated in each $p_T \times \bar{\mu}$ bin. The envelope is taken over 3 cases. PU uncer-
1239 tainty is not increasing with p_T because CR becomes negligible.

1240 To summarize, uncertainty on the SF factor in the given bin (where components are added in
1241 quadrature) is given by

$$\sigma_{SF} = \sigma_{stat} \oplus \sigma_{gen} \oplus \sigma_{\eta} \oplus \sigma_{year} \oplus \sigma_{FS} \oplus \sigma_{PU.est}. \quad (4.9)$$

1242 4.3.4 $Z \rightarrow \ell\bar{\ell} + jets$ samples and validation

1243 As mentioned, both dimuon and dielectron samples are used. Medium muons [47] and tight
1244 electrons [53] are selected. Both single-lepton and multi-lepton triggers are in use, and most of the
1245 statistics come from the former. The starting point for calibration is common ntuples⁹ of MET/PU
1246 sub-group (of ATLAS Jet/Etmiss) - they are produced with METPerformance package [2]. Calibration
1247 is done within METPerfHistogramming[1] package, for which fJVT “module“ was developed.
1248 The purpose of METPerfHistogramming is to produce a correctly normalized set of histograms
1249 with certain selections. The selections needed were described above. Cell timing cut[54] is applied
1250 in all samples.

1251 Run-2 is divided into three campaigns : 2015+2016, 2017, 2018. For each, $Z \rightarrow e\bar{e}$ and $Z \rightarrow \mu\bar{\mu}$
1252 samples are used. Electron and muon trigger scale factors have been available and applied for all
1253 years. The generators are Powheg, Sherpa, and MadGraph.

1254 Run-3 data used for calibration is coming from 2022 and 2023 campaigns. For each, $Z \rightarrow e\bar{e}$
1255 and $Z \rightarrow \mu\bar{\mu}$ samples are used. Among generators, Powheg and Sherpa were considered, but not
1256 MadGraph because the statistics generated don't allow for the necessary statistics for calibration
1257 on all bins required. The muon and electron trigger scale factors were not available for 2023 data,
1258 however no effect on main distributions (fJVT, $\Delta\phi$) is seen and therefore no ad-hoc correction
1259 applied.

1260 Before starting fJVT calibration, it's good to see the absence of strange features in those samples
1261 - both data and MC . As Run-2 largely has the same detector configuration and the same processing
1262 is used, one doesn't expect a significant difference compared with Run-3. In Run-2 2018, some muon
1263 sample plots will be shown as having the most data. In Run-3, for brevity among four possibilities,
1264 only 2022 muon distributions will be shown. 2022 instead of 2023 because trigger SF is available
1265 Muons instead of electrons muons have larger statistics than electrons.

1266 Here, only variables actually used for calibration, $\Delta\phi$ and fJVT are shown on Fig. 4.9, Fig. 4.10
1267 for brevity. all data and MC distributions are normalized to the same area to compare the shape.
1268 Data integral (all the weights are applied) is written in legend near Data*, and MC integrals are
1269 written near relative to data normalization. Relatively good agreement is seen. Other distributions,
1270 including $\bar{\mu}$ (before and after PRW), jet and lepton p_T , jet and lepton η , and some others are in
1271 Appendix A, all showing acceptable agreement. Let's move on to calibration, then.

9. v0.6 ntuples stored in [/eos-atlas/atlas/atlas/groupdisk/perf-jets/Etmiss/METPerformance/METPerformance_v0.6/](https://eos-atlas.cern.ch/atlas/groupdisk/perf-jets/Etmiss/METPerformance/METPerformance_v0.6/)

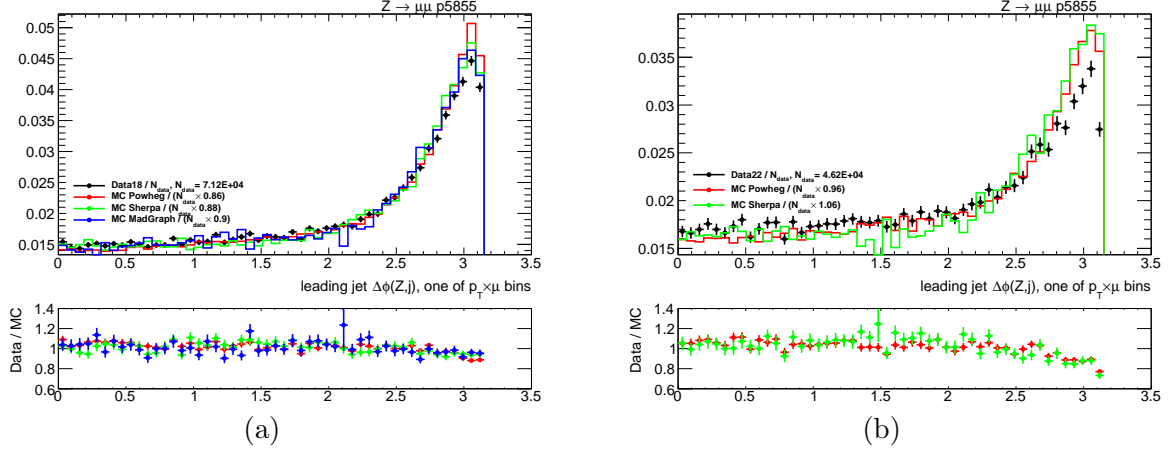


FIGURE 4.9 – Data/MC comparison of $\Delta\phi(jet_1, Z)$, fJVT calibration fiducial selection (a) Run-2 : 2018 $Z \rightarrow \mu\bar{\mu}$ (b) Run-3 : 2022 $Z \rightarrow \mu\bar{\mu}$

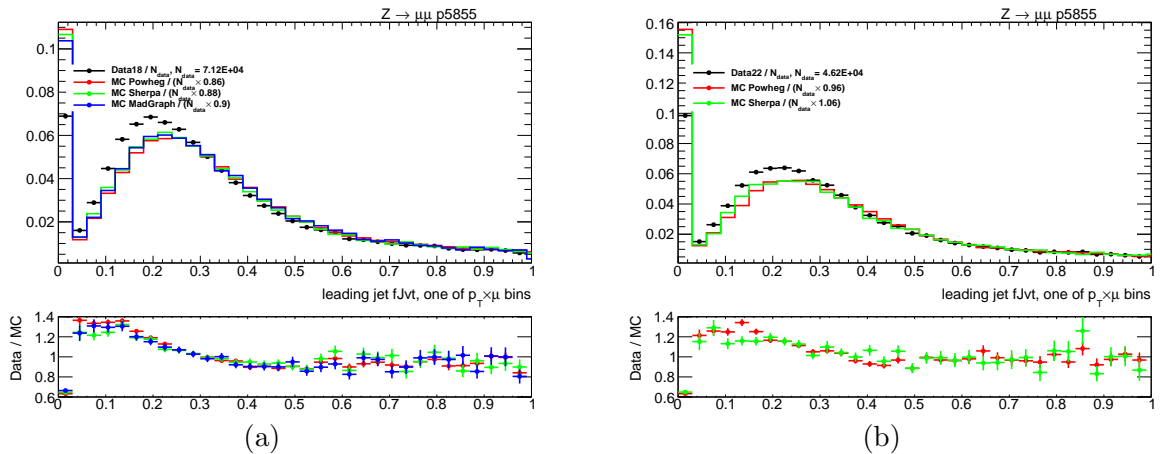


FIGURE 4.10 – Data/MC comparison of $fJVT_{jet1}$, fJVT calibration fiducial selection (a) Run-2 : 2018 $Z \rightarrow \mu\bar{\mu}$ (b) Run-3 : 2022 $Z \rightarrow \mu\bar{\mu}$

4.3.5 Run-2 R22 calibration

Run-2 $\bar{\mu}$ is shown on Fig. 4.11a and $\bar{\mu}$ binning chosen for calibration is $0 < \bar{\mu} \leq 25$, $25 < \bar{\mu} \leq 35$, $35 < \bar{\mu} \leq 45$, $45 < \bar{\mu} \leq \infty$ - to have enough statistics in each bin. Finer binning is possible but not very useful as ε_{HS} vs $\bar{\mu}$ dependence is not that strong. $20 < p_T \leq 30$, $30 < p_T \leq 40$, $40 < p_T \leq 50$, $50 < p_T \leq 60$

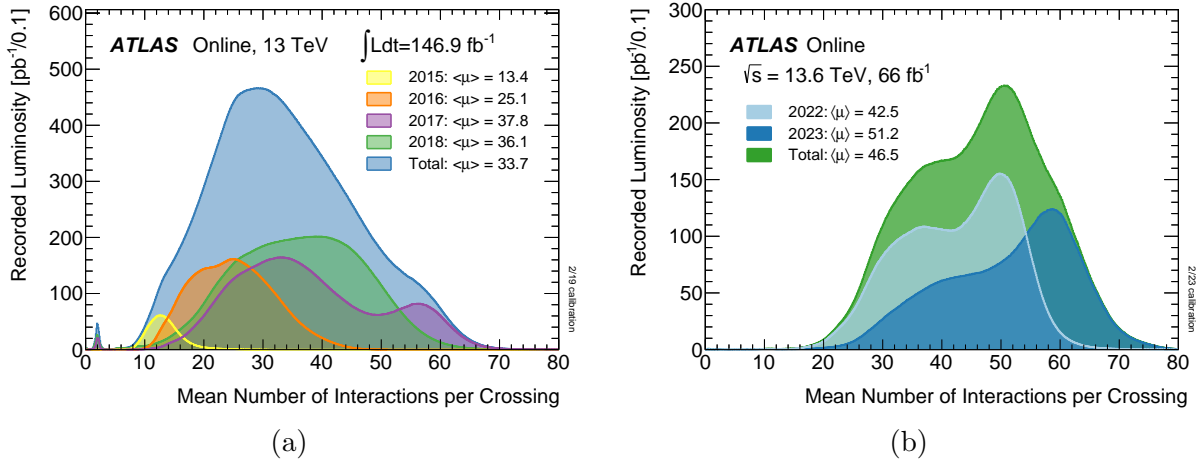


FIGURE 4.11 – $\bar{\mu}$ distributions, total and per year, for campaigns : (a) Run-2 [26] (b) Run-3 [27]

Most of the data is in $35 < \bar{\mu} \leq 45$ bin, and the results of calibration for it, applying the method described above, are shown on Fig. 4.12 for Tight working point (the “medium” one among the three considered) - other two WPs are shown in Appendix B, Appendix C (Fig. B.1, Fig. C.1)

Summary of results, including this time other $\bar{\mu}$ bins, is shown on Fig. 4.13, Fig. 4.14, Fig. 4.15 - this constitutes a recommendation for collaboration. Improvement of efficiency with increasing p_T is again visible together with a decrease with growing $\bar{\mu}$. Scale factors are close to 1 overall, getting closer to 1 for higher p_T . Typically, disagreement with MC is below 5%. A comparison with the previous calibration in a comparable $\bar{\mu}$ bin gave similar results.

4.3.6 Run-3 R22 calibration

Run-3 $\bar{\mu}$ is shown in Fig. 4.11b (at the time of writing, 2024 data-taking is still ongoing and 2024 data is not considered) and binning chosen for calibration is different from Run-2 ; it is : $0 < \bar{\mu} \leq 35$, $35 < \bar{\mu} \leq 45$, $45 < \bar{\mu} \leq 55$, $55 < \bar{\mu} \leq \infty$ - smaller statistics compared to Run-2 but still capture ε_{HS} vs $\bar{\mu}$ dependence.

Similar to the Run-2 section, the biggest $\bar{\mu}$ bin (now it’s $45 < \bar{\mu} \leq 55$) calibration results are shown in Fig. B.2, Fig. 4.16 for Tight working point - other two WPs are shown in Appendix B, Appendix C (Fig. B.2, Fig. C.2).

Summary of results, including this time other $\bar{\mu}$ bins, is shown on Fig. 4.17, Fig. 4.18, Fig. 4.19 - this again constitutes a recommendation for collaboration. Behavior is similar to Run-2 calibration.

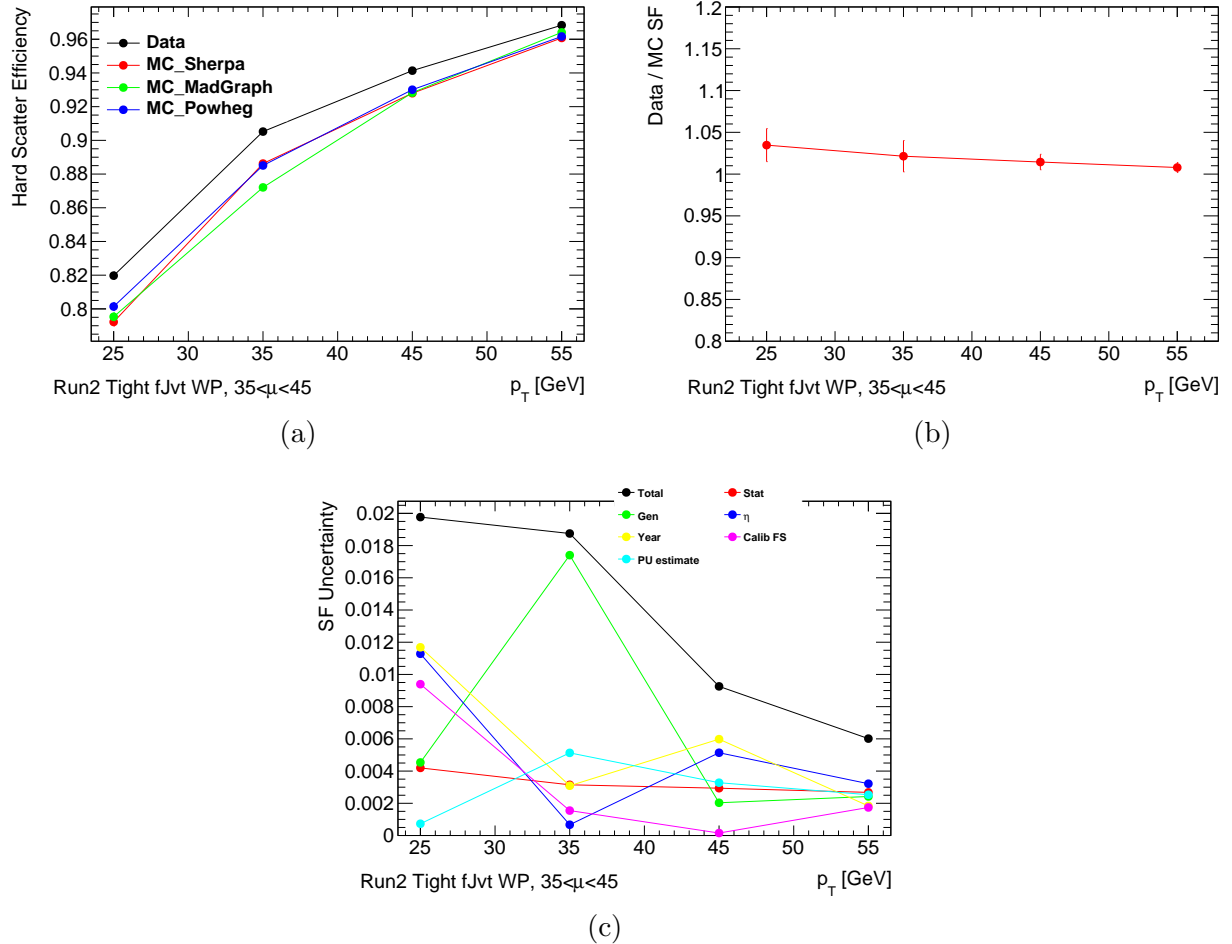


FIGURE 4.12 – Run2 calibration results in $35 < \bar{\mu} \leq 45$, Tight working point (a) Hard-Scatter efficiency (b) Scale Factor (c) Scale Factor uncertainty breakdown

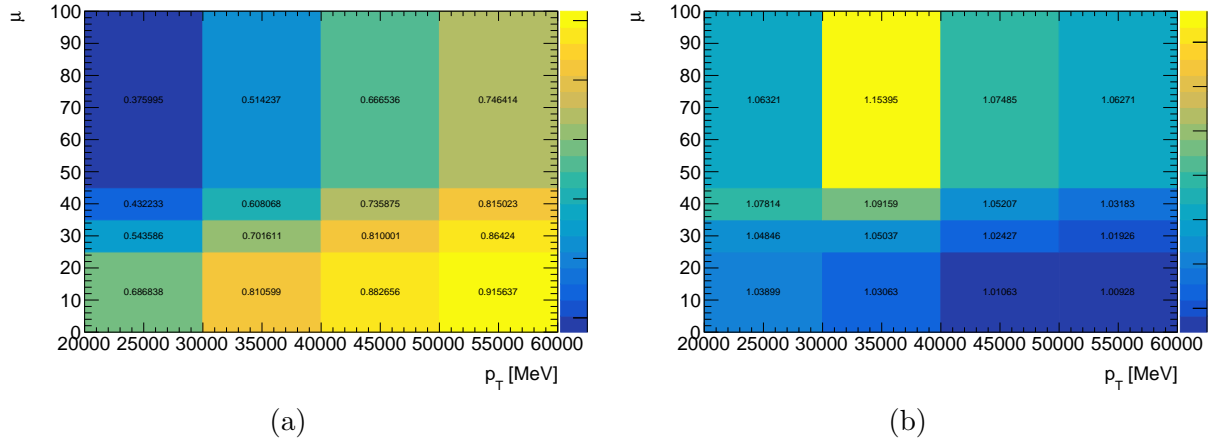


FIGURE 4.13 – Run2 calibration results for Tighter working point (a) MC Hard-Scatter efficiency (b) Scale Factor

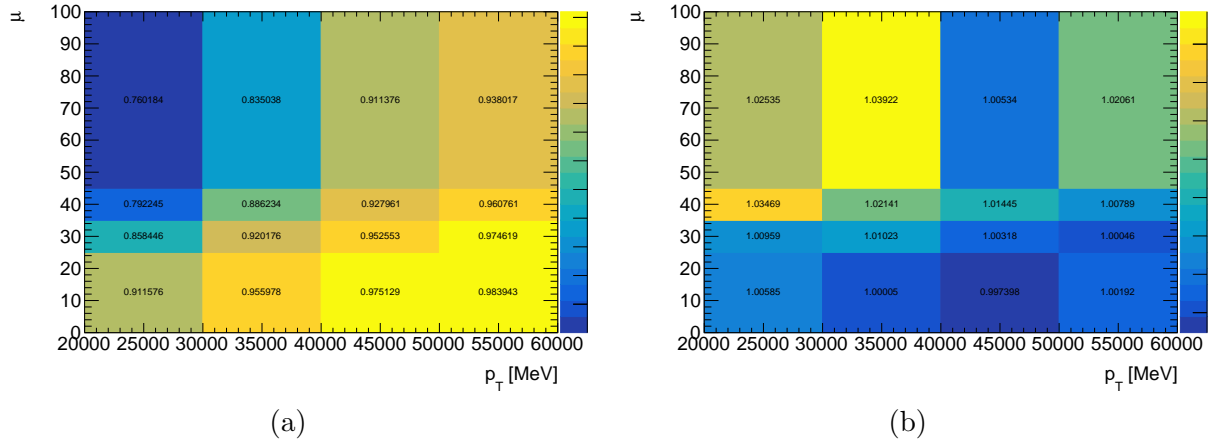


FIGURE 4.14 – Run2 calibration results for Tight working point (a) MC Hard-Scatter efficiency (b) Scale Factor

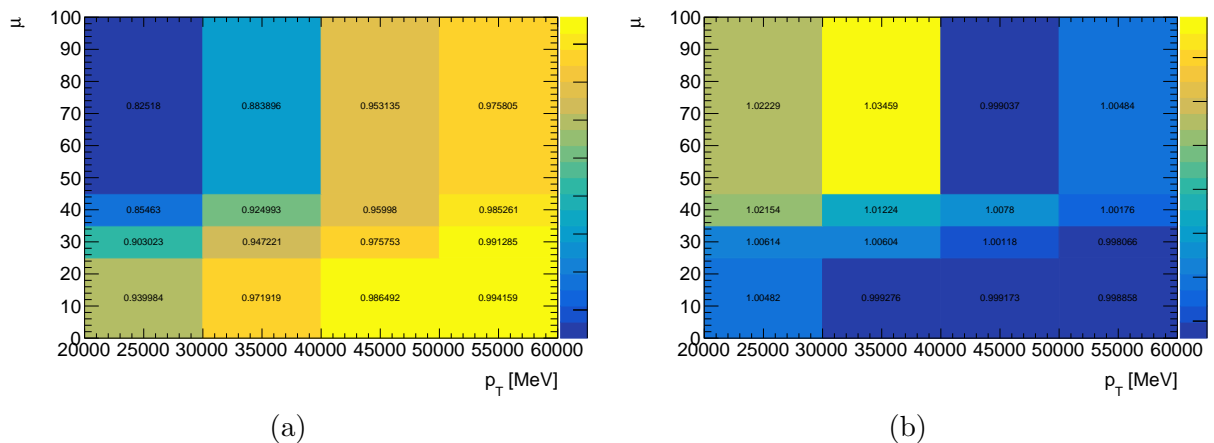


FIGURE 4.15 – Run2 calibration results for Loose working point (a) MC Hard-Scatter efficiency (b) Scale Factor

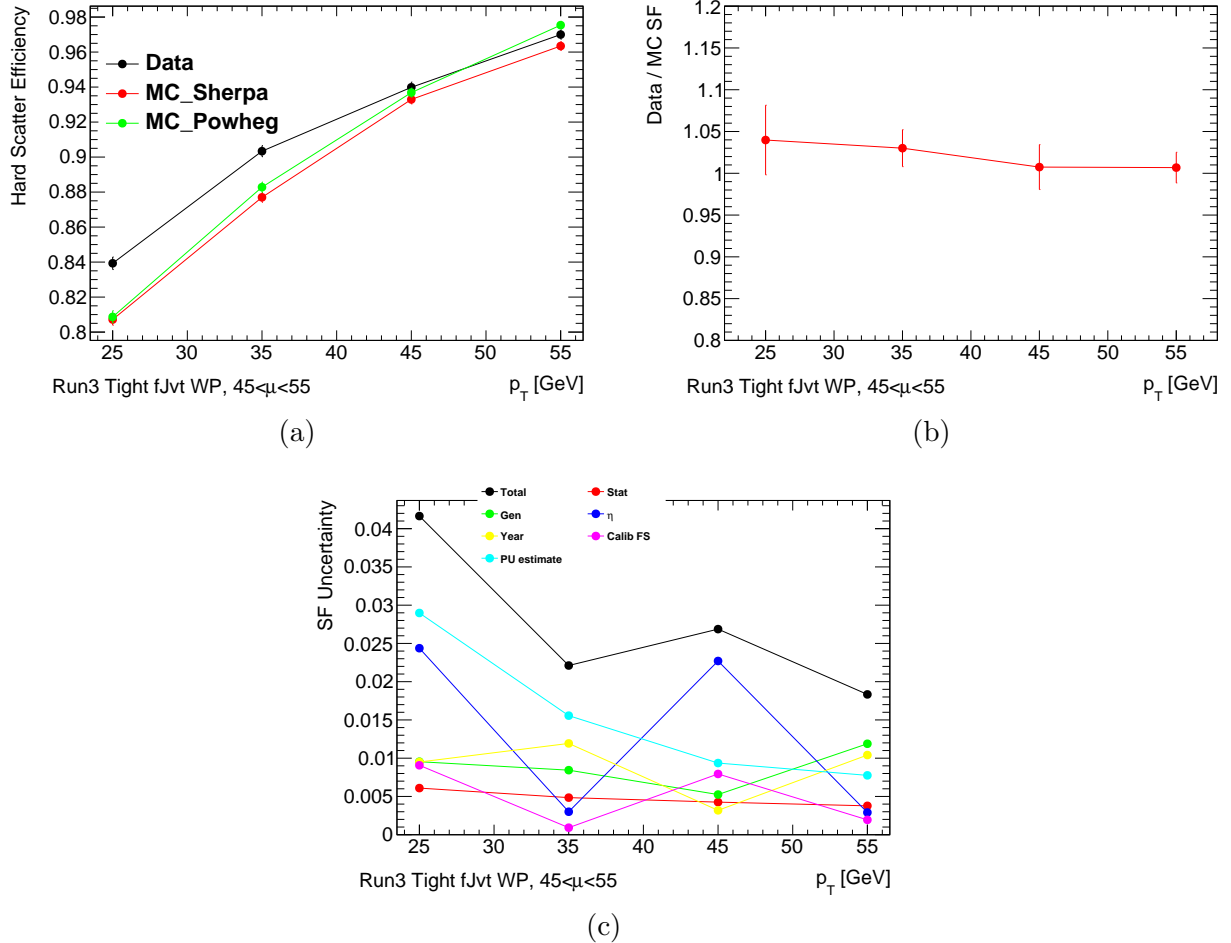


FIGURE 4.16 – Run3 calibration results in $45 < \bar{\mu} \leq 55$, Tight working point (a) Hard-Scatter efficiency (b) Scale Factor (c) Scale Factor uncertainty breakdown

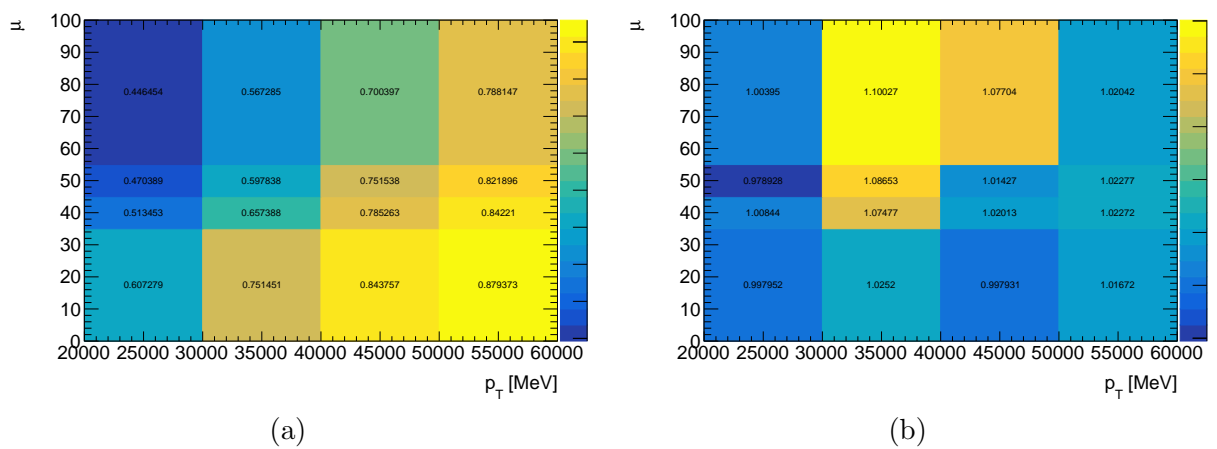


FIGURE 4.17 – Run3 calibration results for Tighter working point (a) MC Hard-Scatter efficiency (b) Scale Factor

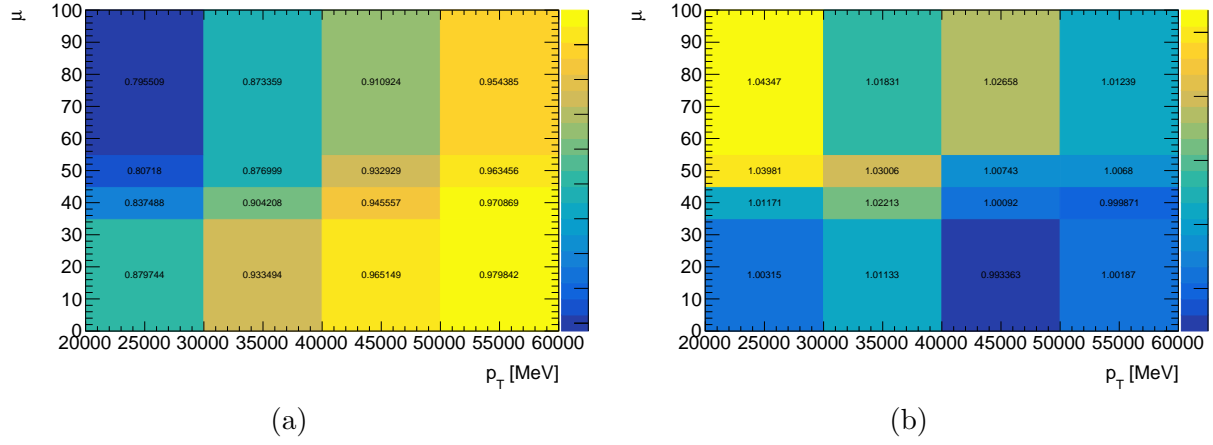


FIGURE 4.18 – Run3 calibration results for Tight working point (a) MC Hard-Scatter efficiency (b) Scale Factor

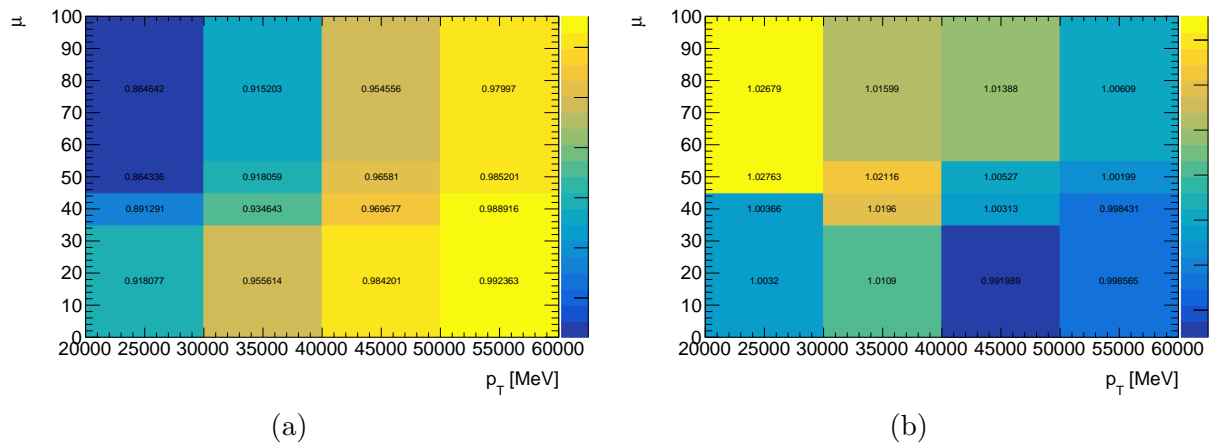


FIGURE 4.19 – Run3 calibration results for Loose working point (a) MC Hard-Scatter efficiency (b) Scale Factor

1295 **4.4 Potential improvement**

1296 **4.4.1 Shape information**

1297 fJVT is not the only possible discriminant against PU ; shape information can also be used. As
 1298 a simple demonstration, one can look at the width calculated according to

$$w = \frac{\sum_k \Delta R(jet, k) p_T^k}{\sum_k p_T^k} \quad (4.10)$$

1299 ATLAS software already has a tool¹⁰ providing the variable. Distribution of width (scaled to get
 1300 nicer numbers) is shown on Fig. 4.20 for $20 < pt \leq 35$ forward jets. It can be calculated more finely
 1301 with topo-towers re-introduced relatively recently. PU jets are seen to peak at higher width values.
 1302 ROC curve obtained by using discrimination by width only is also shown and can be compared
 1303 with “throw a coin“ scenario indicated by a dashed line.

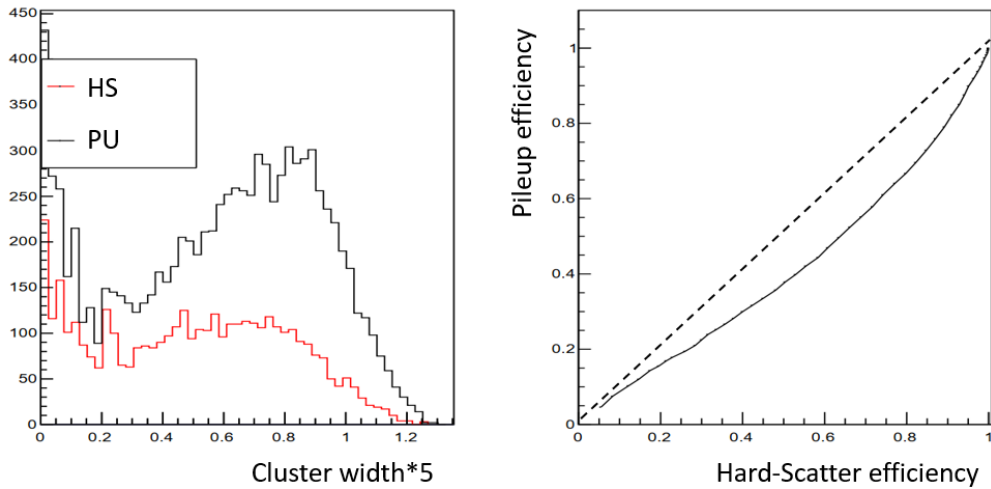


FIGURE 4.20 – For $20 < pt \leq 35$ forward jets in $Z \rightarrow \mu\bar{\mu}$ sample (left) width distributions (no use of topo-clusters) of HS and PU jets (right) ROC curve of ε_{HS} vs. ε_{PU} using the width

1304 Similarly to fJVT, HS/PU separation by width variable is not dramatic ; however, combined
 1305 with fJVT in some kind of BDT has potential. One attempt was done already in 2018[93] however
 1306 did not make into recommendation because of quark-gluon dependence. However, since then, de-
 1307 correlation methods arrived, which gives the potential to revise the approach. Moreover, as both
 1308 quark-gluon and HS-PU discriminations are sensitive to overlapping sets of variables, it makes sense
 1309 to develop a combined quark/gluon/HS/PU tagger.

1310 **4.4.2 Targeting specific type of pile-up**

1311 Hard-scatter and Pile-up discrimination ROC curves were shown on Fig. 4.6a, where there is
 1312 no distinction between QCD and Stochastic Pile-up. It's interesting then to see how fJVT performs
 1313 in distinguishing between specifically (HS, QCD PU) and between (HS, stochastic PU) separately
 1314 - rather surprisingly, there is no difference, as seen from comparison of two ROC curves shown on
 1315 Fig. 4.21, both made for $20 < pt \leq 30$.

1316 However, specialized methods exist for stochastic pile-up tagging. One of them is γ -discriminant [34].
 1317 It relies on the fact that the hard-scatter jet distribution in $\eta \times \phi$ plane displays a sharply peaked
 1318 distribution, while the stochastic pile-up jet distribution is flat with various off-center features,

10. JetWidthTool

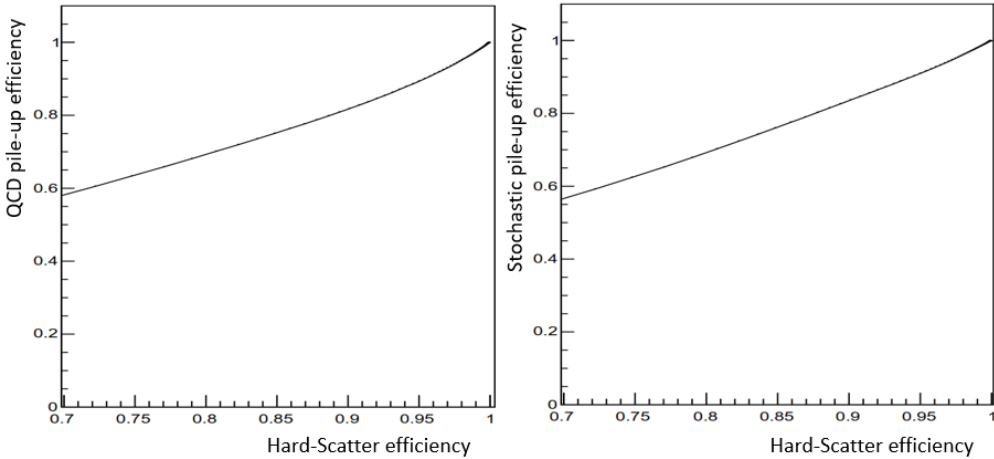


FIGURE 4.21 – For $20 < p_T \leq 30$ forward jets in $Z \rightarrow \mu\bar{\mu}$ sample (left) ROC curve of separating HS jets from QCD PU jets (right) ROC curve of separating HS jets from Stochastic PU jets

reflecting the randomness of the underlying processes. 2D $\eta \times \phi$ distribution is fitted with

$$f = \alpha + \beta \Delta\eta + \gamma e^{-\frac{1}{2}(\frac{\Delta\eta}{0.1})^2 - \frac{1}{2}(\frac{\Delta\phi}{0.1})^2} \quad (4.11)$$

where one of the parameters involved, γ , has different values for stochastic and HS jets. The ROC curve obtained is shown on Fig. 4.22, showing up to 40% better performance compared to how fJVT can distinguish between the two.

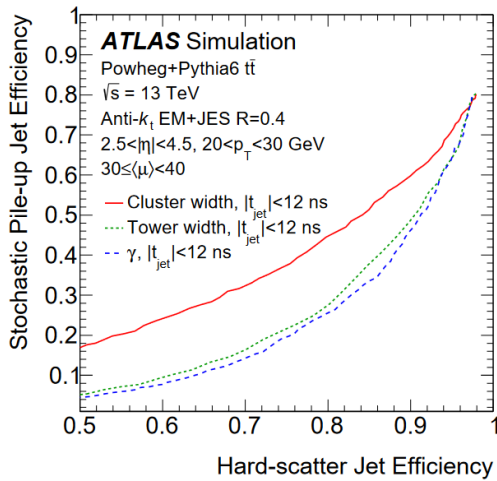


FIGURE 4.22 – Efficiency for stochastic pile-up jets as a function of the efficiency for hard-scatter jets using different shape-based discriminants : $30 < \bar{\mu} \leq 40$ in simulated $t\bar{t}$ events [34]

Therefore, it makes sense not just to have one tagger but several ones depending on the type of pile-up (e.g. use fJVT for to reject QCD PU and γ to reject stochastic pile-up) and then mix them in some way. Given Sec. 4.4.1, it can also make sense to develop a combined quark/gluon/HS/QCD/stochastic tagger.

4.4.3 Adding timing information

The algorithms shown above rely on variables built from spatial information, such as the position of the sensor hit. In addition, knowledge of the time when the sensor was hit is beneficial. A new forward sub-detector called HGTD will be installed for timing measurements, which will be the subject of subsequent chapters.

1332 **4.5 Conclusion**

1333 fJVT algorithm, responsible in ATLAS for forward pile-up rejection, was integrated into upda-
1334 ted ATLAS software. Its performance is validated in MC. Performance is also validated in real data
1335 and disagreement with MC in quantified through scale factors derived in $p_T \times \mu$ bins, for three wor-
1336 king points. Overall, a good agreement between data and MC is seen. Calibration is now released,
1337 covering both Run-2 and early Run-3, and available for the whole ATLAS collaboration [78, 22].
1338 Potential ways for fJVT improvement are briefly discussed.

¹³³⁹ 5 - HL-LHC

¹³⁴⁰ 5.1 Project overview

¹³⁴¹ There is a need to increase the data rate LHC is providing and ATLAS is recording. Moreo-
¹³⁴² ver, the lifetime of some components in terms of radiation in both the accelerator and detector is
¹³⁴³ ending. Therefore, it was decided to upgrade and move on to the High Luminosity Large Hadron
¹³⁴⁴ Collider (HL-LHC) stage, where the design goal is a significant increase of integrated luminosity
¹³⁴⁵ through a five-fold increase in instantaneous number of proton-proton collisions. The adapted ti-
¹³⁴⁶ meline is shown on Fig. 5.1. At the moment of writing, we are at the end of Run-3, the third year of
¹³⁴⁷ data-taking (out of four). At HL-LHC, the center-of-mass will be the same or will increase slightly,
¹³⁴⁸ and bunch spacing of 25 ns will stay the same. The design goal during operation, planned until
¹³⁴⁹ 2040, is to accumulate a dataset of 3000 fb^{-1} , which is roughly a factor ten higher than combined
¹³⁵⁰ Run-2 + Run-3 integrated luminosity. HL-LHC will likely be the end of LHC¹. Already in 2006,
¹³⁵¹ the CERN Council adopted the European Strategy for Particle Physics, and it was agreed that
¹³⁵² “The LHC will be the energy frontier machine for the foreseeable future, maintaining European
¹³⁵³ leadership in the field; the highest priority is to fully exploit the physics potential of the LHC
¹³⁵⁴ ... A subsequent major luminosity upgrade (SLHC), motivated by physics results and operation
¹³⁵⁵ experience will be enabled by focussed R&D; to this end, R&D for machine and detectors has to
¹³⁵⁶ be vigorously pursued now and centrally organized towards a luminosity upgrade ... “[[74](#)]. Strategy
¹³⁵⁷ only works if the budget is allocated, and this was done, particularly in the session of June 2016,
¹³⁵⁸ the CERN Council approved the whole HL-LHC project - where 950 MCHF is until 2026². It is
¹³⁵⁹ planned, as shown in Fig. 5.1, to make a break after Run-3 and install main components over three
¹³⁶⁰ years of Long Shutdown 3 (starting 2026) and commission them for one year afterward.

¹³⁶¹ 5.2 Accelerator upgrades

¹³⁶² Constraints from the detector on manageable level of pile up and from the accelerator on energy
¹³⁶³ deposition lead to the constraint on peak luminosity. Then, one must operate the machine at a lower
¹³⁶⁴ than maximum possible luminosity, shown in the red curve at time=0 on Fig. 5.2. In order to still
¹³⁶⁵ reach target of 3000 fb^{-1} , lower-than-maximum luminosity will be held roughly constant for a
¹³⁶⁶ long periods of time - as shown in a blue curve on Fig. 5.2. This is called luminosity levelling and
¹³⁶⁷ will be done for HL-LHC³. Nominal HL-LHC luminosity is $5 \times 10^{34} \text{ cm}^{-2} \text{s}^{-1}$.

¹³⁶⁸ Luminosity will be increased via reduction of β^* to 15 cm (can be compared to 55 cm in the
¹³⁶⁹ LHC design report), which in turn implies two aspects. One is that IT quadrupole magnets need
¹³⁷⁰ to double the aperture, giving peak field up to 12 T - twice larger than present LHC (uses Nb-Ti
¹³⁷¹ technology), and this calls for the usage of new Nb_3Sn superconducting technology Second aspect is
¹³⁷² larger crossing angle and corresponding reduction of geometrical luminosity factor ($\equiv R$), as shown
¹³⁷³ on Fig. 5.3. The adapted solution is the usage, for the first time at a hadron collider, of novel crab
¹³⁷⁴ cavities (CC). CC generates a voltage kick to rotate each bunch just before the collision. Such two
¹³⁷⁵ trains overlap more - it's illustrated on Fig. 5.4. After the collision, beams are rotated back. CC

1. it's not completely clear what will happen next - one of the scenarios discussed is going to even higher collision energy, 100 TeV, via Future Circular Collider (FCC). The FCC feasibility study is expected to be completed in 2025. If built, existing CERN infrastructure will be re-used, similarly to LHC is being partially built in the LEP tunnel.

2. full cost of HL-LHC project is expected to be 1139.4 MCHF

3. in fact, was already used in Run-3



FIGURE 5.1 – LHC baseline plan for the next decade and beyond showing the collision energy (upper line) and luminosity (lower line). LS2 sees LHC consolidation and the HL-LHC underground excavation, as well as the upgrade the LHC injectors and Phase 1 upgrade of the LHC detectors. After LS3, the machine will be in the high-luminosity configuration. Covid-19 restrictions have led to the shift of the start of Run-3 to February 2022 while the start of LS3 is maintained at end of 2024 [71]

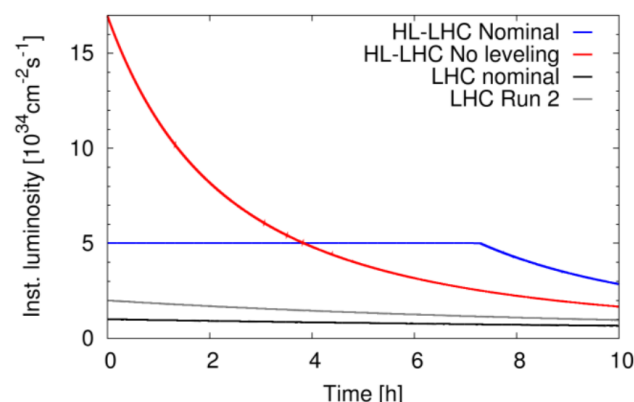


FIGURE 5.2 – Luminosity profile with and without levelling, for a single long run [71]

1376 also can be used as levelling tool.

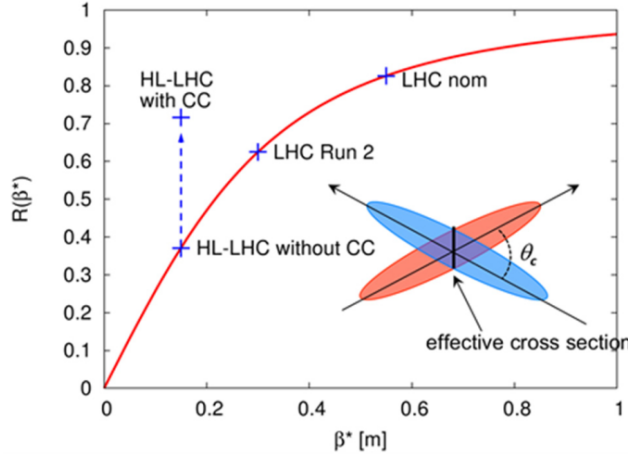


FIGURE 5.3 – Behavior of geometrical reduction factor of luminosity vs. β^* for constant normalized beam separation with indicated various operating points [71].

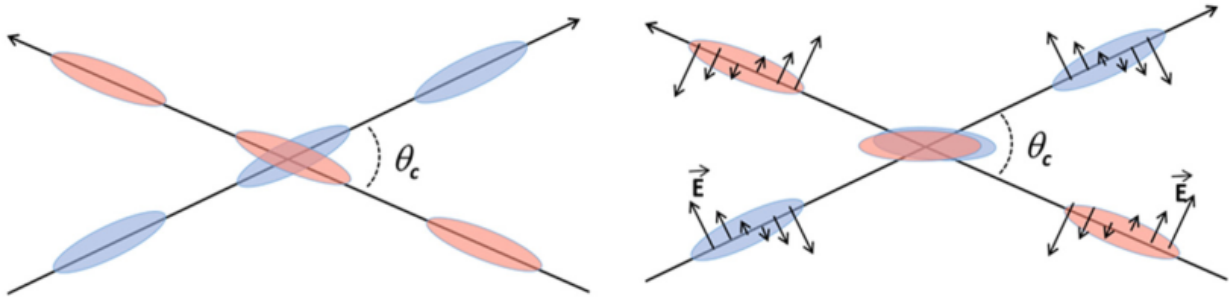


FIGURE 5.4 – Effect of the crab cavity on the beam : left, bunch collision geometry without CC ; right : with CC, small arrows indicate the transverse varying RF Electric field E when crossing the CC [64].

1377 5.3 ATLAS Phase-II upgrades

1378 A detector upgrade is required to cope with up to 200 collisions per bunch crossing (the ATLAS
1379 environment is illustrated at Fig. 5.5) foreseen (in Run-3, peak is at around 50). Mean value, as
1380 shown in [30], given by

$$\mu = \frac{\sigma_{inel} L}{n_b f_r} \quad (5.1)$$

1381 where f_r (revolution frequency) is 11245 Hz, n_b (number of colliding bunches, design value) is 2808.
1382 σ_{inel} is inelastic cross-section, summary of which are shown on Fig. 5.6 as a function of center-of-
1383 mass energy. Flagship measurement of σ_{inel} done by TOTEM - resulting in $\sigma_{inel} = 74.7 \pm 1.7 \text{ mb}$.
1384 Substituting numbers gives $\mu_{mean} \approx 140$ (still around factor three busier than Run-3). The challenge
1385 is increased occupancies in sub-detectors and higher radiation levels. All sub-detectors will be
1386 upgraded in one way or another together with TDAQ - preparation is documented in six Technical
1387 Design Reports⁴ : tracker[37], Liquid Argon[33] and Tile[40] calorimeters, muon[38], HGTD [46]
1388 and TDAQ[39]. Moreover, a corresponding computing upgrade is required, described in [45]. A very
1389 short summary is given below.

4. most of them published in 2017

1390 5.3.1 Trigger and Data Acquisition

1391 Let's look first at the system orchestrating other sub-detectors - Trigger and Data Acquisition
1392 (TDAQ), which, as before, will function in stages. The first stage is a Level-0 hardware trigger
1393 operating with a read-out rate of 1 MHz and a latency of 10 μs . It relies on information from
1394 calorimeter and muon systems. It's possible that tracker information also will be used. Existing
1395 Calorimeter Feature Extractors (FEX) will be kept, but more will be installed (to process forward
1396 calorimeter data), and firmware will be updated. On the other side, the muon trigger processor
1397 would be replaced with upgraded modules to process information from Resistive Plate Cham-
1398 bers (RPC), Thin Gas Chambers (TGC), small-strip Thin Cap Chambers (sTGC), and MicroMe-
1399 gas (MM). The capabilities of the new Global Trigger to execute offline-like algorithms are superior
1400 to current Topological Processor. On the Level-0 trigger decision, detector data is transmitted to
1401 the second trigger stage, Event Filter (EF), though Front-End Link eXchange (FELIX, used by
1402 all sub-detectors). EF makes the final decision, and the events selected are transferred to perma-
1403 nent storage at 10 kHz. There are two options for base EF technology choice : custom electronics
1404 (Hardware Tracking for the Trigger) or the employment of commodity CPUs.

1405 5.3.2 Inner Tracker

1406 Tracker performance is crucial for the reconstruction and identification of charged particles,
1407 photons, and flavor tagging. The current design was made for factor four smaller track density
1408 (compared to HL-LHC). SCT radiation tolerance is 700 fb^{-1} equivalent and 850 fb^{-1} for IBL .
1409 Instead, for HL-LHC, a new tracker system called ITk (Inner Tracker) will be installed. It will be an
1410 all-silicon detector - pixel sensors⁵ closer to the beam, and strip sensors further away. One change
1411 compared to the current design is Pixel Detector $|\eta|$ coverage up to 4 - for better reconstruction of
1412 forward objects (e.g., tagging VBS jets). Strip Detector covers $|\eta| < 2.7$. Different sensors would be
1413 used in different parts : 3D sensors and thin $100 \mu\text{m}$ planar sensors in the inner sections and $150 \mu\text{m}$
1414 planar sensors elsewhere. The front-end electronics will be replaced. The connection between
1415 ASIC and sensors is done with bump-bonding. Assumed pixel cell size is $50 \times 50 \mu\text{m}^2$ everywhere
1416 except first layer of barrel where it would be $25 \times 100 \mu\text{m}^2$. In the innermost layers, shorter strips
1417 of 24.1 mm length will be used and further away from the beam strip length will be increased to
1418 48.2 mm (because of lower occupancy). Granularity is increased, resulting in an average occupancy
1419 of 0.16% in the Pixel and 1.2% in the Strip detectors. The same 2T magnetic field will be used.
1420 The design target is providing 13 (9) hits per track in the barrel (forward) region if transverse
1421 momentum is above 1 GeV . The goal is to use half of the material - to minimize losses from
1422 bremsstrahlung and hadronic interactions.

1423 5.3.3 Calorimeters

1424 "Detection" part of the calorimeter doesn't suffer from irradiation, and this part doesn't need
1425 to be changed - which is not true for electronics : front-end, back-end, and calibration. Moreover,
1426 some of the commercial components originally used are not available anymore. Also, the existing
1427 calorimeter readout structure is incompatible with the HL-LHC trigger (readout rate and latency).
1428 Therefore, all electronics will be replaced. New 1524 LAr Front-End Boards would process 128
1429 signals from calorimeter cells : amplified signal is split into two overlapping linear gain scales, on
1430 which shaping is done. LAr front-end data is sent to 372 LAr Signal Processor modules via 31900
1431 fibers, then to TDAQ . The new calibration system would inject (as now) directly into calorimeter
1432 cells and have better than 0.1% precision over a 16-bit dynamic range. Tile calorimeter would
1433 undergo mechanical structure re-organization - each module will be serviced by four "mini-drawers"

5. there will be five layers and two most inner ones would be replaced due to unsustainable level of
irradiation received

1434 for easier installation and maintenance of 12 PMTs and their (new) electronics.

1435 **5.3.4 Muon**

1436 For muon detectors, part of the upgrade was done already before Run-3 : installation of a
1437 New Small Wheel (NSW) in the endcap. Its primary goal is suppression of fake muon triggers in
1438 the forward region - as material in endcap toroids become activated, the big wheels of the Muon
1439 Spectrometer receive flux of neutrons, creating tracks that look like the tracks from the interaction
1440 region and cannot be vetoed easily without NSW as the previous design doesn't have the necessary
1441 resolution in radial bending direction to match SW (Small Wheel) track to BW (Big Wheel) hit
1442 in TGC . NSW is based on precision sTGC (used for triggering) and MM (used for tracking, new
1443 technology for ATLAS that was not produced at this scale before). Just before Phase-II RPC,
1444 TGC and electronics will be upgraded. A new RPC will be installed in the inner barrel layer and
1445 will have an increased rate capability to provide better robustness and acceptance of the barrel
1446 muon trigger. Part of RPC chambers in $|\eta| < 0.8$ region of middle and outer barrel layers would
1447 be refurbished - goal being operation at reduced high voltage (but without efficiency loss). In the
1448 barrel-endcap transition region, TGC triplets would replace TGC doublets to provide finer readout
1449 granularity that, in turn, allows the implementation of more robust majority logic. Just like in the
1450 case of calorimeters, a significant fraction of on - and off-detector electronics will be upgraded to
1451 be compatible with HL-LHC trigger requirements.

1452 **5.3.5 Higg Granularity Timing Detector**

1453 One new forward sub-detector aiming at making precise timing measurements, HGTD, will be
1454 installed and will be considered separately in Sec. 5.5.

1455 **5.3.6 Computing**

1456 Finally, as no detector is functional without software operating it and processing data from it,
1457 challenges in that area must be overtaken. Challenges arise from both the amount of data (3000 -
1458 4000 fb^{-1}) and its recording rate (10 kHz) - it has to be collected, stored, reconstructed, and
1459 analyzed. Moreover, Monte Carlo needs to be generated in similar numbers. ATLAS currently
1460 spends about 40% of CPU on detector simulation where there are two types : "full" (GEANT4) and
1461 "fast" (GEANT4 except for the calorimeter where the parametrized response model is used). Full
1462 simulation is about factor five CPU-expensive compared to fast. Studies are ongoing to extend to all
1463 parts of the detector, not only the calorimeter. Another big consumer of CPU could be ITk - ATLAS
1464 initiated the ACTS [100] open-source project to develop the next generation tracking software in
1465 a common cross-experiment project, with the aim of using ACTS to achieve both CPU reduction
1466 and excellent physics performance. Athena, the main ATLAS framework, will rely more on multi-
1467 threading - ACTS is one of the examples. Derivations⁶ consume a lot of space, and there is a lot of
1468 overlap between different derivation formats - to avoid this and as preparation to HL-LHC, already
1469 in Run-3 ATLAS started to move to DAOD_PHYS (50KB/event) and DAOD_PHYSLITE (10KB/event)
1470 formats - the first one contains all of the variables needed to apply calibrations to reconstructed
1471 objects, and the second contains pre-calibrated reconstructed quantities, and in consequence, the
1472 variables needed to apply the calibrations do not need to be stored. A two-fold decrease in disk
1473 space is expected. In Run-4, mostly DAOD_PHYSLITE is expected to be used. Storage needs will
1474 grow together with the data accumulated - one of the ideas explored is staging AOD data from
1475 tape to disk only when it's required instead of permanent storage : it can halve the total AOD
1476 permanent volume but also would mean that processing would be less frequent. The backbones of
1477 ATLAS distributed data processing and management - Panda and Rucio will need to be scaled up
1478 to HL-LHC workloads and volumes.

1474 6. One of the data processing stages in ATLAS

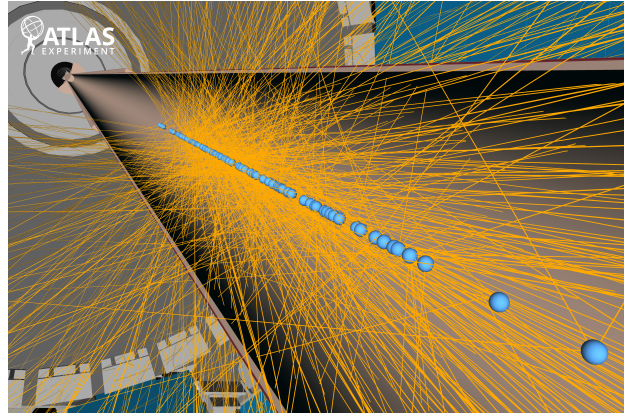


FIGURE 5.5 – Simulated top-antitop pair production in ATLAS at 14 TeV and $\mu = 200$. Blue balls are marking reconstructed primary vertices , and tracks from them are shown as orange lines [20]

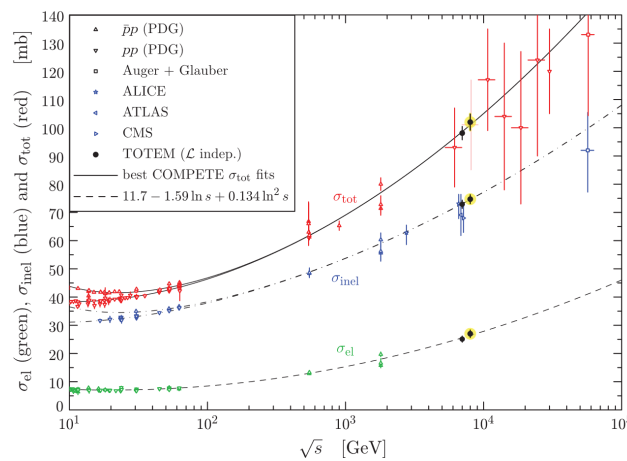


FIGURE 5.6 – Compilation of the total (σ_{tot}), inelastic (σ_{inel}) and elastic (σ_{el}) cross-section measurements from various experiments [59]

1479 5.4 Physics case - VBS

1480 A rich physics program is foreseen at HL-LHC, but only VBS prospects would be mentioned for
1481 brevity. Statistical uncertainty in Run-2 VBS analyses is non-negligible. Measured fiducial cross-
1482 sections for electroweak production in $W^\pm W^\pm$ analysis [55] has 0.22 fb statistical and 0.19 fb
1483 systematic uncertainty. For $W^\pm Z$ analysis [56] (ZZ [50], 4-lepton channel) they are 0.037 (0.12) fb
1484 and 0.059 (0.076) fb respectively. Therefore, VBS analyses will benefit from a larger dataset collec-
1485 ted at HL-LHC. Also, forward upgrades like HGTD and extended $|\eta|$ tracker coverage should be
1486 beneficial, as the signature of VBS is two forward jets - in Run-2, all analyses relied on this.

1487 Both ATLAS and CMS projected analysis sensitivities (maintaining analysis strategy used for
1488 Early Run-2 data but with more data) for measuring cross-sections of electroweak VBS in $W^\pm W^\pm$
1489 [43], $W^\pm Z$ [42] and ZZ [41] processes. If possible, ATLAS results will be considered for comparison
1490 with Run-2 section. Projections shown (and their CMS counterparts) became part of CERN Yellow
1491 Report [65] and Snowmass White Paper (American counterpart of ESPP) [21].

1492 Leptonic decays are considered everywhere. Luminosities range roughly from Run-2 dataset size
1493 to 3000 fb^{-1} (nominal HL-LHC) to 8000 fb^{-1} (optimistic ATLAS and CMS combined). Semilep-
1494 tonic analysis projection was also done. However, analysis changed significantly since therefore and
1495 will not be considered here.

1496 Apart from EW cross-section, it is interesting in VBS to measure the case where both bosons
1497 are longitudinally polarized - because in the SM, this process is unitarized thanks to the presence
1498 of Higgs boson contributions and deviations from this would indicate the presence of BSM physics
1499 - due to the cross-section being even smaller, this is a challenging but essential part of the HL-LHC
1500 physics program.

1501 5.4.1 $W^\pm W^\pm$ analysis

1502 Statistical uncertainty

1503 For the EFT combination, dilepton mass distribution was fitted - projected distribution at
1504 3000 fb^{-1} is shown on Fig. 5.7a. Statistical uncertainty on the cross-section as a function of lumi-
1505 nosity is shown at the black curve of Fig. 5.7b; it starts from the value of Run-2 luminosity. With
1506 a nominal luminosity of 3000 fb^{-1} , it's expected to decrease by more than factor three and reach
1507 plateau.

1508 $W_L^\pm W_L^\pm$ prospects

1509 Two variables are seen to be sensitive to polarization - dijet azimuthal separation $\Delta\phi(j, j)$ where
1510 Longitudinal-Longitudinal (LL) distribution is seen to be shaper around larger value and leading
1511 p_T lepton p_T^{lep1} (LL distribution is larger around bigger value) - this is shown on Fig. 5.8. Expected
1512 significance of the observation of the $W_L^\pm W_L^\pm jj$ is shown on Fig. 5.9, where for baseline estimation
1513 rate uncertainties on the backgrounds are halved and in "optimistic" set of uncertainties where
1514 the uncertainties on the non-data-driven backgrounds are aggressively reduced. It can be seen that
1515 using any of the two sets of uncertainties with all sources uncertainties, after ten years of data-
1516 taking and combination with CMS ATLAS will only reach 1.8σ - therefore, just having more data
1517 will not solve the problem and analysis optimizations would be required.

1518 5.4.2 ZZ analysis

1519 Statistical uncertainty

1520 Extended tracker coverage helps with improving four-leptons detection efficiency. Main sys-
1521 tematics for 4ℓ channel is theoretical modeling of the QCD-ZZjj background - for projection, three

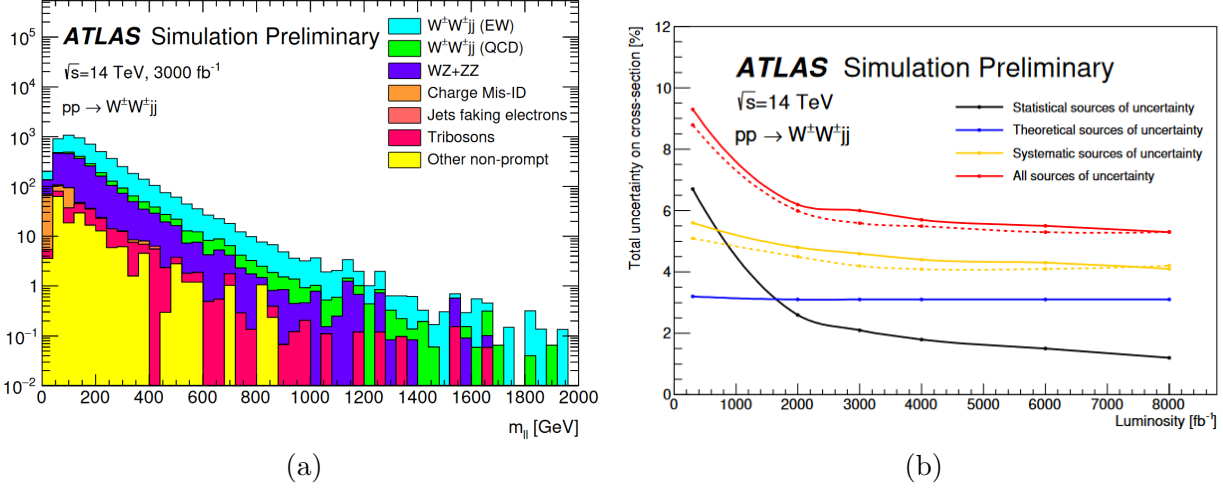


FIGURE 5.7 – (a) Dilepton invariant mass distribution for events passing all selection criteria of the signal region, with event selection applied [43] (b) Projection of the statistical (black), theoretical (blue), systematic (yellow), and total (red) uncertainties on the cross-section as a function of integrated luminosity for the optimized event selection using the baseline scenario (solid lines). The dashed lines show the systematic and total uncertainties on the cross-section for the optimistic scenario. The theoretical uncertainty refers only to the signal [43]

scenarios are considered : conservative 30% (relying on PDF4LHC recommendation), optimistic 5% (assuming enough data events from QCD enriched control region at the HL-LHC could be used to provide constraints on the theoretical modeling of QCD-ZZjj processes) and intermediate 10%. Distributions of two variables that were previously used for aQGC fit, m_{jj} and $m_{4\ell} \equiv m_{ZZ}$ are shown on Fig. 5.10 but now, with the HL-LHC expected dataset. Distributions obtained as

$$\sigma = \frac{N_{\text{pseudo-data}} - N_{\text{QDC-ZZjj}}}{L \times C_{\text{EW-ZZjj}}}, C_{\text{EW-ZZjj}} = \frac{N_{\text{EW}}^{\text{detector}}}{N_{\text{EW}}^{\text{particle}}} \quad (5.2)$$

where $N_{\text{pseudo-data}}$ is the expected number of data events with 3000 fb^{-1} luminosity, $N_{\text{QDC-ZZjj}}$ and $N_{\text{EW-ZZjj}}$ are the number of predicted events from QCD-ZZjj and EW-ZZjj processes, respectively. The $C_{\text{EW-ZZjj}}$ factor refers to the detector efficiency for EW-ZZjj processes, calculated as the number of selected signal events at the detector level ($N_{\text{EW}}^{\text{detector}}$), divided by a number of selec-

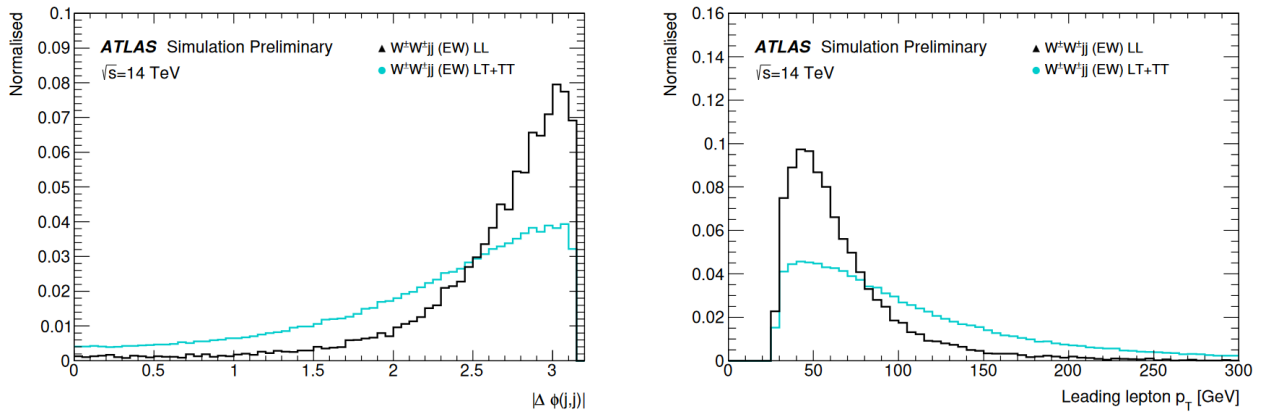


FIGURE 5.8 – Shape comparisons for the dijet azimuthal separation $\Delta\phi(j,j)$ (left) and leading lepton p_T (right) distributions for the purely longitudinal (LL) and combined mixed and transverse (LT+TT) $W^{\pm}W^{\pm}$ jj events [43]

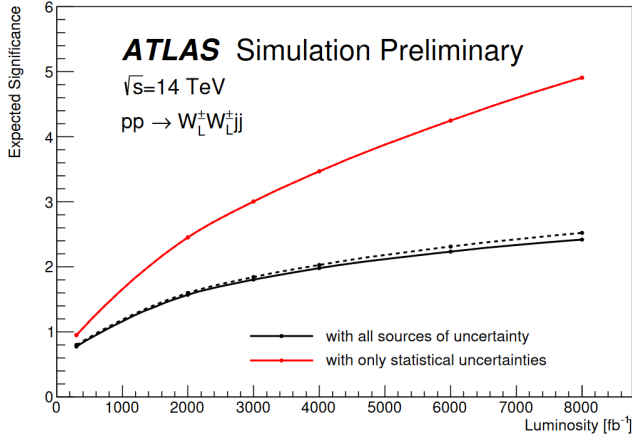


FIGURE 5.9 – Projection of the expected significance of the observation of the $W_L^\pm W_L^\pm jj$ process as a function of integrated luminosity, for the optimized event selection using the baseline scenario, considering all the sources of uncertainty (black) or only the statistical uncertainty (red) [43]

ted events at the particle level in the fiducial phase space ($N_{EW}^{particle}$). Uncertainty may significantly change (Fig. 5.10) in case conservative 30% theoretical uncertainty scenario is realized.

1533 $Z_L Z_L$ prospects

1534 ATLAS did not perform VBS $Z_L Z_L \rightarrow 4\ell$ sensitivity study, but it was done by CMS. The most
 1535 sensitive variable is $\cos\theta^*$ where θ^* is the angle between the lepton direction in the Z decay rest
 1536 frame and Z momentum in the laboratory frame. This variable, together with other polarization-
 1537 sensitive variables and variables used for discrimination from QCD background, are combined into
 1538 BDT used to separate $Z_L Z_L$ from $Z_T Z_T, Z_L Z_T$. It's assumed that ratio will be measured instead
 1539 of absolute $Z_L Z_L$ cross-section - to cancel systematics. The result is shown on Fig. 5.11 - as in
 1540 $W^\pm W^\pm$ case, just increasing the dataset is not enough for observation.

1541 5.4.3 $W^\pm Z$ analysis

1542 CMS projection will be shown as the study of uncertainty reduction with luminosity was done,
 1543 unlike for ATLAS. Typical selections are made. MC samples with full detector simulation at 13
 1544 TeV are used, and for projection, they are scaled from to 14 TeV using SM predictions. Data-driven
 1545 background estimates are used and scaled using an appropriate mixture of simulated events. The
 1546 additional scaling factor is applied to increase pseudo-rapidity coverage at HL-LHC . With this at
 1547 3000 fb^{-1} , 2757 EW-WZjj events are expected, and 3486 of QCD-WZjj. Important backgrounds are
 1548 tV/VVV (1374), non-prompt (1192), and VV, $Z\gamma$. To extract the EW signal, CMS used distribution
 1549 projection of which is shown on Fig. 5.12a - it's a m_{jj} discriminant unrolled in bins of $\Delta R(j, j)$.
 1550 Relative uncertainty on EW cross-section is shown on Fig. 5.12b for different integrated luminosity
 1551 values - close to two-fold reduction is seen at 3000 fb^{-1} , where the plateau is also reached.

1552 $W_L^\pm Z_L$ prospects

1553 CMS (again) studied the double longitudinal process. The same distribution is fitted, shown
 1554 in Fig. 5.13a - LL configuration in some bins differs from non-LL by up to 7%. The significance
 1555 of EW-WZjj LL as a function of luminosity is shown on Fig. 5.13b - not reaching discovery value
 1556 again, and we can see that systematic uncertainties are sizeable.

1557 5.5 HGTD

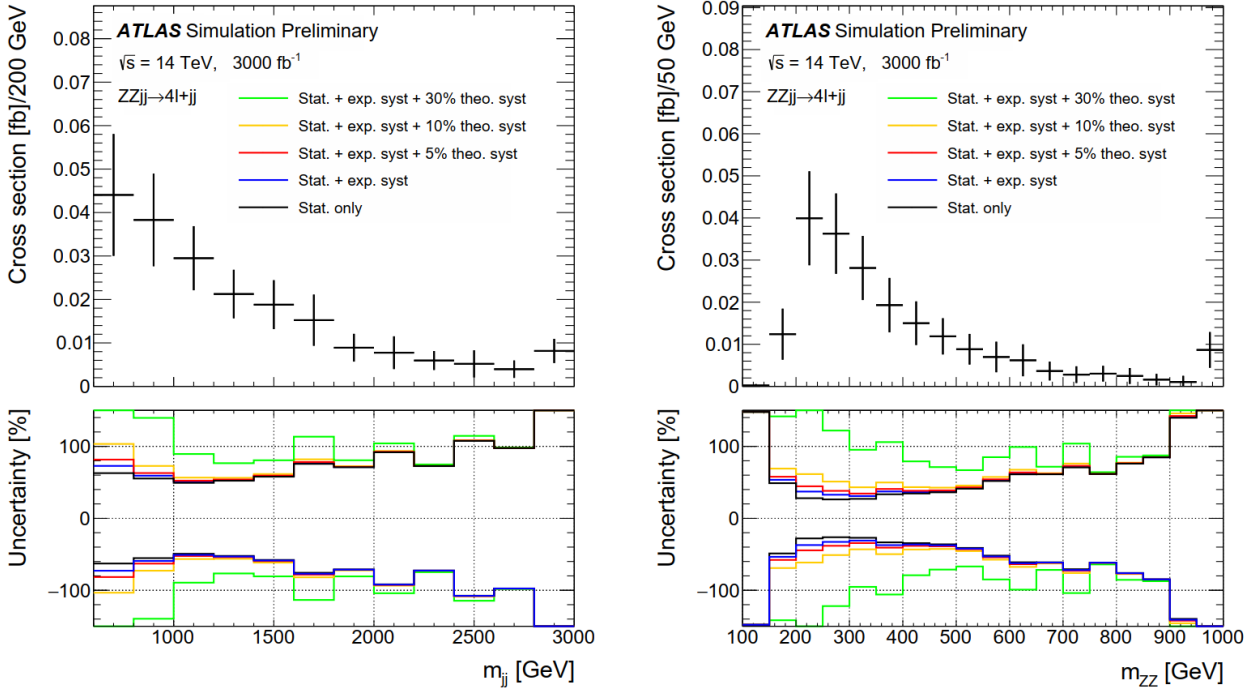


FIGURE 5.10 – Expected differential cross sections at 14 TeV for the EW-ZZjj processes as a function of m_{jj} (left) and m_{ZZ} (right) . Results are shown with different sizes of systematic uncertainties [41].

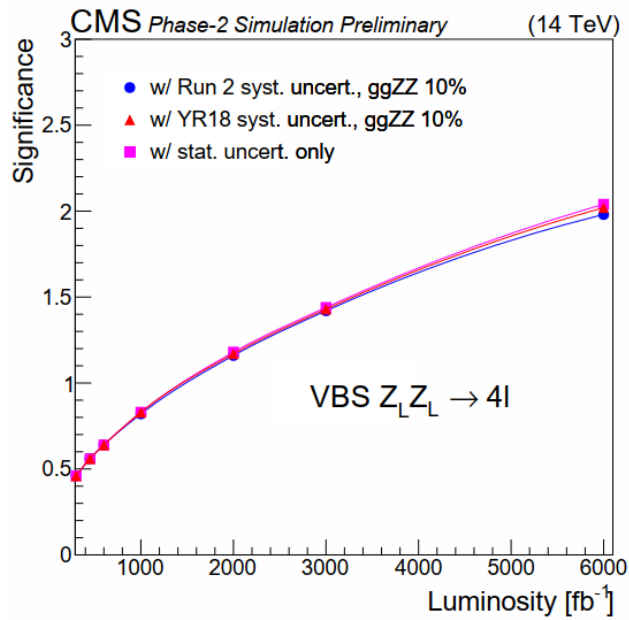


FIGURE 5.11 – Expected significance for the VBS $Z_L Z_L$ fraction as a function of the integrated luminosity and for different systematic uncertainties scenario, as well as with only the statistical uncertainties[58].

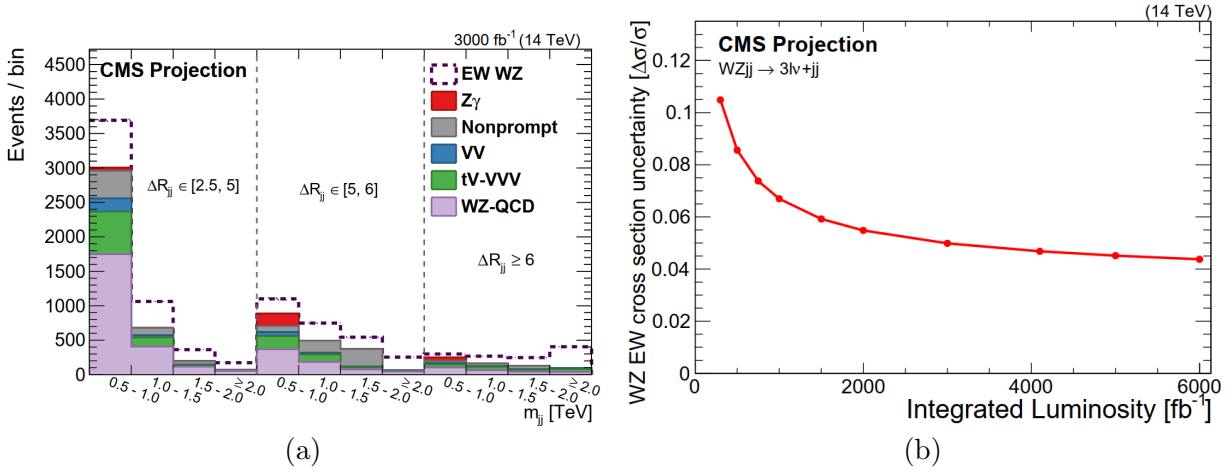


FIGURE 5.12 – (a) The m_{jj} distributions in bins of $\Delta R(j, j)$ for 3000 fb^{-1} [57] (b) Expected relative uncertainty on cross-section as a function of integrated luminosity [57]

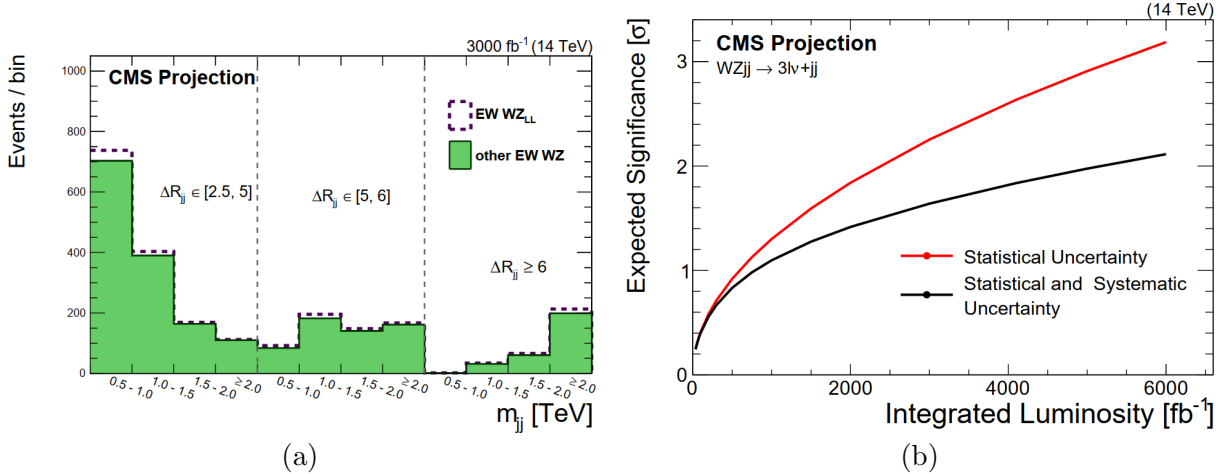


FIGURE 5.13 – (a) The m_{jj} distributions in bins of $\Delta R(j, j)$ for 3000 fb^{-1} , for two cases : EW WZ doubly longitudinal and other polarization configurations [57] (b) Significance of the $W_L^\pm Z_L$ observation with and without systematic error [57]

Increased pileup density (as what matters is not the number of p-p interactions but how far they are separated) poses a significant challenge for object reconstruction (and analysis using them) at HL-LHC. The luminous region will have an estimated Gaussian spread of 30–60 mm along the beam direction. Distributions comparing Run-2 conditions ($\bar{\mu} = 30$) and HL-LHC is shown on Fig. 5.14a - a seven-fold increase of mean value is foreseen; the same applies for maximum value. How busy events can be is demonstrated on Fig. 5.14b in time and space planes using one top pair event - the prerequisite for the experiment to reconstruct physics objects is to distinguish HS vertex (marked with a red star) from all the others. Using spatial information from ITk (with a resolution of about 4,5 mm), one would select the x-axis slice, but there are still many vertices there. In addition, knowing the interaction time, displayed in the y-axis, would allow one to do another slice - significantly reducing the number of candidate events. Time should be measured more precisely than what is currently possible (for example, in LAr with resolution ≈ 1 ns). Therefore, a new

1570 sub-detector called High Granularity Timing Detector (HGTD) will be installed for this.

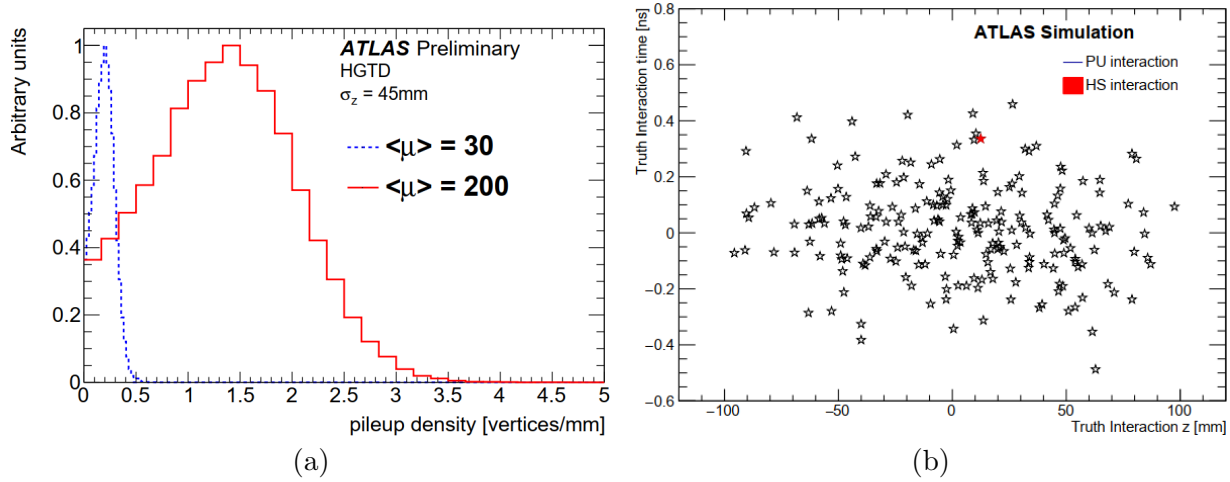


FIGURE 5.14 – (a) Local pileup vertex densities at generator level for two values of $\bar{\mu} : \bar{\mu} = 30$ and $\bar{\mu} = 200$ [46] (b) Visualisation of the truth interactions in a single bunch crossing in the $z-t$ plane, showing the simulated Hard Scatter (HS) $t\bar{t}$ event interaction (red) with pileup interactions superimposed (black) for $\bar{\mu} = 200$ [46]

1571 5.5.1 Detector overview

1572 HGTD will be installed in the forward region, outside the ITk volume, and in front of the end-
 1573 cap and forward calorimeters, illustrated in Fig. 5.15. HGTD will provide timestamp⁷ for tracks
 1574 with $2.4 < |\eta| < 4$. Fig. 5.16 illustrates why having timing information only in this $|\eta|$ region is
 1575 enough : for low momentum and high $|\eta|$ resolution of the determination of the track longitudinal
 1576 impact parameter by the ITk grows significantly. Still, one wants it to be much smaller than the
 1577 average inverse pileup density (will be $700 \mu\text{m}$ for the HL-LHC) for good identification of the
 1578 primary vertex. For low $|\eta|$, spatial information from ITk alone is enough to separate vertices.
 1579 Fig. 5.17 shows the benefit of using HGTD for pileup jet rejection in comparison with ITk-only
 1580 reconstruction. The pileup jets rejection for $30 < p_T < 50 \text{ GeV}$ and $2.4 < |\eta| < 4.0$ is shown as a
 1581 function of the efficiency for selecting hard-scatter jets. For example, for 85% efficiency, it can be
 1582 seen that if we use the HGTD, the rejection is better by approximately a factor of 1.5.

1583 The radial extend of the HGTD is from 110 mm to 1000 mm. It is divided into three active
 1584 regions : $120 \text{ mm} < r < 230 \text{ mm}$, $230 \text{ mm} < r < 470 \text{ mm}$, and $470 \text{ mm} < r < 640 \text{ mm}$, which
 1585 are visible on Fig. 5.15 . Peripheral electronics occupy the fourth inactive region with $640 \text{ mm} < r < 1000 \text{ mm}$. Fig. 5.18a shows HGTD components : it consists of one hermetic vessel, two ins-
 1586 trumented double-sided layers (mounted on two cooling/support disks), and two moderator pieces
 1587 placed inside and outside the hermetic vessel. Each cooling/support disk is physically separated
 1588 into two half circles. Furthermore, the layers are rotated in opposite directions with respect to one
 1589 another by 15° to 20° to maximize the hit efficiency and provide space for cooling pipes. Three
 1590 different active regions have different overlaps between two sides of instrumented layers, which is
 1591 illustrated in Fig. 5.18b. Regions closer to the beam have higher overlap to compensate for faster
 1592 degradation (compared to outer regions) of resolution per hit and obtain less steep drop in reso-
 1593 lution per track. The average number of hits per track is 2.6 (inner radial region), 2.4 (middle
 1594 region), and 2.0 (outer region). The overall spacing and the overlap between modules are optimized
 1595 to maintain a constant time resolution per track as a function of $|\eta|$.

7. HGTD also will be used for bunch-by-bunch luminosity measurement

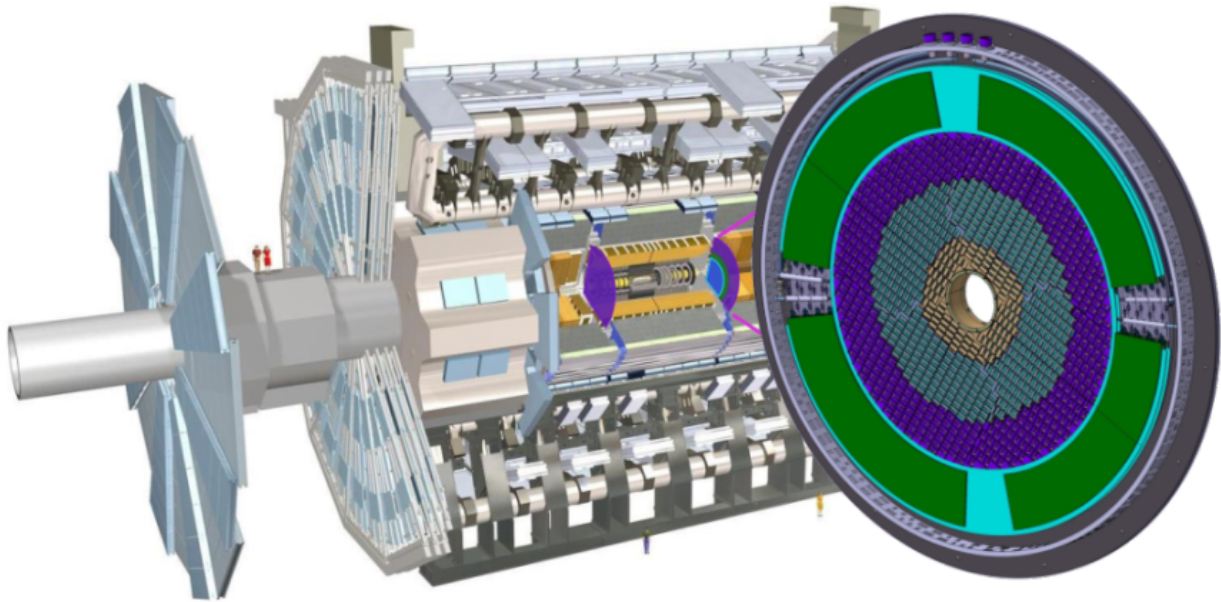


FIGURE 5.15 – Position of the HGTD within the ATLAS Detector. The HGTD acceptance is defined as the surface covered by the HGTD between a radius of 120 mm and 640 mm at a position of $z = \pm 3.5$ m along the beamline, on both sides of the detector [46]

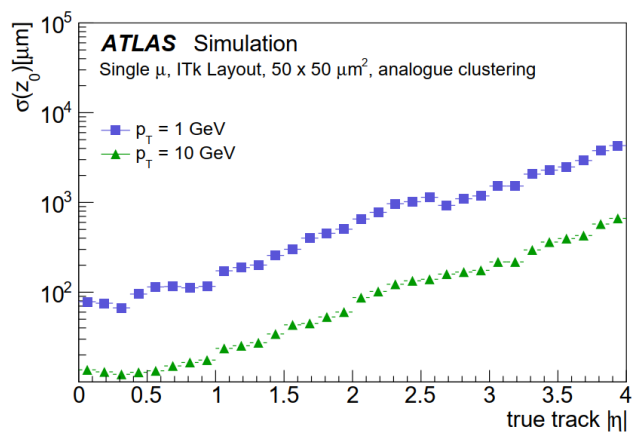


FIGURE 5.16 – Resolution of the longitudinal track impact parameter, z_0 , as a function of h for muons of $p_T = 1$ GeV and $p_T = 10$ GeV using ITk alone [46]

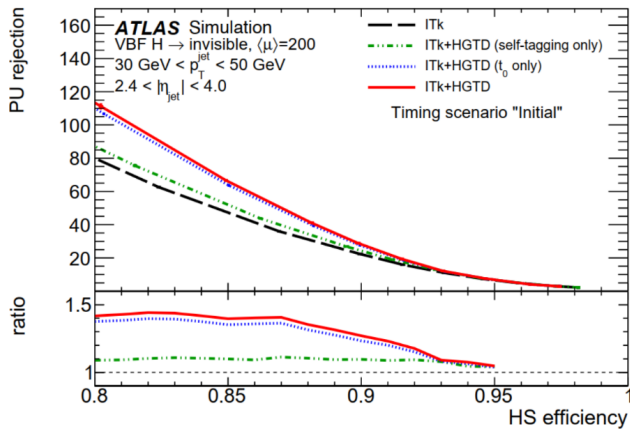


FIGURE 5.17 – Pileup jet rejection (for jet with $30 < p_T < 50$ GeV) as a function of hard-scatter jet efficiency in the $2.4 < |\eta| < 4.0$ region at the beginning of the lifetime of the detector, VBF H to invisible sample, for the ITk-only and combined ITk + HGTD reconstruction [46]

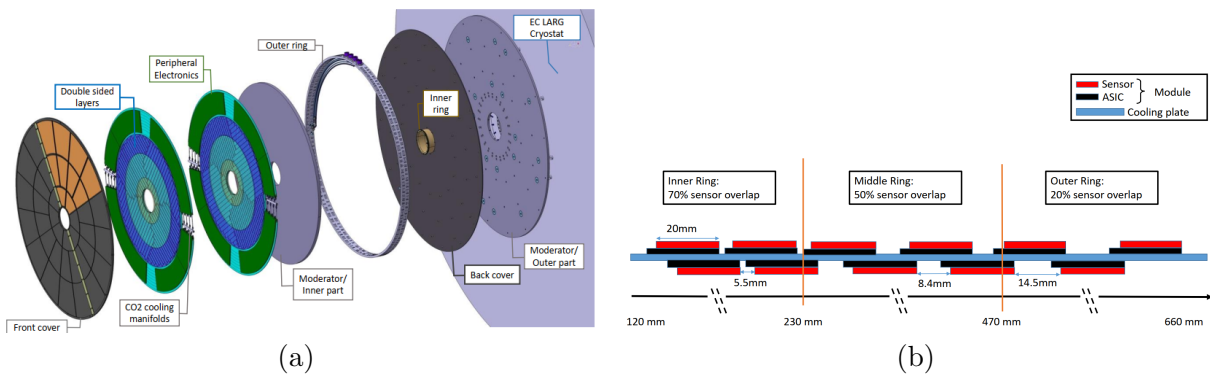


FIGURE 5.18 – (a) Global view of the HGTD to be installed on each of two end-cap calorimeters. The various components are shown : hermetic vessel (front and rear covers, inner and outer rings), two instrumented double-sided layers (mounted in two cooling disks), two moderator pieces placed inside and outside the hermetic vessel [46] (b) The schematic drawing shows the overlap between the modules on the front and back of the cooling disk. There is a sensor overlap of 20% for $r > 470\text{mm}$, 54% for $230\text{mm} < r < 470\text{mm}$ and 70% for $r < 230\text{mm}$ [46]

HGTD should be able to maintain its outstanding performance in the extremely harsh irradiation conditions of the forward region for the entirety of the HL-LHC lifetime : it must survive a nominal neutron-equivalent fluence of $8.3 \times 10^{15} \text{ neq/cm}^2$ (at the lowest radius of HGTD) and a total ionizing dose of 7.5 MGy, that will be reached at the end of the HL-LHC. Low-Gain Avalanche Detector (LGAD, Si sensor chosen for HGTD that will be briefly described below) sensors cannot provide the required charge given this radiation damage. Therefore, the region closest to the beam radially, where the radiation damage is the highest, will be replaced three times. The middle layer will be replaced once. The outer layer will not be replaced.

The HGTD active area comprises $4 \times 2\text{cm}^2$ modules. Module consists of a two LGAD sensors each with size $1.3 \text{ mm} \times 1.3 \text{ mm}$, two read-out Application-Specific Integrated Circuits (ASIC), and a flex board that provides connection with flex cable. The flex cable is used to connect the module and the peripheral electronics.

Expected occupancy is shown on Fig. 5.19 : rises for regions closer to the beam compared to the innermost layer, primarily caused by the increased probability of initiating showers due to hadronic interactions as more material is traversed. Dependency was obtained in minimum bias events with

1612 the highest expected pileup.

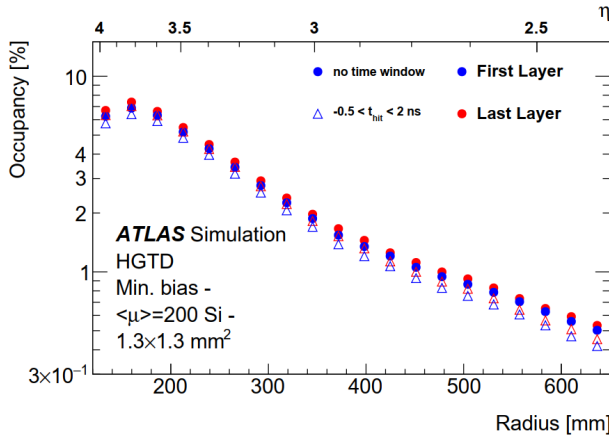


FIGURE 5.19 – The occupancy per module as a function of the radius and $|\eta|$ for a pad size $1.3 \text{ mm} \times 1.3 \text{ mm}$ at a pileup of $\bar{\mu} = 200$. [46]

5.5.2 Sensor

1614 Average time resolution per hit is required to be ≈ 35 ps at the start of an operational lifetime
 1615 and ≈ 70 ps in the end. Components of time resolution will be considered later ; for the time being,
 1616 it's enough to say that to achieve such a resolution, the sensor cannot have a time resolution larger
 1617 than per hit resolution. Low-Gain Avalanche Diode (LGAD) sensors are chosen to provide the
 1618 needed radiation tolerance and excellent timing performance. The design is based on a traditional
 1619 n-in-p silicon detector. The p-n junction is inversely polarized by an externally applied bias voltage,
 1620 thus creating a large depletion region. When a charged particle crosses the sensor, it creates electron-
 1621 hole pairs that, due to the applied electric field, drift in opposite directions toward the cathode and
 1622 the anode, respectively. Unlike traditional sensors, LGAD has a highly doped p+ layer below the
 1623 cathode. This modification causes a large increase of the electric field over a thin avalanche region,
 1624 as shown in Fig. 5.20. In this region, the number of charge carriers will be multiplied. The total
 1625 generated current is a sum of the currents induced by the movement of both primary and avalanche
 1626 holes and electrons. It can be shown that the optimum gain for LGAD is 20. Fig. 5.22 shows the
 1627 LGAD signal in comparison with the signal from a traditional sensor, where it can be seen that
 1628 the LGAD signal has a bigger amplitude and longer pulse duration. As shown on Fig. 5.21, a time
 1629 resolution smaller than 70 ps per hit (which is close to the required resolution) is achievable if the
 1630 charge is above four fC. With increasing radiation damage, the charge will go below, which is why
 1631 one needs to replace sensors during the HL-LHC phase.

1632 LGAD development reached a stage where irradiated sensors (alone, without ASIC) were tested
 1633 with particles - results for key quantities are shown in Fig. 5.23 - all key requirements are reached,
 1634 Those are carbon-enriched sensors, as it was seen to improve radiation hardness. The next step is
 1635 to test those sensors together with ASIC .

5.5.3 Time resolution components

1636 35 ps per hit average time resolution (in the beginning of operation) is composed of contributions
 1637 coming from sensor, read-out electronics, and clock

$$\sigma_{total}^2 = \sigma_L^2 + \sigma_{elec}^2 + \sigma_{clock}^2 \quad (5.3)$$

1638 σ_L^2 arises because of the non-uniformity of the energy deposition process by an impinging charged
 1639 particle in silicon. The local density of electron-hole pairs created along the trajectory is not the

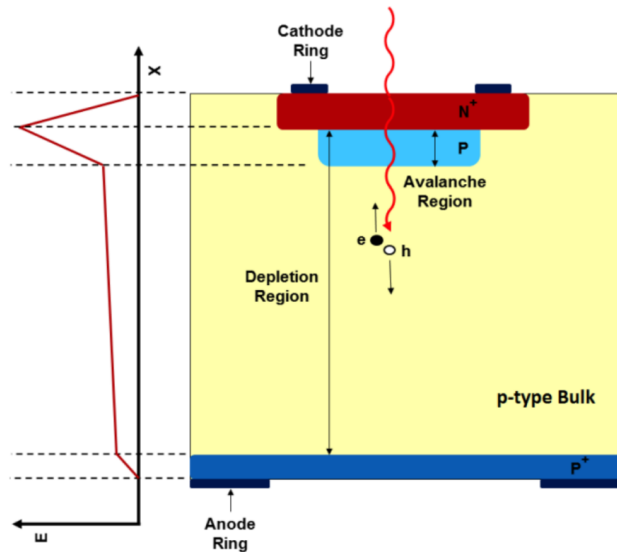


FIGURE 5.20 – Schematic of LGAD electric field and layers [46]

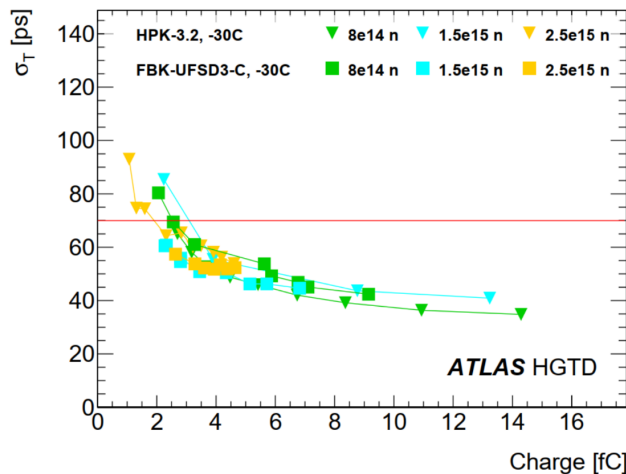


FIGURE 5.21 – LGAD current signal and traditional sensor signal [46]

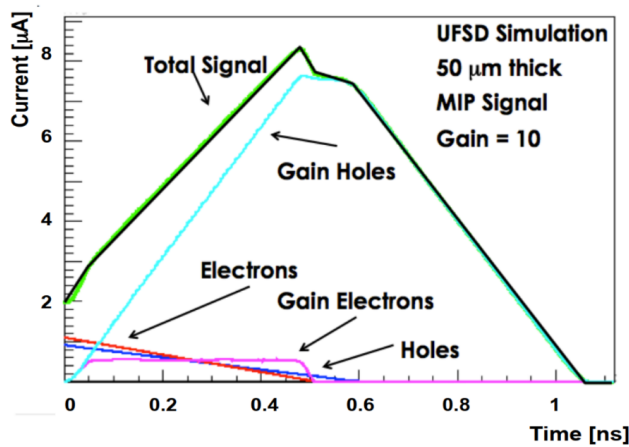


FIGURE 5.22 – Time resolution as a function of the collected charge for neutron-irradiated LGADs from different manufacturers with a 50 μm active thickness [46]

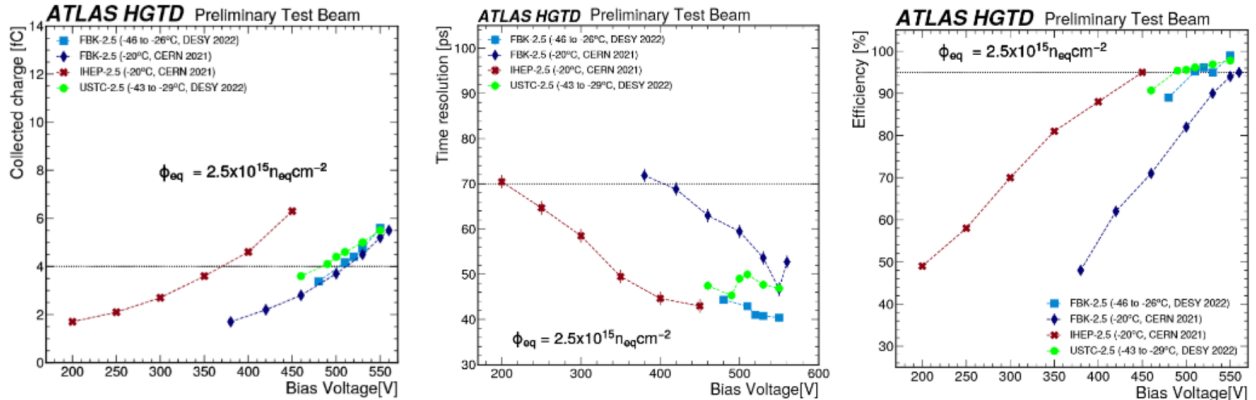


FIGURE 5.23 – Performance of carbon-enriched irradiated LGAD in testbeam (left) collected charge depending on bias voltage (middle) time resolution depending on bias voltage (right) hit efficiency vs bias voltage [95]

same in each event - this produces irregularities in the current signal (Landau noise). Also, the total number of electron holes will vary. With a chosen $50 \mu\text{m}$ thick LGAD sensor, the Landau term is approximately 25 ps. σ_{clock}^2 is the contribution from the reference clock : one measures the time of a hit with respect to the LHC clock, which should be precisely distributed to each of the channels. Imperfections of the clock distribution are estimated to give a contribution of 15 ps. σ_{elec}^2 in fact consists of three terms :

$$\sigma_{elec}^2 = \sigma_{TimeWalk}^2 + \sigma_{Jitter}^2 + \sigma_{TDC}^2 \quad (5.4)$$

σ_{TDC}^2 arises because one is doing a digitization of the time measurement with Time-to-Digital Converters (TDC) that have some finite non-zero binning. If bins are of equal size ΔT , the contribution is $\Delta T / \sqrt{12}$. In HGTD, the read-out ASIC will minimize this term by using a fine ≈ 20 ps binning. $\sigma_{TimeWalk}^2$ arises because of the unavoidable effect that more significant signals cross a given threshold earlier than smaller ones. This is illustrated on Fig. 5.24. Results of time measurements have a dependence on the amplitude of the signal. Assuming a linear signal, it can be shown that

$$\sigma_{TimeWalk} \propto \left(\frac{V_{threshold}}{S/t_{rise}} \right)_{RMS} \quad (5.5)$$

Where $V_{threshold}$ is the threshold value, S is signal amplitude, and t_{rise} is the signal rise time. Therefore, the time-walk is minimized by systems with a high slew rate. Also, time-walk can be corrected using Time over Threshold (TOT) information - the HGTD front-end ASIC is designed to make the TOT information available.

σ_{Jitter}^2 represents the uncertainty in the time measurement due to the presence of noise in the signal, which is illustrated on Fig. 5.24. The discriminator will be fired later or earlier because of this noise. Again, assuming constant slope and denoting system noise as N , one can write

$$\sigma_{Jitter} = \frac{N}{dV/dT} \sim \frac{t_{rise}}{S/N} \quad (5.6)$$

5.5.4 Front-end electronics

ATLAS LGAD Timing Read-Out Chip (ALTIROC) is a front-end ASIC for the HGTD. The read-out electronics timing performance must be comparable to benefit fully from the LGAD timing performance. Requirements for ALTIROC are summarized below.

Be able to process the four fC charge and therefore, the minimum threshold should be two fC . The cross-talk between channels should be kept below 5% for such a low threshold. The dynamic

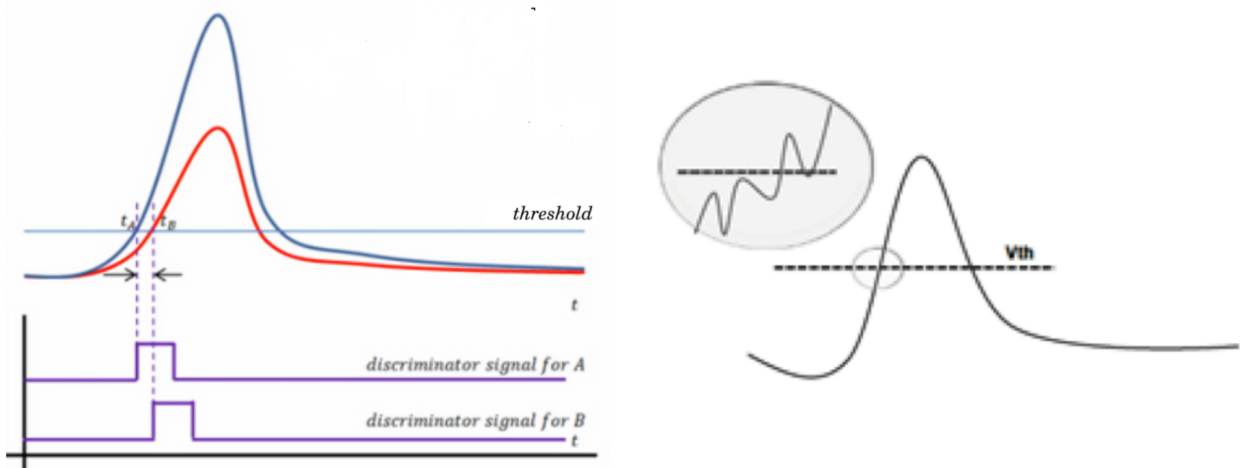


FIGURE 5.24 – (left) Time-walk : signals of different amplitude cross a fixed threshold at different times (right) Jitter : noise crossing the threshold value

range should be 4 - 50 fC . Jitter should be < 25 ps at 10 fC and < 70 ps at 4 fC. σ_{TDC} is below 10 ps. $\sigma_{TimeWalk}$ should be also below 10 ps. Single-pad noise should be below 0.5 fC . The clock phase adjustment precision should be below 100 ps to properly center the 2.5 ns measuring window at the bunch-crossing. The chip should survive the HGTD radiation levels within the replacement plan foreseen. Conversion time should be below 25 ns to finish before the next proton-proton collision begins. Capability of handling up to $5\mu A$ leakage current from the sensor without degrading the ASIC performance. Average power dissipation should be below 1.2 W per ASIC because one doesn't have a lot of space for cooling. Have the necessary memory to save data during L0/L1 trigger latency.

The chip will have a size of 20 mm \times 22 mm with 225 channels organized in a 15 \times 15 matrix. Fig. 5.25 shows the general architecture of a chip with a channel matrix organized along columns for the read-out and with the common digital electronics at the bottom. The schematic of one electronics channel is displayed on top of the channels matrix.

Single-channel electronics is the same in all 225 channels : digital and analog block. The digital front-end block is responsible for identifying and storing the hits (including the separate block for processing the luminosity information). Analog block, shown on Fig. 5.27 : preamplifier, discriminator, and two TDCs. The sensor signal is amplified using a preamplifier. Two types of preamp were initially studied : Voltage Preamplifier (VPA) and Trans Impedance (TZ). The preamplifier is followed by a fast discriminator, which produces an output signal when the input signal goes above a certain threshold. Time of start of the signal, Time of Arrival (TOA, illustrated on Fig. 5.26), is digitized with a dedicated 7-bit TDC . The TOA measurement is done in a 2.5 ns window centered on the bunch crossing. Since the expected time dispersion of the hits is around 300 ps, this window allows for the full collection of hits. The TOA time-walk problem is solved by using Time-over-Threshold (TOT, illustrated on Fig. 5.26) information since TOT is a proxy for signal amplitude. TOT uses the second 9-bit TDC .

There are leading and falling-edge discriminators (only used for Time of End measurement in TOT). A leading-edge discriminator is connected to the preamplifier's output and compares the preamp signal to a threshold voltage. `en_hyst` (see Fig. 5.27) is a part of the hysteresis system integrated to avoid re-triggering on the noise of the falling edge of discriminator - the principle is illustrated in Fig. 5.28 : As soon as there is a discriminator pulse, the threshold voltage of the discriminator is automatically slightly decreased. This is done by adding a small current ($\approx 1\mu A$) in one of the branches of the discriminator input differential pair. When the discriminator output

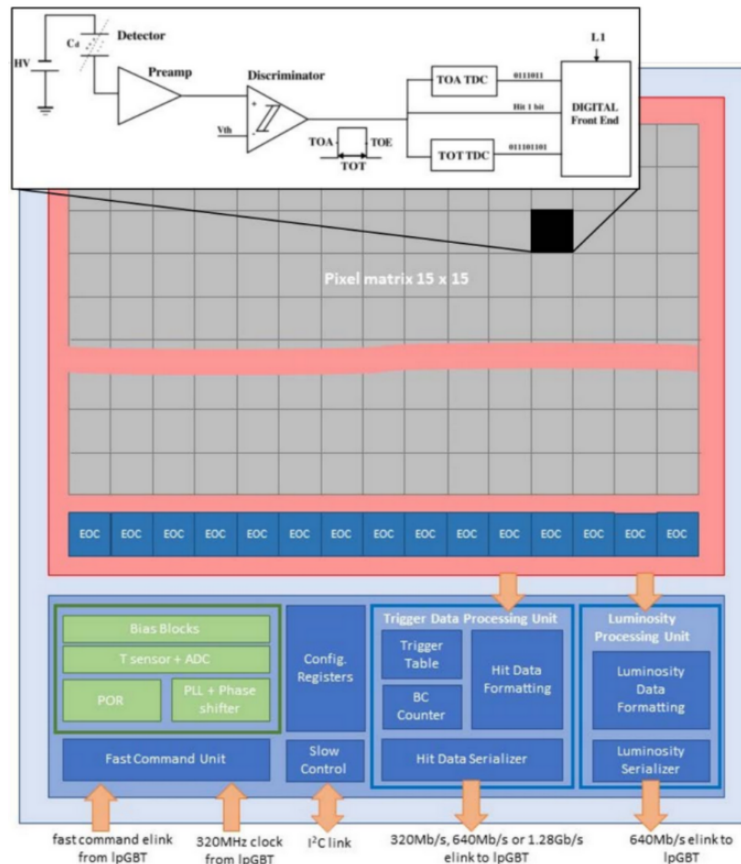


FIGURE 5.25 – Global architecture of the ALTIROC ASIC. The schematic of one Front End electronics channel is displayed on top of the channels matrix, with the preamplifier followed by a discriminator, two TDCs, and a digital front-end block [46]

1699 goes back to 0, the threshold returns to its initial value.

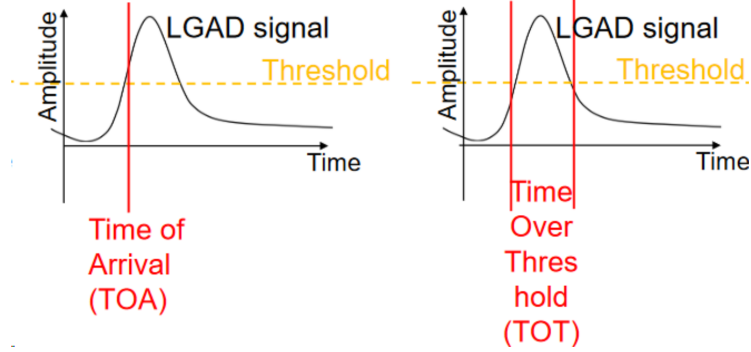


FIGURE 5.26 – Illustration of (left) TOA and (right) TOT

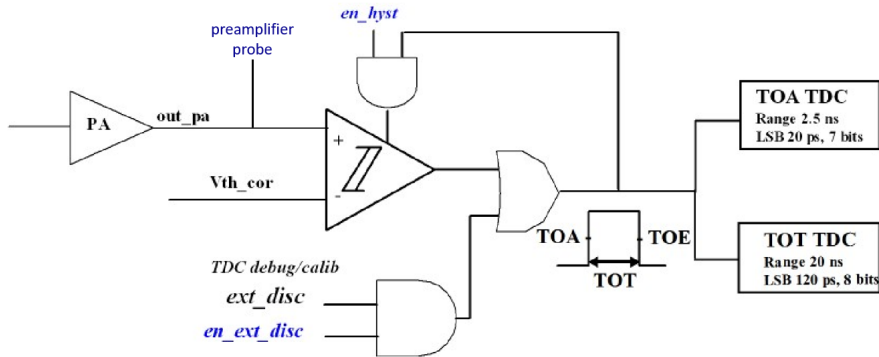


FIGURE 5.27 – ALTIROC single pixel analog part. Adapted from [72]

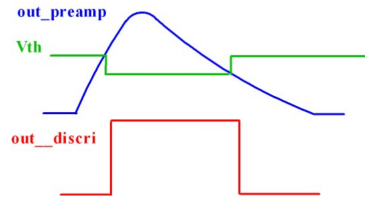


FIGURE 5.28 – Hysteresis principle [72]

1700 In practice, VPA and TZ preamplifiers are different by fall time of signal - it's about factor 5
 1701 longer for VPA . A comparison of waveforms is shown on Fig. 5.29. Therefore, one might think that
 1702 having a longer signal is better for accurate amplitude proxy measurement (TOT) and timewalk
 1703 correction. As will be shown, the VPA signal is too long because it picks up unwanted coupling
 1704 that breaks the proportionality between amplitude and TOT value - unlike TZ .

1705 End-of-column logic reads the data along each of the 15 columns and transfers data to the digital
 1706 part. The digital part is common to all channels. It prepares the received data for transmission to the
 1707 peripheral electronics and transmits data. It also contains a phase-locked loop, a phase shifter, and a
 1708 command decoder. The event timing data from the ASIC will be sent to the peripheral electronics
 1709 for further processing when the trigger signal arrives at the ASIC. The luminosity information
 1710 is the number of hits per ASIC and is sent at every bunch - for a fraction of ASICs (to save
 1711 bandwidth). ALTIROC will measure the sum of hists within two different time windows - where
 1712 smaller window (of size 3.125 ns) is inside of the larger window (of adjustable size N×3.125 ns).
 1713 Larger window allows to get information about the background.

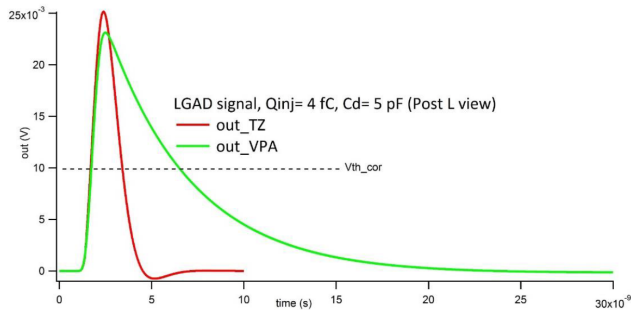


FIGURE 5.29 – VPA and TZ output waveforms [72]

5.5.5 ASIC characterization aspects

Work on ALTIROC R&D started in 2016. Since there, multiple prototype versions been produced, latest being ALTIROC-A (2024) - summary is given below.

Prototype versions

Version	Description
ALTIROC0	2x2 pixel array only preamplifier and discriminator stages of the analog part
ALTIROC1v1	5x5 pixel array TDC and channel memory blocks included
ALTIROC1v2	improved TDC - both VPA and TZ included
ALTIROC1v3	VPA only TDC
ALTIROC1v3b	TZ TDC brought back
ALTIROC2	first prototype with 225 channels ; VPA and TZ TDCs
ALTIROC3	radiation hard full-scale prototype ; TZ-only
ALTIROC-A	pre-production chip

TABLE 5.1 – Brief recap of ALTIROC prototypes

TDC discretization step

TOA and TOT are measured in separate TDCs. Each of them has their own discretization step, also called Least Significant Bit (LSB). LSB is a conversion factor with units of time ; in our case, picoseconds typically are convenient :

$$\begin{cases} TOA[ps] = LSB_{TOA}[ps] \times TOA[binary] \\ TOT[ps] = LSB_{TOT}[ps] \times TOT[binary] \end{cases} \quad (5.7)$$

Architecture of the TOA TDC relies on the Vernier delay line (as the target LSB is smaller than the gate-propagation delay in the 130 nm technology) and illustrated on Fig. 5.30. The START pulse corresponds to the rising edge of the discriminator. It comes first and initializes the TDC operation. The STOP pulse corresponds to the first rising edge of the 40 MHz TDC clock (The clock can be shifted from the rising edge of the external discriminator signal, and this is used routinely for calibration) that follows the START signal (notice TOA is measured concerning the falling edge of the current cycle), with a delay that represents the time interval to be digitalized.

1729 At each tap of the Delay Line, the STOP signal catches up to the START signal by the difference
 1730 of the propagation delays of cells in Slow and Fast branches of the delay line : i.e., $140\text{ps} - 120\text{ps}$
 1731 = 20ps, and this is what gives the TOA TDC LSB. The number of cells necessary for the STOP
 1732 signal to surpass the START signal represents the result of TDC conversion. TDC range is equal
 1733 to $128 \times TOALSB \approx 128 \times 20 \text{ ps} = 2.56 \text{ ns}$.

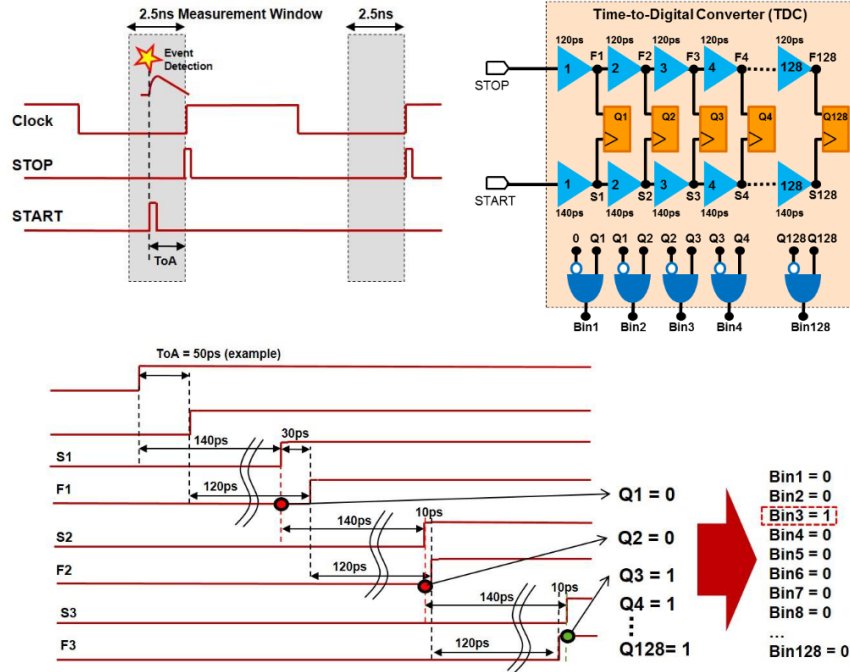


FIGURE 5.30 – TDC for TOA measurement : principle and delay Vernier line [72]

1734 ALTIROC1 and ALTIROC3, ALTIROC-A TOT TDC have two LSBs : coarse and fine because
 1735 digitization is done in two steps. In step 1, coarse delay line with $\approx 160 \text{ ps}$ LSB. After that, the
 1736 signal goes to Vernier line similar to TOA TDC but now with LSB of $\approx 40\text{ps}$.

1737 TDC Differential and Integral Non-linearity

1738 Differential Non-linearity (DNL) is a measure of the variation in the step size of the converter.
 1739 It quantifies the deviation of the actual step size between adjacent digital codes from the ideal step
 1740 size. DNL is expressed in terms of LSB. Ideally, each step in the TDC should correspond to one
 1741 LSB (in case of TOA - 20ps), but DNL measures the deviation from this ideal (in practice, the
 1742 average is taken), for code i (0-127 for TOA) according to

$$DNL_i = \frac{LSB(ps)_i - LSB(ps)_{average}}{LSB(ps)_{average}} \quad (5.8)$$

1743 Integral Non-linearity (INL) is used to characterize the deviation of the actual transfer function
 1744 of the TDC from the ideal transfer function. Ideally, for a TDC, each step in the digital output
 1745 code should correspond precisely to a consistent time interval. However, due to imperfections in the
 1746 circuitry (true for Vernier architecture) and manufacturing variations, the actual transfer function
 1747 may deviate from the ideal. Integral Non-linearity is quantified by measuring the cumulative devia-
 1748 tion of the actual transfer function from the ideal one over the entire range of input time intervals.
 1749 INL is often expressed in terms of LSB :

$$INL_i = \frac{\sum_0^i LSB_i(ps)_i - center(ps)_i}{LSB(ps)_{average}} \quad (5.9)$$

1750 **Calibration systems**

1751 Coming back to Fig. 5.27, ext_disc block is visible - responsible for external discriminator signal
1752 delivered by the command pulse generator module located in the digital periphery or from the
1753 I/O PAD. External discriminator signals can be injected into TDC to simulate a discriminator
1754 pulse instead of using the discriminator output of the pixel. In that case, the discriminator must
1755 be bypassed/ switched off. Alternatively, the threshold value can be set to a high value to prevent
1756 the discriminator from being triggered. The width of the external discriminator signal is tunable.

1757 Another way of calibration is using an internal pulser, which is common to all channels. The
1758 amplitude of the resulting voltage step is equal to $V_{step} = -R \times I_{DAC}$, where I_{DAC} is selected by
1759 the user, and it flows into R=50K Ohm resistor. Amplitude is sent to the selected internal C_{test}
1760 capacitor (200 fF in ALTIROC1) of each channel, simulating an input charge $Q_{inj} = C_{test} \times V_{step}$.
1761 In that way, whole analog chain is involved, not just the TDC, as in the case of an external trigger.

1762 **Preamplifier probe**

1763 Checking preamplifier output is possible, as illustrated on Fig. 5.27. This is the best estimate
1764 of what is going into the ASIC after the preamplifier, and this signal is typically digitized during
1765 testbeams to be later used for timewalk correction. The preamplifier probe can be enabled only for
1766 one pixel at a time.

1767 **Occupancy**

1768 For LSB calibration it will be important how many pixels are injected. It only makes sense to
1769 do the calibration within the range of expected occupancy - shown on Fig. 5.19, where it can be
1770 seen that it can be as high as 10%.

¹⁷⁷¹ 6 - ALTIROC1 testbeam

¹⁷⁷² The first results with ALTIROC1 in testbeam were published in [15], preceded by ALTIROC0
¹⁷⁷³ paper [16]. This section shows a more detailed analysis of the ALTIROC1 performance.

¹⁷⁷⁴ 6.1 Campaign overview

¹⁷⁷⁵ ALTIROC1 testbeam measurements were performed in October 2021 with the ASIC bump-
¹⁷⁷⁶ bonded to the LGAD (this object is called hybrid later in the text).

¹⁷⁷⁷ The goal of this testbeam was to determine the hybrid performance limit (time resolution of
¹⁷⁷⁸ a single pixel) at the beginning of HGTD operation (before some of the sensors will be replaced)
¹⁷⁷⁹ meaning before any irradiation as a result of which the deposit charge by a MIP will be decreased.
¹⁷⁸⁰ The LGAD used is HPK2 W42 5×5 -pad sensor produced by Hamamatsu Photonics ; it is a second
¹⁷⁸¹ sensor prototype version from HPK [73] production focused on the research and development for
¹⁷⁸² the ATLAS and CMS timing detectors. The hybrid was exposed to a 120 GeV pion beam at CERN
¹⁷⁸³ SPS (North Area, H6B beamline).

¹⁷⁸⁴ The testbeam setup is shown on Fig. 6.1. It consists of

- An ASIC+LGAD hybrid (the device we're testing) mounted on a custom ASIC readout board - shown on Fig. 6.3, mounted on movable stage
- An FPGA board (not marked on the picture) used for controlling the chip and receiving the data from it and the FPGA-ASIC interface board (not marked on the picture), used to reduce the noise contributions of various powering and digital signals to the ASIC
- Two Cherenkov counters consisting of a 6×6 mm² quartz bar coupled to a 5×5 mm² Silicon photomultiplier (SiPM) is used for timing reference. Two are needed to extract the time resolution of the hybrid
- A Lecroy oscilloscope with a sampling rate of 20 GSamples/s and a bandwidth of 2.5 GHz, used to record ASIC preamplifier probe pulse, 40 MHz clock, and SiPMs
- EUDET telescope [79] (only used for the alignment) based on six MIMOSA pixel planes, combined with an FE-I4 [82] readout module (chip-based)
- A programmable Trigger Logic Unit (TLU) [60] which handles the trigger logic
- Power supplies
- Several computers to control the setup remotely and store the recorded data

¹⁸⁰⁰ A trigger was issued by ALTIROC1 when a hit was recorded, initiating the data acquisition of
¹⁸⁰¹ the oscilloscope. While the digital data acquisition was done continuously, the oscilloscope buffered
¹⁸⁰² the data until its memory was full. At this point, it was necessary to pause the data acquisition
¹⁸⁰³ and transmit the oscilloscope data. Therefore, a “busy” logic was implemented in the FPGA to
¹⁸⁰⁴ stop the ASIC acquisition while the oscilloscope was read out. A common event number provided
¹⁸⁰⁵ a unique mapping between the two data streams.

¹⁸⁰⁶ The testbeam period and equipment were shared between the hybrid tests and standalone
¹⁸⁰⁷ LGAD sensor measurements (with custom non-HGTD readout) so that only at the end of the
¹⁸⁰⁸ period hybrid data at cold were recorded.

¹⁸⁰⁹ The challenge with using SiPMs for reference was that their performance degrades significantly
¹⁸¹⁰ with beam irradiation as shown on Fig. 6.2. The vertical lines show the start of the dedicated periods
¹⁸¹¹ of data recorded and used in analysis (Table 6.1). The SiPM2 shows worse degradation with more
¹⁸¹² than 100 ps resolution during the first week of data taking, so it was decided to replace it with a
¹⁸¹³ single pad reference LGAD (LGA35) of size 1.1×1.1 mm² after day 11. This sensor, readout by a
¹⁸¹⁴ custom electronics, had been used in measurement many times and was expected to have a time

1815 resolution of about 30 ps. Meanwhile, during the low-temperature data taking, the resolution of
 1816 SiPM1 also reached 100 ps and special care had to be taken to extract results - low-temperature
 1817 results will not be shown.

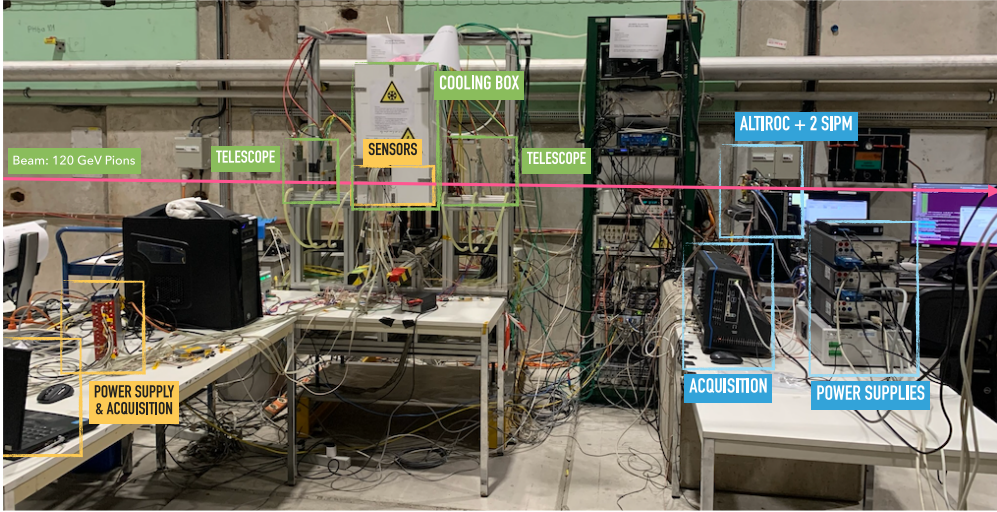


FIGURE 6.1 – ALTIROC1+LGAD hybrid testbeam setup at CERN SPS. Not marked on the picture : FPGA, FPGA-ASIC interface board, Trigger Logic Unit[61].

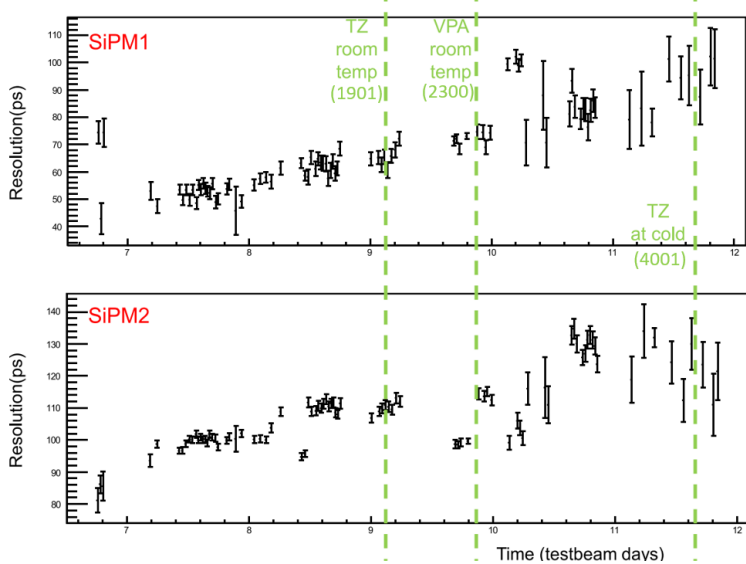


FIGURE 6.2 – Degradation of reference SiPM time resolution during testbeam. The green vertical line shows the start of the data-taking periods for batches from Table 6.1. Resolution against testbeam days shown for (top) quartz+SiPM1 system (bottom) quartz+SiPM2 system

1818 In this chapter, the results obtained at room temperature will be presented. Within two weeks,
 1819 the total number of events recorded in various configurations is ≈ 18 million. At the time of this
 1820 testbeam, the preamplifier choice (TZ or VPA) was not made, so the data were taken with both.
 1821 A run is the smallest data block taken with the same parameters (ASIC threshold, bias voltage,
 1822 preamplifier probe output of which pixel is ON). The size of a run is typically taken around
 1823 100000 events (total across all pixels in the beam) - not too small (restart is done by shifter and
 1824 humans tend to make mistakes while repeating similar operation many times, also restart takes
 1825 time and doing this too often leads to larger fraction of beam time left unrecorded) but also not

Batch number	num events	channel activated	preamp type	temperature	reference devices
1901	1.86 million	11	TZ	room	SiPM1+SiPM2
2300	0.68 million	15	VPA	room	SiPM1+SiPM2

TABLE 6.1 – Summary of data-taking conditions and parameters used to collect the data used for results presented in this chapter

1826 too large (simpler to deal with smaller files overall, particularly reject runs which ended up being
 1827 bad for whatever reason). Runs are grouped into batches (unique identifier of configuration). The
 1828 description of batches used in this chapter is given in Table 6.1. For all these runs, a preamplifier
 1829 probe was always ON, and the sensor bias voltage was 265 to have the maximal charge (about
 1830 15 fC) while staying safe with respect to the breakdown voltage. Finally, the ASIC discriminator
 1831 threshold was set to about 5 fC, low enough to guarantee a good hit detection efficiency.

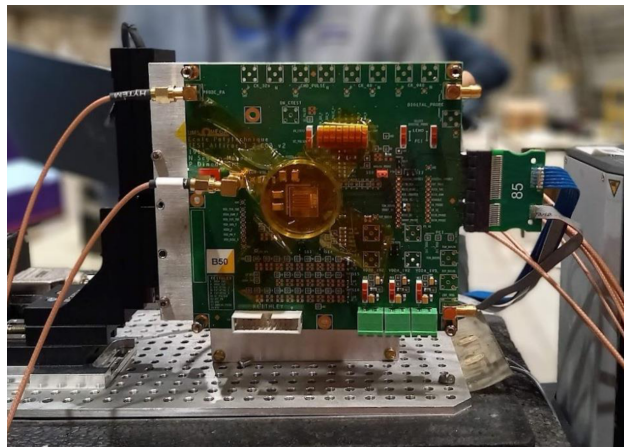


FIGURE 6.3 – ALTIROC1+LGAD hybrid mounted on dedicated ASIC read-out board. The board is mounted on a movable stage.

1832 6.2 Method of time resolution extraction

1833 Having three devices (two reference SiPMs and ASIC+LGAD hybrid), we can extract the time
 1834 resolution of each ($\sigma_0 \equiv \sigma_{SiPM1}$, $\sigma_1 \equiv \sigma_{SiPM2}$, $\sigma_2 \equiv \sigma_{hybrid}$) by assuming no correlation between
 1835 each measurement and solving the 3x3 system shown in Eq. 6.1.

$$\begin{cases} \sigma_{\Delta T01} = \sigma_0 \oplus \sigma_1 \\ \sigma_{\Delta T02} = \sigma_0 \oplus \sigma_2 \\ \sigma_{\Delta T12} = \sigma_1 \oplus \sigma_2 \end{cases} \quad (6.1)$$

1836 The main interest is σ_{hybrid} . However, knowing reference $\sigma_{SiPM1}, \sigma_{SiPM2}$ is also helpful for de-
 1837 bugging, especially if it gets much larger than the target resolution σ_{hybrid} , then results are not
 1838 accurate. On the Left Hand Side (LHS) of Eq. 6.1 are the quantities we measure from data - they
 1839 are the widths of three unique time differences between 3 devices. For example, to obtain $\Delta T01$,
 1840 here the difference of times between SiPM1 and SiPM2, one starts from the time when each device
 1841 was fired (what is meant by this is explained in Sec. 6.3). The distribution of the difference between
 1842 these times is (hopefully) Gaussian. This distribution is fitted with Gaussian width obtained from
 1843 fit is $\sigma_{\Delta T01}$ and fit error on this parameter gives $\sigma_{\sigma_{\Delta T01}}$. Uncertainties on $\sigma_0, \sigma_1, \sigma_2$ are expressed in

1844 terms of $\sigma_{\Delta T_{ij}}$, $\sigma_{\sigma_{\Delta T_{ij}}}$ by Eq. 6.2 - the equation is obtained using the usual uncertainty propagation
 1845 rules.

$$\frac{1}{4\sigma_i} \sqrt{(2\sigma_{\Delta T01}\sigma_{\sigma_{\Delta T01}})^2 + (2\sigma_{\Delta T02}\sigma_{\sigma_{\Delta T02}})^2 + (2\sigma_{\Delta T12}\sigma_{\sigma_{\Delta T12}})^2} \text{ where } i = 1, 2, 3 \quad (6.2)$$

1846 6.3 SiPM time reconstruction and it's matching with hybrid

1847 $\Delta T01$, width of which is used in Eq. 6.1, is given by Eq. 6.3. Constant fraction discrimination
 1848 (CFD) is used to determine the time when the individual device was fired and allows to
 1849 suppress the timewalk effect. tCFD is a moment when a signal crosses a certain fraction of its
 1850 amplitude. CFDs are obtained from the numerical calculation on SiPM signal digitized by an oscil-
 1851 loscope (Lecroy with 20 GSamples/s sampling rate), and the reference time axis is provided by the
 1852 scope. This axis is used in tCFD calculation. The time of each SiPM device $tCFD$ is obtained with
 1853 the software CFD, i.e. the time is computed event-by-event at a constant fraction of the amplitude,
 1854 therefore insensitive to the timewalk effect. The time is extracted from scope data sampled at 20
 1855 Gsample/s and interpolated to the precise threshold. A 20% threshold is used later in the analysis
 1856 (for both SiPMs), and $\Delta T01$ is defined as Eq. 6.3. 20% fraction choice allows to get the best SiPM
 1857 resolution while solving Eq. 6.1, which is shown in Fig. 6.4a (dependency obtained with batch 1901
 1858 data). CFD30 is comparable and also can be used. Both $tCFD20_{SiPM1}$ and $tCFD20_{SiPM2}$ are in
 1859 picoseconds and referenced to a consistent time axis so that they can be subtracted from each other
 1860 (contrary to the other two differences, where hybrid participates).

$$\Delta T01 = tCFD20_{SiPM1} - tCFD20_{SiPM1} \quad (6.3)$$

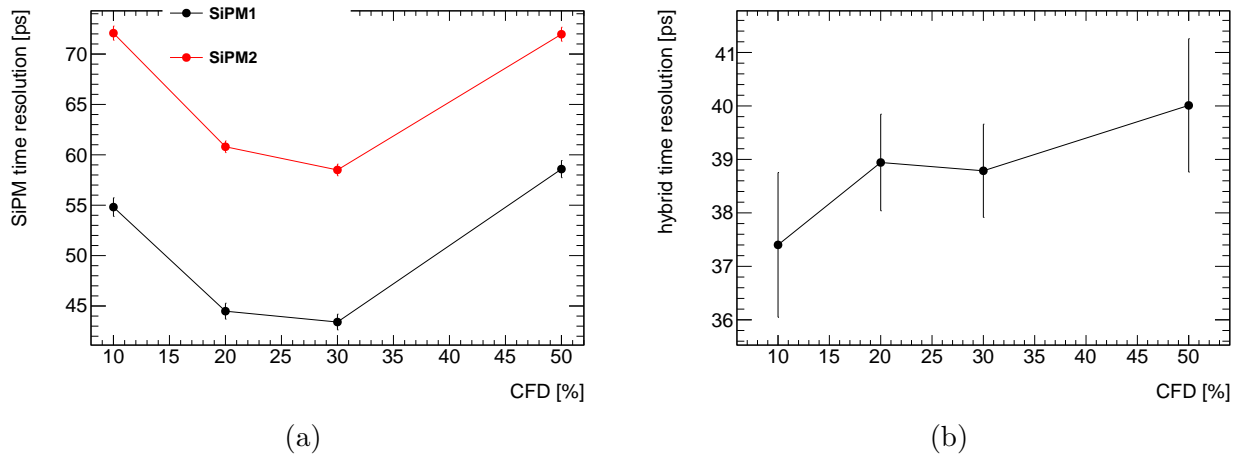


FIGURE 6.4 – Effect of varying (a) SiPM’s CFD[%] on quartz+SiPM1 and quartz+SiPM2 systems time resolution. (b) SiPM’s CFD[%] on hybrid time resolution.

1861 $\Delta T02$ and $\Delta T12$, width of which is used in Eq. 6.1, is given by

$$\Delta T0(1)2 = -TOA \times TOALSB - tCFD20_{0(1)} - t_{clock} \quad (6.4)$$

1862 However, because the trigger was issued by ALTIROC when a hit was recorded, referencing to clock
 1863 is done by construction and one can drop t_{clock} , giving

$$\Delta T0(1)2 = -TOA \times TOALSB - tCFD20_{0(1)} \quad (6.5)$$

1864 The time when the hybrid is fired is given by TOA measured by the ASIC (in raw TDC unit);
1865 it can be converted to picoseconds by multiplying TOA with TOA quantization step (also cal-
1866 led TOALSB standing for TOA Least Significant Bit) , which is obtained for each channel from
1867 testbench measurements and expected to be $\approx 20\text{ps}$. CFD for ASIC data is not used; instead,
1868 timewalk is corrected using measured TOT¹ . TOA in picoseconds can be compared to the CFD
1869 of two reference devices. $t_{CFD20_{1(2)}}$ in principle should be $(t_{CFD20_{1(2)}} - t_{clock})$ (it is done in
1870 this way with ALTIROC2 where trigger setup was different), but it is not done because we trigger
1871 on ALTIROC and including t_{clock} will only give a constant shift (identical in every event) - what
1872 matters is a shape and width of ΔT , not the absolute value so t_{clock} contribution is dropped. The
1873 minus sign in front of TOA is because TOA measures time until the falling edge of the 40 MHz
1874 clock, not the rising edge.

1875 As shown in Fig. 6.4b, and as a sanity check, the extracted hybrid resolution has little sensitivity
1876 to the SiPM CFD fraction.

1877 6.4 Resolution obtained with TZ preamplifier

1878 This section uses batch 1901 ; its parameters are shown in Table 6.1.

1879 6.4.1 TOA-TOT coupling caveat

1880 The TOT measured with the TDC is expected to be independent of its TOA as the energy
1881 deposition of the particles should be similar whenever the arrival time is with respect to the 40 MHz
1882 clock. However, the Fig. 6.5a shows a clear unexpected dependence. This S-shape variation depends
1883 on the ASIC discriminator threshold. The effect is attributed to a digital coupling synchronized
1884 with the 40 MHz clock. The digital activity at the channel level generates a 40 MHz digital noise
1885 that is partially injected through the ground of the preamplifier and amplified by it. The effect is
1886 also observed in testbench measurements but only with hybrid, not when the ASIC alone is used.

1887 Another way to see the coupling is shown on Fig. 6.5b : average preamplifier probe pulse (each
1888 pulse is digitized and recorded by the oscilloscope, then 100000 pulses averaged) in three TOA bins.
1889 The time the pulse is over a certain threshold (fraction of amplitude) is not the same for different
1890 TOA values. While the rising edges are similar, the falling edges are clearly not - inducing a TOT
1891 dependence vs TOA .

1892 6.4.2 Event selections

1893 The common event selections for all correction variables are related to TOA and SiPM am-
1894 plitudes. TOA of the pixel selected is non-saturated : the maximum value TOA can take is 127,
1895 so events with $\text{TOA} < 127$ are taken, which leaves us with 10% of events recorded since the mea-
1896 surement window of 2.5 ns is ten times smaller than the period of the 40MHz clock. Amplitude
1897 of both reference SiPMs should be above MPV of corresponding distribution, shown on Fig. 6.6,
1898 to get better SiPM resolution (as it is improving with amplitude). The downside of using tighter
1899 SiPM amplitude cuts is that statistics decrease. For SiPM1, amplitude also should be below 140
1900 mV since this is where the saturation peak appears (caused by misconfiguration of oscilloscope
1901 channel recording SiPM1)

1902 6.4.3 Uncorrected resolution

1. CFD is complex to do at the ASIC level since it requires frequent signal sampling, and even if it is possible, power consumption is too large to be fitted within HGTD requirements. ZCD (Zero Crossing Discrimination) was considered as a timewalk correction method in earlier ASIC prototypes, and results obtained were insufficient - TOT correction is used instead

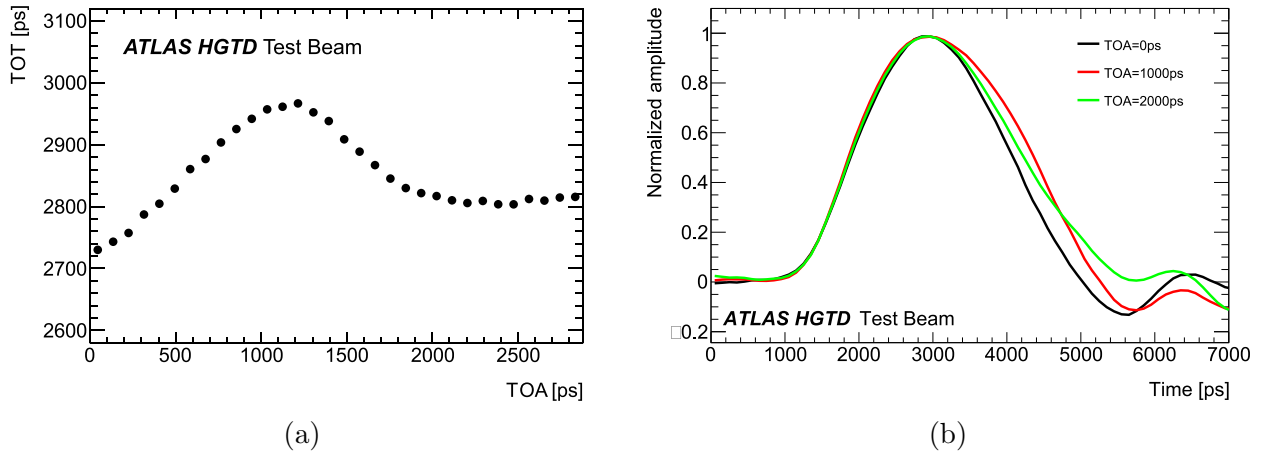


FIGURE 6.5 – (a) TOT as a function of the TOA. (b) Preamplifier probe waveform for various TOA values.

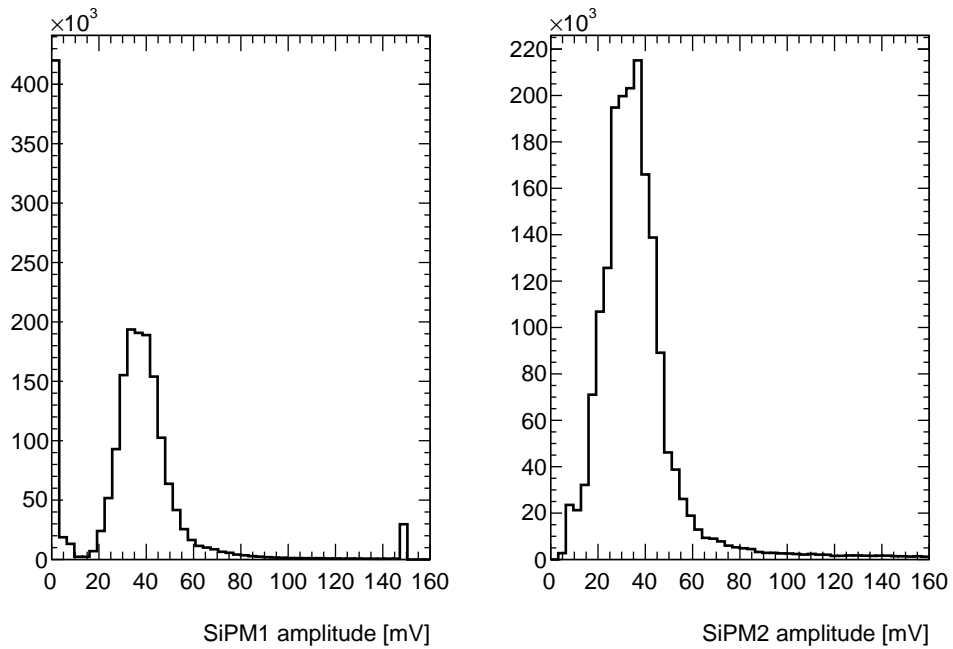


FIGURE 6.6 – Pulse amplitude distribution of (left) SiPM1 (right) SiPM2.

1903 An example of three ΔT s used in Eq. 6.1 is shown in Fig. 6.7 with black (batch 1901, before time-
 1904 walk correction) together with their width obtained from Gaussian fit. Fit gives $\sigma_{\Delta T01}$, $\sigma_{\Delta T02}$, $\sigma_{\Delta T12}$
 1905 entering LHS of Eq. 6.1. The uncorrected σ_{hybrid} , before timewalk correction, is 73.5 ± 0.7 ps - only
 1906 statistical uncertainty is considered.

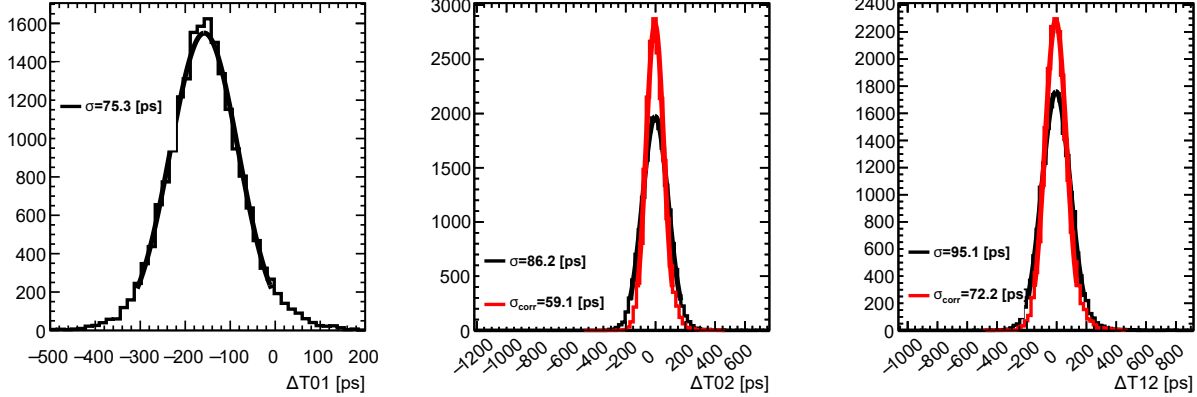


FIGURE 6.7 – Three ΔT distributions used to extract hybrid time resolution : (left) time difference between the quartz+SiPM1 system ($\equiv 0$ in ΔT) and quartz+SiPM2 system ($\equiv 1$ in ΔT). (middle) time difference between the quartz+SiPM1 system and hybrid ($\equiv 2$ in ΔT) before (black) and after (red) timewalk correction with the preamplifier probe amplitude. (right) time difference between the quartz+SiPM2 system and hybrid before and after timewalk correction with preamplifier probe amplitude. For (middle) and (right), the black/red lines show Gaussian fits of timewalk uncorrected/corrected, and corresponding numbers are widths obtained from the fit.

6.4.4 Timewalk correction variables

1907 The ASIC measures the TOT because the TOT is a proxy for the LGAD signal amplitude, and
 1908 “amplitude” is needed for timewalk correction. The timewalk correction can significantly improve
 1909 time resolution. The complete list of variables used as TOT proxies for timewalk correction is :
 1910 probe amplitude, probe TOT, corr probe TOT (those three will not be available in actual HGTD,
 1911 derived from digitized preamplifier probe pulse) and ASIC TOT, corr ASIC TOT (those two would
 1912 be available). Those that will not be available in actual HGTD are useful for debugging to obtain
 1913 lower (best) limit on performance.
 1914

1915 Probe amplitude

1916 In testbeam, we can estimate the signal amplitude from the preamplifier probe, shown on
 1917 Fig. 6.8a is a distribution of a per-event maximum of digitized preamplifier probe pulse. This is our
 1918 best estimation of signal amplitude. The application of timewalk correction is shown in Fig. 6.9
 1919 (looks the same for $\Delta T12$, so only one plot is shown). The left figure shows the smooth dependence
 1920 of the time difference with the preamplifier probe amplitude, called timewalk. The right figure
 1921 presents the same time difference after a correction with polynomial fit (subtracting ΔT fit values
 1922 in each amplitude bin). The procedure is applied for the two differences with the SiPM reference
 1923 devices, but this is redundant as they are identical up to a constant shift. The timewalk correction
 1924 for two SiPMs is not needed because it was already taken into account with CFD, so $\sigma_{\Delta T01}$ is used to
 1925 solve for timewalk corrected σ_{hybrid} is the same as in the uncorrected case. $\sigma_{\Delta T02}^{corr}$ obtained by fitting
 1926 with a Gaussian $\Delta T02$ distribution after correction. Similarly, for $\Delta T12$. After this correction, the
 1927 contribution of the timewalk to the resolution is negligible.

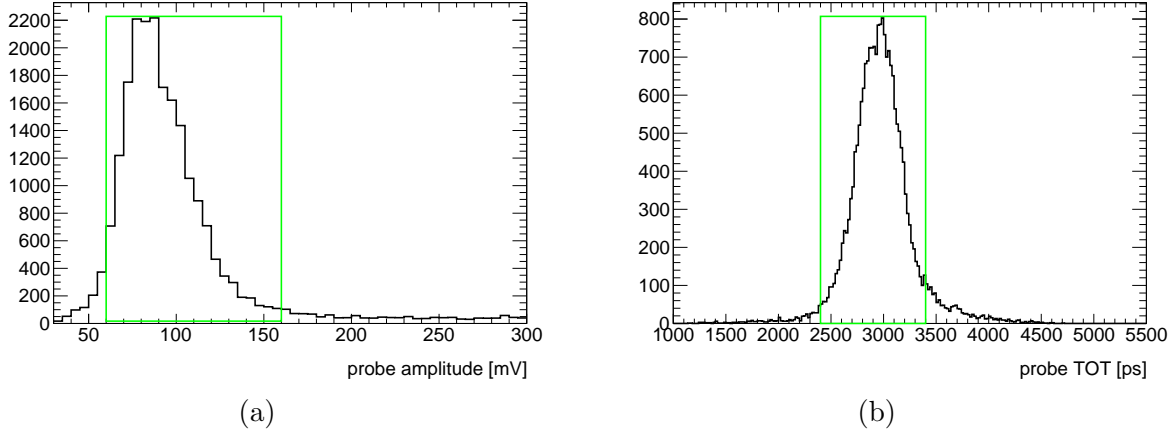


FIGURE 6.8 – For a single TZ channel, room temperature : (a) preamplifier probe amplitude distribution. (b) Preamplifier probe TOT distribution (single TZ channel, room temperature). For both (a) and (b), the region marked with green is used to extract time resolution.

1928 Probe TOT

1929 Probe TOT is shown on Fig. 6.8b - time during which probe signal is above a certain threshold
 1930 which we choose during processing. The dependence of probe TOT against probe amplitude is
 1931 shown in Fig. 6.10a. Probe TOT resolution in probe amplitude bins is shown in Fig. 6.12b.

1932 Fig. 6.11 is showing timewalk dependence of $\Delta T02$ as function probe TOT on the left plot,
 1933 together with residual timewalk dependence as function of the same variable, on middle plot.

1934 ASIC TOT

1935 ASIC TOT is shown on Fig. 6.13 , composed of coarse TOT with nominal 160 ps quantization
 1936 step (TOTC LSB) and fine TOT with 40 ps LSB as $TOT[ps] = TOTC * 160 - TOTF * 40$. Nominal
 1937 values of TOT LSBs are used for simplicity, and because the resolution obtained is independent of
 1938 absolute TOT value - only relation with TOA is relevant. The dependence of ASIC TOT on probe
 1939 amplitude is shown in Fig. 6.15a , where the TOT plateau can be seen for a wide range of values
 1940 in the probe tail. However, in a region where most events are, TOT is reasonably linear. TOTF is
 1941 available, but it is probably not worth having it : Fig. 6.12a shows that TOT resolution is larger
 1942 than TOTF bin (40ps)

1943 Fig. 6.14 is showing timewalk dependence of $\Delta T02$ as a function ASIC TOT on the left plot,
 1944 together with residual timewalk dependence as function of the same variable, on middle plot.

1945 TOA-TOT coupling correction and corr ASIC TOT

1946 Sometimes, the result obtained after timewalk correction is not the best possible result because
 1947 the TOA-TOT coupling mentioned above and shown in Fig. 6.5a is still contributing. It is possible
 1948 to introduce a new variable, let us call it corr TOT (TOT corrected for coupling), which is flat as a
 1949 function of TOA . Fig. 6.16 shows on the left TOA-TOT histogram together with the mean value
 1950 of TOT in each TOA bin.

1951 In ATLAS, correction of the timewalk only will be possible through the TOT information.
 1952 However, as shown in Fig. 6.5a, the TOT is showing a variation with the TOA which will be
 1953 a limitation to the timewalk correction. Consequently, this dependence should first be corrected
 1954 and a new variable corr TOT is introduced. Fig. 6.16 show this dependence before and after a

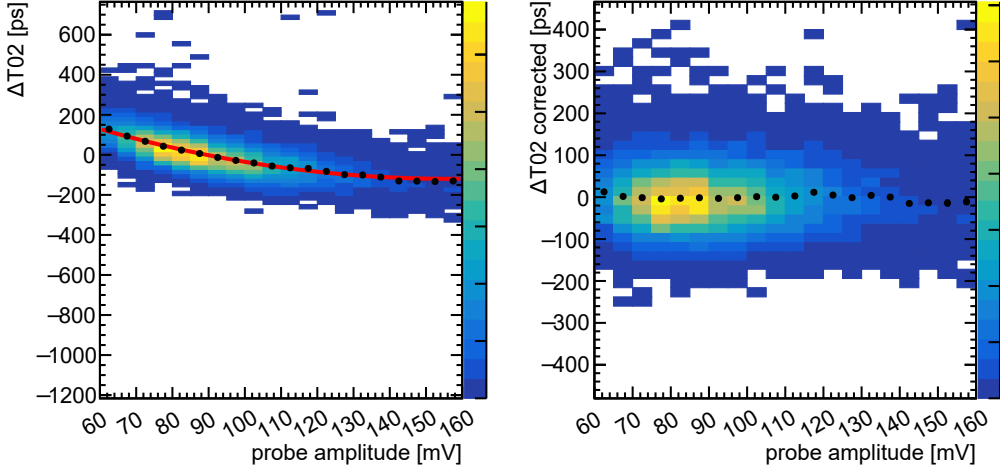


FIGURE 6.9 – Distribution of the time difference (ΔT mean shifted to zero) between the quartz+SiPM system ($\equiv 0$ in ΔT) and hybrid ($\equiv 2$ in ΔT) as a function of the preamplifier probe amplitude (left) before timewalk correction, the red line is a fit used to perform the timewalk correction with probe amplitude (right) after timewalk correction using fit shown on (left). In both plots, the dots correspond to the mean value of the ΔT distribution.

1955 bin to bin correction. After correction a TOT value is centered around 0 in all TOA bins², as
 1956 shown on the right plot of Fig. 6.16. corr TOT obtained in this way is then used to perform
 1957 timewalk correction, just like it was done above with preamplifier probe amplitude. Fig. 6.17 is
 1958 showing timewalk dependence of ΔT_{02} as a function corr ASIC TOT on the left plot, together
 1959 with residual timewalk dependence as function of the same variable, on middle plot.

1960 ASIC TOT corr resolution as a function of probe amplitude is improved compared to the original
 1961 ASIC TOT, as shown in Fig. 6.12a. The distribution from which resolution is obtained is shown
 1962 in Fig. 6.15b.

1963 Corr probeTOT

1964 Corr probe TOT is the transformation of probe TOT, used because probe TOT, similarly to
 1965 ASIC TOT, is not flat as a function of TOA (which is consistent). Comparison of corrected probe
 1966 TOT and original probe TOT resolutions in probe amplitude bins is shown in Fig. 6.12b and
 1967 corrected probe TOT resolution is better - distribution from which resolution is obtained is shown
 1968 on Fig. 6.10b.

1969 Fig. 6.18 is showing timewalk dependence of ΔT_{02} as a function corr probeTOT on the left
 1970 plot, together with residual timewalk dependence as function of the same variable, on middle plot.

1971 Results

1972 Three resulting corrected ΔT s with probe amplitude are shown in Fig. 6.7 together with their
 1973 width in red. It can be seen that the width of both ΔT_{02} and ΔT_{12} are significantly reduced
 1974 compared to uncorrected cases. Three corrected widths, as before, allow to obtain the individual
 1975 device resolution through Eq. 6.1. For the correction using probe amplitude, $\sigma_{hybrid} = 38.9 \pm 0.9$ ps,
 1976 so the quadratic improvement obtained from timewalk correction here is 63 ps (expressed in this
 1977 way in order to obtain $\sigma^{timewalk}$ contribution from $\sigma^{uncor} = \sigma^{cor} \oplus \sigma^{timewalk}$). The gain will be
 1978 smaller while using ASIC-only information. Correction with other variables will be below. The

2. the value around which TOT is centered is irrelevant and can be anything; 0 used is a natural choice

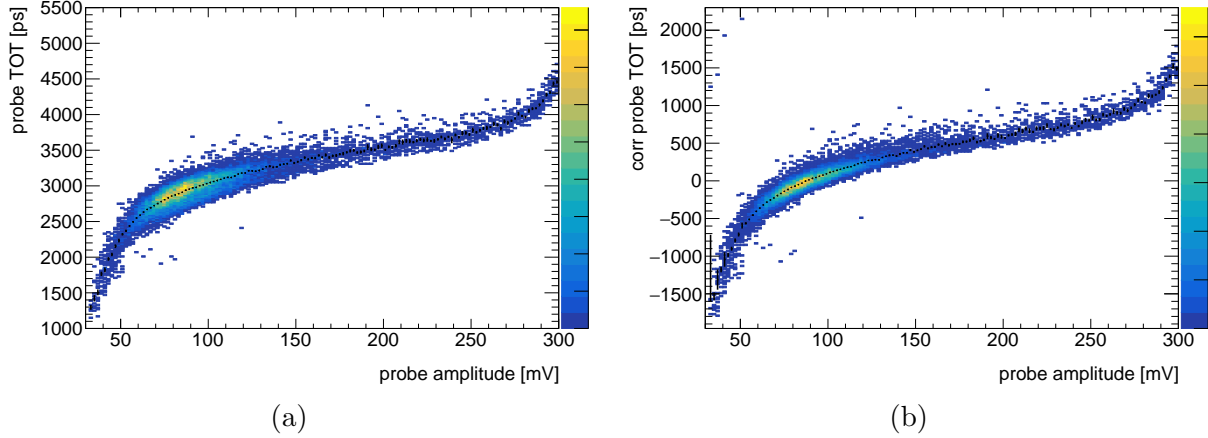


FIGURE 6.10 – (a) probe TOT against preamplifier probe amplitude. The threshold used for probe TOT calculation is 27.7 mV. (b) corrected probe TOT against preamplifier probe amplitude.

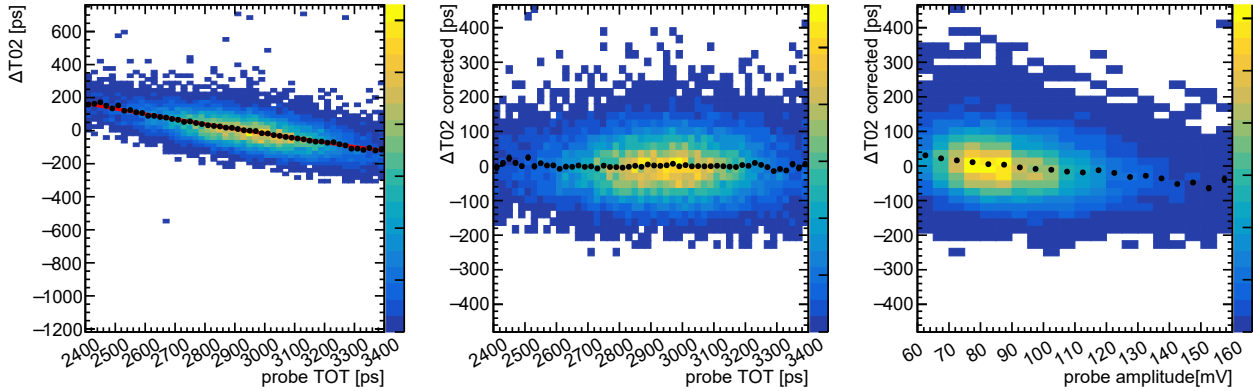


FIGURE 6.11 – Distribution of the time difference (ΔT mean shifted to zero) between the quartz+SiPM system ($\equiv 0$ in ΔT) and hybrid ($\equiv 2$ in ΔT) (left) as a function of the preamplifier probe TOT, before timewalk correction, the red line is a fit used to perform the timewalk correction with preamplifier probe TOT (middle) as a function of the preamplifier probe TOT, after timewalk correction with preamplifier probe TOT (fit shown on (left) is used) (right) as a function of the preamplifier probe amplitude after timewalk correction with preamplifier probe TOT.

timewalk correction using the ASIC information (TOT) is not as efficient and will be discussed below.

The expectation is that probe amplitude correction will give the best result; ASIC TOT and probe TOT are hopefully similar (the same applies to corr ASIC TOT and corr probe TOT). Right plots of Fig. 6.11, Fig. 6.14, Fig. 6.17, Fig. 6.18 show a dependence of $\Delta T02$ after correction as a function of probe amplitude - this slope is an estimation of residual timewalk, which was not corrected away. It can be seen that residual timewalk is reduced on corr probe TOT compared to probe TOT correction and on corr ASICTOT compared to ASIC TOT correction. Also, the residual slope is similar between probe TOT and ASIC TOT ; and between corr probe TOT and corr ASIC TOT corrections.

Obtaining time resolution in a way described in Sec. 6.2 with different timewalk correction variables gives results shown in Table 6.2. For probe TOT, the threshold of 27.7 mV was used to compare with ASIC TOT . Event selection for particular variables does not rely on other timewalk correction variables ; for example, in order to obtain resolution with ASIC TOT correction, cut is

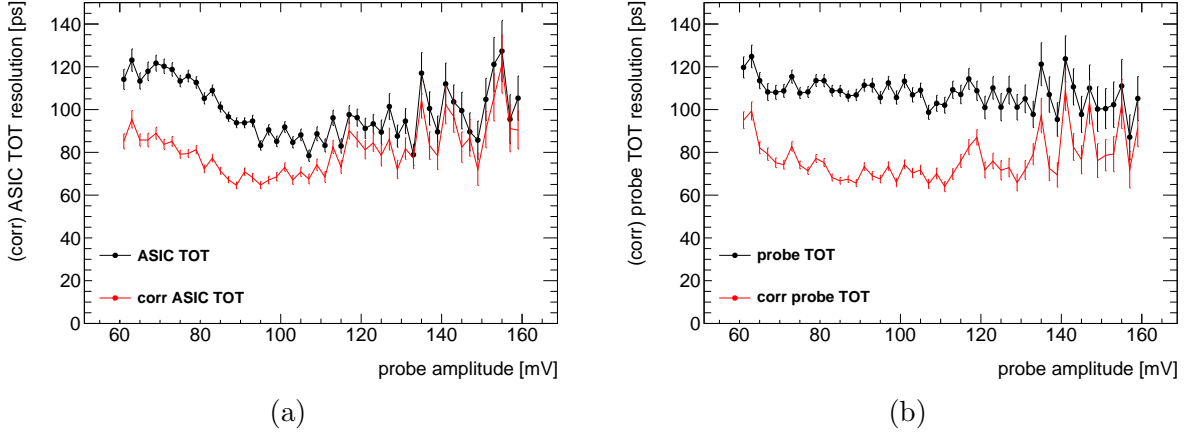


FIGURE 6.12 – (a) ASIC TOT and corr ASIC TOT resolutions as a function of probe amplitude (b) probe TOT and corr probe TOT resolutions as a function of probe amplitude. Threshold used for probe TOT is 27.7 mV. Both (a) and (b) obtained obtained from RMS of their distributions in corresponding preamplifier probe amplitude bin.

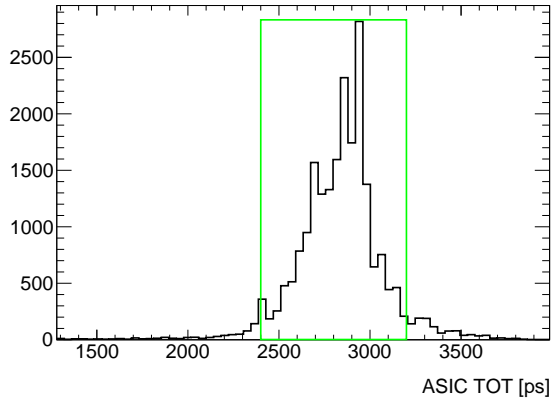


FIGURE 6.13 – ASIC TOT distribution (single TZ channel, room temperature). The region marked with green is used to extract time resolution.

1993 done by selecting the core of TOT distribution (marked by green box shown on Fig. 6.13) where it
 1994 is roughly linear (shown on Fig. 6.15a) and plateau is rejected. The same is done with other “TOT”
 1995 variables - the green box on Fig. 6.8a (Fig. 6.8b) shows the core of probe amplitude (probe TOT)
 1996 distribution.

1997 Looking at uncorrected and corrected resolution columns in Table 6.2, it can be seen that
 1998 despite different selection cuts (selections for uncorrected resolutions are not relying on variables
 1999 that will not be used later for correction), we start more or less from the same value. The biggest
 2000 gain from timewalk correction is achieved with the probe amplitude, which is expected. The results
 2001 of the two types of TOT (probe and ASIC) are similar, demonstrating that the TDC works well.
 2002 Correcting for TOA-TOT dependence and using corr probe TOT and corr ASIC TOT gives similar
 2003 gain for both probe and ASIC TOT and equals to in quadrature to ≈ 24 ps (75.9-51.3 for probe
 2004 TOT).

2005 The best resolution obtained with ASIC-only information (which we are mostly interested in) is
 2006 45.7 ps (which can be compared to target time resolution 35 ps), obtained after timewalk correction
 2007 with corr ASIC TOT. As a baseline, one can look at probe amplitude correction that gives 38.9 ps.
 2008 Right plot of Fig. 6.17 displays residual slope, seen by probe but left uncorrected by corr ASIC

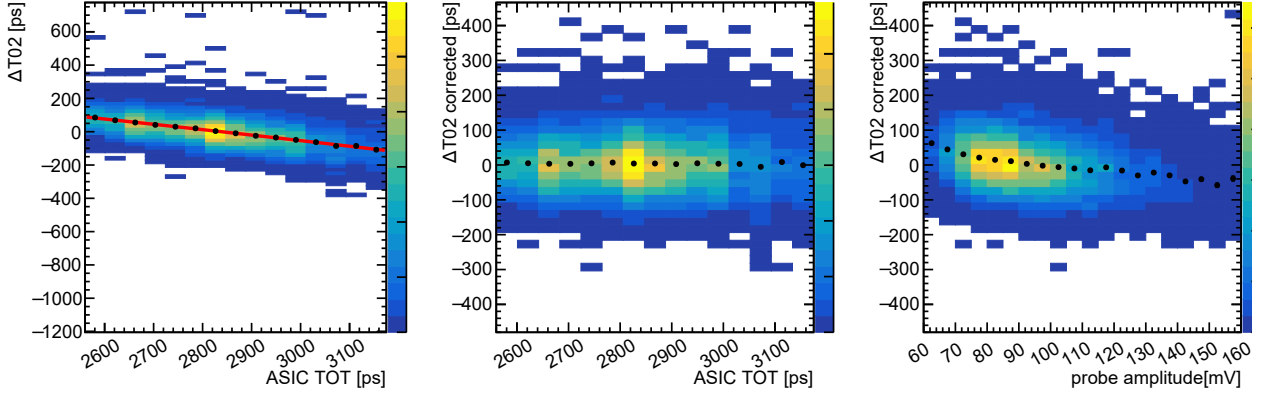


FIGURE 6.14 – Distribution of the time difference (ΔT mean shifted to zero) between the quartz+SiPM system ($\equiv 0$ in ΔT) and hybrid ($\equiv 2$ in ΔT) (left) as a function of the ASIC TOT, before timewalk correction, the red line is a fit used to perform the timewalk correction with ASIC TOT (middle) as a function of the ASIC TOT, after timewalk correction with ASIC TOT (fit shown on (left) is used) (right) as a function of the preamplifier probe amplitude after timewalk correction with ASIC TOT.

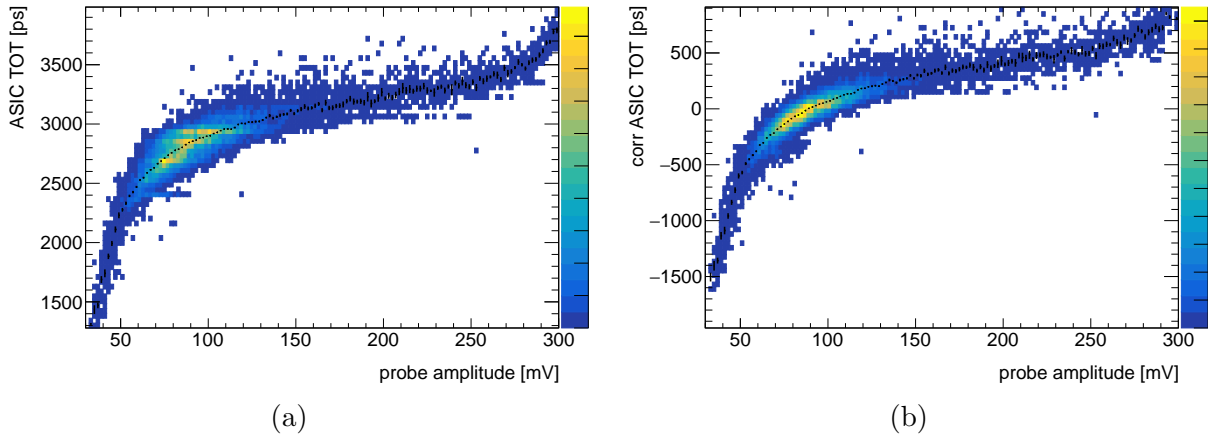


FIGURE 6.15 – (a) ASIC TOT against preamplifier probe amplitude (b) corrected ASIC TOT against preamplifier probe amplitude.

2009 TOT.

2010 The $TOA > 1600$ column in Table 6.2 adds to selections described above one that selects region
2011 where TOA-TOT is flat, as shown on Fig. 6.5a $TOA > 1600$ ps result for probe TOT correction is
2012 close to corr probe TOT result without $TOA > 1600$ ps, cut, showing that correction for TOA-TOT
2013 dependence can partially compensate for TOA-TOT dependence. However, there is still a gain in
2014 going from probe TOT to corr probe TOT when the $TOA > 80$ cut is applied in both cases. The
2015 same is observed for ASIC TOT, corr ASIC TOT. Both corr ASIC TOT and corr probe TOT with
2016 $TOA > 1600$ ps cut cannot reach probe amplitude correction result.

2017 Once data is taken, we cannot check the resolution after ASIC TOT correction with different
2018 ASIC thresholds. However, with comparable thresholds, ASIC TOT and probe TOT corrections
2019 give similar results, as was shown in Table 6.2. In this way, we can simulate the result with a different
2020 threshold by using probe TOT and varying threshold for its calculation. Probe TOT threshold used
2021 is to be compared with MPV of probe amplitude distribution (≈ 80 mV). Resolution (after probe
2022 TOT timewalk correction) depending on threshold is shown on Fig. 6.19 together with result of one

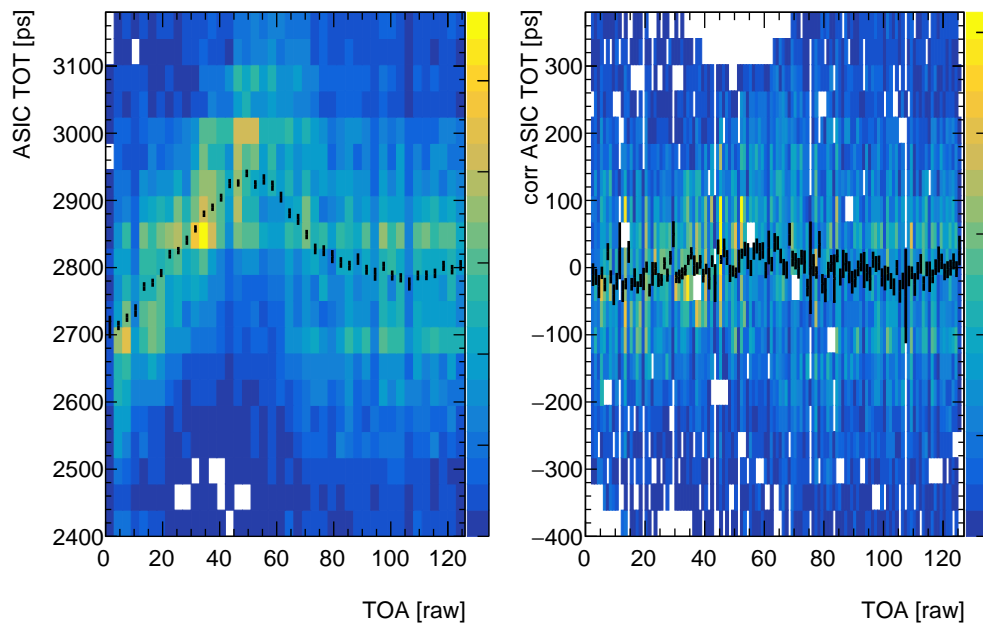


FIGURE 6.16 – (left) ASIC TOT dependence on TOA. (right) corr ASIC TOT as a function of TOA, obtained with subtraction of average ASIC TOT in each TOA bin from ASIC TOT shown in (left).

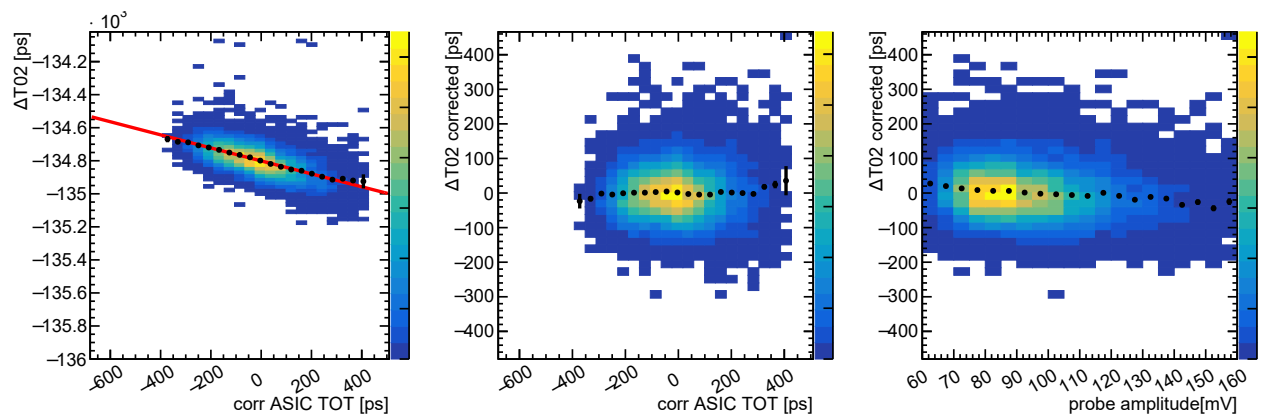


FIGURE 6.17 – Distribution of the time difference (ΔT mean shifted to zero) between the quartz+SiPM system ($\equiv 0$ in ΔT) and hybrid ($\equiv 2$ in ΔT) (left) as a function of the corr ASIC TOT, before timewalk correction, the red line is a fit used to perform the timewalk correction with corr ASIC TOT (middle) as a function of the corr ASIC TOT, after timewalk correction with corr ASIC TOT (fit shown on (left) is used) (right) as a function of the preamplifier probe amplitude after timewalk correction with corr ASIC TOT.

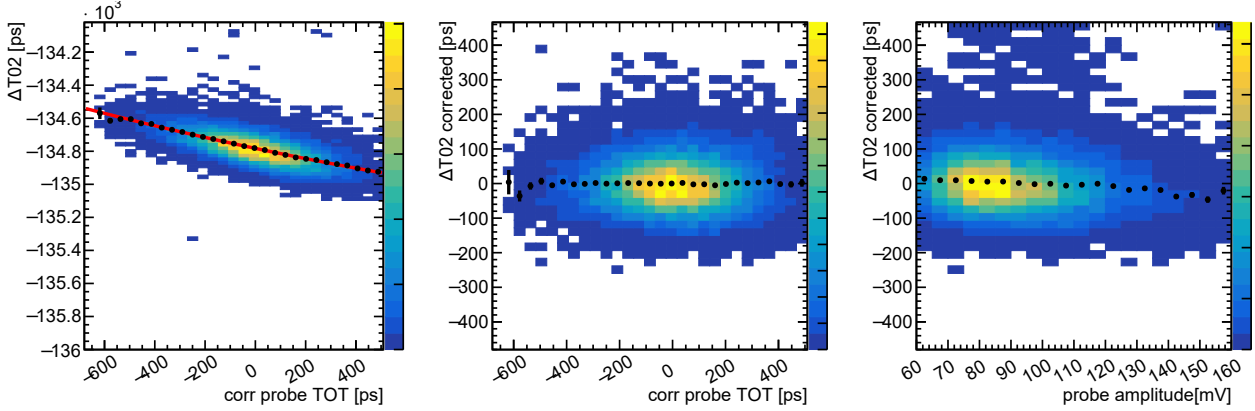


FIGURE 6.18 – Distribution of the time difference (ΔT mean shifted to zero) between the quartz+SiPM system ($\equiv 0$ in ΔT) and hybrid ($\equiv 2$ in ΔT) (left) as a function of the corr Probe TOT, before timewalk correction, the red line is a fit used to perform the timewalk correction with corr Probe TOT (middle) as a function of the corr Probe TOT, after timewalk correction with corr Probe TOT (fit shown on (left) is used) (right) as a function of the preamplifier probe amplitude after timewalk correction with corr Probe TOT.

Timewalk correction variable	Uncorrected resolution [ps]	Corrected resolution [ps]	Corrected resolution [ps], TOA>1600 ps
probe amplitude	73.5	38.9	37.0
probe TOT	75.9	51.3	46.6
corr probe TOT	75.9	45.7	42.3
ASIC TOT	76.7	51.8	44.1
corr ASIC TOT	76.7	45.7	42.8

TABLE 6.2 – ALTIROC1+LGAD hybrid time resolutions obtained after timewalk correction with different variables, with one TZ ASIC channel (number 11) of batch 1901. Uncertainty on all resolutions is ≈ 1 ps. Selections to obtain uncorrected resolution is not relying on variables that will not be used for timewalk correction.

2023 measurement with ASIC TOT correction - two timewalk correction methods agree if same threshold
 2024 is used. Also, in Fig. 6.20 , a possible explanation is shown as to why resolution increases with a
 2025 lower threshold : amplitude (difference between maximum of Y axis appearing near $TOA \approx 70$ and
 2026 minimum appearing near $TOA \approx 0$) of TOA-TOT coupling “wave“ (seen with probe TOT where
 2027 it’s easy to vary threshold in software) decreases.

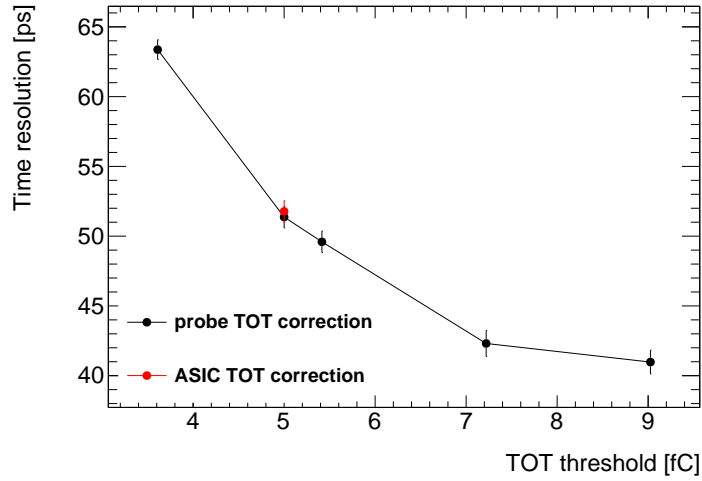


FIGURE 6.19 – Time resolutions obtained with probe TOT correction and different thresholds to calculate probe TOT. ASIC TOT correction result with a threshold of batch 1901 is shown for comparison.

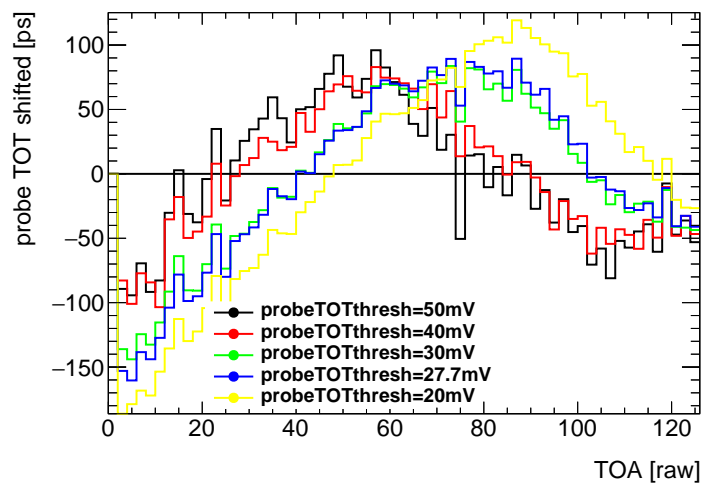


FIGURE 6.20 – Mean preamplifier probe TOT (shifted to be centered around 0) against ASIC TOA shown for different probe TOT thresholds (values used are written in legend).

6.4.5 Amplitude dependence

The time resolution is expected to depend on the signal amplitude. Fig. 6.21 shows this dependence (after timewalk correction with probe amplitude) as a function of the probe amplitude. It can be seen that the resolution has a minimum where the probe amplitude is near its MPV, and the resolution is degraded when going away from MPV. This behavior comes from the LGAD itself (not from ASIC and not from the connection between the ASIC and the LGAD, not from trigger setup) as explained in [25],[97] : “The events in the high tail of the Landau are mostly due to the presence of localized clusters of ionization. Given that the ionization is very non-uniform for these events, their temporal resolution is worse than that of signals with an amplitude around the Landau most probable value“. In low tail $\sigma_{jitter} = \frac{t_{rise}}{S/N}$ is also contributing to degradation since S (amplitude) is lower. Similar dependence is observed when correcting with two types of TOT available in bins of TOT, as shown in Fig. 6.22a and Fig. 6.22b. The minimum doesn’t precisely coincide with the minimum of the amplitude proxy because relation between amplitude and probe TOT, ASIC TOT is not precisely linear (see Fig. 6.10a, Fig. 6.15a) - e.g. higher ASIC TOT value contains a mixture of probe amplitude values and establishing direct correspondence from probe amplitude distribution maximum to probe/ASIC TOT distribution maximum is not possible. Finally, Fig. 6.21 also shows the time resolution obtained with the probe amplitude and two types of TOT where all are plotted in bins of the probe amplitude : it can be seen if we select the probe amplitude peak, all corrections give similar result. However, this is not the test to compare the timewalk correction methods because in each bin, especially in small bins near the amplitude peak : the timewalk effect envelope is small, and the correction does not bring much difference.

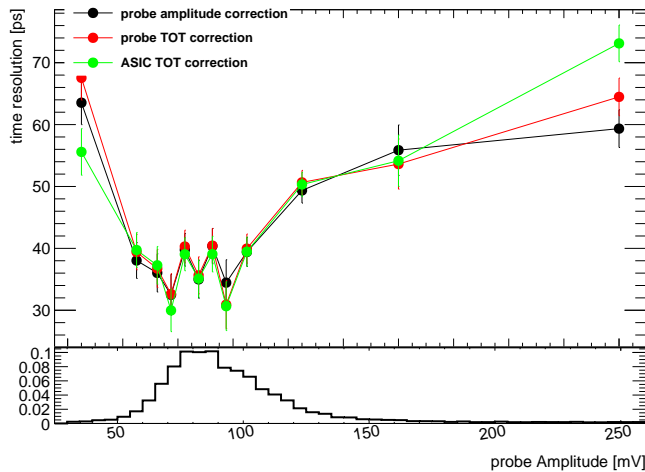


FIGURE 6.21 – (top) Time resolution obtained after correction with preamplifier probe amplitude, preamplifier probe TOT (with a 27.7 mV threshold), and ASIC TOT, all plotted against preamplifier probe amplitude. (bottom) Normalized preamplifier probe amplitude distribution.

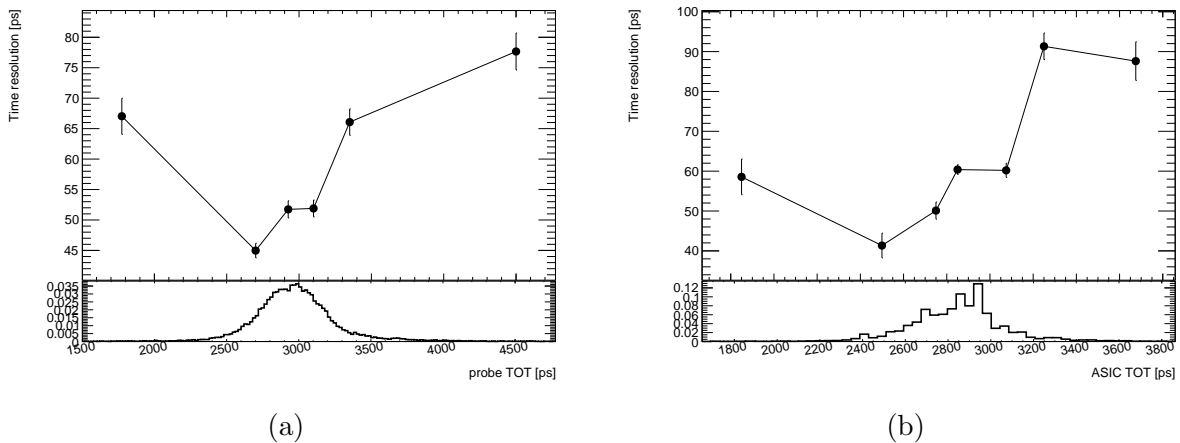


FIGURE 6.22 – Time resolution obtained (a) after correction with preamplifier probe TOT (27.7 mV threshold) plotted against preamplifier probe TOT. On the bottom, the normalized preamplifier probe TOT distribution is shown. (b) after correction with ASIC TOT plotted against ASIC TOT. On the bottom, the normalized ASIC TOT distribution is shown.

2049 6.4.6 Impact of TDC DNL

2050 It was observed during testbeam that the TOA distribution shown in Fig. 6.23 is not uniform.
 2051 It is expected to be uniform because the beam is not synchronized with the data taking, and
 2052 particles can hit the hybrid at any time within the measurement window with equal probability.
 2053 Then, the TOA non-uniformity is interpreted as a variation of the TOALSB value in each bin of
 2054 TOA - instead of nominal ≈ 20 ps LSB, we have in each bin different LSB (this is due to the
 2055 differential non-linearity of the TDC and also seen in the testbench). The bin with a population
 2056 larger (smaller) than the average means the LSB is larger (smaller) than the average LSB .

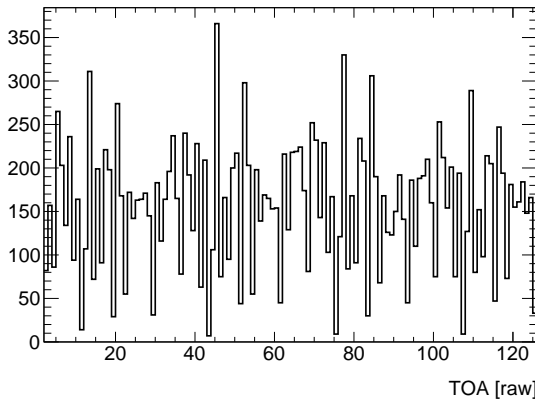


FIGURE 6.23 – TOA distribution (single TZ channel, room temperature), non-uniformity of which is attributed to non-uniform TOA LSB.

2057 The impact of having non-uniform LSB on time resolution was investigated. To obtain TOALSB
 2058 in each TOA bin, it is assumed that the mean TOA value corresponds to TOALSB measured
 2059 in testbench (for the configuration and the pixel considered, it is 22.5 ps), then LSB_i is obtained
 2060 by the ratio of the number of events in a particular bin to the mean TOA value. The re-
 2061 sulting TOALSB distribution is shown in Fig. 6.24a. Instead of using a uniform LSB for each
 2062 bin as done previously (multiplying TOA [raw] count i by TOALSB value measured in test-
 2063 bench : $TOA_{uniform}[ps] = i \times TOALSB$), the TOA can be computed using the real bin size
 2064 as $TOA_{non-uniform}[ps] = \sum_{i=1}^{TOA} TOALSB_i$. Fig. 6.24a shows real bin sizes. Fig. 6.24b shows this
 2065 new TOA corrected from the differential non-linearity as a function of the TOA assuming a constant
 2066 LSB . Applying the timewalk correction with the probe preamplifier amplitude as explained before
 2067 and using the corrected TOA, the extracted hybrid time resolution is 39.2 ps, quite similar to the
 2068 time resolution obtained assuming a constant TOALSB, demonstrating that in ALTIROC1 the
 2069 differential non-linearity has a negligible impact on the final resolution.

2070 6.5 Resolution obtained with VPA preamplifier

2071 Some data were taken with the VPA preamplifier to compare it with TZ; however, it was
 2072 known already from testbench measurements and [16] that VPA TOT is problematic : TOT does
 2073 not scale proportionally with the injected charge, which is shown with testbeam data (batch 2300
 2074 from Table 6.1) on Fig. 6.25. Also, Fig. 6.26 shows VPA TOT distribution. The TOT measure-
 2075 ments are perturbed by the couplings at the input of the preamplifiers, and the VPA TOT is more sensitive
 2076 since the VPA pulse is longer than the TZ pulse. VPA TOT cannot be used to correct the time-walk
 2077 effect, but this is the only reason to measure TOT. VPA TOT (Fig. 6.25) has a core of distribution
 2078 at ≈ 10000 ps (value depends on the threshold), but in addition, several other peaks are present at
 2079 ≈ 6000 ps, ≈ 11000 , ≈ 12000 ps which was not the case for TZ TOT (Fig. 6.15a)

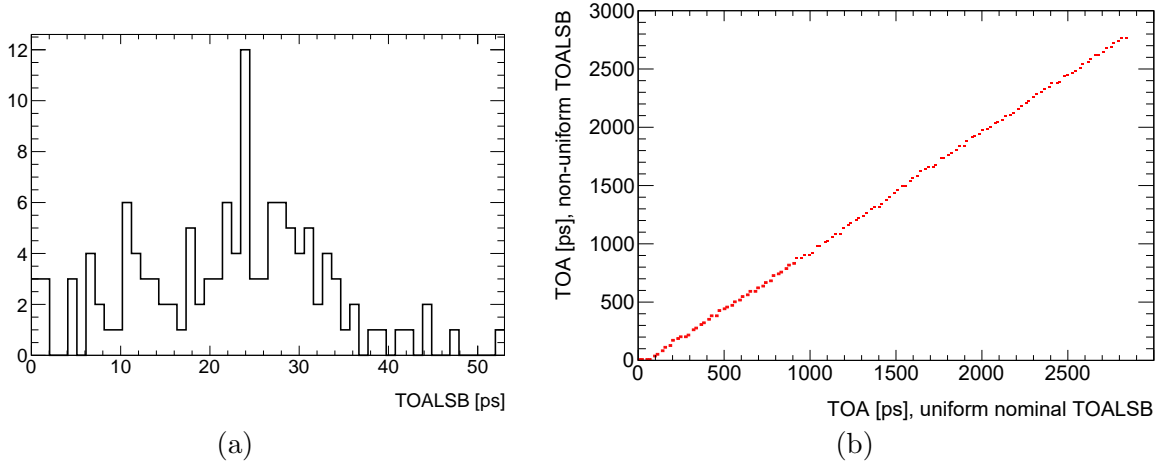


FIGURE 6.24 – (a) Bin TOALSB values obtained from TOA non-flatness (Fig. 6.23). (b) TOA obtained with non-uniform LSB against usual TOA obtained under the uniform TOALSB value assumption.

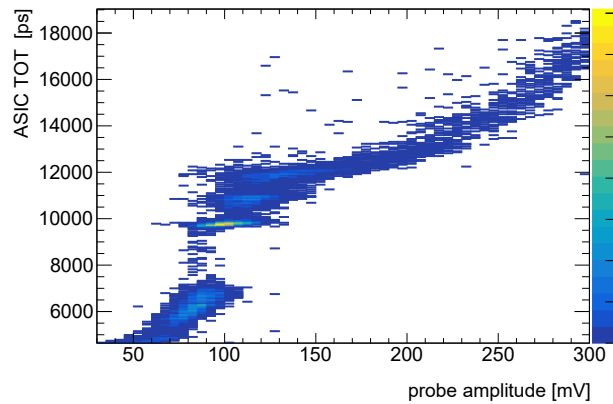


FIGURE 6.25 – VPA ASIC TOT as a function of probe amplitude.

2080 Due to a problem with VPA TOT, only timewalk correction with probe amplitude was per-
 2081 formed in two TOT regions shown with green and red boxes in Fig. 6.26 - results are shown in
 2082 Table 6.3, and they are worse than the TZ result, even worse than the TZ correction with ASIC
 2083 TOT .

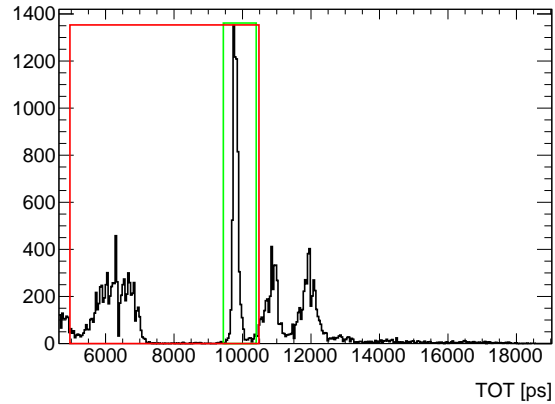


FIGURE 6.26 – VPA ASIC TOT distribution (projection of Fig. 6.25) . The regions marked with green and red boxes are used to extract time resolution.

TOT selection	Uncorrected resolution [ps]	Corrected resolution [ps]
$4640 \leq TOT \leq 10400$ (core and second largest peak)	113.9	87.9
$9440 \leq TOT \leq 10400$ (core)	81.6	76.1

TABLE 6.3 – Time resolution obtained with VPA preamplifier after timewalk correction with probe amplitude. Uncertainty on all resolutions is ≈ 1 ps.

2084 7 - ALTIROC2 testbench

2085 ALTIROC2 ASIC, first full-size prototype, was produced in 2021 and went through an intensive
2086 series of testbench measurements to characterize it - they are summarized in this chapter.

2087 7.1 LSB calibration

2088 ALTIROC2 is equipped with the TOA and TOT TDC, each providing results of their measure-
2089 ments in binary and having some LSB (see Sec. 5.5.5). Therefore, the (in)accuracy of the knowledge
2090 of the LSB can directly influence the timing performance. It will be shown later how mismeasured
2091 TOA LSB significantly degrades the timing performance in testbeam. The TOT LSB is of the least
2092 importance as TOT is only used for timewalk correction - TOT is, therefore, required to be a good
2093 proxy for amplitude, however, the value of the proportionality constant between the amplitude and
2094 TOT is of less importance. Nevertheless, for TOT LSB, just as for TOA LSB, it's good to check
2095 that the value is roughly in an expected range, which is 160 [ps] for TOT (coarse) and 20 [ps] for
2096 TOA. For TOT, the focus has been mainly on the TOT coarse calibration, as it was observed in
2097 the previous analysis that the addition of TOT fine does not improve timewalk significantly.

2098 7.1.1 Methodology

2099 There are two methods to calibrate the TOA LSB and one for TOT LSB .

2100 Using external trigger¹ both TOA and TOT LSB can be measured. The signal is injected
2101 directly at the input of the TDC, bypassing the preamplifier and discriminator. The injected signal
2102 is a square signal with both the start time (indirectly, though changing TDC clock delay) and
2103 width of this signal can be varied accurately (at each step, the output of the TDC is saved),
2104 allowing to scan both the TOA and TOT range. Delay is obtained by combining coarse (step of
2105 1562 picoseconds) and fine (step of 97 ps) steps. Width can be selected in steps of 1562 picoseconds.
2106 Fig. 7.1a shows the measured TOT as a function of the injected pulse width for one of the pixels
2107 (step of scan is larger than the minimum possible to have the faster scan). As expected, the behavior
2108 is linear, and the TOT LSB can be extracted. A 1/slope of the linear fit gives LSB . Similarly, the
2109 measured TOA is shown in Fig. 7.1b as a function of TDC clock delay. Saturated values (127 for
2110 TOA and 255 for TOTC) are removed. The requirement is to have a set of at least three widths
2111 or delay values ; otherwise, the fit is not performed. Points with anomalously high jitter have been
2112 removed, which has not happened often. The size of the measurement window is 3000 ps starting
2113 from the first good point - size of the window chosen to safely cover ASIC's ≈ 2.5 ns measurement
2114 window² and points outside of this window are removed.

2115 TOA calibration with "pulser" is the second way for TOA LSB calibration. With this method,
2116 the whole pixel chain is used instead of going directly to TDC : a certain charge is injected (high
2117 enough to avoid being close to the threshold) at the entrance of the TDC, and the TDC clock delay
2118 is varied. The comparison between two ways of obtaining TOA LSB is shown on Fig. 7.2 where it
2119 can be seen that the two methods give similar results up to a shift in the mean.

2120 All three types of LSB measurements can be done differently regarding pixel activation pattern
2121 and into which pixels injection is done. Typical injection patterns are per column or row (meaning
2122 15 pixels simultaneously receiving ext trigger or pulser signal) and per pixel (used less often than
2123 the other two because it takes too long to obtain results for all 225 channels). Pixel into which

1. external relative to the preamplifier and discriminator, not the ASIC - the signal comes from within
the ASIC

2. obtained from the product of maximum TOA value (127) and expected TOA LSB value (20 [ps])

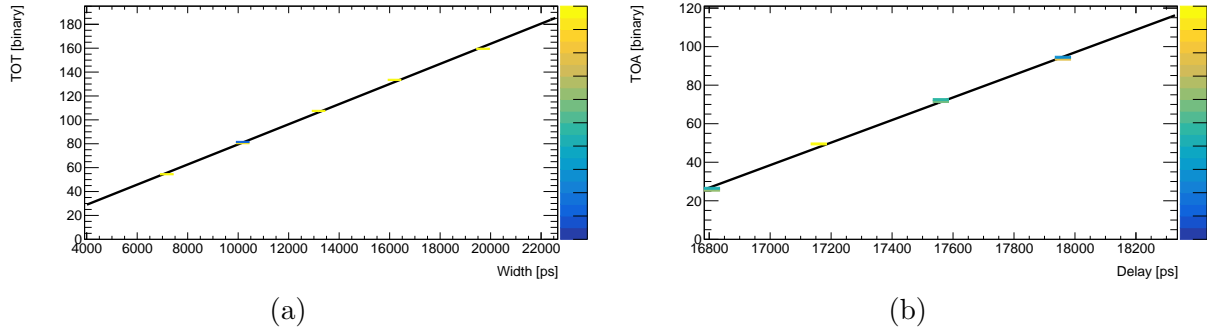


FIGURE 7.1 – (a) Example of TOT LSB extraction in testbench, one of the pixels : distribution of TOT vs injected width together with the fitted mean of the distribution. X bins of distribution are enlarged for visual purposes. The TOT LSB is given by 1/slope. (b) Example of TOA LSB extraction in testbench, one of the pixels : distribution of TOA vs TDC clock delay together with the fitted mean of the distribution. The TOA LSB is given by 1/slope.

injection is done should also be activated : typically, the whole matrix is activated (all preamplifiers, discriminators, and TDCs), but there is a possibility in the software³ developed to activate per column or some selected number of columns if there is a need to do so.

7.1.2 General trends observed

The resulting TOA and TOTC LSBs with an external trigger, measured with whole matrix activated and with injection per column , for one board, are summarized in Fig. 7.3 and Fig. 7.4 respectively. The number written in each cell is an LSB of the corresponding pixel. For the board and configuration shown (similar behavior for the other boards) it can be seen that LSB grows along the column. Overall mean value can be tuned, but the trend stays the same. Per-pixel LSB also can be tuned in principle but this was not used as one would measure the value per-pixel anyway, it's not a problem if they are different in different parts of the chip as long as one knows the value. No general trend is seen for LSB along the row. TOA and TOT LSB more or less grow together, which is shown on Fig. 7.5 : one point corresponds to one pixel, which gives TOTC and TOA LSB .

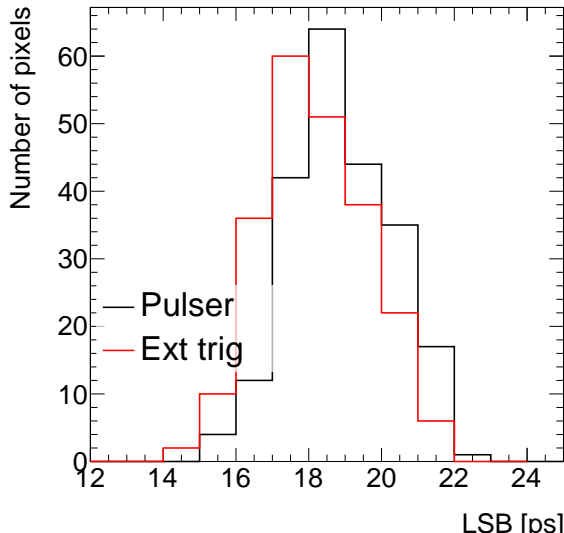
The activation pattern doesn't matter much for LSB values, as it can be seen from slope ≈ 1 on Fig. 7.6. As mentioned above, different numbers of pixels can be "turned on", which is separate from the injection pattern. Different pixel electronic read-out blocks can be chosen for the pixels selected to be activated. The plot shows the correlation of TOA LSBs injected per column, comparing the cases with

- All preamplifiers are turned on and the case with all pixels turned on
- All preamplifiers are turned on and only one column (the one into which injection is done) is turned on.

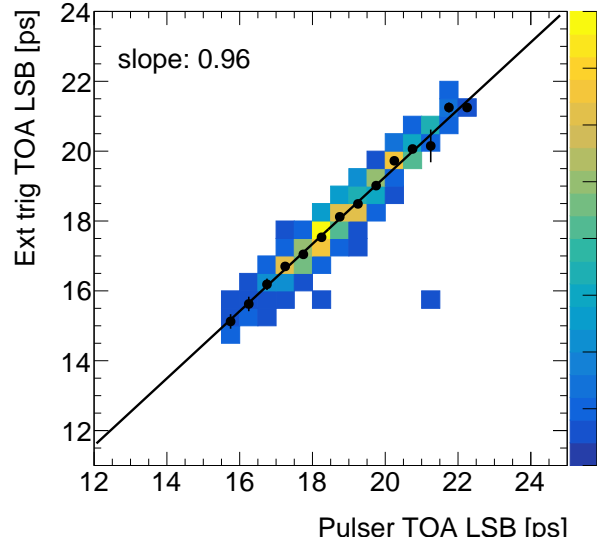
The conclusion is the same for TOTC LSB and other boards.

Doing similar measurements, now varying injection pattern instead of activation shows that, on the contrary, injection the pattern typically does matter for the LSB value, as can be seen from Fig. 7.7. Comparing slopes of correlations obtained per row, column, and pixel injection shows that only (row, pixel) combination gives the same result while others do not - suggesting that not only the number of pixels into which injection is done one at a time but also into which pixels injection is done can change the outcome of the measurement. In the future HGTD typical occupancy will reach 10% in some $|\eta|$ regions, and LSB calibration process should replicate detector conditions.

3. FADA : <https://gitlab.cern.ch/atlas-hgtd/Electronics/FADA/-/tree/master/software>



(a)



(b)

FIGURE 7.2 – TOA LSB obtained in the same configuration but in two ways : external trigger and pulser (a) TOA LSB distributions (b) correlation of the two measurements

2154 Based on measurements shown, modification to next chip iteration (ALTIROC3) were done.
 2155 Latest ALTIROC3 measurements show weaker dependence of LSB on number of pixels injected.

2156 7.1.3 More on LSB dependence on injection

2157 A more detailed investigation on LSB, depending on pixel injection, was done. Two additional
 2158 types of measurement were done.

2159 First is LSB dependence with a number of pixels from the same column that are injected :
 2160 one picks one pixel to monitor, and as a reference and injection is done into only this one pixel.
 2161 In the next step, injection is done into two pixels : one being the monitor and another one, which
 2162 can be the pixel just nearby or on another end of the column. Then, injection is done into three
 2163 pixels : one being monitored and two nearby or two on the other end of the column. More pixels are
 2164 added until the whole column is full. This was done for several pixels at the bottom of the column,
 2165 each pixel giving two curves. They are shown on Fig. 7.8. Overall, the change for both TOA and
 2166 TOT LSB is related to voltage drops along the column (effect was simulated and reproduced by
 2167 OMEGA engineers). For the TOT case, both ways of adding pixels result in the same starting
 2168 value (injection into a single pixel that is being monitored) and full column value - showing the
 2169 closure of the procedure. What happens between endpoint values is similar in having a kink at half
 2170 of the pixels (seven-eight) and a bigger slope after the kink ; the exact values within the trend are
 2171 different, though. TOT LSB value changes by $\approx 4\%$ between the endpoints. TOA LSB dependence
 2172 measurement shows less stability because the full column value does not precisely agree between
 2173 two ways of adding more pixels (same as the starting value but to a smaller degree) - there each
 2174 value in between can be assumed to be different by $19.4/19 = 2\%$. Nevertheless, the overall trend,
 2175 although less clean compared to the TOT case, is conserved and gives about $\approx 7\%$ increase of LSB
 2176 value between injection into 1 pixel and the whole column.

2177 Another type of measurement is the LSB dependence as a function of the number of columns
 2178 into which injection is done. As before, nearby or faraway columns can be added. In case we monitor
 2179 column 0 for the point with injection into three columns, this gives : (col0, col1, col2) and (col0,
 2180 col14, col13) contributing. Fig. 7.9 shows TOTC LSB dependence. In the case of TOT, it's visible

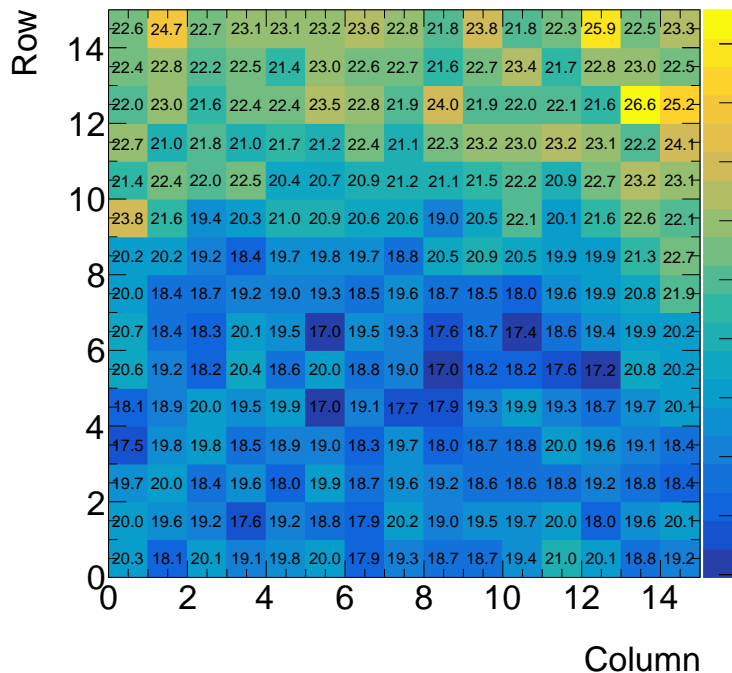


FIGURE 7.3 – ALTIROC2 15x15 pixel matrix of TOA LSB values

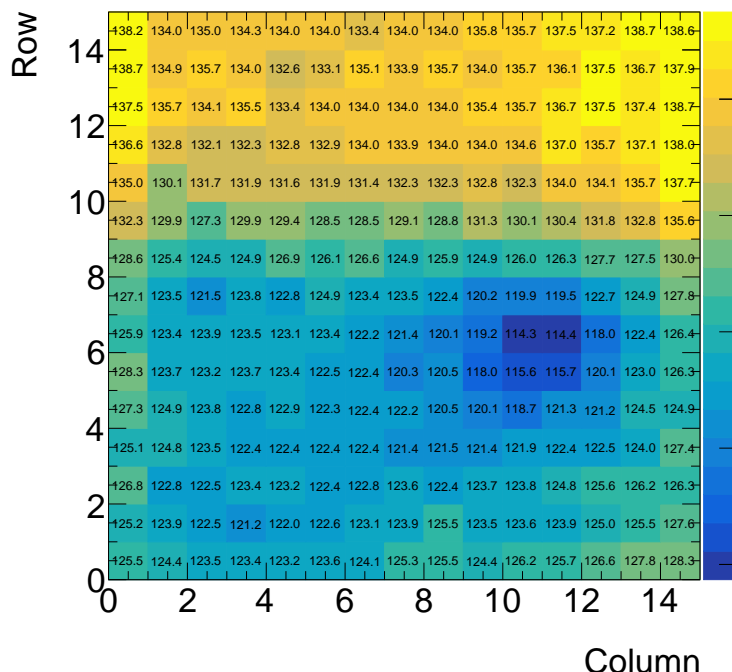


FIGURE 7.4 – ALTIROC2 15x15 pixel matrix of TOTC LSB values

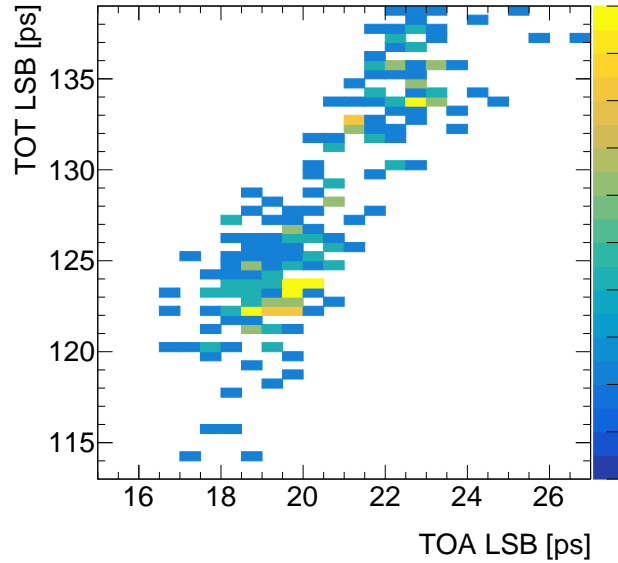


FIGURE 7.5 – Correlation of the TOTC LSB vs TOA LSB

2181 that the slope is larger when for the first \approx half of the columns when neighboring columns are
 2182 being added - contrary to the case of faraway columns being added, which gives a higher slope
 2183 after eight columns are injected simultaneously. This suggests that not only the number of columns
 2184 into which injection is simultaneously done, but also that they are close by. Similar Fig. 7.10 shows
 2185 TOA LSB dependence, where the overall endpoint-endpoint change is smaller than in the case of
 2186 TOT, and it's harder to see the slope change. As a side note, this is too much of a stress test for
 2187 the system, as the typical expected occupancy is below 10%, and under normal conditions, even
 2188 half of the pixels should not be hit simultaneously.

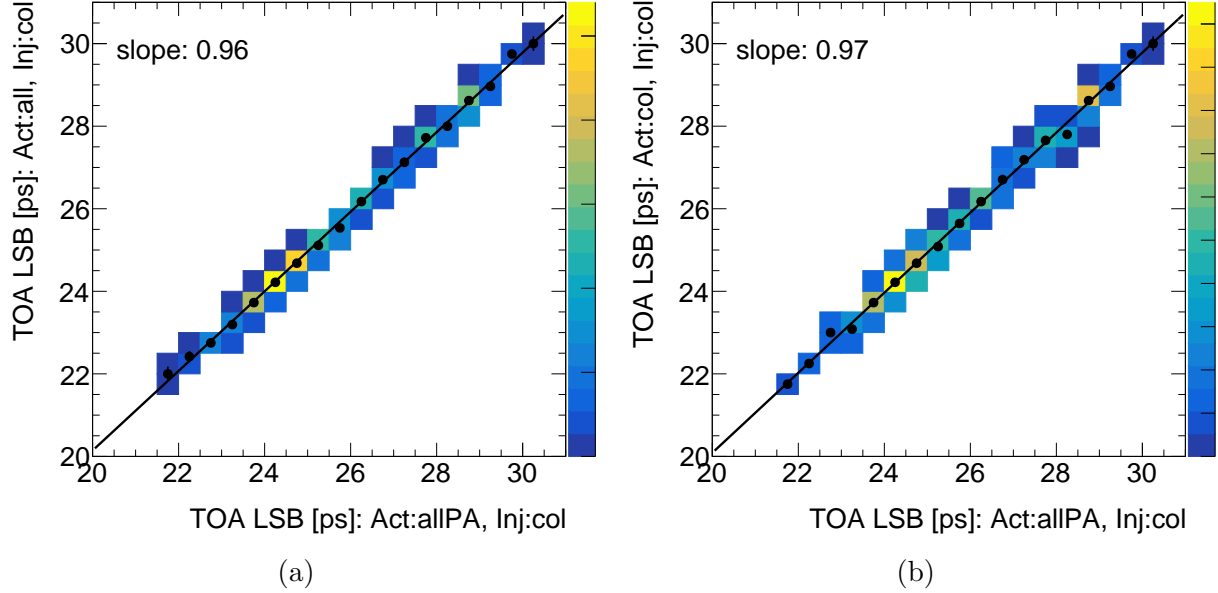


FIGURE 7.6 – Correlation of TOA LSBs with different activation patterns (a) whole matrix activated vs only preamplifiers activated (b) only one column activated vs only preamplifiers activated

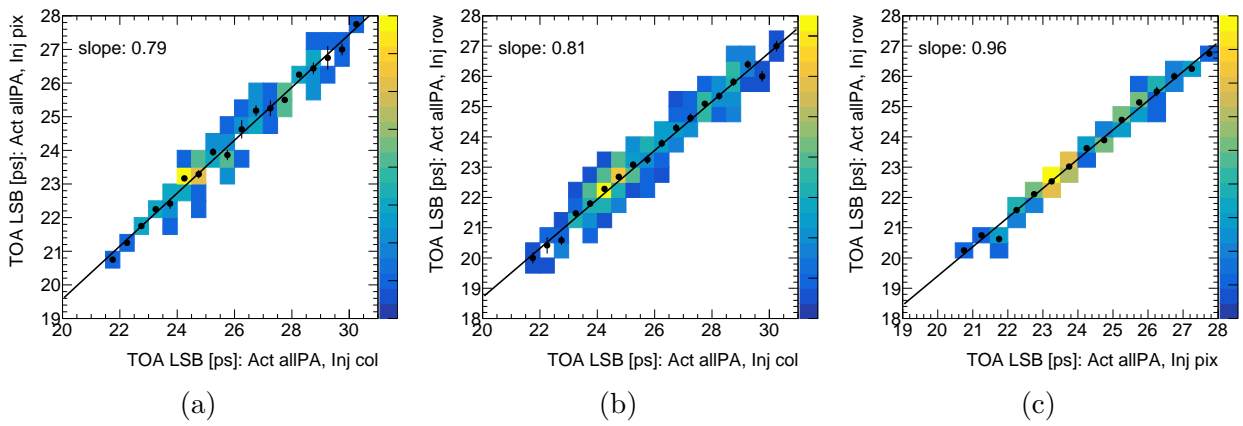


FIGURE 7.7 – Correlation of TOA LSBs with different injection patterns (a) per pixel vs per column (b) per row and vs. per column (c) per pixel vs. per row

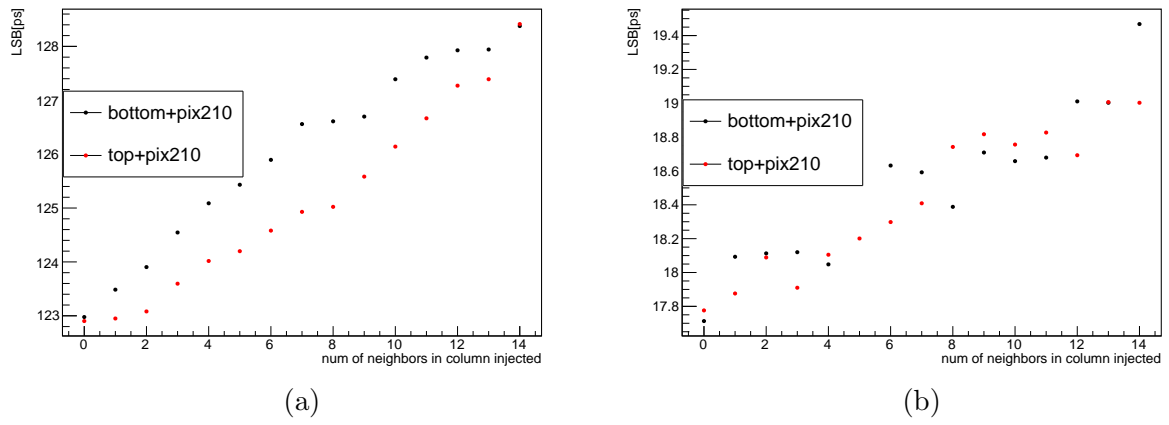


FIGURE 7.8 – LSB for one of the pixels depending on the number of pixels in the same column injected, starting from the bottom (black dots) or top (red dots) of the column (a) TOT (b) TOA

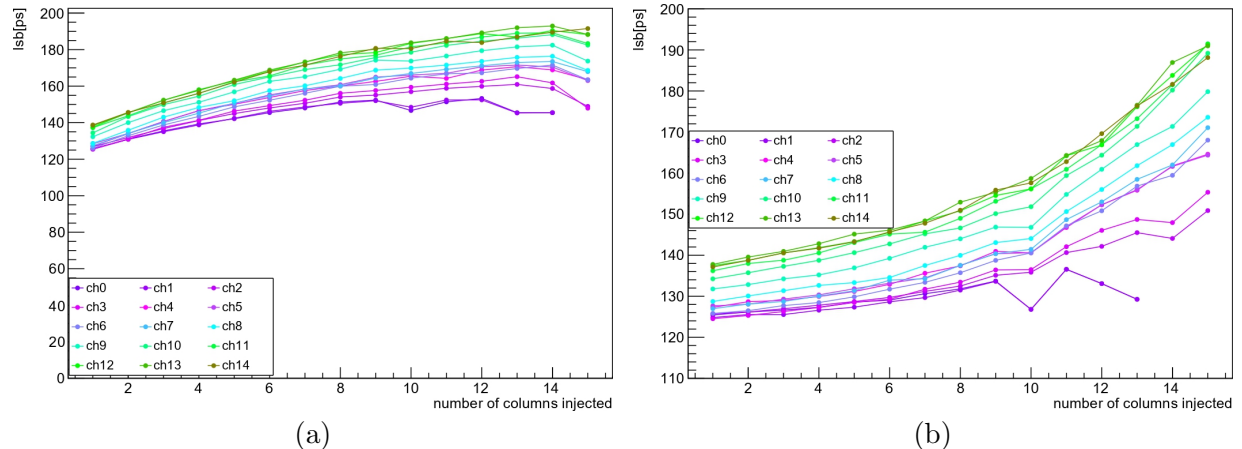


FIGURE 7.9 – LSB TOT for column 0 (a) adding nearby columns first (b) adding faraway columns first

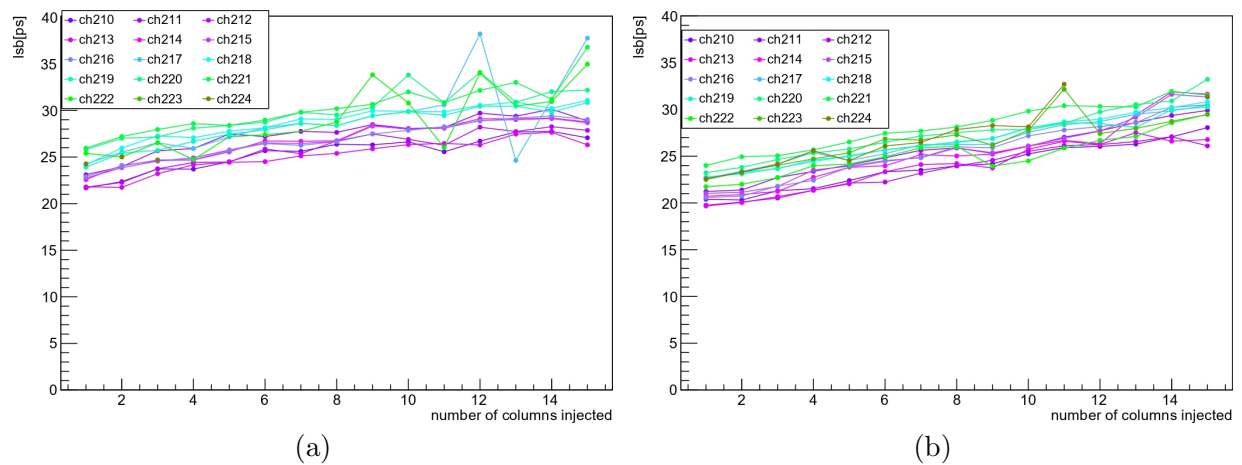


FIGURE 7.10 – LSB TOA for column 14 (a) adding nearby columns first (b) adding faraway columns first

2189 7.2 Lowest detectable charge and associated jitter

2190 According to TDR requirements, ALTIROC should be able to set a threshold as low as 2 fC .
 2191 This value was chosen to work comfortably with an LGAD signal of 4 fC (LGAD output charge
 2192 after irradiation and before replacement, as expected when writing the TDR). The tests shown
 2193 in this section were done while having TDR sensor-driven requirement in mind ; however, by the
 2194 moment of writing, this requirement was relaxed.

2195 First, the threshold must be tuned to measure the lowest detectable charge. There are two types
 2196 of thresholds : global per chip and individual per pixel. The total threshold used by pixel combines
 2197 the per-pixel threshold applied on top of the per-ASIC threshold. Both thresholds are determined
 2198 by varying the threshold for a fixed injected charge. With both thresholds known as a consistency
 2199 check, the reverse is done : the injected charge is varied for the determined lowest threshold. The
 2200 resulting charge should be close to the charge which gave the threshold.

2201 Two thresholds (global and per-pixel) and the minimal charge are determined through the
 2202 S-curve turn-on⁴ . One set of such curves for the global threshold is shown on Fig. 7.11, where
 2203 each line represents one pixel. Efficiency is the ratio between the number of pulses sent of a fixed
 2204 charge and the number of pulses seen by ASIC . For the low threshold, the ASIC pixel is triggered
 2205 by noise events, and the efficiency is 100%. When increasing the threshold, the efficiency stays at
 2206 100% is higher than the preamplifier output for this injected charge. The preamplifier noise gives
 2207 the slope of this efficiency. Two populations can be observed below and above threshold ≈ 650 ,
 2208 corresponding respectively to the columns equipped with VPA or TZ preamplifier. The value that
 2209 gives 50% efficiency gives threshold value per pixel and among them, because there should be only
 2210 one value per board, median value is chosen (not average to be less sensitive for outliers)

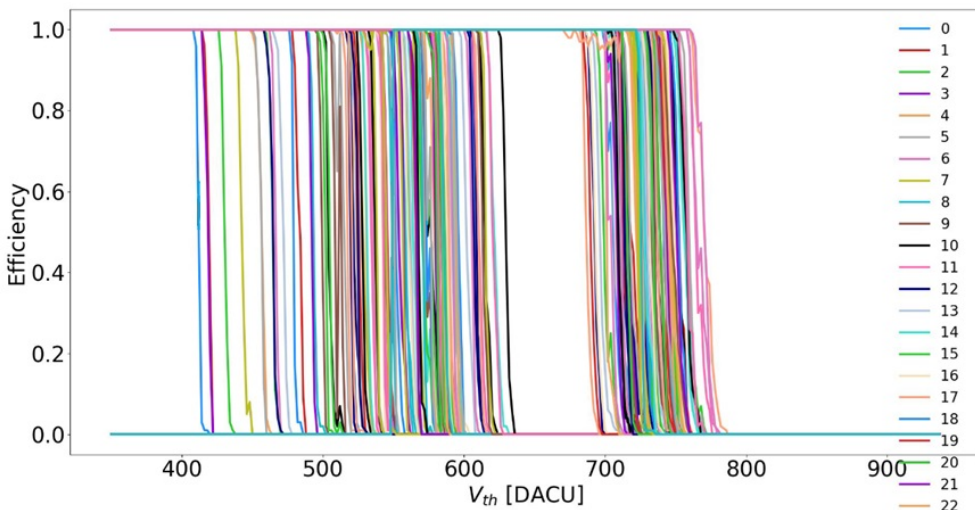


FIGURE 7.11 – Efficiency as a function of the per-ASIC threshold. Each curve represents one pixel.

2211 With the global threshold, the S-curves are quite dispersed, and to be able to trigger with each
 2212 pixel at the same lowest charge, they need to be aligned with the in-pixel threshold.

2213 Fig. 7.12 shows the S-curve as a function of the in-pixel threshold for the global ASIC threshold
 2214 560. Tuning values obtained for each pixel are shown in the same picture.

2215 Finally, the lowest detectable charge was obtained. The requirement for the threshold to be
 2216 qualified as the lowest is that

- 2217 1. Efficiency at zero charge is zero - otherwise, we're triggering on noise

4. probably should be called turn-off curves for per-ASIC thresholds

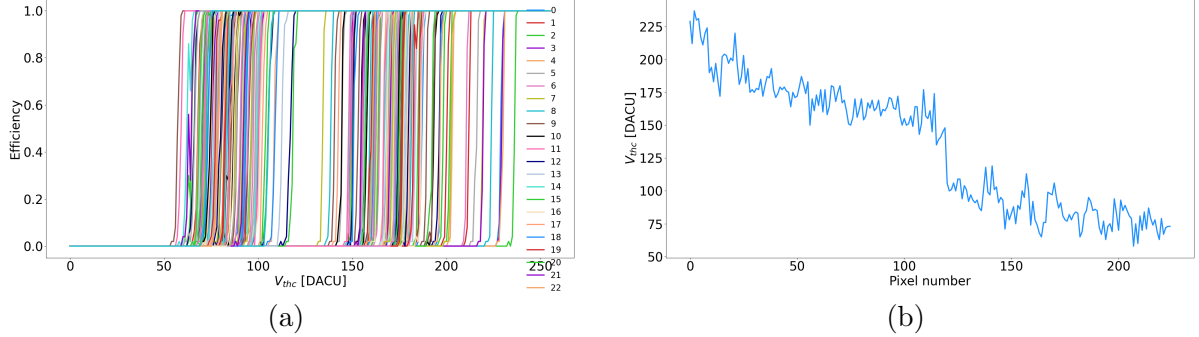


FIGURE 7.12 – (a) Per-pixel threshold S-curves curves (b) resulting threshold values per pixel

2218 2. There is no large spread between pixels or spikiness of each

2219 3. The slope is reasonably steep.

2220 Example charge s-curves are shown on Fig. 7.13 , where it can be seen that requirements 1) and 2)
 2221 are satisfied. Typically, the lowest detectable charge on this plot is $\approx 6 \text{ fC}$. Requirement 3) is also
 2222 visible to be good on the same plot, but additionally shown on Fig. 7.14 - to obtain it, turn-on
 2223 curves are fitted with an error function whose $\sigma \equiv \text{noise}$. All pixels noise has small values, and the
 2224 difference is visible in values between first eight columns and last seven columns corresponding to
 2225 VPA and TZ columns, respectively.

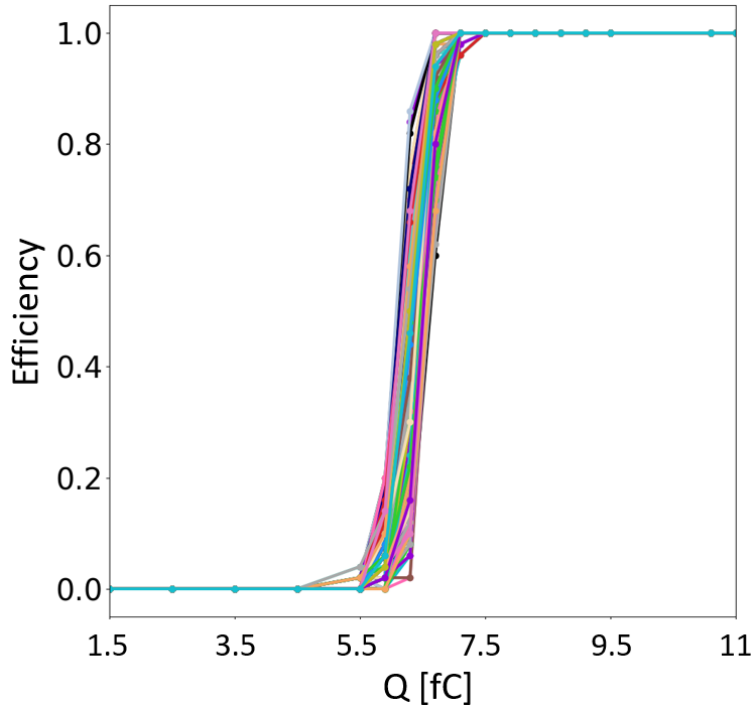


FIGURE 7.13 – Lowest detectable charge S-curves

2226 The lowest charge measurements were repeated for different boards in different configurations
 2227 - a summary of them is given in Table 7.1. It can be seen that the target 2 fC threshold was
 2228 unreachable with ALTIROC2. Between two boards without a sensor and two boards with a sensor,
 2229 the results are compatible. The higher (worst) the lowest charge with the sensor indicates that the
 2230 combination of sensor and ASIC degrades performance. In all cases, injection is done per column
 2231 (15 at the time), and when only one, same column, is activated, a better result is obtained compared

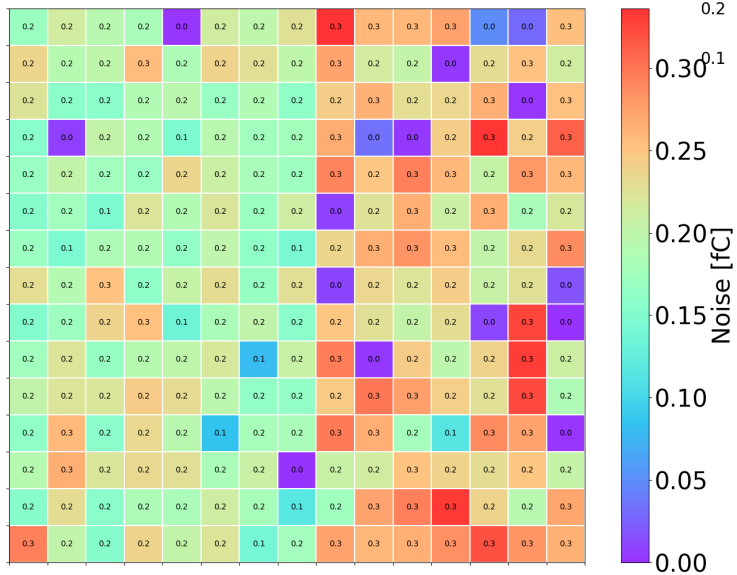


FIGURE 7.14 – Table of noise (fit function width) seen in charge scan

Board	Sensor	Whole matrix ON	One column ON
8	No	4.3 fC	3 fC
108	No	4.3 fC	3 fC
16	Yes	6 fC	3.8 fC
17	Yes	5.5 fC	3.8 fC

TABLE 7.1 – Summary of lowest charge measurements

2232 to the whole matrix turned ON : 3.8 fC with the sensor. As was mentioned above, the ALTIROC
 2233 threshold requirement changed compared to TDR due to progress in sensor design : it turned out
 2234 in sensor testing that after irradiation, the charge obtained is higher than four fC expected before
 2235 - therefore, the threshold doable by ALTIROC can also be higher.

2236 Having a low enough (or not) minimum charge is not enough for ASIC to be considered opera-
 2237 tional in this configuration : the jitter requirements for the HGTD are defined in the TDR by the
 2238 TOA jitter⁵ of the ASIC at 10 fC (expected charge before irradiation) and at 4 fC (after irradia-
 2239 tion). The same dataset for the lowest charge is used to determine jitter because TOA and TOT
 2240 values are always saved in the measurement. Jitters have been extracted from the TOA dispersion
 2241 at a given charge, multiplied by the TOALSB to convert to picoseconds, and are summarized in
 2242 Table 7.2. At large charge when the electronics noise is negligible, both the ASIC alone and the
 2243 boards with the sensor give about 30–35 ps jitter (no specific threshold optimization was done).
 2244 At 4 fC jitter increase to 52 ps (respectively 99 ps) for the ASIC alone (respectively with sensor)
 2245 due to the noise increases, and the minimal threshold is too high for a good time resolution. Doing
 2246 jitter measurement at 4 fC only makes sense if the lowest detectable charge was lower than 4 fC -
 2247 which, from Table 7.1 is only valid for non-sensor boards with one column activated, right at the
 2248 boundary for sensor boards with one column ; maybe it can work for no-sensor with all matrices,
 2249 but that is not the case for sensor boards and all matrices activated. Therefore, boards 16,17 jitter
 2250 measurements are exploding at four fC jitter ; With no sensor boards at 4 fC, the requirement is
 2251 almost satisfied with the whole matrix and good enough with one column.

2252 Based on the measurements taken, engineers made modifications to the design of ALTIROC3.

5. Also, the TOT jitter should be low for TOTC to be usable in timewalk correction

Board	Sensor	10 fC Whole matrix ON	10 fC One column ON	4 fC Whole matrix ON	4 fC One column ON
8	No	35 ps	30 ps	75 ps	52 ps
108	No	30 ps	32 ps	80 ps	52 ps
16	Yes	35 ps	32 ps	x	99 ps
17	Yes	35 ps	31 ps	x	96 ps

TABLE 7.2 – Summary of jitter at lowest threshold

2253 Typically, pixels at the top of the column had a higher lowest charge, which was attributed to
 2254 voltage drop along the column, due to which the injected signal appeared smaller than the one seen
 2255 by pixels lower in the column. Re-routing improved this behavior. Also, high voltage decoupling
 2256 was optimized (for the capacitor mounted on the board, specific value was chosen), giving lower
 2257 noise. The latest testbench measurements show ALTIROC3 having a 2.5 fC threshold at cold.

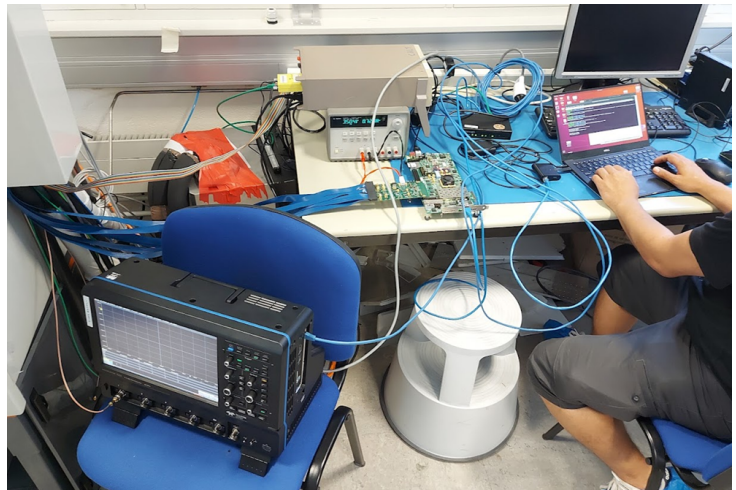
7.3 TID test

2259 ALTIROC2 board 7 (one without a sensor) underwent a Total Ionizing Dose (TID) test : goal
 2260 is to irradiate with a dose that the chip will receive during HGTD operation before the foreseen
 2261 replacement (200 Mrad). To cover uncertainty on dose rate delivered, chip was irradiated with
 2262 225 Mrad dose. During irradiation all the key quantities, part of them was shown above, were
 2263 monitored. The hope for this test was that the chip would be able to maintain the initial or close-to
 2264 level of performance, compared to unirradiated.

2265 Tests were done at CERN with X-ray. The setup is shown on Fig. 7.15. The chip is mounted
 2266 on the board (used for the rest of the measurements) and put inside the X-ray “box“. The board is
 2267 positioned under the beam (whose diameter is 5.1 cm) in the center. The distance from the board
 2268 chip to the source is chosen so that the whole chip receives the dose as uniformly as possible. This
 2269 distance is 10.2 ± 0.1 cm. The dose rate is chosen to be 2.99 ± 0.05 Mrad/h to get the needed
 2270 dose within the time setup was available for us (less than one week). The numbers were optimized
 2271 through software provided by the X-ray facility⁶. The temperature was stabilized at 22 degrees
 2272 via chiller. The board inside of the X-ray setup is shielded and connected to the rest of the setup
 2273 (through long cables) located outside : the oscilloscope, multimeters, power supplies, and computer
 2274 to control everything.



(a)



(b)

FIGURE 7.15 – (a) Board 7 positioning under X-ray (b) setup outside of X-ray box to control/read the chip

2275 To capture any potential anomaly, measurements should be continuously repeated. As measur-
 2276 ing all columns takes time, it was decided to measure only one VPA and one TZ column (at the
 2277 time VPA rejection was not finalized). The plots shown in this chapter are for TZ (15 pixels from
 2278 column 8). All preamplifiers, discriminators, and TDCs in the column were turned ON (but not the
 2279 whole matrix). The injection was made into the entire column simultaneously to measure the global
 2280 threshold at two charges ($Q = 4.8$ fC, 9.6 fC), the per-pixel thresholds at two charges ($Q = 2.4$
 2281 fC, 4 fC), and the corresponding lowest charge, TOA and TOT LSB . From charge and TOA LSB
 2282 measurements combined, jitter vs time dependence in picoseconds was obtained. Keithley multi-
 2283 meter was used to monitor chip internal voltage parameters like vdda (supply voltage for the ASIC
 2284 analog part) vddd (supply voltage for the ASIC digital part). An oscilloscope was used to measure

6. <https://ade-pixel-group.web.cern.ch/xray/>

2285 the amplitude and noise from the preamplifier probe.

2286 Fig. 7.16 shows the ASIC current and v_{ddd} values as monitored during the entire period. At
2287 about 150 Mrad, both an increase of the current and a decrease of the v_{ddd} have been observed.
2288 After power resets, the measurements returned to the nominal value and stayed stable, showing that
2289 this effect is probably not due to the irradiation itself. Such a behavior had already been observed
2290 over long measurements also on the testbench and attributed to instability in the firmware of the
2291 data-taking board. Therefore, v_{ddd} drop is not qualified as a problem caused by the dose received.
2292 TID measurements were repeated later with ALTIROC3, and no v_{ddd} drop was observed. A short
2293 period of instability will be rejected later for the analysis (as it is unrelated to the test being done),
2294 except for the noise plot.

2295 On most plots below, the first red vertical line marks the moment when a sudden v_{ddd} change
2296 happened. The green vertical line marks the moment of irradiation start, and the measurements
2297 were taken before that with an unirradiated board for reference. Each colored point corresponds
2298 to one pixel, the number of which is indicated in the legend, and the black line is the average over
2299 pixels at a given dose. The gap in data points at around 150 Mrad is related to data cleaning.

2300 The main quantities being monitored are :

- 2301 • Noise extracted from the width of S-curve ($Q=2.4$ fC) fit - Fig. 7.17. The drop at 150 Mrad is
2302 correlated to the abovementioned problem, but there is no noise increase under irradiation.
2303 Later, noise recovers and stays stable at the previous value (about 0.25 fC)
- 2304 • Amplitude, as obtained from the difference between the global thresholds at $Q = 9.6$ fC and
2305 $Q = 4.8$ fC. A global threshold instead of a per-pixel was chosen because of finer granularity.
2306 Dependence is shown on Fig. 7.18, and a negligible decrease is observed
- 2307 • Per-pixel threshold (Fig. 7.19a) is shown only for one of the charges because the other one
2308 behaves similarly. A slight increase in the pixel threshold is observed
- 2309 • The lowest threshold (Fig. 7.19b) is also shown only for one of the charges. No variation is
2310 observed, which is compatible with the fact that the noise and the amplitude are not seen to
2311 vary.
- 2312 • TOA LSB measured with the pulser (Fig. 7.20a) is well stable as is the respective jitter at
2313 4 fC or 10 fC, shown in Fig. 7.21

2314 Measurement with the external trigger has shown some variations in dose of TOT LSB (as
2315 it is illustrated on Fig. 7.20b - the absolute value of the TOTLSB is irrelevant for the timewalk
2316 correction, and this is not a significant problem) and completely failed for TOA LSB (therefore not
2317 shown).

2318 Globally, this first ASIC full-size version has shown satisfactory results against TID irradiation.
2319 Given that later similar measurements were repeated with a different board, and there was no
2320 problem with an external trigger - board 7 external trigger behavior is interpreted as bad luck.

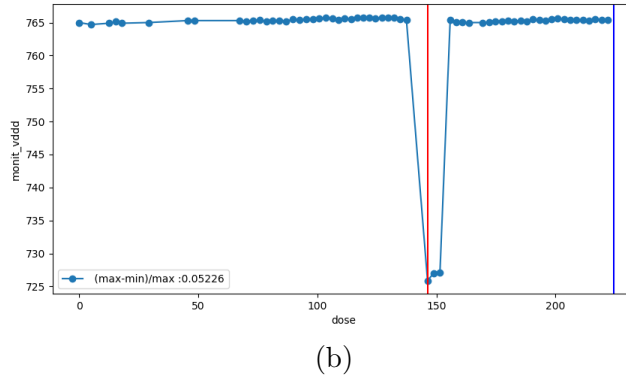
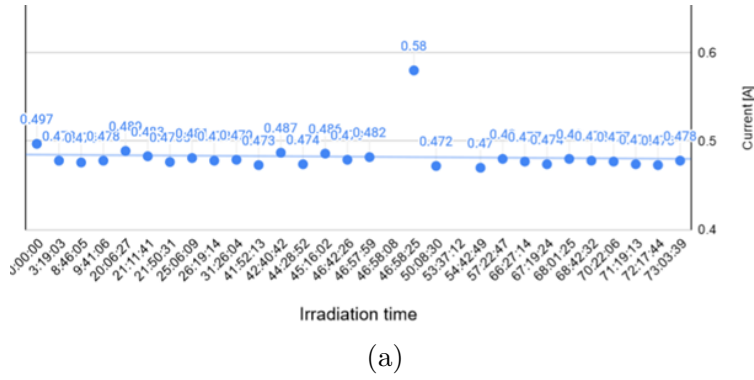


FIGURE 7.16 – Observed during TID but not related to it (a) Voltage drop (b) Corresponding current drop

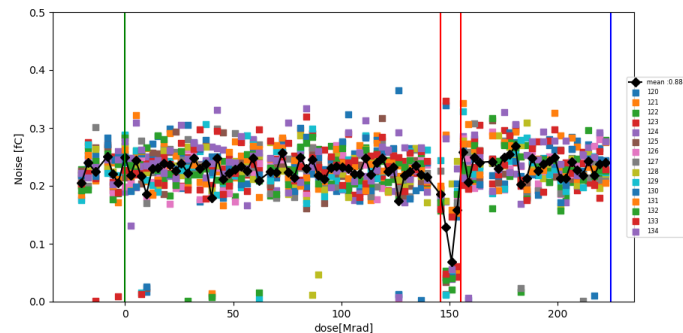


FIGURE 7.17 – Effect of voltage drop shown in Fig. 7.16 on noise seen in charge scan

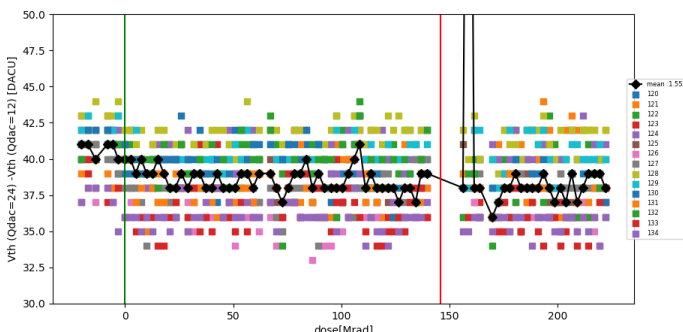


FIGURE 7.18 – Amplitude proxy as function of dose

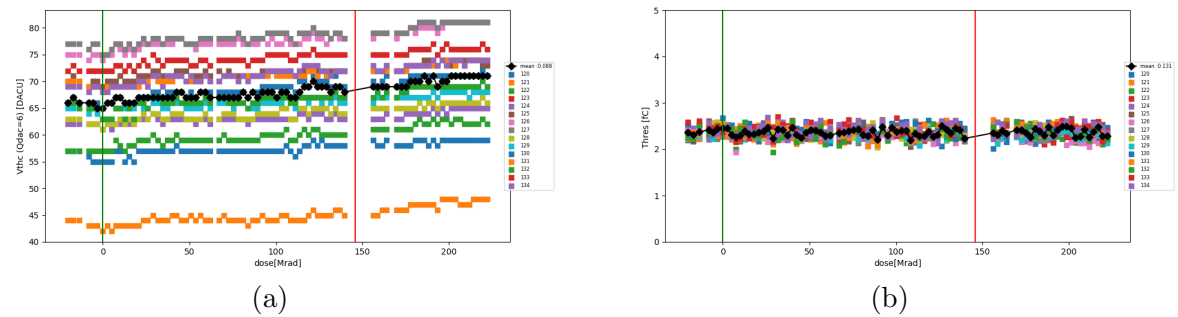


FIGURE 7.19 – (a) Per-pixel threshold as a function of dose (b) Charge scan with threshold determined in Fig. 7.19a as function of dose

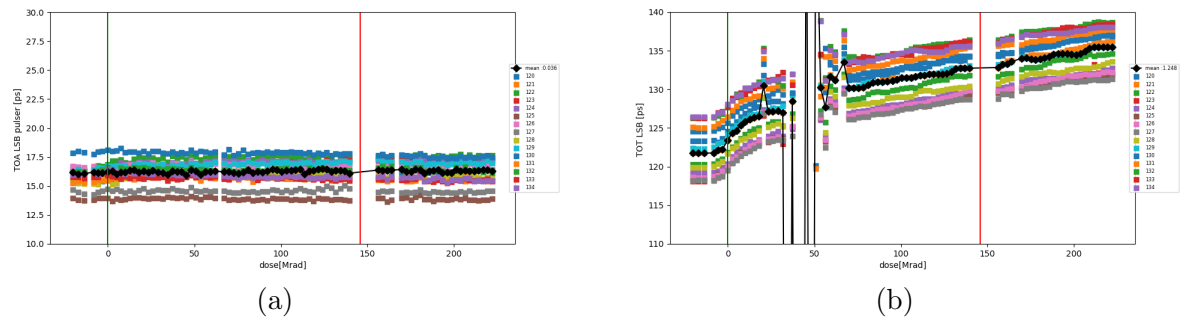


FIGURE 7.20 – (a) TOA LSB (pulser) as a function of dose (b) TOT LSB as a function of dose

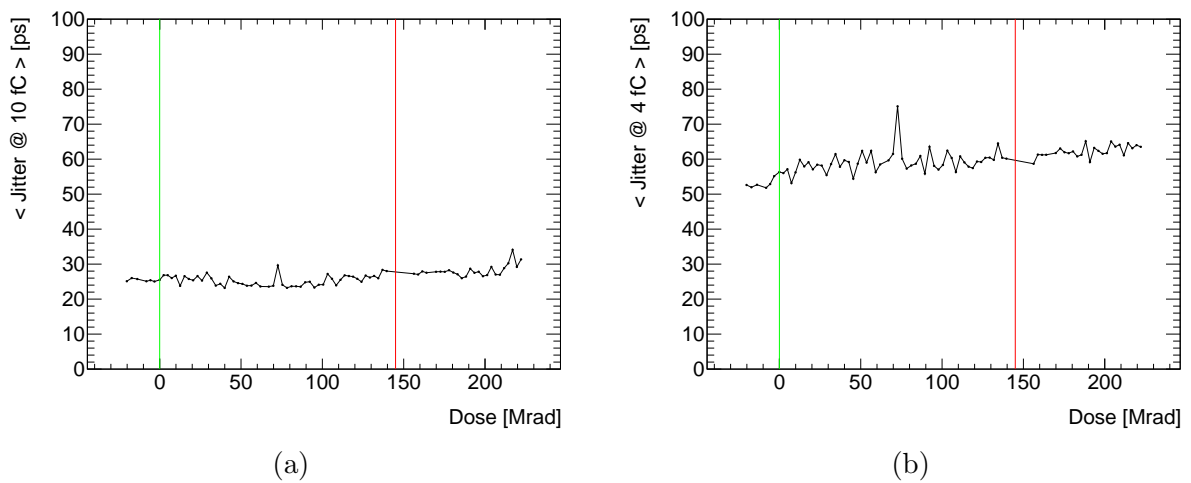


FIGURE 7.21 – Average TOA jitter (over pixels) as function of dose (a) 10fC (b) 4fC

2321 **7.4 Low temperature test**

2322 In the future HGTD, the ASICs, among everything else, would be located in the cold vessel and
2323 operated at a temperature ≈ -30 °C. Consequently, the performance of the ASIC was measured at
2324 cold temperatures.

2325 The climate chamber at OMEGA was used, shown in Fig. 7.22. The board inside is also partially
2326 visible. The rest of the setup is the same as in other tests : the FPGA is visible on top of the climate
2327 chamber connected with a long cable to a board that goes through a “gap” in a climate chamber.
2328 A computer with FADA (see Footnote 3) software controls the FPGA, which in turn controls the
2329 chip. The ASIC board and FPGA are powered by power supplies, as also shown in the picture.
2330 Keithley multimeter is also connected and constantly recorded.

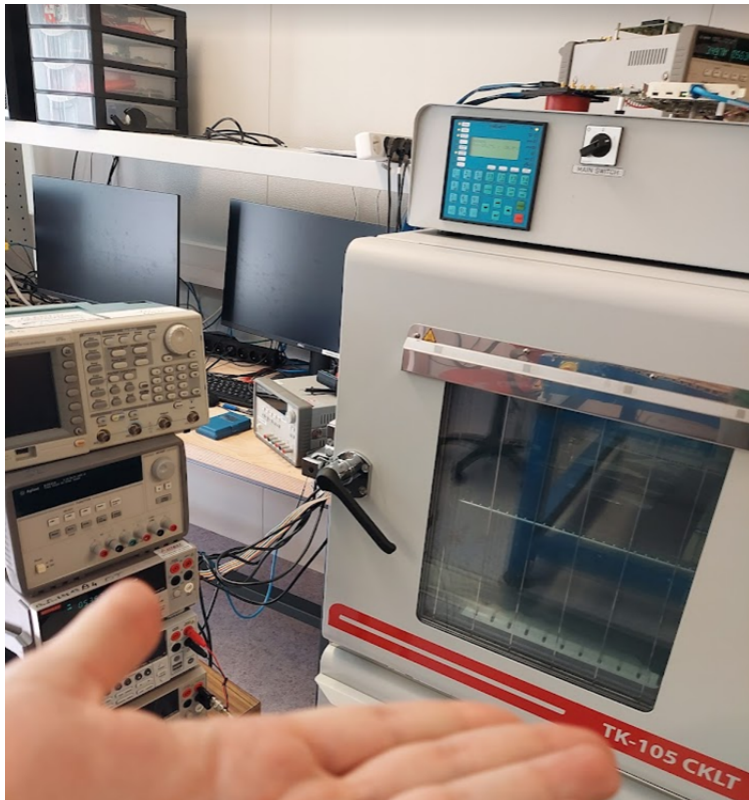


FIGURE 7.22 – Climate chamber at OMEGA and the rest of the low-temperature setup

2331 Two ASICs (both without a sensor) were operated under different temperatures up to as low
2332 as the target -30 °C. Results from only one will be shown because they are similar. Another board
2333 in another climate chamber was tested by a different group with the same conclusion and will not
2334 be shown here. After putting the board into the climate chamber, one needs to wait sometime
2335 before measuring for the chip temperature to stabilize, which is not instantaneous, and a chip
2336 internal temperature monitor can be used for monitoring : `vtemp` voltage is seen to be linear with
2337 temperature, as expected, shown on Fig. 7.23.

2338 The injection was done into one column (TZ) simultaneously, and the whole column was acti-
2339 vated. The same quantities as in the case of the TID test are shown on Fig. 7.24–Fig. 7.27b as a
2340 function of the temperature. Each temperature point is an average over several “batches” (same
2341 configuration taken multiple times), separately per pixel. Most quantities are reasonably stable.
2342 One exception is the per-pixel threshold drifting - this is expected⁷ and compensated by the out-

7. not surprising overall as the transistor threshold voltage is known to vary with temperature

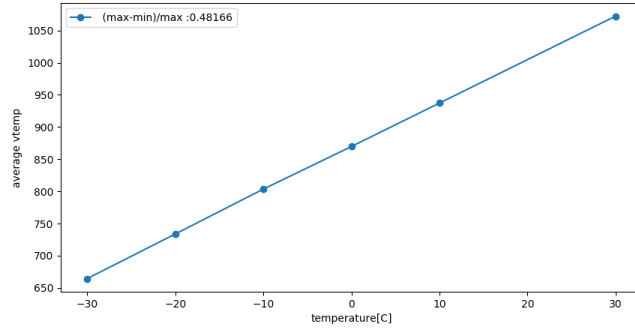


FIGURE 7.23 – Vtemp against temperature

put DC level of the preamplifier also drifting, but also that calibration derived at room temperature should be re-done at low temperatures like -30°C . There is also some increase of TOA jitter at a lower charge, only at hot room temperature (30°C), that drops to plateau already at 10°C . Also, a small TOTLSB dependence is seen.

The performance of the ASIC at -30°C is expected to be quite similar to that at room temperature.

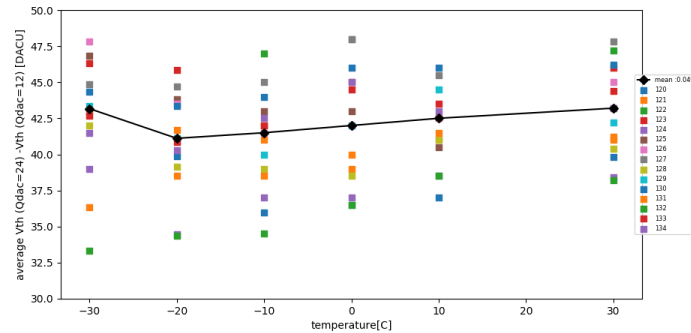


FIGURE 7.24 – Amplitude proxy as a function of temperature

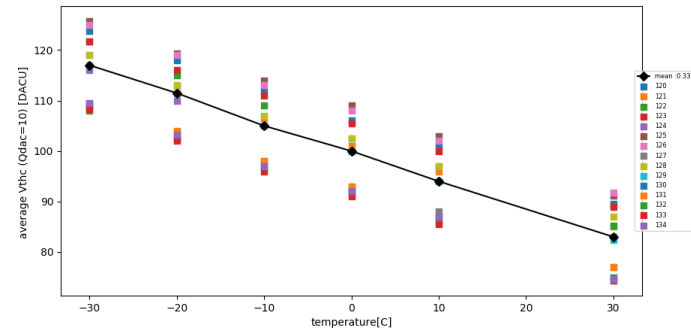


FIGURE 7.25 – Per-pixel threshold as a function of temperature

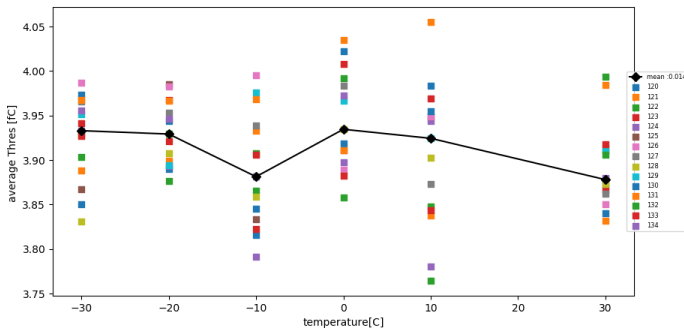


FIGURE 7.26 – Charge scan with threshold determined in Fig. 7.25 as function of temperature

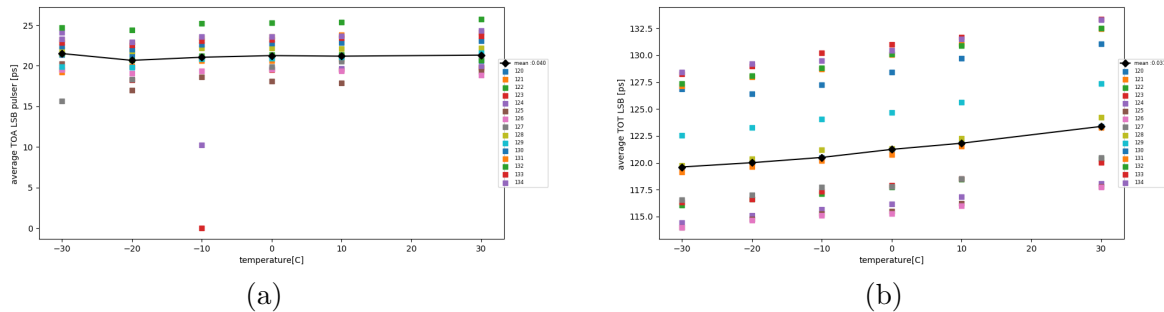


FIGURE 7.27 – (a) TOA LSB (pulser) as a function of temperature (b) TOT LSB as a function of temperature

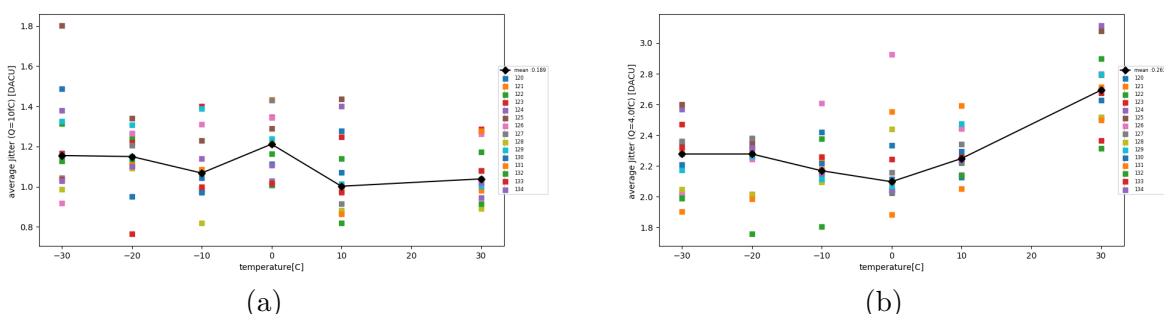


FIGURE 7.28 – TOA jitter as a function of temperature at charge (a) 10 fC (b) 4 fC

2349 8 - ALTIROC2/3 testbeam

2350 8.1 Setup

2351 ALTIROC2, the first full-scale chip prototype, had a new DAQ system (compared to ALTI-
 2352 ROC1), developed at IJCLab (Orsay) and Omega (Palaiseau) - this also meant that the testbeam
 2353 setup needed to be adjusted. Testbeam-specific DAQ development was done by IFAE Barcelona.
 2354 Sensor is the same as in ALTIROC1. The setup used at CERN SPS (pion beam) is shown on Fig. 8.1.
 2355 and key components are labeled - this setup is also used for measurements shown in Sec. 8.2. AL-
 2356 TIROC3 timing measurements (Sec. 8.4) were done in DESY with an electron beam, but the setup
 2357 is mostly the same. An additional component is a trigger interface board (developed at IFAE) that
 2358 receives a trigger from TLU and tells ASIC to save data. ASIC data taking is done through Alvin¹
 2359 ,integrated into the EUDAQ framework. Alvin output format is a text file with output from several
 2360 (typically five) bunch crossings, recorded at each trigger. If there were a pixel hit at a given bunch
 2361 crossing, in output it's represented with a line containing number of pixel, TOA and TOT . The
 2362 converter was written to translate this text file in ROOT ntuple, compatible with the software
 2363 written for ALTIROC analysis. As in the ALTIROC1 case, the ASIC+LGAD hybrid, telescope,
 2364 and time reference device are the main components.

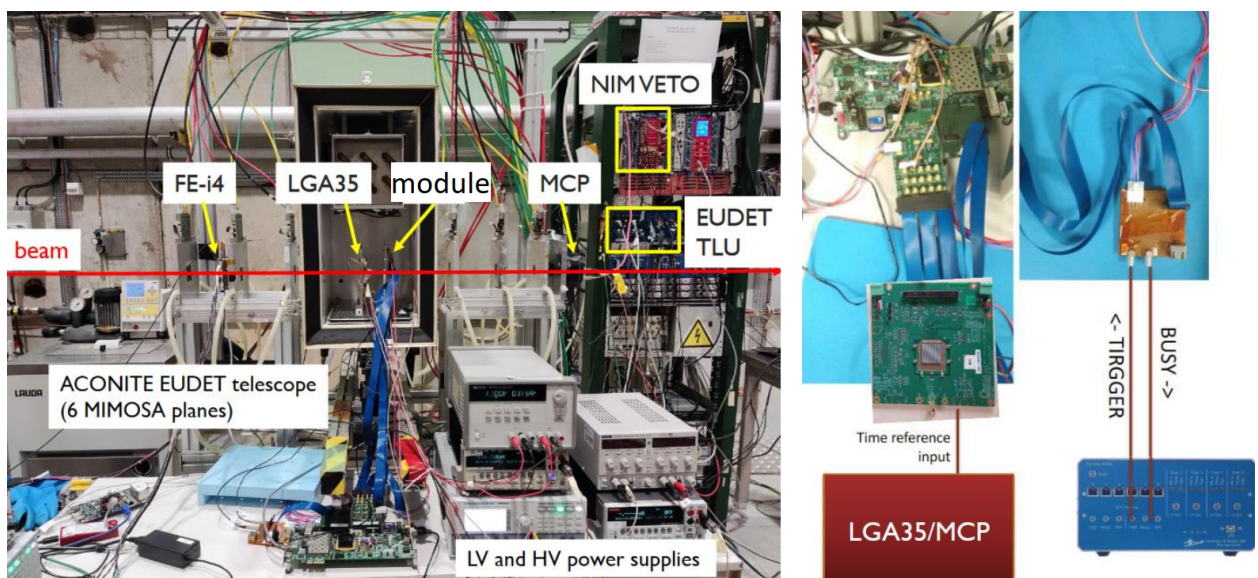


FIGURE 8.1 – ALTIROC 2/3 SPS testbeam setup

2365 The telescope is the same as for the ALTIROC1 case, it is an EUDET telescope consisting of
 2366 6 planes (sometimes not all of them are used if one turns out to be noisy), each with pixel side
 2367 of $18.5\mu m$. Positions of plane hits are fitted with a straight line, this line is then extrapolated to
 2368 hybrid plain providing position where ASIC was hit.

2369 Time reference is new compared to the previous setup - here it's MicroChannel Plate (MCP)
 2370 Photomultiplier Tube with negligible time resolution compared to hybrid's, therefore instead of
 2371 solving a system of equations, one can just take and fit the difference in the form

$$\Delta T = \underbrace{-TOA \times LSB_{TOA}}_{t_{ASIC}} - \underbrace{t_{MCP}^{trig,CFD} - t_{clock}}_{t_{MCP}} \quad (8.1)$$

1. <https://gitlab.cern.ch/ifaepix/alvin>

2372 The minus sign in front of TOA is due to falling edge reference used by the TDC . The LSB is taken
 2373 from calibration measurements, similarly to Sec. 7.1.1 where FADA is used, but for testbeam done
 2374 with Alvin for consistency with Alvin data taking. Clock is implicitly always there for TOA and
 2375 inserted explicitly for t_{MCP}^{trig} reference to do an apple-to-apple comparison. Contrary to ALTIROC1
 2376 setup, the scope trigger is not issued from the ASIC and is not synchronous with the 40 MHz clock,
 2377 so the MCP time should be referenced to the clock. The trigger is based on a region of interest
 2378 in the FEI4 plane and is handled by the Trigger Logic Unit (TLU). When triggered, the TLU
 2379 sends commands to the ASIC (through custom trigger board) to save the timing data (through
 2380 FPGA), oscilloscope to save full waveforms of the MCP and analogue ASIC probe and telescope
 2381 to save the tracking data. Both t_{MCP}^{trig} and t_{clock} are obtained from digitized by oscilloscope MCP
 2382 and clock pulses, respectively. The recorded pulse is analyzed with PyAna², giving $t_{MCP}^{trig,CFD}$ the
 2383 moment where MCP pulses cross certain amplitude fraction and t_{clock} is the moment when the
 2384 clock pulse crosses zero voltage (for which clock pulses are shifted such amplitude oscillates around
 2385 zero). Resulting ΔT distribution is looking Gaussian, and the sigma of its Gaussian fit gives the
 2386 hybrid time resolution.

2387 MCP resolution was checked in 3 ways, all methods giving 3–7 ps $\ll \sigma_{hybrid}$:

- Directly by solving the time resolution system as before with a third device being LGA35 (time resolution comparable to ASIC)
- Looking at resolution of time difference between LGA35 and MCP - which is close to the resolution of LGA alone that would be impossible with large MCP resolution
- Using the slope of the average (over many events) digitized MCP pulse, jitter is expected to be given by $N/dV/dt = t_r/A/N$ with N (noise) and A (amplitude), also measured from the oscilloscope data

2395 With MCP resolution checked, CFD was selected by solving for MCP resolution with different
 2396 CFD values. Resulting in choice of CFD at 50% of the amplitude (denoted as CFD50) for Eq. 8.1,
 2397 consistent with the fact that MCP amplitude derivative is maximal near half of the amplitude.
 2398 However, CFD optimization does not bring much because MCP pulse is very sharp.

2399 An example of testbeam event, seen by the oscilloscope, is shown on Fig. 8.2. The periodic green
 2400 line is the clock, in black - MCP pulse, in blue - preamplifier pulse (also digitized by the scope).
 2401 On trigger, all the event data is saved to the PC controlling the setup. Event data includes three
 2402 independent streams : ASIC output, telescope output (not shown in the picture), and oscilloscope
 2403 information.

2404 Both ASIC and oscilloscope information are needed to find the ΔT shown in Eq. 8.1, and they
 2405 need to be synchronized for the difference to work : the event labeled N from the ASIC stream
 2406 should also be event number N from the oscilloscope stream - due to the complexity of the software
 2407 chain and hardware setup, possible unintentional re-configuration between different runs, nothing
 2408 guarantees synchronization. It can be checked in two ways : with TOA and TOT information,
 2409 results of which are shown on Fig. 8.3. Comparison of TOA as provided by ASIC and t_{MCP} should
 2410 give linear dependence, which is the case. Comparing TOT (from ASIC) and probe amplitude (from
 2411 oscilloscope) should give a known linear dependence at the beginning and then reach a plateau, as
 2412 seen before in ALTIROC1. Both were observed, except for missynchronization for small part of data
 2413 as seen on TOT-amplitude correlation via “blob” at low probe amplitude values and TOT around
 2414 20. Those TOT values really belong to the core of distribution. It only happens at the end of the
 2415 runs. No correction was needed in ALTIROC2, “blob” was removed by probe amplitude selection.
 2416 However, it will not be the case for ALTIROC3 setup (see Sec. 8.4). To obtain the tracking results,
 2417 the telescope and the ASIC streams should be synchronized, and the oscilloscope is not used. As
 2418 ASIC and oscilloscope synchronization was confirmed and ASIC and telescope information follow

2. <https://gitlab.cern.ch/atlas-hgtd/TestBeam/PyAna>

2419 the same “data path“, ASIC and telescope are assumed to be synchronized.

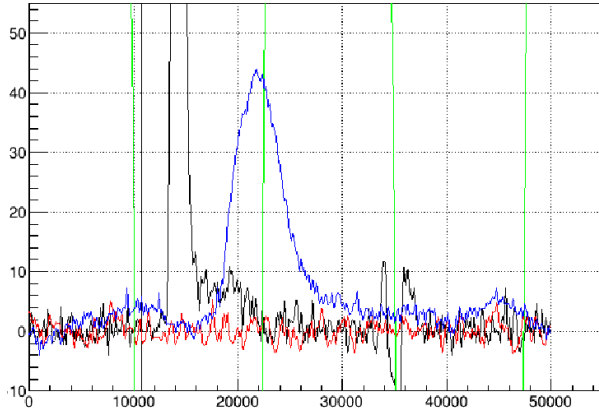


FIGURE 8.2 – One testbeam event. MCP is shown in black, preamplifier probe in blue. Green lines are half-periods of 40 MHz clock with much larger amplitude.

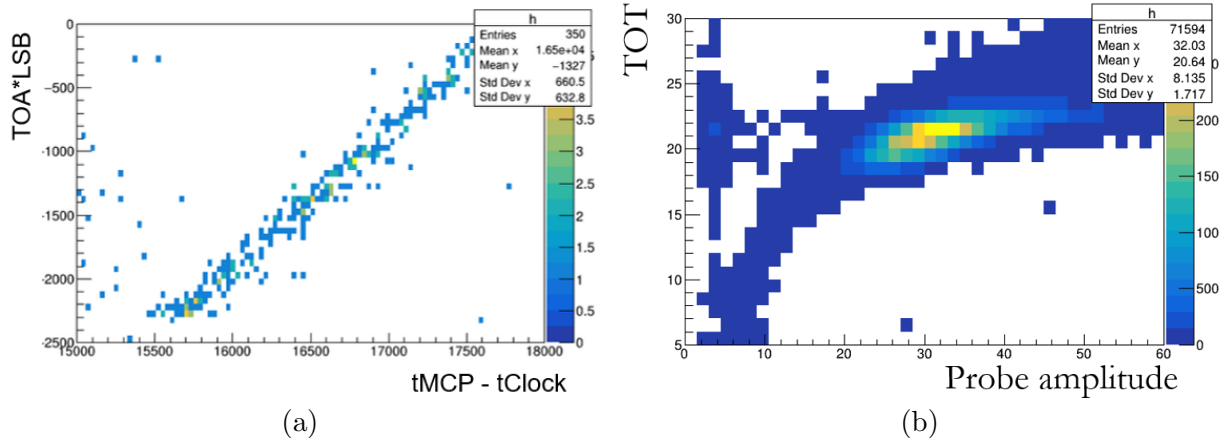


FIGURE 8.3 – ASIC-oscilloscope data streams synchronization with (a) TOA (b) TOT

2420 Therefore, the updated testbeam setup (hardware and software) was verified, and one can move
2421 on to measurements with it.

2422 8.2 ALTIROC2 timing

2423 The hope for ALTIROC2 time resolution is that it should not degrade much compared to
2424 ALTIROC1, and overall behavior should be similar. It has been observed that the TOA-TOT
2425 coupling is still there, similar to ALTIROC1 (Fig. 8.4). It was also observed that “amplitude“ of
2426 coupling depends on the threshold : the difference between the minimum and maximum of the
2427 S-shape is larger for a lower threshold, as shown on Fig. 8.4.

2428 The starting point for time resolution extraction has changed, as described above : two reference
2429 SiPMs were replaced by MCP, and therefore, there is no need to solve the system. The timewalk
2430 correction is done in the same way. A summary of the configurations tested at room temperature
2431 is given in Table 8.1. The bias voltage is chosen to be as high as possible without creating noise.
2432 All TZ pixels are activated (half of all the pixels), and the beam was positioned (by moving the
2433 ASIC relative to it) to be roughly in the center of TZ pixels. Two thresholds of 8 and 4.8 fC

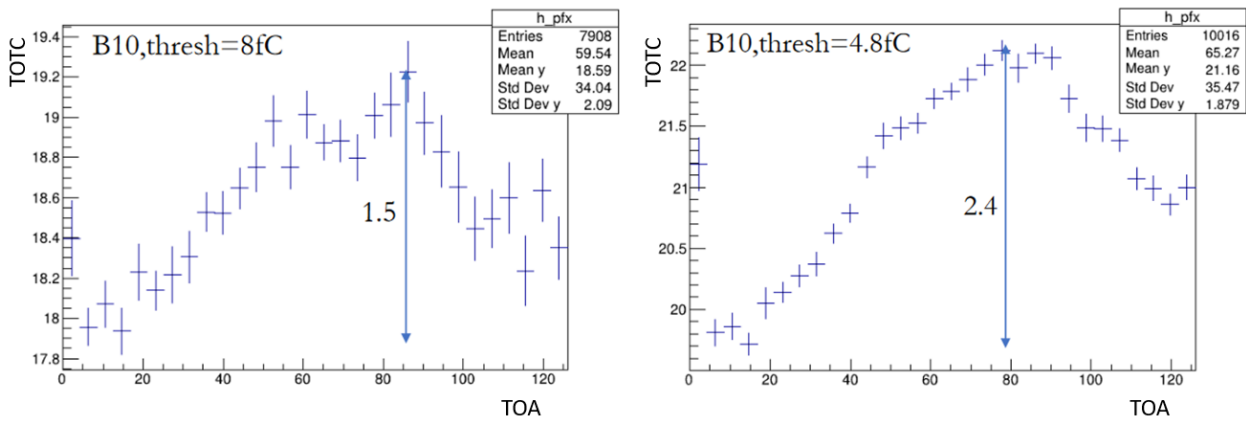


FIGURE 8.4 – TOA-TOT mean with (a) 8 fC threshold (b) 4.8 fC threshold

were tested. The preamplifier probe was activated and connected to pixel 156. Despite ALTIROC2 having many more pixels than ALTIROC1, at the time, the focus was on measuring resolution in one pixel - the one from which the preamplifier probe was outputted³. As a validation of the new prototype, measurements were re-done similarly to ALTIROC1. Measurements of many pixels were done in ALTIROC3 (which doesn't have major modifications compared to ALTIROC2), and shown in Sec. 8.4.

Batch	Board	Bias voltage	Pixels activated	ASIC threshold	Probe pixel
301	B10	-200 V	all TZ	4.8 fC	156
302	B10	-200 V	all TZ	8 fC	156

TABLE 8.1 – Summary of ALTIROC2 testbeam batches

For organizational reasons, TOA LSB was not known during the data-taking, and workaround was introduced to find the right value : scanning over LSB values and assuming that the right LSB value is the one that minimized the resolution. The variation of ΔT distributions (before timewalk correction) with different LSBs is shown on Fig. 8.5. From set of LSBs on figure nominal LSB turns to be the one that minimizes the resolution. Using instead value smaller by 1.1 ps, resolution degrades by 13 ps. Using the LSB value larger by 1.1 ps gives resolution 3.5 ps larger and taking even larger LSB values degrades resolution even more, until the point when distribution becomes non-Gaussian. Later, when the calibration became available, it was checked that the LSB obtained from the minimization is the same as the calibration value. The overall idea is that one cannot minimize the resolution lower than what it is ; however, the approach should be used with care (it was only used because no other alternative was available) : in future HGTD, there would be no reference devices to calibrate LSB in that way ; one should be able to obtain the right value from the calibration (it will turn out to be difficult, as will be shown in ALTIROC3 section) and a poor knowledge of the LSB translates into systematic uncertainty on time resolution.

A summary of the time resolutions obtained with different timewalk correction methods is shown in Table 8.2, and it can be seen that they are similar to ALTIROC1. Correction for TOA-TOT non-uniformity was applied but did not improve the resolution. As before, time resolution dependence on amplitude is seen, as indicated by improvement in “Probe amplitude, distribution core” column.

3. It was pixel 156

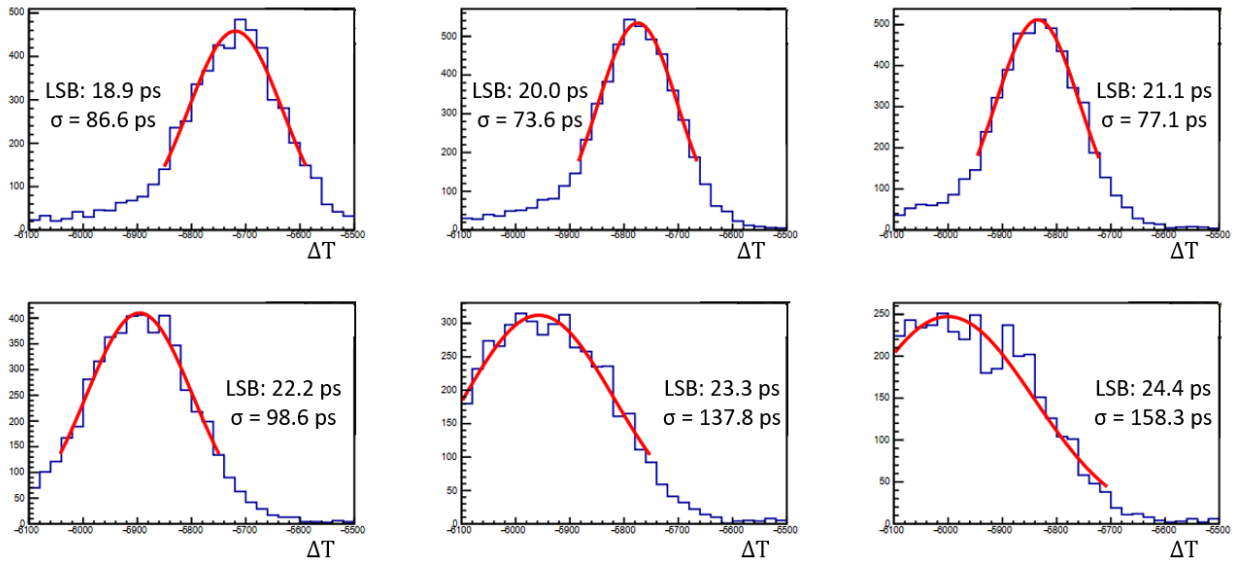


FIGURE 8.5 – change of ΔT with LSB

Batch	TW-uncorrected	Probe amplitude TW	Probe amplitude TW, distribution core	ASIC TOT TW	probe TOT TW
301	77 ps	49 ps	45 ps	50 ps	51 ps
302	64 ps	45 ps	42 ps	53 ps	46 ps

TABLE 8.2 – Summary of ALTIROC2 testbeam results with Table 8.1 batches

2459 **8.3 Tracking, efficiency and interpad**

2460 The tracking efficiency of the ALTIROC2 hybrid device have been measured using the telescope
 2461 information. Hit efficiency is

$$\varepsilon_{hit} = \frac{N_{tracks}^{ASICfired}}{N_{tracks}} \quad (8.2)$$

2462 For this measurement, a MIMOSA telescope is used, with around 10 microns spatial resolution of
 2463 extrapolated to ASIC plane track position. From each plane of MIMOSA, a straight line is fitted
 2464 using the PaTrack⁴ software and extrapolated at the hybrid front face. Only events with a single
 2465 track reconstructed are kept in analysis to avoid any potential ambiguities. If the track matched
 2466 the hybrid, a hit associated with a TOA and TOT should be recorded in the ASIC data stream.

2467 The resulting efficiency, defined with Eq. 8.2, is shown on Fig. 8.6. This map is obtained as
 2468 the ratio of the other two maps : distribution of tracks going through the ASIC with hit registered
 2469 divided by just distribution of tracks. The color code shows the efficiency from 0 to 1. Each square
 2470 (in yellow with 100% efficiency) corresponds to an ASIC pixel with an expected side size of roughly
 2471 1.3 mm. Between the pixels is the interpad region, which is a no-gain region, and when the particle
 2472 is going through the hit is typically not registered - this is expected. Only 20 ASIC pixels are shown
 2473 corresponding to the size of the tracking device used for the trigger.

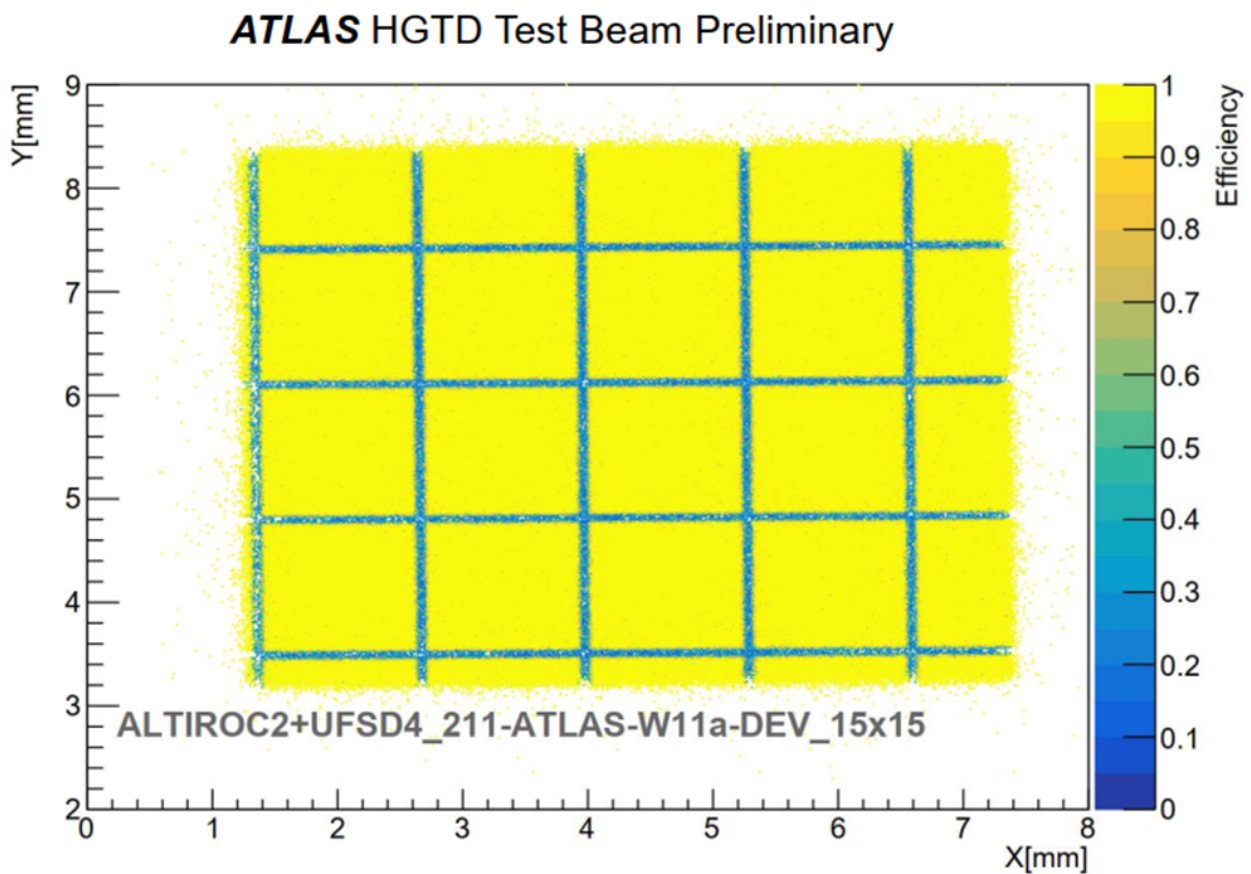


FIGURE 8.6 – Efficiency map of ALTIROC2+UFSD4_211-ATLAS-W11a-DEV_15x15measured as ratio of the reconstructed tracks with a hit seen in ALTIROC to all the reconstructed tracks penetrating the module area. 100% efficiency was achieved outside of inter- pad region. Only fraction of 15x15 pixel matrix is visible because of triggering on smaller pre-defined area.

4. <https://gitlab.cern.ch/atlas-hgtd/TestBeam/PaTrack/-/tree/master>

2474 A near 100% efficiency is obtained in the core of the pixel, but it's also important to check
 2475 that the area on which efficiency is high is as large as it should be - determined by the size of
 2476 the interpad region. It can be seen already on Fig. 8.6 that interpad size is uniform (there are no
 2477 columns/rows that are much larger than others) and that the size of interpad is smaller than 100
 2478 microns. A more detailed investigation was done. For gaps seen to be parallel to the Y axis, each
 2479 gap can be looked at separately by taking the relevant slice and projecting it into the X axis. For
 2480 example, to obtain the distribution for a vertical gap in the top-right corner, one would make the
 2481 selections $Y > 7.5$ and $X > 6$ to isolate that one gap and project it into X . The resulting efficiency
 2482 for one gap is shown on Fig. 8.7a. Drop corresponds to the center of interpad where if the track is
 2483 going through, the hit never gets registered. Efficiency is around one near the edges because those
 2484 are pixels (only part of their 1.3 mm size is shown). All the other individual gaps are obtained the
 2485 same way, with one difference being for horizontal gaps - they are projected in Y .

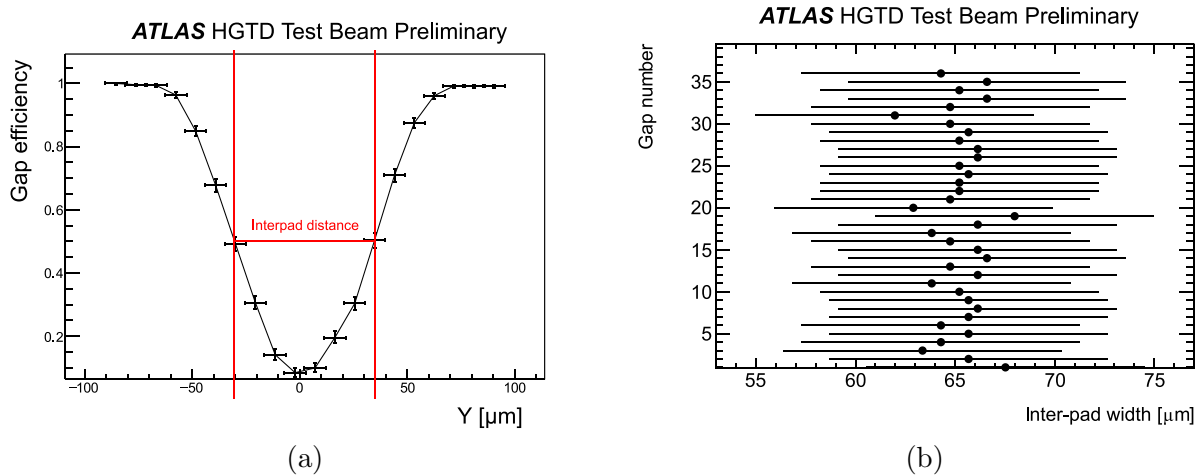


FIGURE 8.7 – (a) Efficiency versus y of ALTIROC2+UFSD4_211-ATLAS-W11a-DEV_15x15zoomed around an interpad region. Vertical lines mark 50% efficiency obtained with linear interpolation, difference in their positions is taken as the interpad distance. (b) ALTIROC2+UFSD4_211-ATLAS-W11a-DEV_15x15 : gaps widths taken from 50%-50% efficiency, obtained from linear interpolation, shown for each gap from 2D efficiency map, together with uncertainty. Vertical and horizontal gap widths are combined in this plot.

2486 The gap size is defined as width at 50 percent efficiency and is obtained from a linear interpolation
 2487 ⁵. Interpolation is visible on Fig. 8.7a. For that one gap shown, the gap size is 67.5 microns.
 2488 All the gap sizes are shown on Fig. 8.7b. Each gap visible in Fig. 8.6 is assigned a unique number
 2489 (Y axis) and plotted against its width. How the gap number is assigned is irrelevant because all of
 2490 them are seen to have a similar width of roughly 65 microns, well overlapping within uncertainty.
 2491 The gap size obtained is within the sensor requirements. With the gap size known, one can obtain
 2492 the fill factor, which is defined as the ratio of the gain area (where hit can be registered) to the
 2493 total. The dependence of the fill factor on gap size is shown on Fig. 8.8, where it can be seen that
 2494 the measured gap size corresponds to the fill factor around 90%, satisfying the requirement.

5. Alternative is making S-curve fit similar to Fig. 7.13 but given the tracking resolution it will not change anything

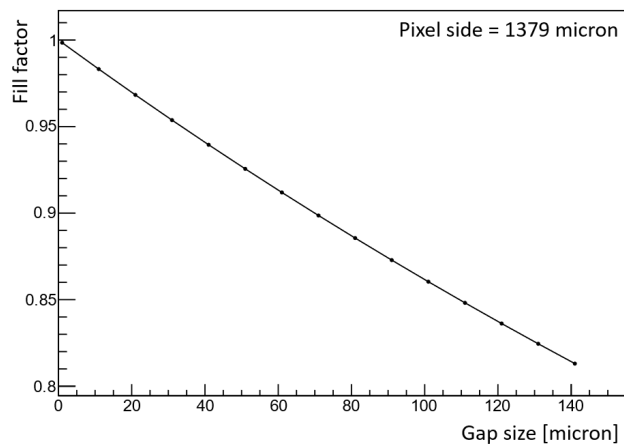


FIGURE 8.8 – Hybrid fill factor depending on gap size (given by sensor)

2495 8.4 ALTIROC3 timing

2496 First ALTIROC3 testbeams were done at DESY in September, November 2023 and the setup
 2497 together with the board 27 are shown in Fig. 8.9. At DESY, there is an electron beam instead of a
 2498 pion, with lower energy than SPS . Tracks reconstructed in the telescope are no longer straight lines
 2499 due to multiple scattering⁶ . Another difference compared to the SPS setup is the usage of a digitizer
 2500 instead of the oscilloscope to digitize analog signals like a clock and preamplifier probe amplitude -
 2501 the advantage of a digitizer is that it has more channels, which is convenient to test multiple sensors
 2502 in parallel to ASIC, but for ASIC itself no advantage is gained. The software was adjusted to use
 2503 a digitizer with a new output format. The software was adjusted to use EUDAQv2, as previously
 2504 used EUDAQv1 had already become obsolete. Contrary to ALTIROC2, missynchronization was
 2505 seen for large fraction of the data (unlike Fig. 8.3) and was corrected by a dedicated algorithm.

2506 Results shown in this section are mostly obtained with batch 1103 (board 27, IME-IHEPv3
 2507 sensor without carbon, bias voltage 149 V, all 225 pixel activated, threshold 10.8 fC, -30 °C) data
 2508 of the November testbeam - except the last section (Sec. 8.4.5) where summary is given.

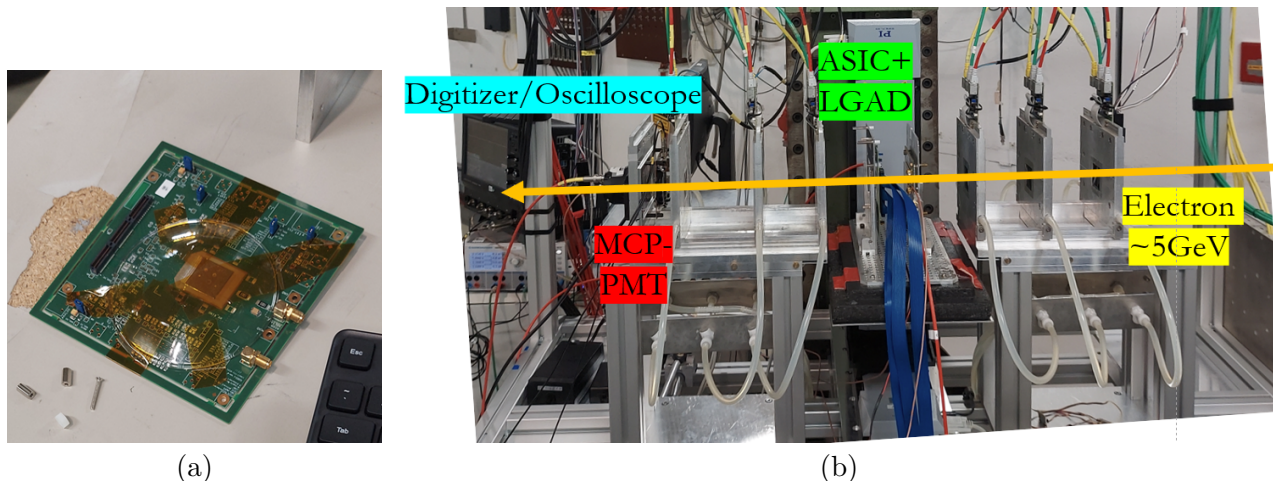


FIGURE 8.9 – (a) ALTIROC3 board tested at DESY (b) DESY testbeam setup

2509 MCP is still used as a time reference, and the resolution is extracted according to Eq. 8.1.
 2510 This time, measurements were done for many pixels, for each pixel, LSB from calibration was used,
 2511 resulting in timewalk-uncorrected time resolutions shown in Fig. 8.10, where it can be seen that
 2512 they are outside of the HGTD requirement and much above⁷ the ones seen in ALTIROC1,2.

2513 Investigation showed that there are two problems :

- 2514 • LSB from calibration does not give the correct value (overall scale problem)
- 2515 • There is not just one LSB valid for the whole TOA range (0-127), but at least two LSB values
 2516 that should be used. Once overall LSB scale is fixed, tuning is still needed to have the correct
 2517 value, depending on the TOA sub-region

2518 8.4.1 LSBs from resolution minimization

2519 Overall scale can be found by minimizing time resolution as a function of LSB, which was
 2520 introduced in ALTIROC2 (see Fig. 8.5). The resulting dependence of resolution on LSB is shown
 2521 on Fig. 8.11 for one of the pixels for $TOA \ 0 < TOA < 127$ (inclusive) on the green curve. The
 2522 minimum of parabola obtained shows the right TOA LSB ballpark, in this case at around 17.5 ps,

6. tracking results are not used for timing measurements shown in this section

7. part of the discrepancy, as was found later, is due to bug in calibration software

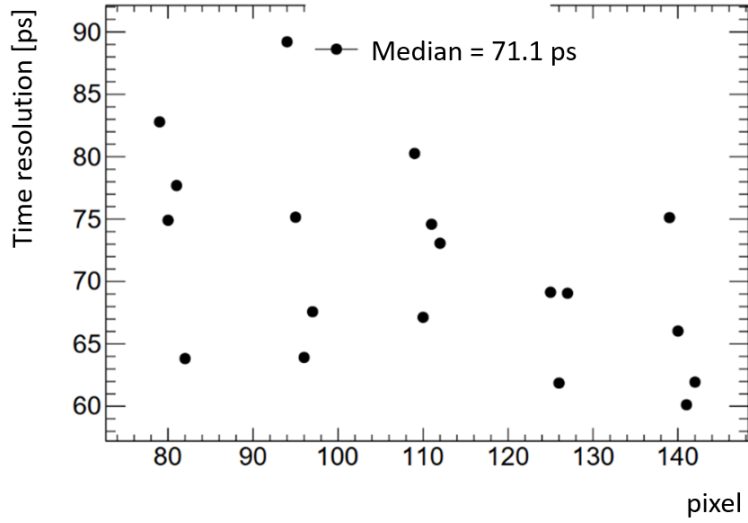


FIGURE 8.10 – ALTIROC3 time resolutions without timewalk correction and using LSB obtained from calibraiton

with a resolution of around 55 ps. The parabola is quite sharp, showing that LSB mismeasured by ± 1 ps can lead to resolution degradation of up to 10 ps.

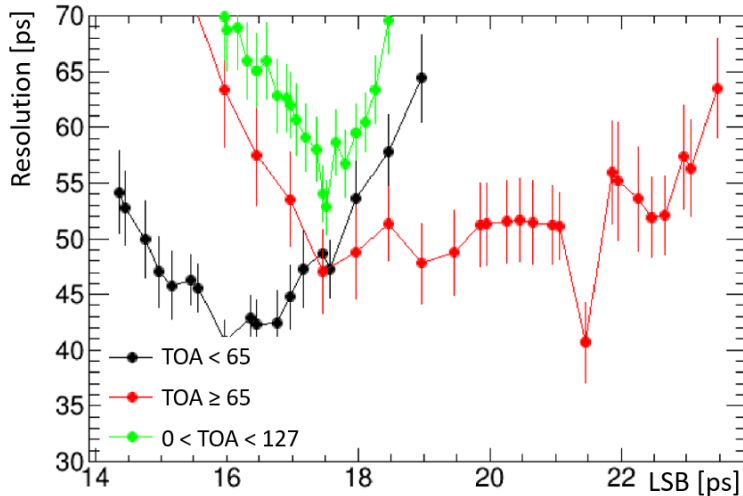


FIGURE 8.11 – ALTIROC3 time resolution dependence on TOA LSB. Green curve curve obtained for $0 < TOA < 127$. Black (red) curve obtained for $TOA < 65$ ($TOA \geq 65$).

In Fig. 8.11 black and red curves show LSB minimization done separately for $TOA < 65$ (later called left (L) TOA sub-region with L LSB) and $TOA \geq 65$ (later called right (R) TOA sub-region with R LSB), respectively. The division is done at 65 because it was observed by looking at TOA distribution, showed on Fig. 8.12a, that the mean count clearly changes around that value. This would not be the case if all TOA bins had the same size in time units, but this observation suggests LSB non-uniformity with a larger value in the second TOA half-range. Sub-range parabolas on Fig. 8.11 shows that

- LSB of lowest sub-range is lower compared to higher sub-range
- The width of the sub-range parabola is wider than the full range, making sub-ranges less sensitive to having a wrong LSB . LSB of two sub-ranges are different by 2–3 ps

In the way minimization method was used, it is subject to instability : significant downward fluctuations can be created during manipulation of ΔT through LSB adjustment : two (lowest in

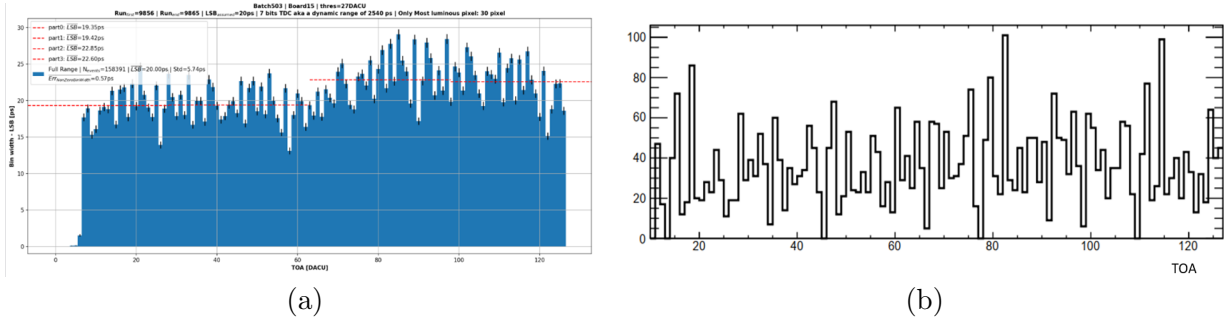


FIGURE 8.12 – (a) ALTIROC3 testbeam TOA distribution, mixed from many pixels [76] (b) ALTIROC3 testbeam one pixel initial TOA distribution

resolution) points in the scan are very close to neighbors in terms of LSB but better in resolution by 5 ps. It can be improved though, by, for example, fitting the parabola and taking and the minimum of fit - in order to smooth the dependence.

8.4.2 LSBs from $t_{MCP} : TOA$ fit

To avoid LSB extraction from spiky unstable dependence shown above, another method was introduced, relying on linearity between time of the MCP measured by digitizer⁸ and TOA of ASIC - it is shown on Fig. 8.13. Focusing on the black line for a moment : it is a fit of correlation, assuming that LSB is the same in the whole TOA range. Its value is 16 ps. This method of getting the LSB is more stable than the one shown on Fig. 8.11 and will be used to obtain final numbers for the resolutions.

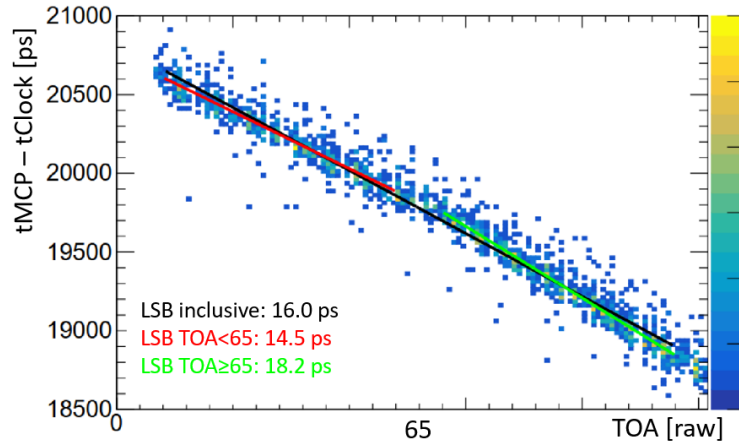


FIGURE 8.13 – ALTIROC3 time of the MCP(digitizer) vs TOA (ASIC) linearity used for TOA LSB extraction

Comparison between LSB obtained from calibration and the one obtained from fit using digitizer information gives different results by up to 2 ps. Same applies to method shown in Sec. 8.4.1 for TOA inclusive case. This is part of the reason why the first attempt of LSB extraction shown in Fig. 8.10 gives bad results - overall LSB scale is wrong.

With the overall scale being fixed, one can look again at Fig. 8.13 focusing now on TOA sub-range dependence. Sub-range fits are shown in red and green, and values obtained⁹ are written in legend - L,R LSBs are different by ≈ 4 ps. At the moment of writing, it is not possible to reproduce

8. now used instead of the oscilloscope

9. this is a different pixel from the one shown on Fig. 8.11

2554 the same behavior in testbench¹⁰ - as shown on Fig. 8.14 (obtained by mixing TOA distributions
 2555 of many pixels). Inclusive LSB is between the left (L), right (R) LSBs - using inclusive TOA LSB
 2556 does not give the minimum of either sub-range, which is why the resolution is worse when using
 2557 only one LSB .

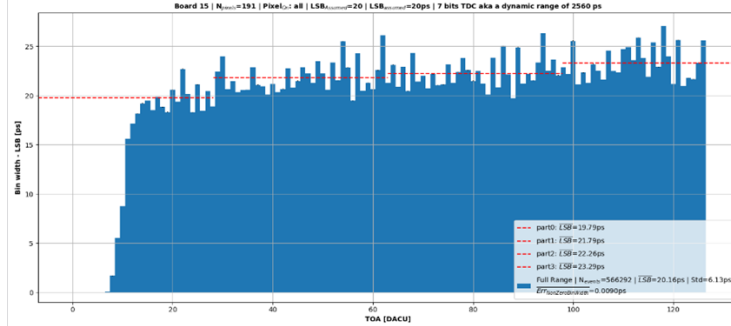


FIGURE 8.14 – ALTIROC3 testbench TOA distribution, mixed from many pixels [76]

2558 8.4.3 Correction for DNL

2559 It would be convenient to bring left and right TOA sub-ranges on equal footing by using the same
 2560 LSB in both of them. LSB uniformization was introduced for this purpose. It was already used in
 2561 Sec. 6.4.6 but no large impact was seen, unlike ALTIROC3. The disadvantage of the method is that
 2562 it's unclear whether it can be used in future HGTD or not, but in any case, it allows us to see the
 2563 magnitude of double-slope by removing it. Starting point of uniformization is TOA distribution per
 2564 pixel, as seen in testbeam¹¹ - an example of such distribution is shown on Fig. 8.12b. Non-uniformity
 2565 is a proxy for Differential Non-Linearity (DNL). The y-axis is the number of counts observed per
 2566 batch per pixel before any cuts. Uniformization is done before applying event selections (like TOTC,
 2567 number of hits etc.) as they can modify the shape of the TOA distribution. It can be seen again
 2568 that the L average count is lower, and the goal is to correct that : for this count in each TOA bin
 2569 (integer) is divided by the average count across all TOA bins (around 30 in this example). The
 2570 average count here sets the overall LSB scale and the uniformization corrects for deviations from it.
 2571 In this way, one corrects for DNL and obtains instead the original TOA_i another variable denoted
 2572 $uniTOA_i$ (short-hand for uniformized TOA)

$$uniTOA_i = \frac{\int_0^{TOA_i} dTOA}{\langle \#TOA \rangle_{0-127}} \quad (8.3)$$

2573 Distribution $uniTOA_i$ of which is shown on Fig. 8.12b. It's expected to be TOA corrected for
 2574 DNL . It's no longer supposed to be an integer because of the division from which it is obtained.
 2575 Relationship between original and uniformized TOA is shown on Fig. 8.15, showing deviation from
 2576 starting line after half-range, showing that correction is happening. With uniformized TOA derived,
 2577 selections are applied, and they are minimal : only one pixel is fired (to avoid noisy events), TOT
 2578 value above 14 (for the same purpose), MCP amplitude above 30 mV (to have a clean time reference
 2579 signal), removal of saturated $TOA > 126$ events.

2580 As mentioned, the uniformization corrects the relative deviation from the overall LSB, but it
 2581 does not give the absolute value of it. To find new proportionality constant¹² between time and

10. testbench partially reproduces absense of hits at low TOA values - but this is a separate issue

11. same can be done in principle with testbench TOA, however, it was seen not to reproduce testbeam TOA and therefore not used

12. words discretization step or LSB are avoided because the variable is not an integer anymore

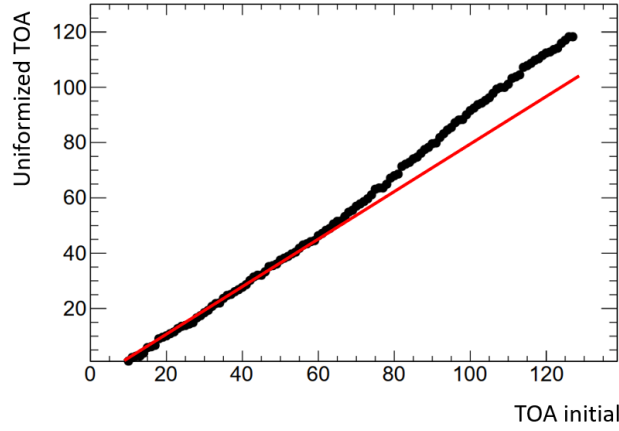


FIGURE 8.15 – Uniformized TOA against original TOA. Red line is a “fit“ on $TOA < 65$ and extrapolated to whole TOA range.

2582 binary TDC same approach as shown in Fig. 8.13 is used, this time on uniformized TOA instead
 2583 of the original one. Example is shown on Fig. 8.16, where single line is describing well the whole
 2584 uniTOA range - this was the goal. While in the previous case, the double-line is visible by comparing
 2585 with sub-range fits, and the whole range fit is overshooting the mean near $TOA=0$ and overshooting
 2586 near $TOA=127$ as a consequence.

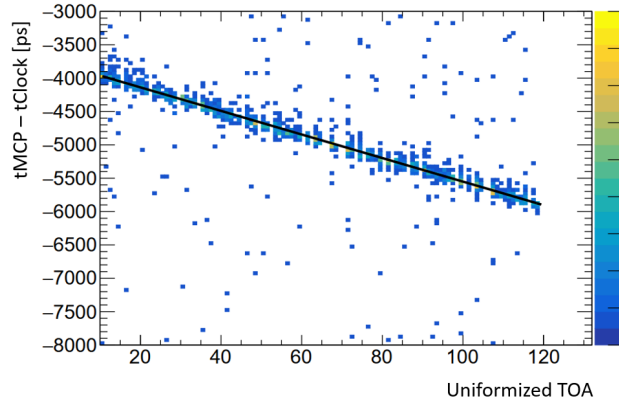


FIGURE 8.16 – Extraction of proportionality constant between uniformized TOA and time

2587 With uniformized TOA and associated LSB obtained, the remainder of time resolution extrac-
 2588 tion is similar to Eq. 8.1 but now with new variables. Familiar ΔT gaussian is obtained, shown for
 2589 one pixel in Fig. 8.17.

$$\Delta T = \underbrace{-uniTOA \times LSB_{uniTOA}}_{t_{ASIC}^{uni}} - \underbrace{t_{MCP}^{trig,CFD} - t_{clock}}_{t_{MCP}} \quad (8.4)$$

2590 8.4.4 TOT-inclusive timewalk correction

2591 Lastly, timewalk correction is applied, shown on Fig. 8.18a. Contrary to previous studies, upper
 2592 TOT cut is not applied to avoid possible under-estimation of resolution (event in the tail is known
 2593 to have a worse resolution, but the tail is included which degraded the resolution by ≈ 1 ps). The
 2594 timewalk correction, however, is not giving much improvement because, as can be seen from the
 2595 distribution, dominating fraction of events is concentrated in small ASIC TOT slice - width of
 2596 projection into Y (time resolution) has a small contribution from the timewalk slope - there is not

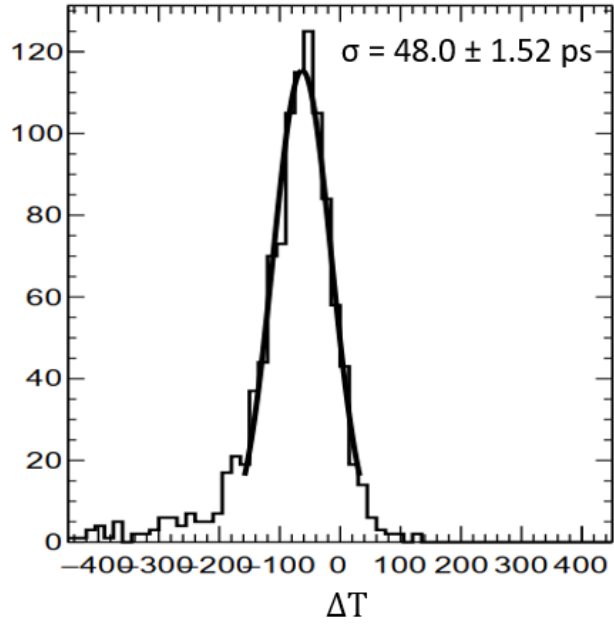


FIGURE 8.17 – Uniformized ΔT together with fit used in time resolution, before timewalk correction

much to correct in the first place because of the high bias voltage used and high amplitude as a consequence. Resulting ΔT is shown on Fig. 8.18b

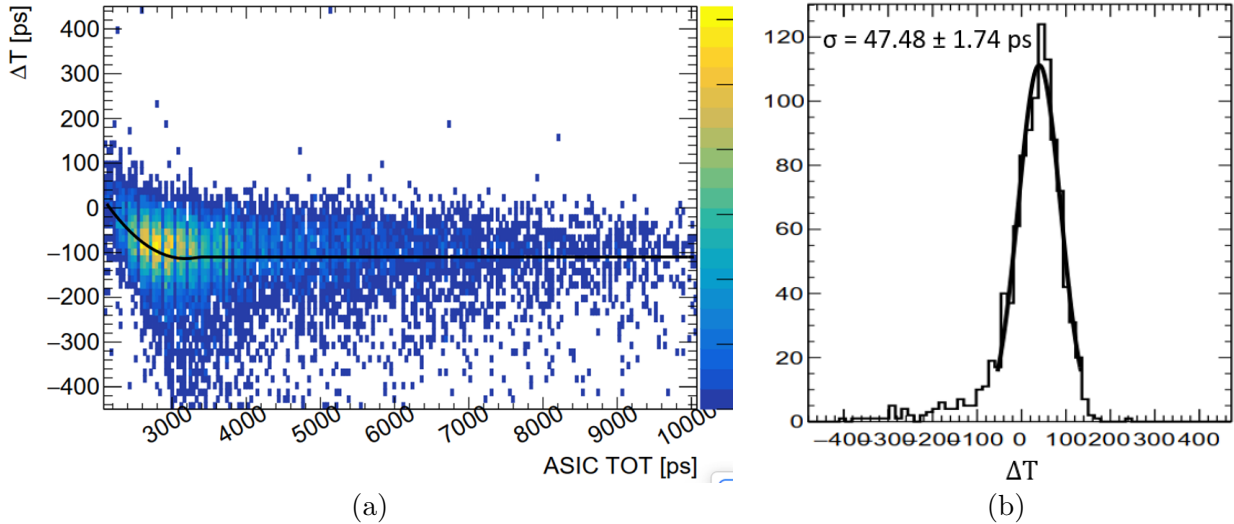


FIGURE 8.18 – (a) ASIC TOT timewalk correction (b) Uniformized ΔT together with fit used in time resolution after timewalk correction with ASIC TOT

With uniformization and timewalk correction applied, one can compare results with separate sub-ranges. Four sub-ranges result is shown on Fig. 8.19, showing that all four sub-ranges have comparable time resolution at the level of 43 ps. This result can be compared to the uniformized time resolution shown in Fig. 8.20. Without uniformization, the average is 48.4 ps; therefore, the quadratic contribution of the non-linearity is ≈ 20 ps.

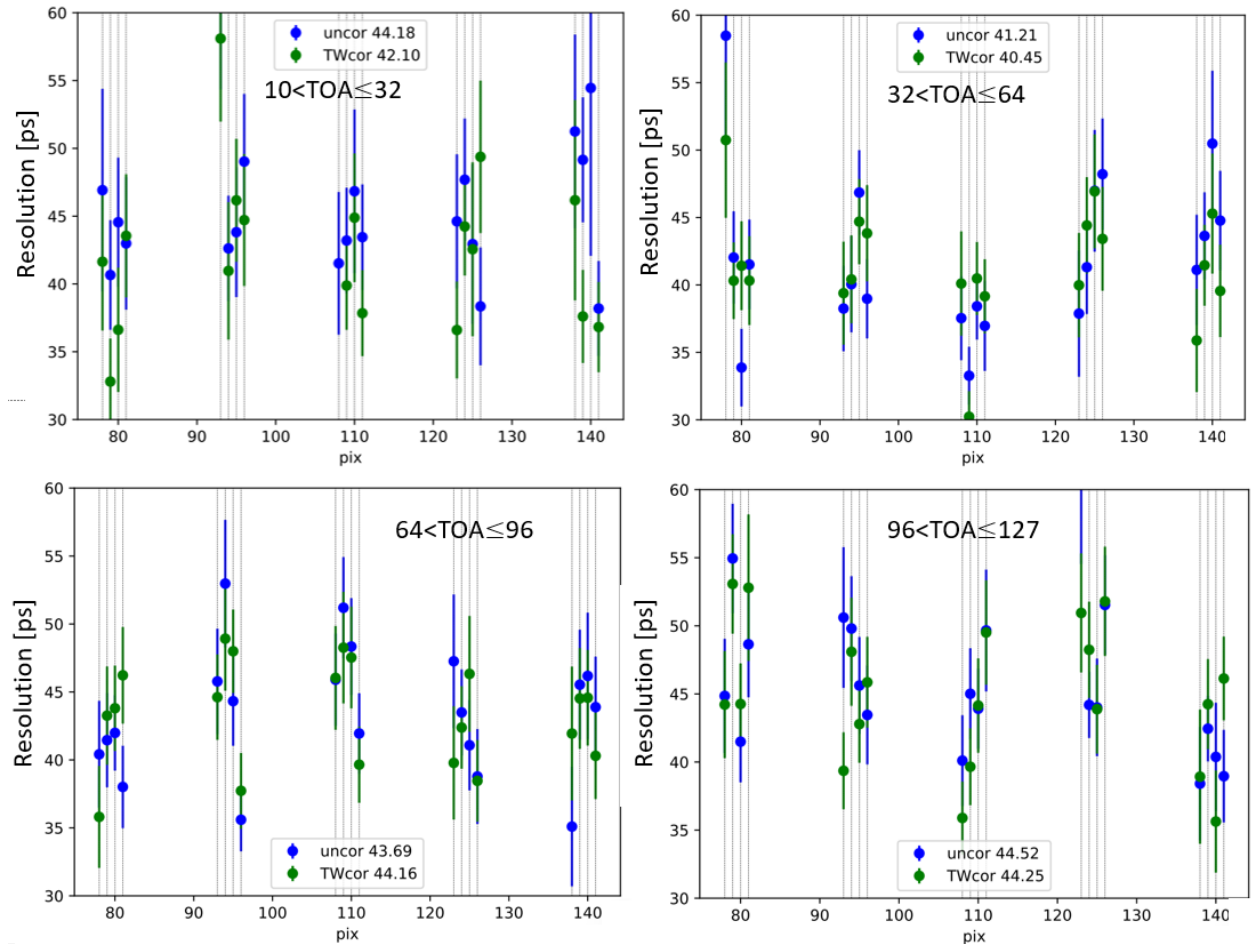


FIGURE 8.19 – ALTIROC3 time resolution before and after timewalk correction in four TOA sub-ranges, without uniformization

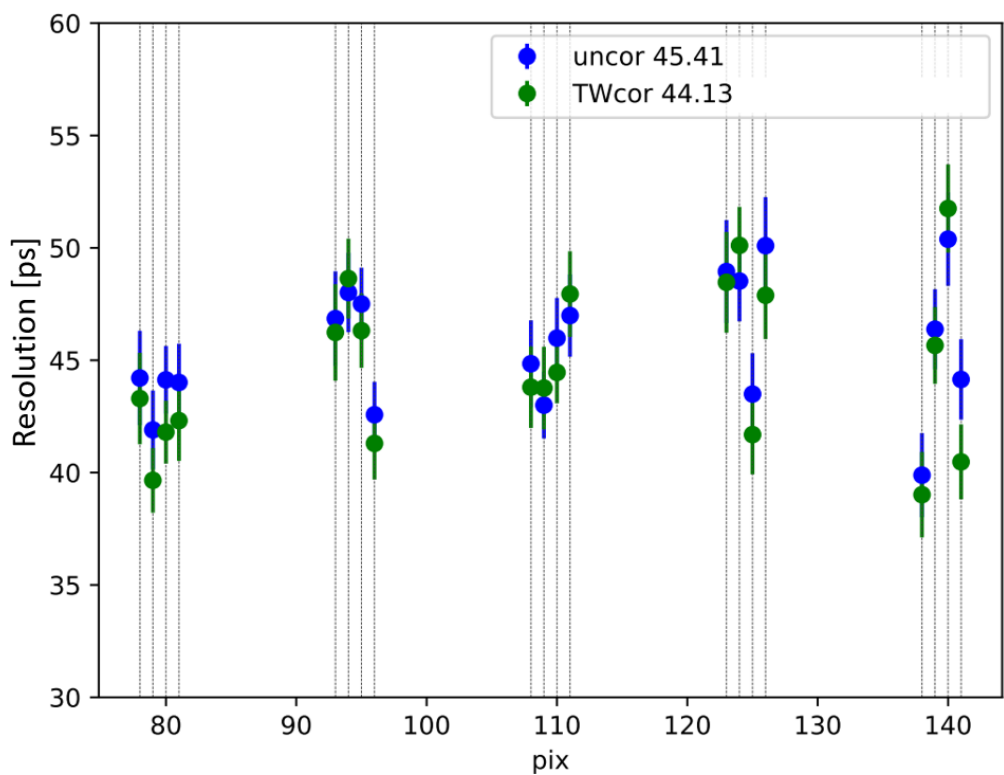


FIGURE 8.20 – ALTIROC3 time resolution before and after timewalk correction, after uniformization

8.4.5 Summary of different configurations

Measurements were done for two boards in different configurations, summarized in Table 8.3, also including measurements at low temperatures. For all batches the threshold is 10.8 fC (with expected signal, 20 fC, being much larger) and all pixels are activated. Temperature listed was not stabilized. Time resolutions obtained are summarized in Table 8.4, showing average resolution over typically ≈ 20 pixels. Uncertainty is at the level of 0.5 ps. No upper amplitude (TOT) cut is applied. For both TOA and uniTOA, whole range of values is used. The timewalk correction, done with ASIC TOTC+TOTF, is only helpful at lower voltages as shown in “TW corr gain in quadrature“ column. The TOA uniformization gain is at the level of 19–30 ps in quadrature - see “uniTOA gain in quadrature“ column.

Batch	Board	Temp	Voltage
300	B27	room	200 V
314	B27	room	193 V
1103	B27	-30	146 V
502	B15	room	200 V
504	B15	room	195 V
506	B15	room	203 V

TABLE 8.3 – Summary of ALTIROC3 testbeam batches

Batch	TOA	TOA, TW corr	uniTOA	uniTOA, TW corr	uniTOA gain in quadra- ture	TW corr gain in quadra- ture
300	55.1	55.0	48.4	48.8	25.0	10.8
314	60.18	59.0	53.0	50.2	30.1	17.0
1103	48.8	48.4	45.4	44.1	19.8	-
502	58.4	59.0	53.5	49.9	31.5	19.3
504	58.5	59.0	56.7	50.2	30.1	26.3
506	57.6	55.2	52.1	47.6	27.8	21.2

TABLE 8.4 – Summary of ALTIROC3 testbeam results with Table 8.3 batches

₂₆₁₄ A - $Z \rightarrow \ell\bar{\ell} + \text{jets}$ basic distributions

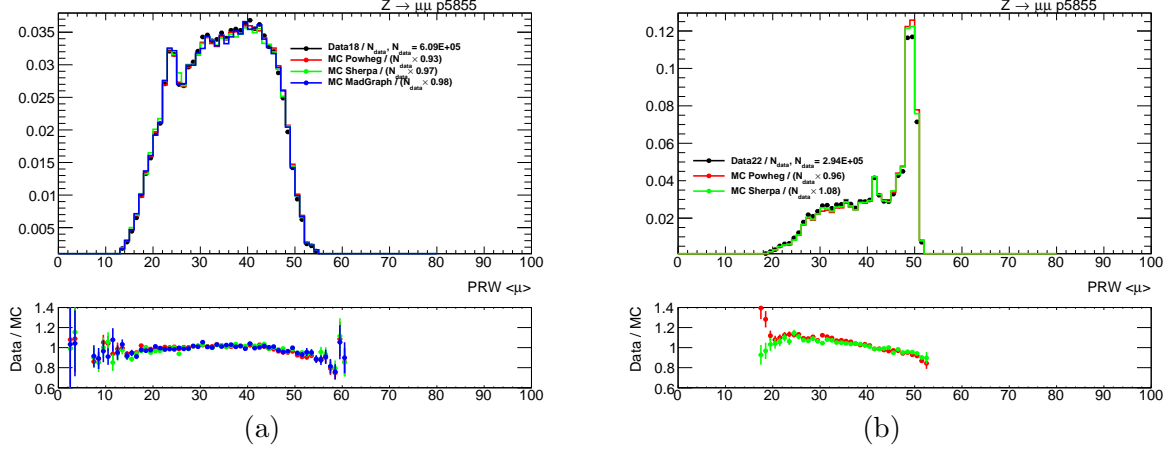


FIGURE A.1 – Data/MC comparison of Pileup Reweighted $\bar{\mu}$, fJVT calibration fiducial selection
(a) Run-2 : 2018 $Z \rightarrow \mu\bar{\mu}$ (b) Run-3 : 2022 $Z \rightarrow \mu\bar{\mu}$

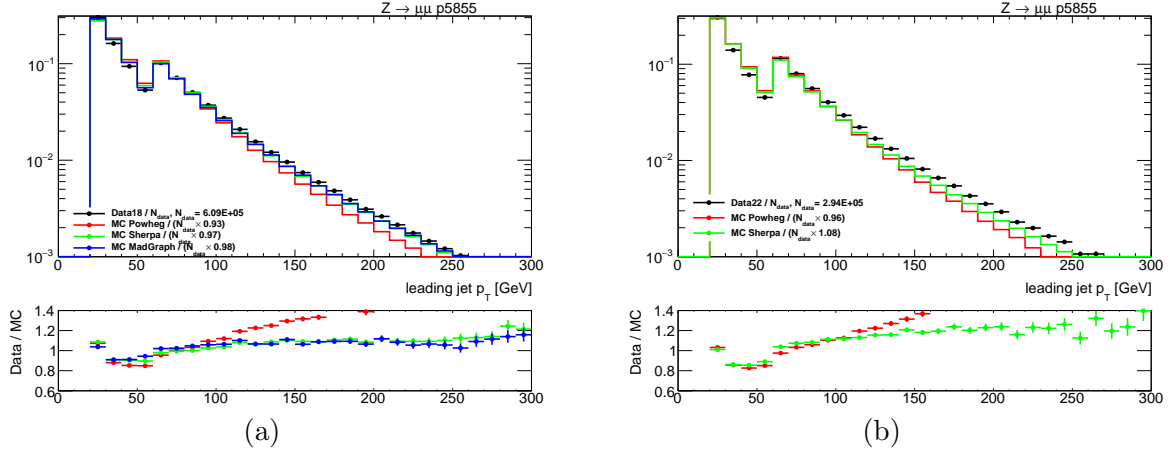


FIGURE A.2 – Data/MC comparison of p_T -leading jet p_T , fJVT calibration fiducial selection (a)
Run-2 : 2018 $Z \rightarrow \mu\bar{\mu}$ (b) Run-3 : 2022 $Z \rightarrow \mu\bar{\mu}$

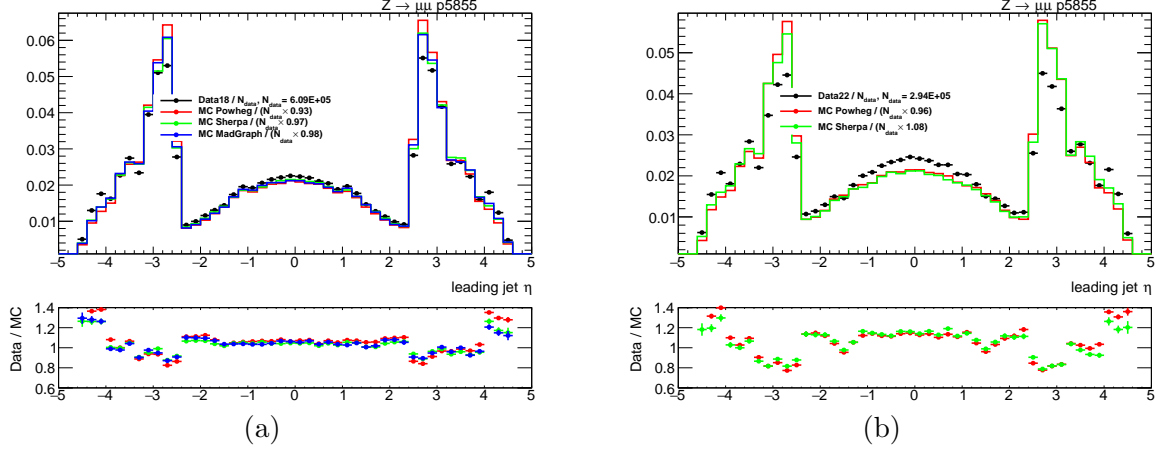


FIGURE A.3 – Data/MC comparison of p_T -leading jet η , fJVT calibration fiducial selection (a) Run-2 : 2018 $Z \rightarrow \mu\bar{\mu}$ (b) Run-3 : 2022 $Z \rightarrow \mu\bar{\mu}$

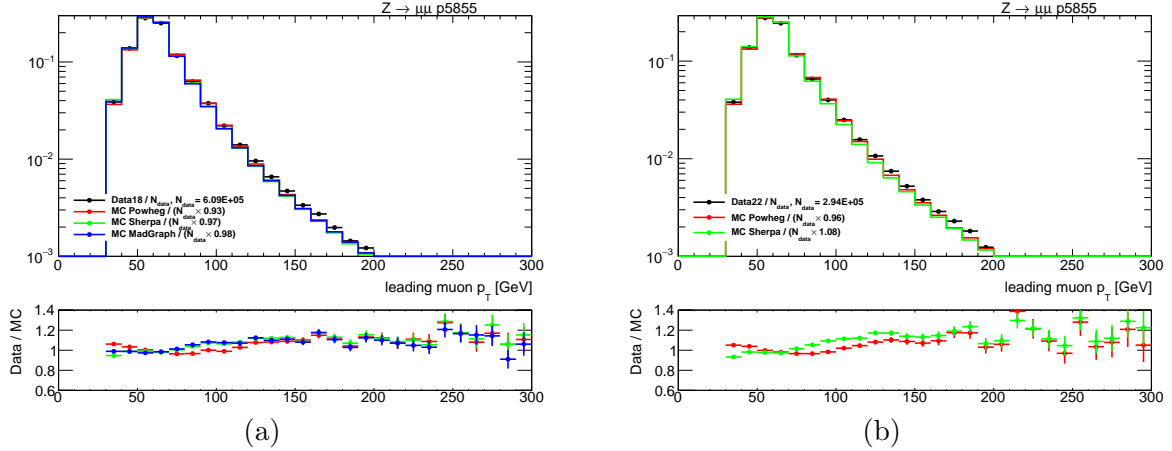


FIGURE A.4 – Data/MC comparison of p_T -leading muon p_T , fJVT calibration fiducial selection (a) Run-2 : 2018 $Z \rightarrow \mu\bar{\mu}$ (b) Run-3 : 2022 $Z \rightarrow \mu\bar{\mu}$

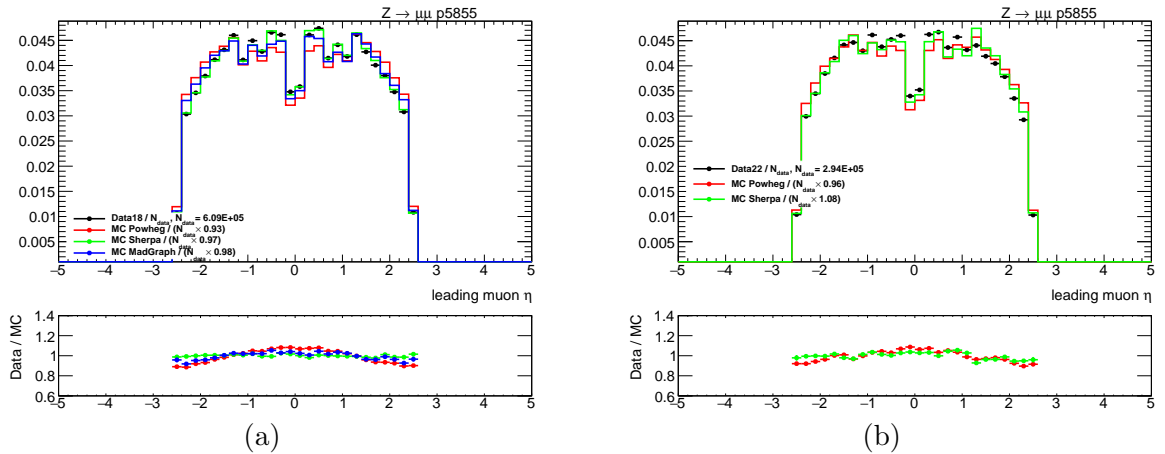


FIGURE A.5 – Data/MC comparison of p_T -leading muon η , fJVT calibration fiducial selection (a) Run-2 : 2018 $Z \rightarrow \mu\bar{\mu}$ (b) Run-3 : 2022 $Z \rightarrow \mu\bar{\mu}$

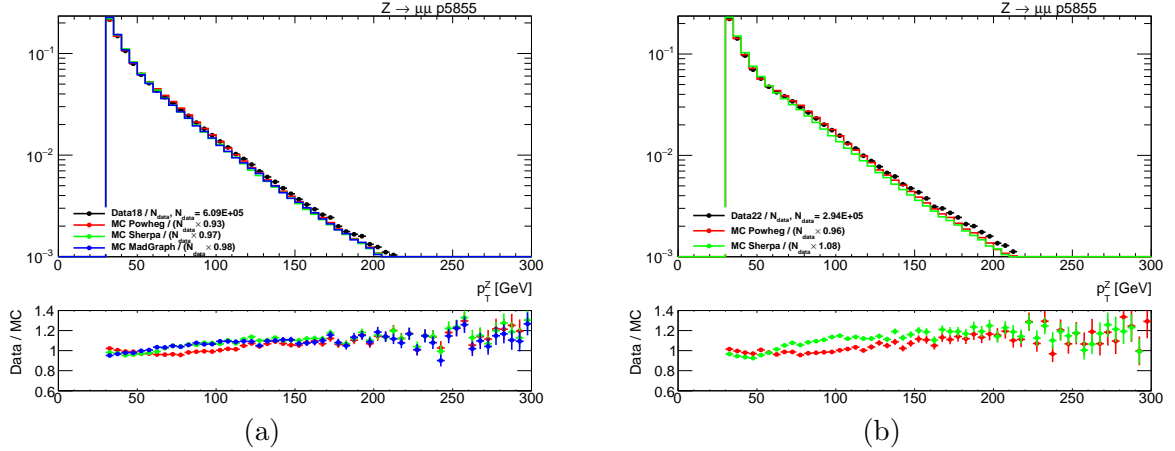


FIGURE A.6 – Data/MC comparison of p_T^Z of Z reconstructed from two leptons, fJVT calibration fiducial selection (a) Run-2 : 2018 $Z \rightarrow \mu\bar{\mu}$ (b) Run-3 : 2022 $Z \rightarrow \mu\bar{\mu}$

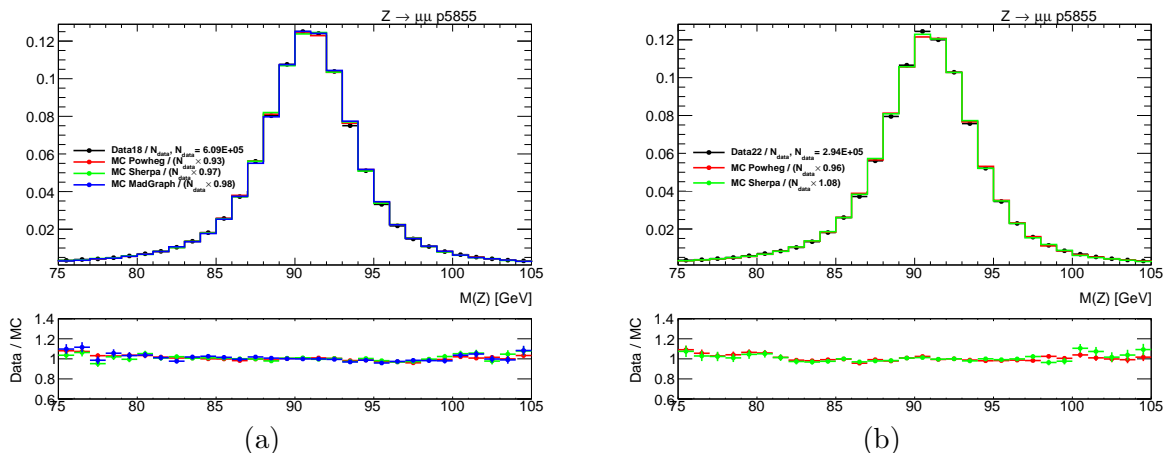


FIGURE A.7 – Data/MC comparison of m_Z of Z reconstructed from two leptons, fJVT calibration fiducial selection (a) Run-2 : 2018 $Z \rightarrow \mu\bar{\mu}$ (b) Run-3 : 2022 $Z \rightarrow \mu\bar{\mu}$

₂₆₁₅ B - ε_{HS} , SF, σ_{SF} for Tighter WP

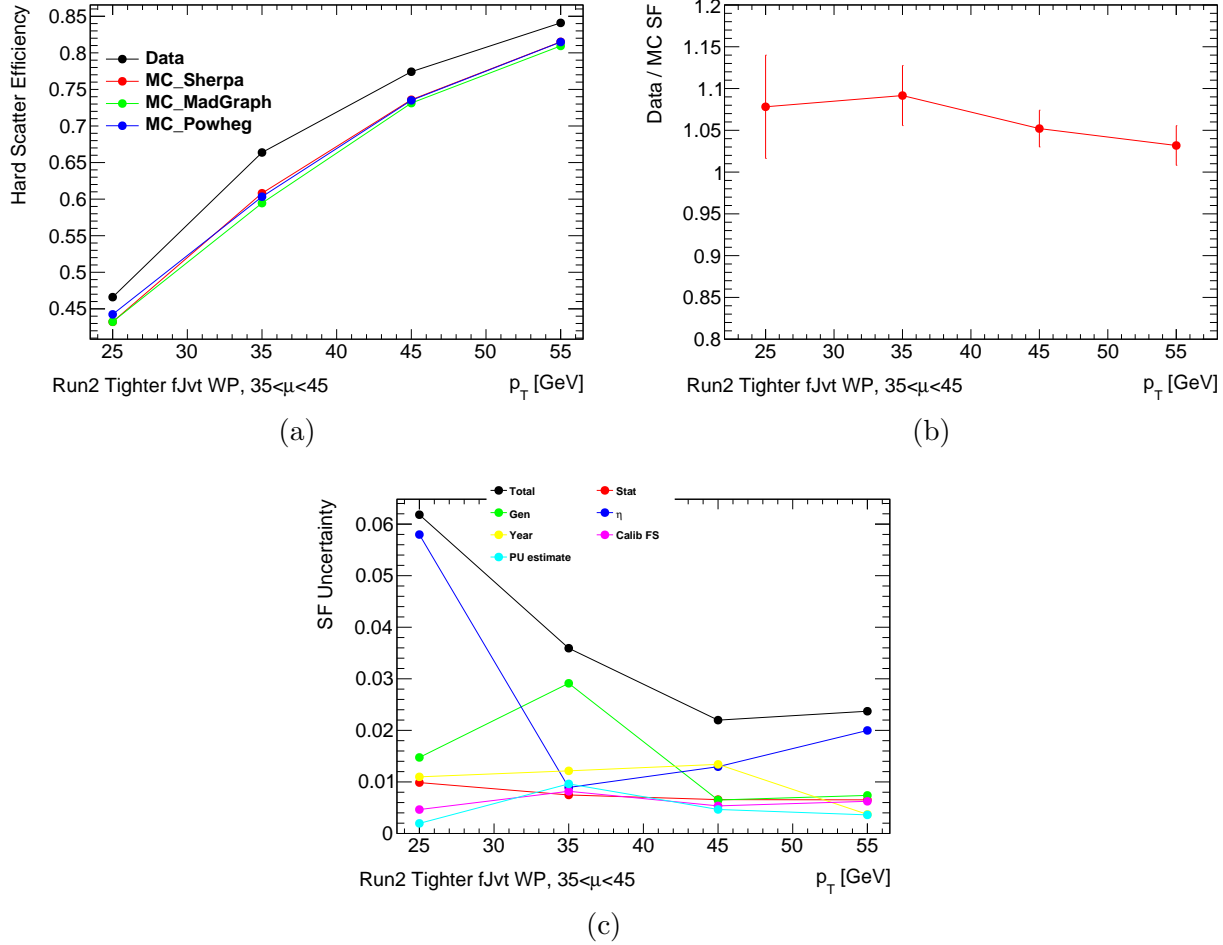


FIGURE B.1 – Run2 calibration results in $35 < \bar{\mu} \leq 45$, Tighter working point (a) Hard-Scatter efficiency (b) Scale Factor (c) Scale Factor uncertainty breakdown

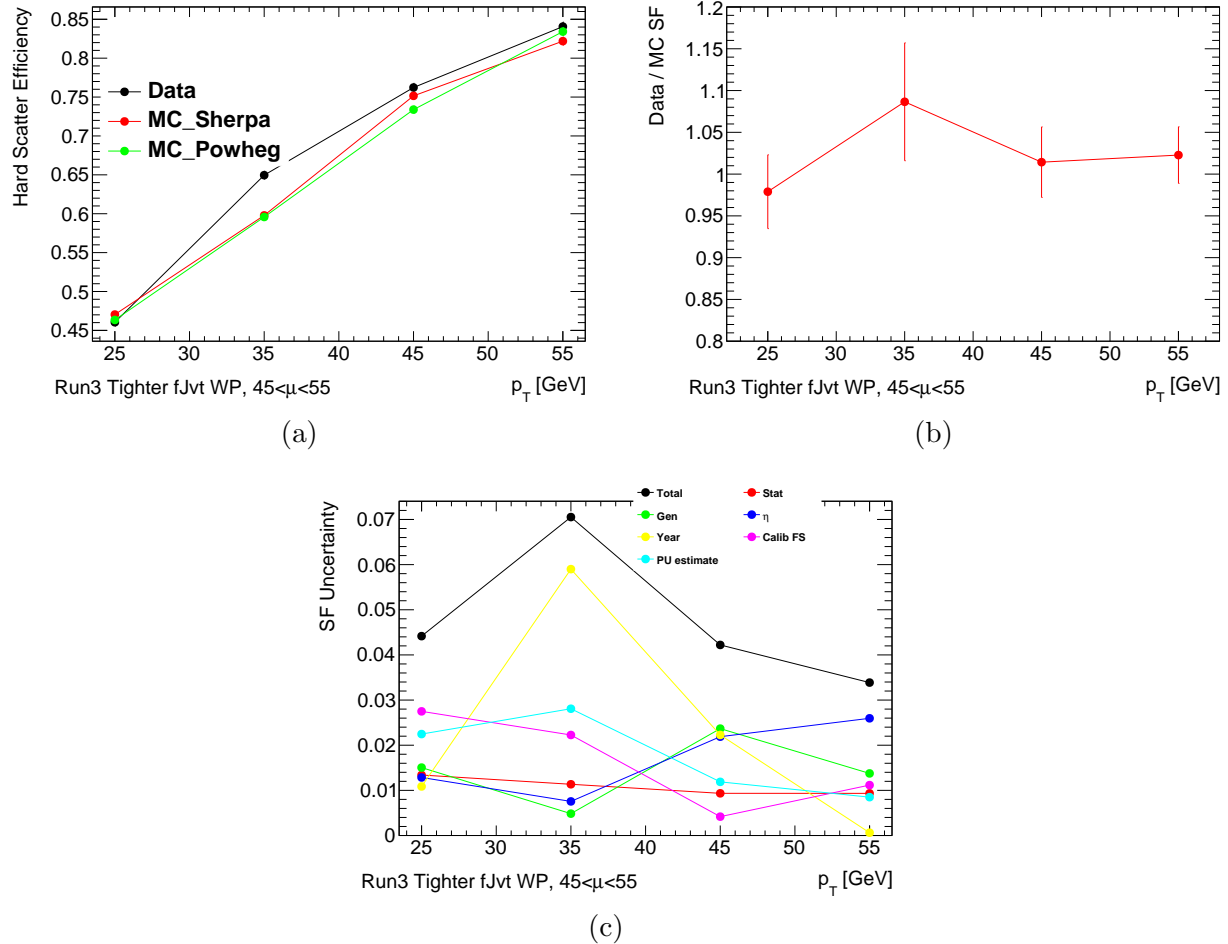


FIGURE B.2 – Run3 calibration results in $45 < \bar{\mu} \leq 55$, Tighter working point (a) Hard-Scatter efficiency (b) Scale Factor (c) Scale Factor uncertainty breakdown

₂₆₁₆ C - ε_{HS} , SF, σ_{SF} for Loose WP

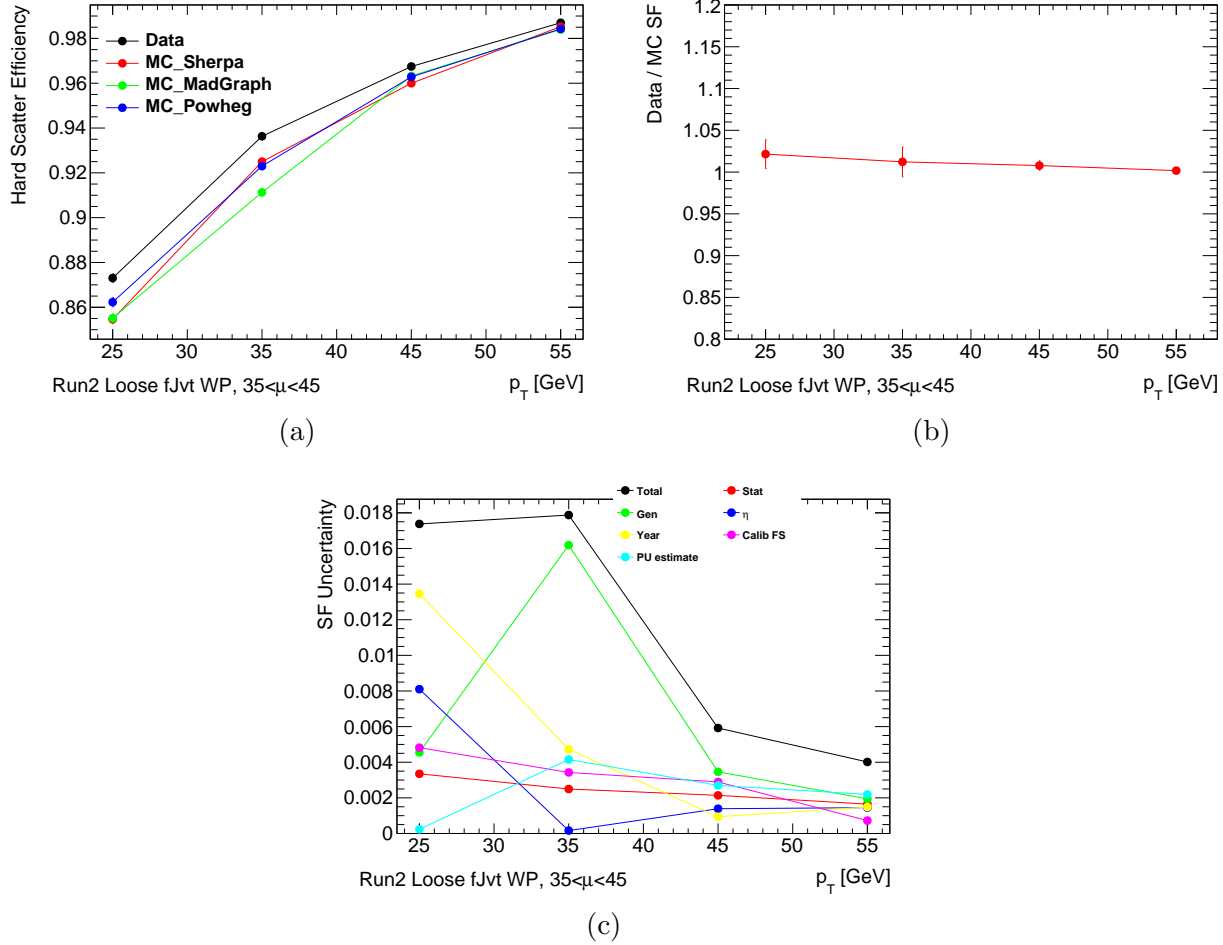


FIGURE C.1 – Run2 calibration results in $35 < \bar{\mu} \leq 45$, Loose working point (a) Hard-Scatter efficiency (b) Scale Factor (c) Scale Factor uncertainty breakdown

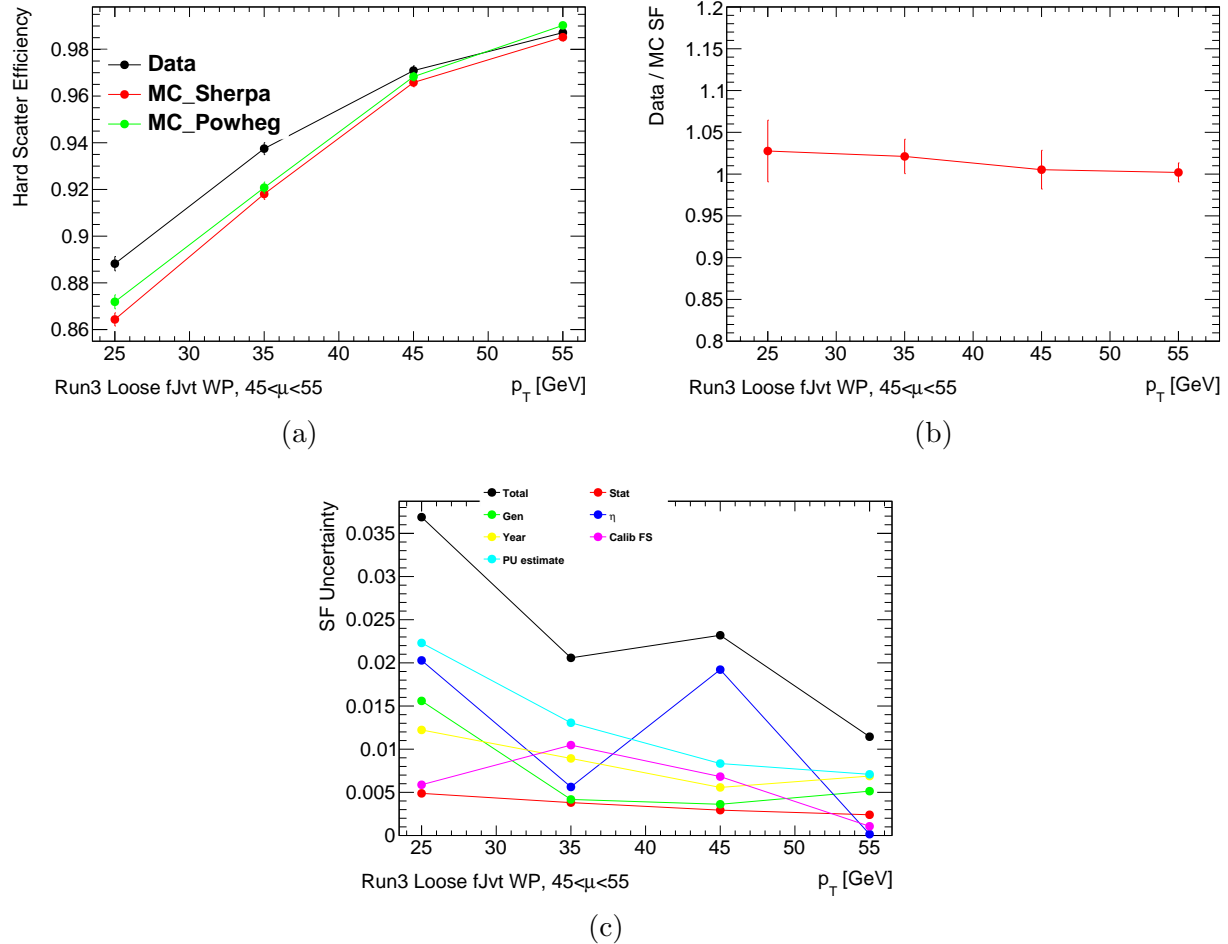


FIGURE C.2 – Run3 calibration results in $45 < \bar{\mu} \leq 55$, Loose working point (a) Hard-Scatter efficiency (b) Scale Factor (c) Scale Factor uncertainty breakdown

₂₆₁₇ D - $Z(\rightarrow \bar{\nu}\nu)\gamma$ replacements

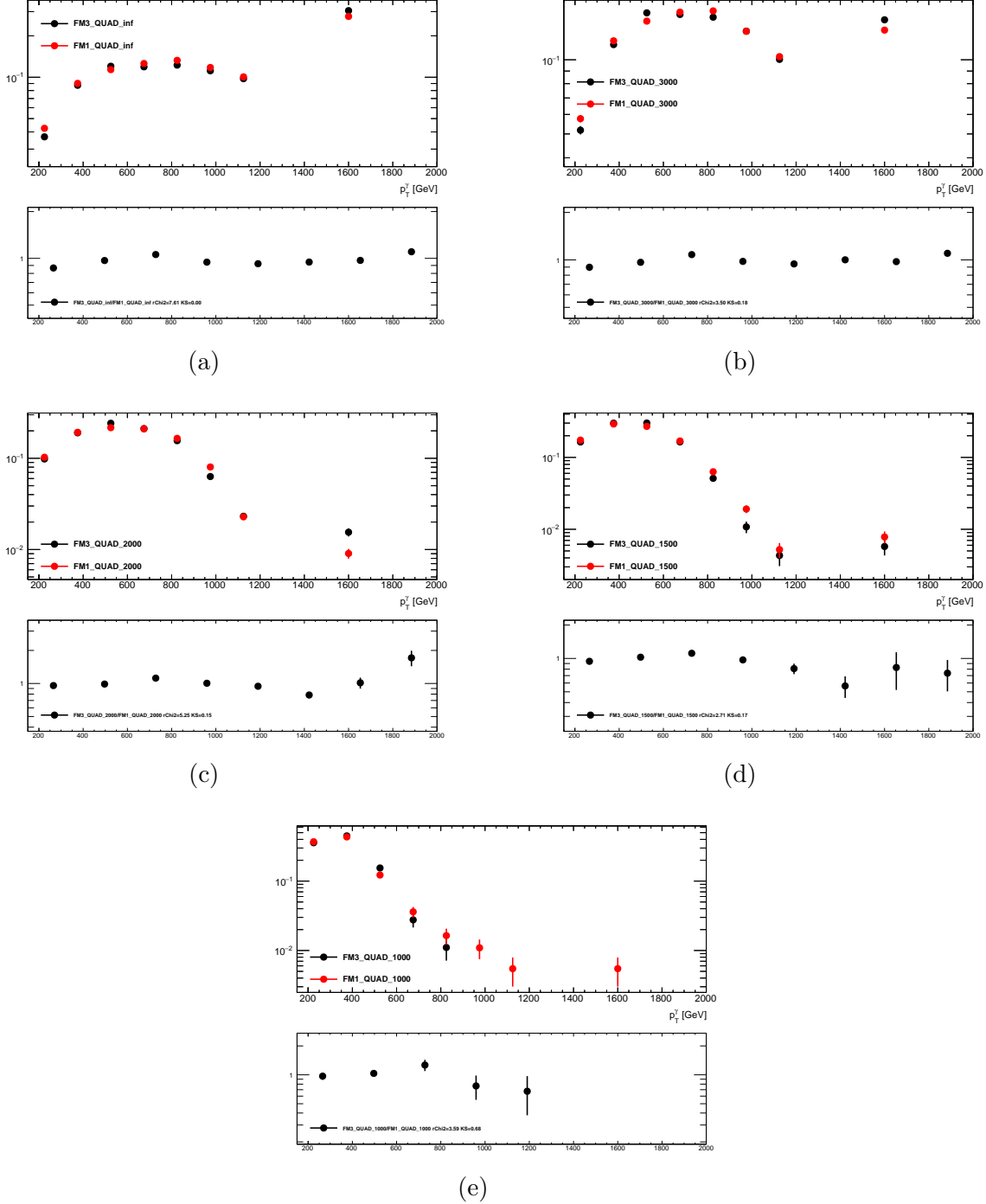


FIGURE D.1 – FM3vsFM1 shape comparison obtained in $Z(\rightarrow \bar{\nu}\nu)\gamma$ sample, replicating analysis selections. Bins match those used in the analysis. The bottom pad is the ratio between two operator shapes (a) without clipping (b) clipping=3000 (c) clipping=2000 (d) clipping=1500 (e) clipping=1000

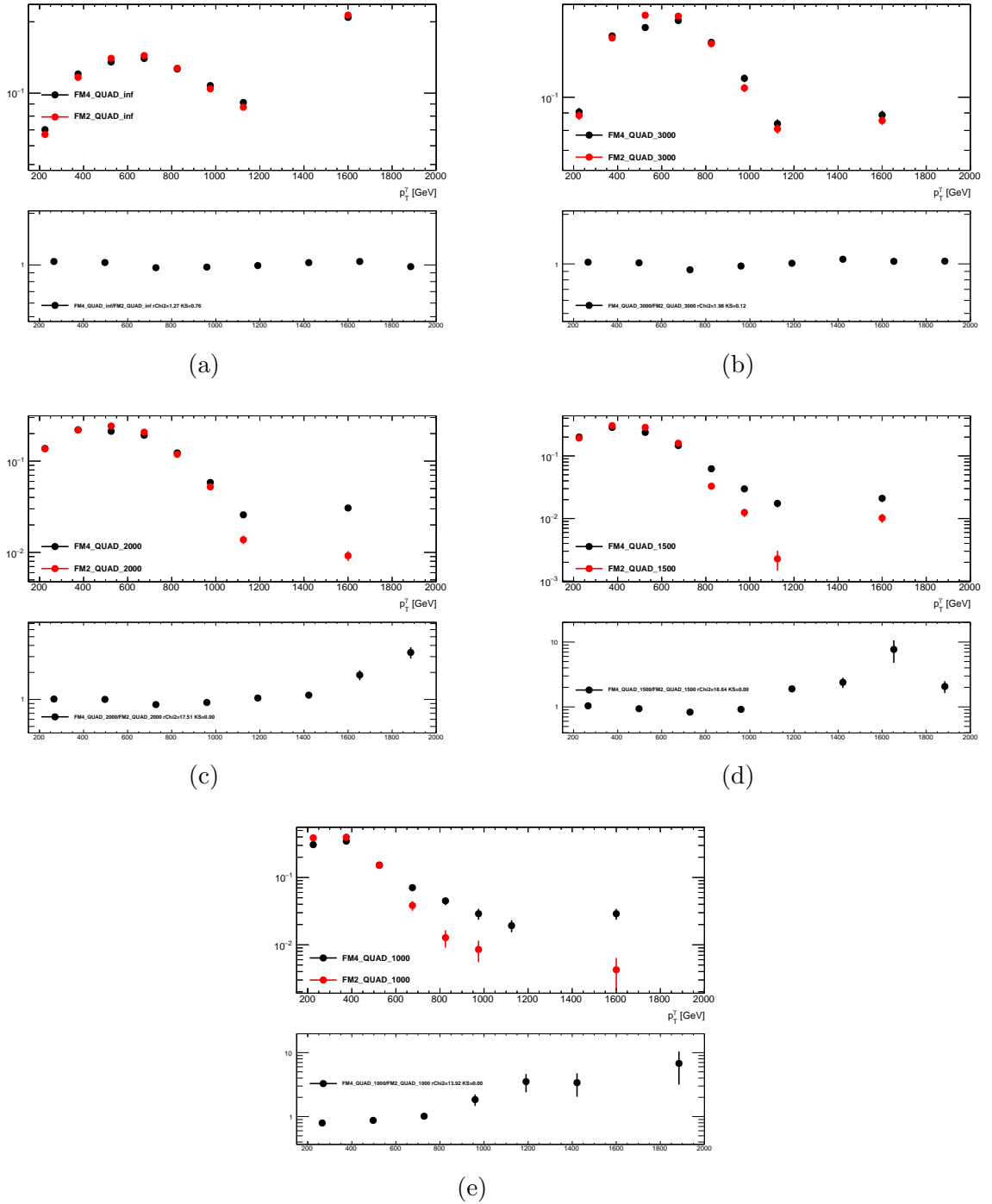


FIGURE D.2 – FM4vsFM2 shape comparison obtained in $Z(\rightarrow \bar{\nu}\nu)\gamma$ sample, replicating analysis selections. Bins match those used in the analysis. The bottom pad is the ratio between two operator shapes (a) without clipping (b) clipping=3000 (c) clipping=2000 (d) clipping=1500 (e) clipping=1000

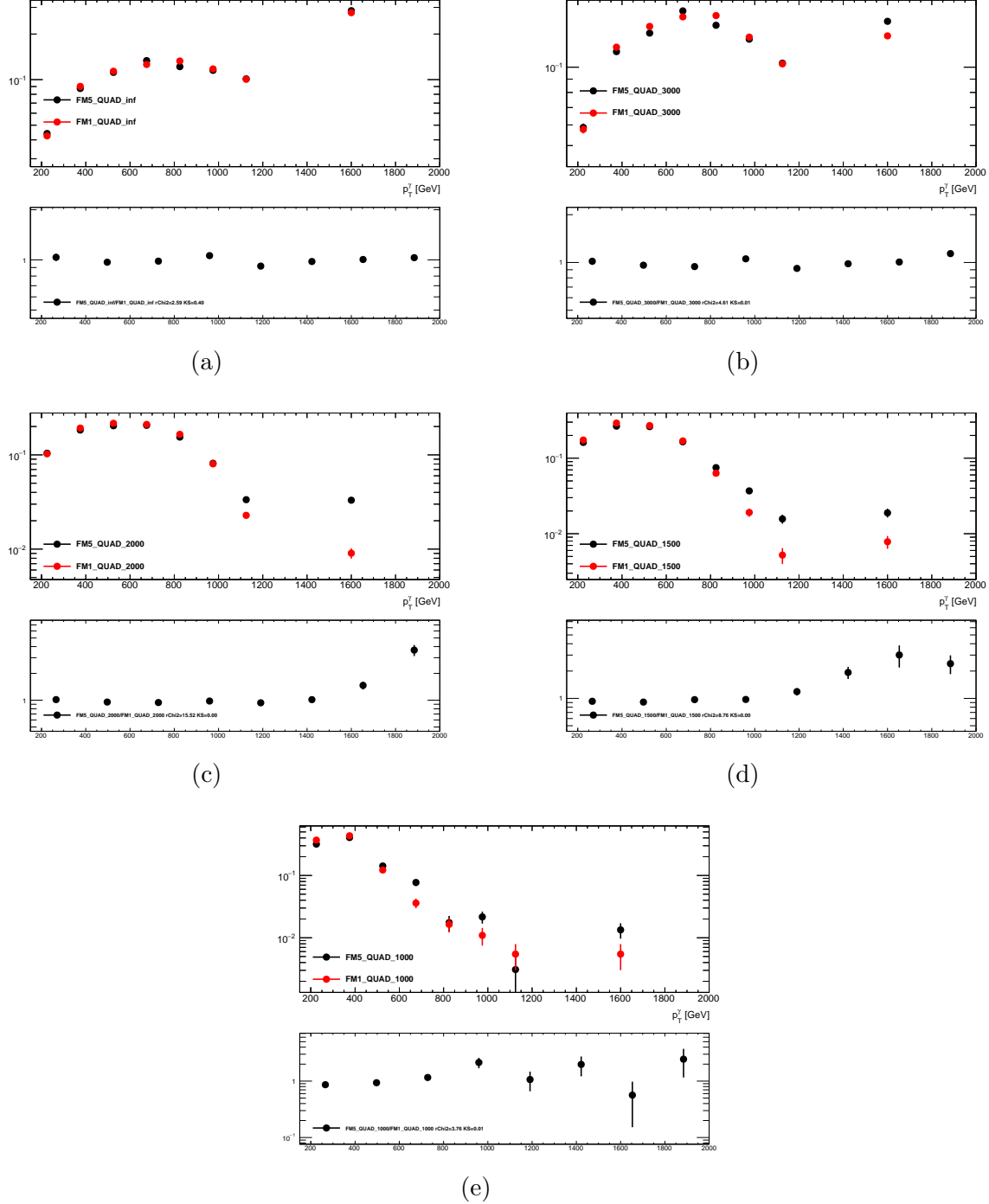


FIGURE D.3 – FM5vsFM1 shape comparison obtained in $Z(\rightarrow \bar{\nu}\nu)\gamma$ sample, replicating analysis selections. Bins match those used in the analysis. The bottom pad is the ratio between two operator shapes (a) without clipping (b) clipping=3000 (c) clipping=2000 (d) clipping=1500 (e) clipping=1000

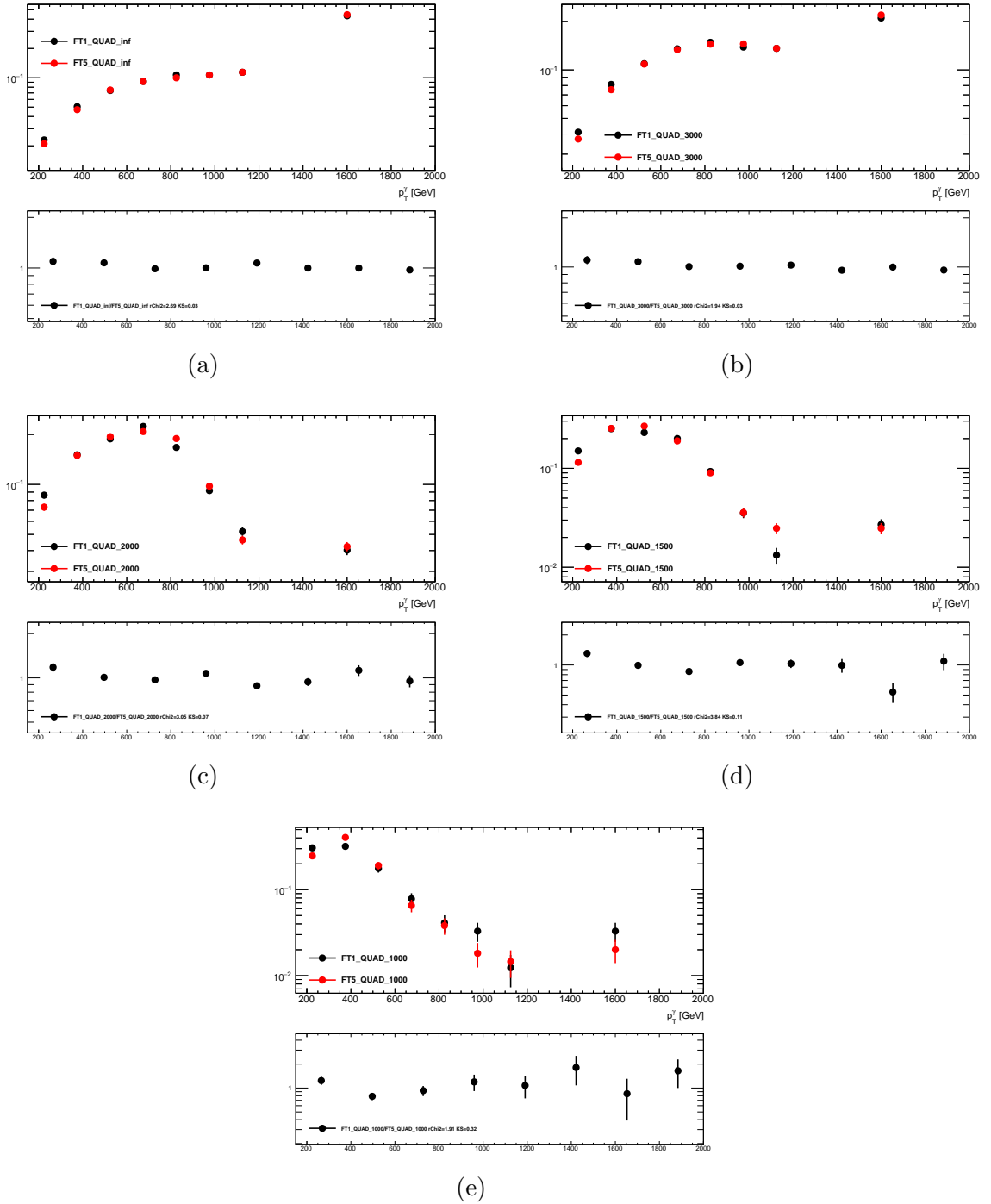


FIGURE D.4 – FT1vsFT5 shape comparison obtained in $Z(\rightarrow \bar{\nu}\nu)\gamma$ sample, replicating analysis selections. Bins match those used in the analysis. The bottom pad is the ratio between two operator shapes (a) without clipping (b) clipping=3000 (c) clipping=2000 (d) clipping=1500 (e) clipping=1000

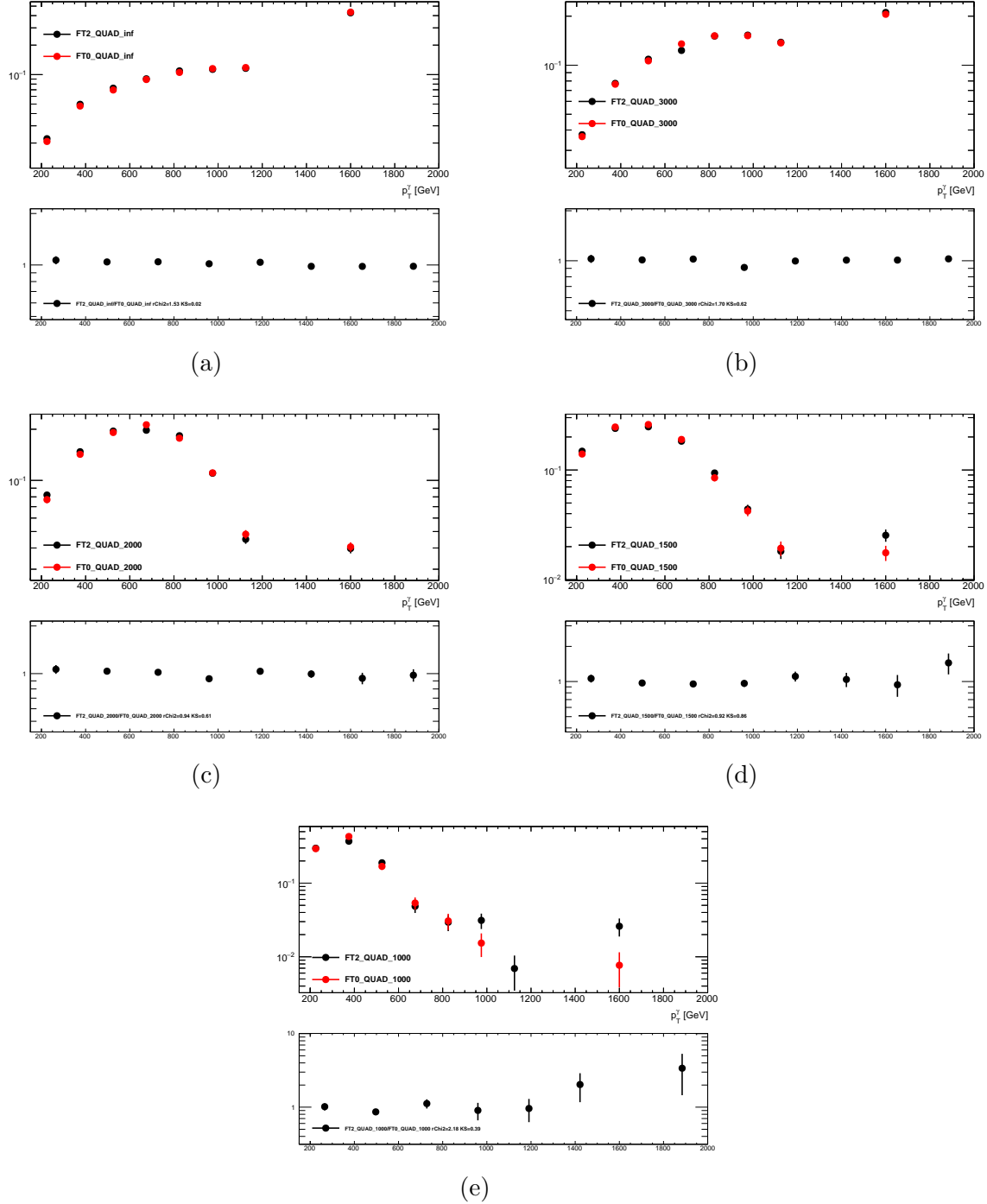


FIGURE D.5 – FT2vsFT0 shape comparison obtained in $Z(\rightarrow \bar{\nu}\nu)\gamma$ sample, replicating analysis selections. Bins match those used in the analysis. The bottom pad is the ratio between two operator shapes (a) without clipping (b) clipping=3000 (c) clipping=2000 (d) clipping=1500 (e) clipping=1000

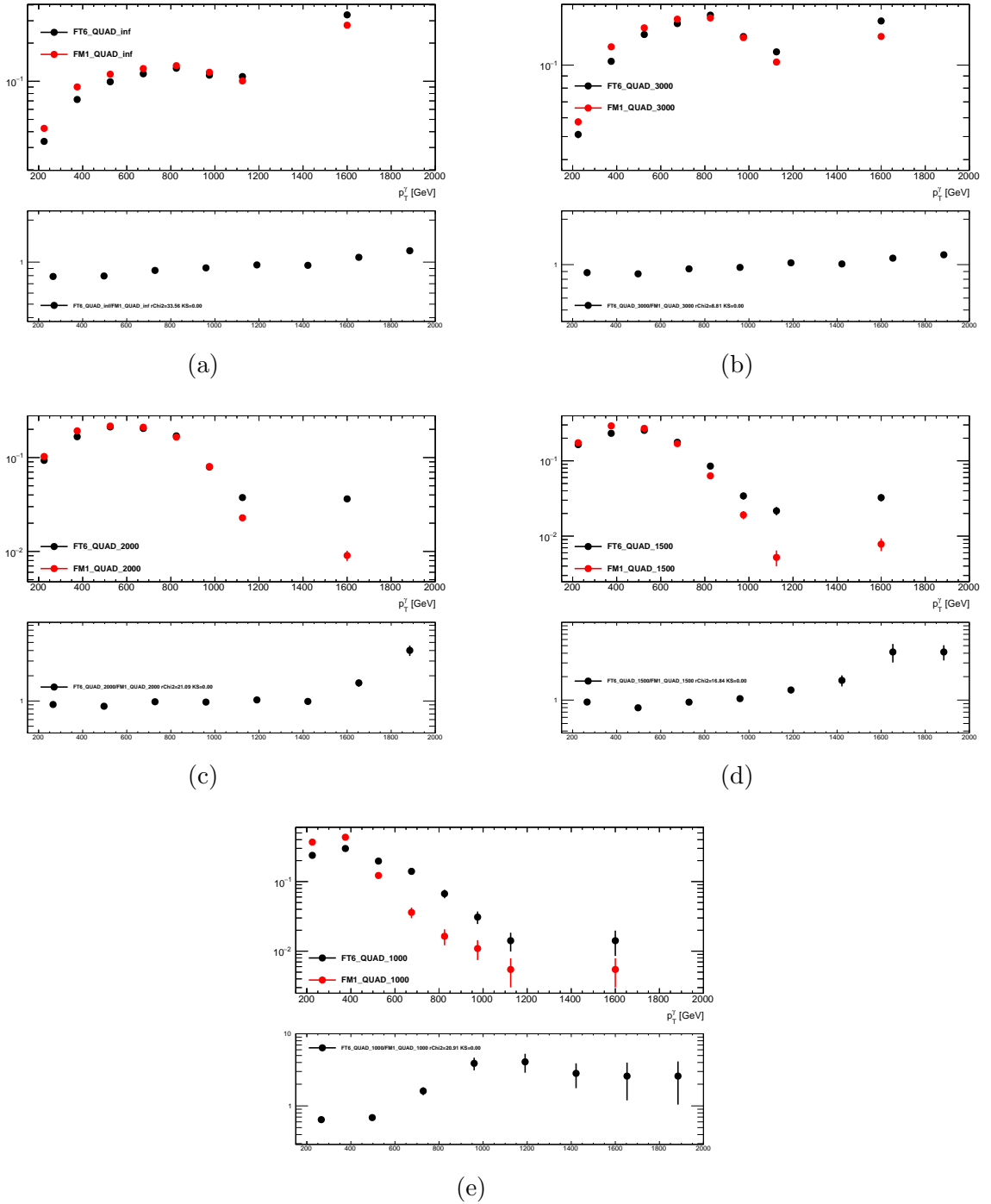


FIGURE D.6 – FT6vsFM1 shape comparison obtained in $Z(\rightarrow \bar{\nu}\nu)\gamma$ sample, replicating analysis selections. Bins match those used in the analysis. The bottom pad is the ratio between two operator shapes (a) without clipping (b) clipping=3000 (c) clipping=2000 (d) clipping=1500 (e) clipping=1000

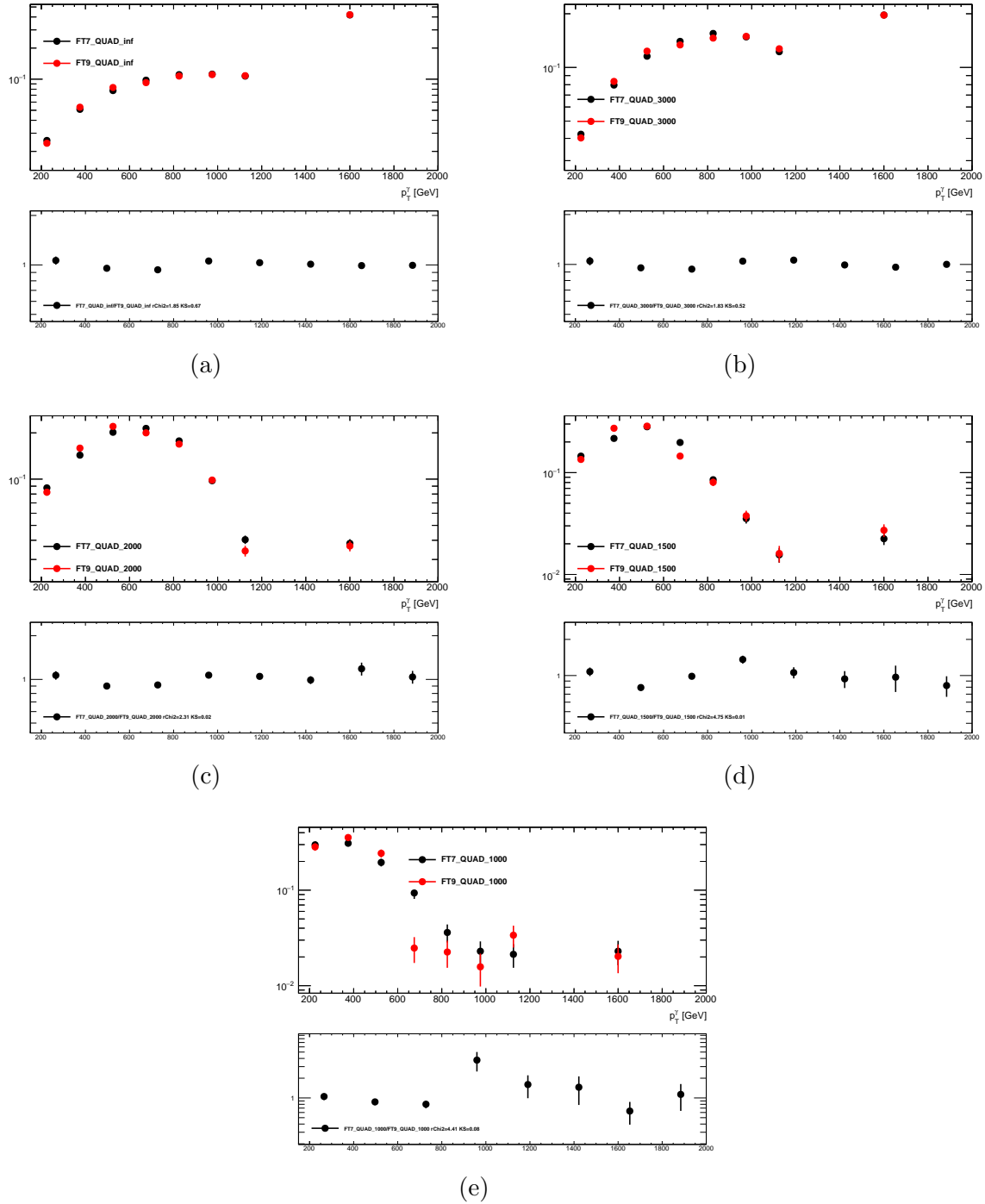


FIGURE D.7 – FT7vsFT9 shape comparison obtained in $Z(\rightarrow \bar{\nu}\nu)\gamma$ sample, replicating analysis selections. Bins match those used in the analysis. The bottom pad is the ratio between two operator shapes (a) without clipping (b) clipping=3000 (c) clipping=2000 (d) clipping=1500 (e) clipping=1000

₂₆₁₈ E - $Z(\rightarrow \bar{\nu}\nu)\gamma$ replacements validation fits

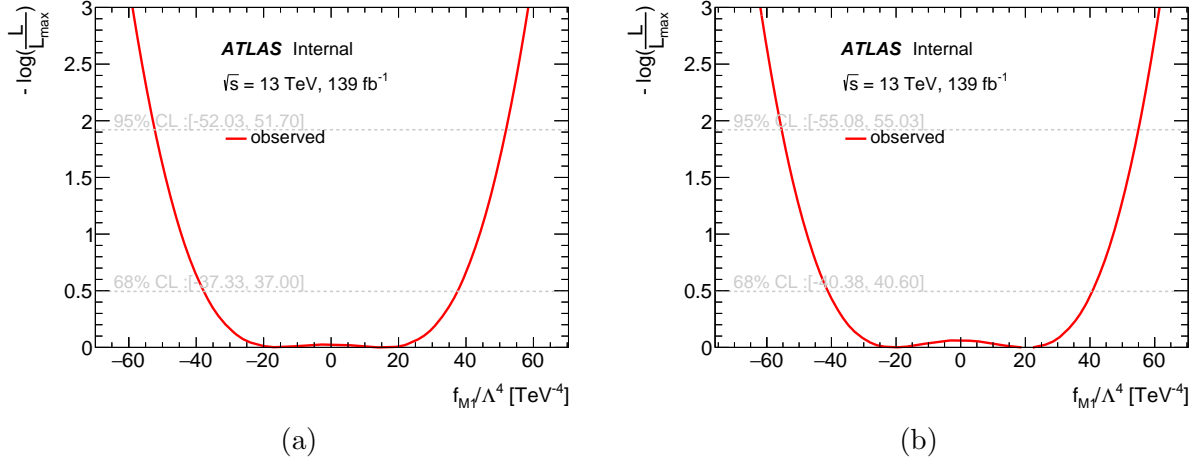


FIGURE E.1 – $Z(\rightarrow \bar{\nu}\nu)\gamma$ analysis replacement validation : comparison between M1 (a) original limit (b) replaced limit

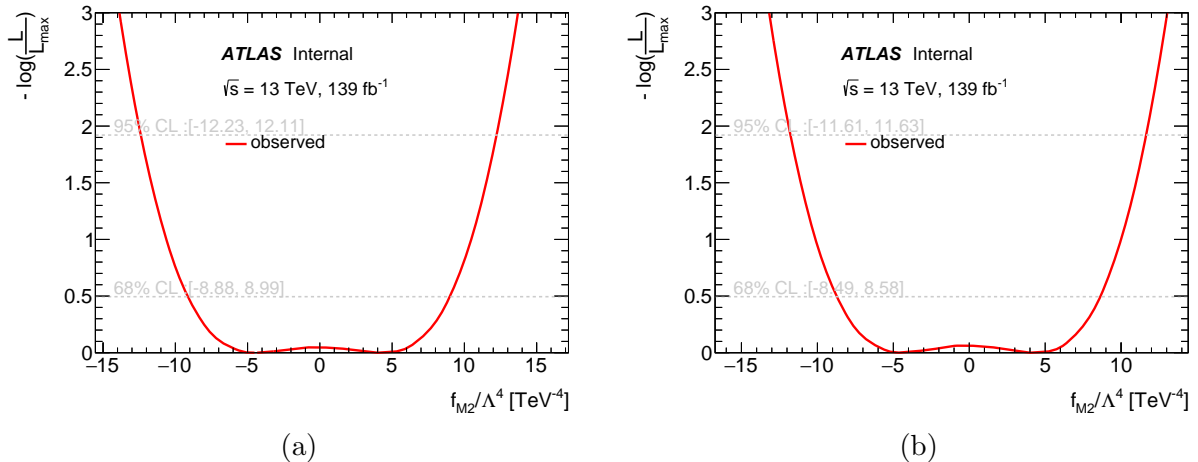


FIGURE E.2 – $Z(\rightarrow \bar{\nu}\nu)\gamma$ analysis replacement validation : comparison between M2 (a) original limit (b) replaced limit

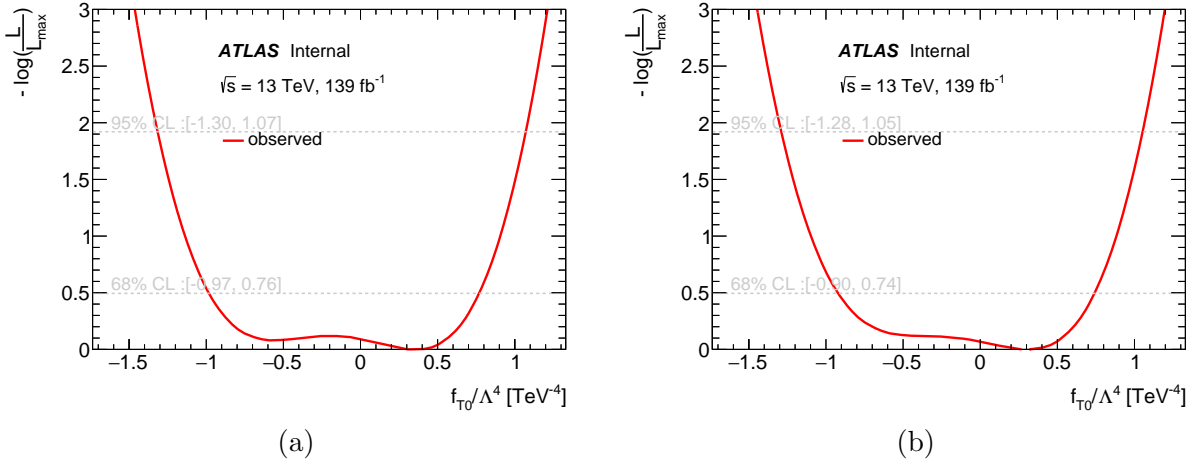


FIGURE E.3 – $Z(\rightarrow \bar{\nu}\nu)\gamma$ analysis replacement validation : comparison between T0 (a) original limit (b) replaced limit

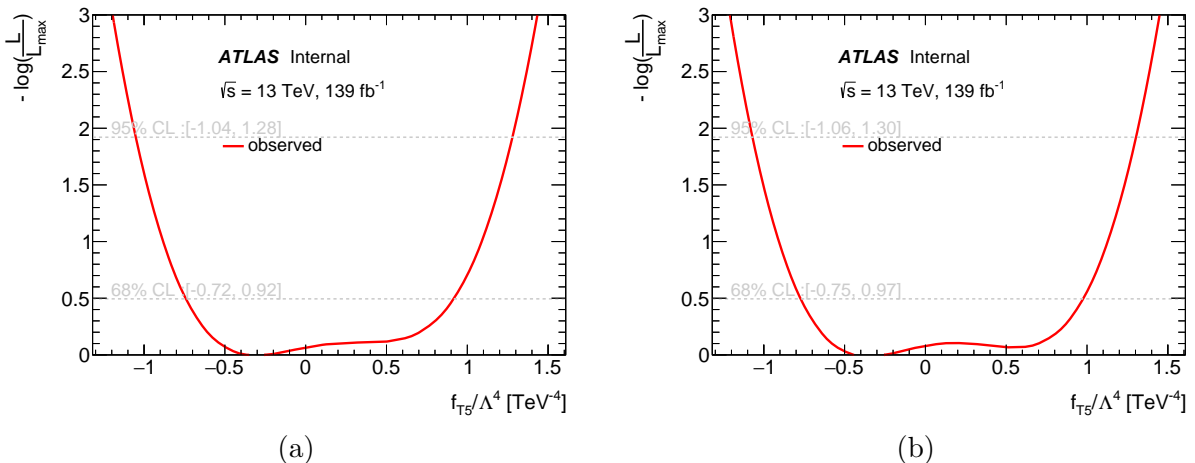


FIGURE E.4 – $Z(\rightarrow \bar{\nu}\nu)\gamma$ analysis replacement validation : comparison between T5 (a) original limit (b) replaced limit

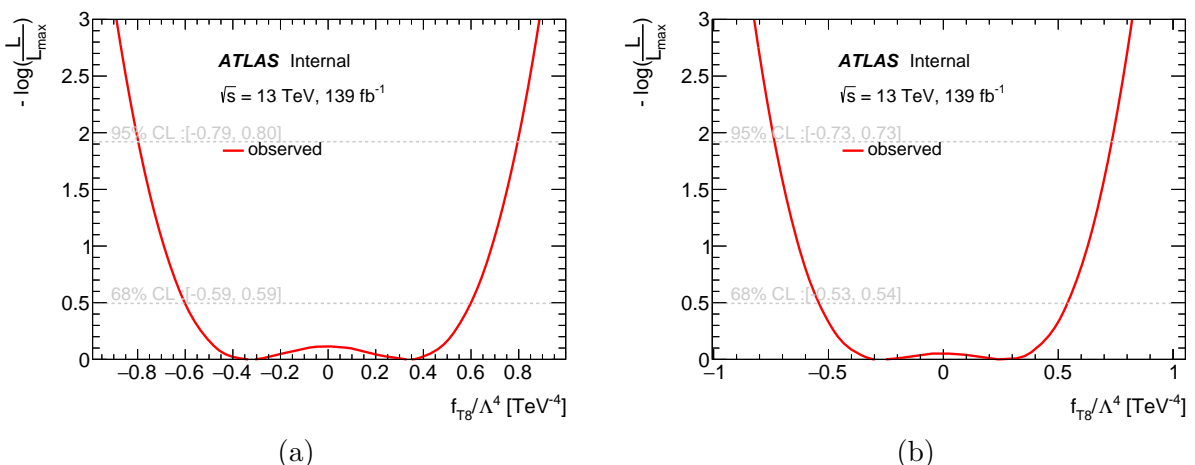
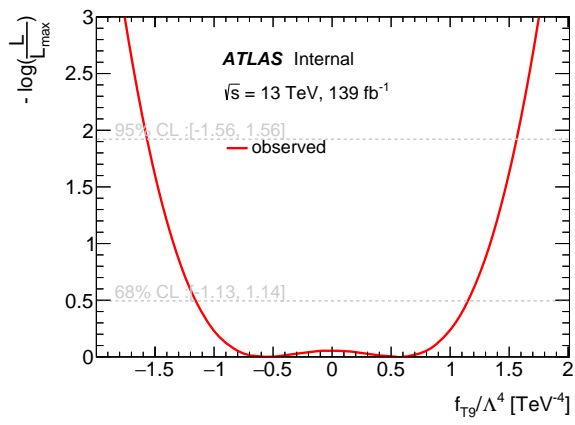
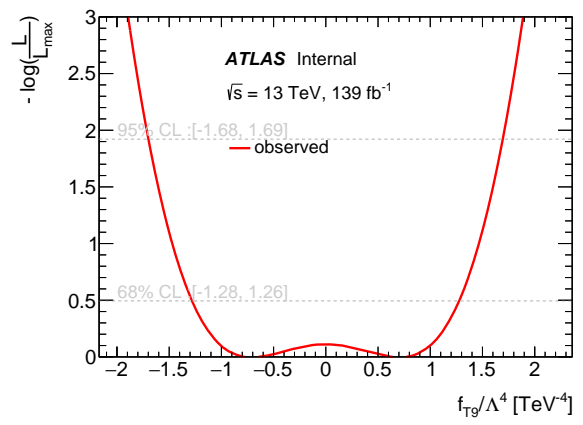


FIGURE E.5 – $Z(\rightarrow \bar{\nu}\nu)\gamma$ analysis replacement validation : comparison between T8 (a) original limit (b) replaced limit



(a)



(b)

FIGURE E.6 – $Z(\rightarrow \bar{\nu}\nu)\gamma$ analysis replacement validation : comparison between T9 (a) original limit (b) replaced limit

2619 Bibliographie

- 2620 [1] Metperfhistogramming. [https://gitlab.cern.ch/atlas-jetetmiss/etmiss/
2621 metperformancestudies/metperfhistogramming](https://gitlab.cern.ch/atlas-jetetmiss/etmiss/metperformancestudies/metperfhistogramming). GitLab repository.
- 2622 [2] Metperformance. [https://gitlab.cern.ch/atlas-jetetmiss/etmiss/
2623 metperformancestudies/metperformance/-/tree/master?ref_type=heads](https://gitlab.cern.ch/atlas-jetetmiss/etmiss/metperformancestudies/metperformance/-/tree/master?ref_type=heads). GitLab
2624 repository.
- 2625 [3] ATLAS : letter of intent for a general-purpose pp experiment at the large hadron collider at
2626 CERN. 1992.
- 2627 [4] *ATLAS : technical proposal for a general-purpose pp experiment at the Large Hadron Collider
2628 at CERN*. LHC technical proposal. CERN, Geneva, 1994.
- 2629 [5] Performance of pile-up mitigation techniques for jets in pp collisions at $\sqrt{s} = \text{tev}$ using the
2630 atlas detector. *The European Physical Journal C*, 76(11), October 2016.
- 2631 [6] Jet reconstruction and performance using particle flow with the atlas detector. *The European
2632 Physical Journal C*, 77(7), July 2017.
- 2633 [7] Topological cell clustering in the atlas calorimeters and its performance in lhc run 1. *The
2634 European Physical Journal C*, 77(7), July 2017.
- 2635 [8] *ATLAS – A 25 Year Insider Story of the LHC Experiment*. WORLD SCIENTIFIC, 2019.
- 2636 [9] Observation of electroweak production of a same-sign w boson pair in associateion with two
2637 jets in pp collisions at $\sqrt{s} = 13 \text{ tev}$ with the atlas detector. *Physical Review Letters*, 123(16),
2638 October 2019.
- 2639 [10] Observation of electroweak $W^\pm Z$ boson pair production in association with two jets in pp
2640 collisions at $\sqrt{s} = 13 \text{ tev}$ with the atlas detector. *Physics Letters B*, 793 :469–492, June 2019.
- 2641 [11] Jet energy scale and resolution measured in proton–proton collisions at $\sqrt{s} = 13 \text{ tev}$ with the
2642 atlas detector. *The European Physical Journal C*, 81(8), August 2021.
- 2643 [12] Observation of electroweak production of two jets in association with an isolated photon and
2644 missing transverse momentum, and search for a higgs boson decaying into invisible particles
2645 at 13 TeV

2646 with the atlas detector. *The European Physical Journal C*, 82(2), February 2022.

- 2647 [13] Combined effective field theory interpretation of $W^\pm Z jj$ and $W^\pm W^\pm jj$ measurements using
2648 ATLAS 13 TeV data. Technical report, CERN, Geneva, 2023.
- 2649 [14] New techniques for jet calibration with the atlas detector. *The European Physical Journal
C*, 83(8), August 2023.
- 2650 [15] Christina Agapopoulou. *Search for supersymmetry with the ATLAS detector and development
2651 of the High Granularity Timing Detector*. PhD thesis, université Paris-Saclay, 2020.
- 2652 [16] Christina Agapopoulou, S Blin, A Blot, L Castillo Garcia, M Chmeissani, S Conforti Di Lo-
2653 renzo, C de La Taille, P Dinaucourt, A Fallou, J Garcia Rodriguez, et al. Performance of
2654 a front end prototype asic for picosecond precision time measurements with lgad sensors.
Journal of Instrumentation, 15(07) :P07007, 2020.
- 2655 [17] Ana Alboteanu, Wolfgang Kilian, and Jürgen Reuter. Resonances and unitarity in weak
boson scattering at the lhc. *Journal of High Energy Physics*, 2008(11) :010–010, nov 2008.

- 2656 [18] Adam Alloul, Neil D. Christensen, Céline Degrande, Claude Duhr, and Benjamin Fuks. Feyn-
 2657 rules 2.0 - a complete toolbox for tree-level phenomenology. *Computer Physics Communica-*
 2658 *tions*, 185(8) :2250–2300, August 2014.
- 2659 [19] J. et al. Alwall. The automated computation of tree-level and next-to-leading order differential
 2660 cross sections, and their matching to parton shower simulations. [https://doi.org/10.1007/JHEP07\(2014\)079](https://doi.org/10.1007/JHEP07(2014)079), 2014.
- 2662 [20] The ATLAS and CMS Collaborations. Expected pile-up values at the hl-lhc. <https://twiki.cern.ch/twiki/bin/view/AtlasPublic/UpgradeEventDisplays>. ATLAS EXPERIMENT
 2663 - PUBLIC RESULTS.
- 2665 [21] The ATLAS and CMS Collaborations. Snowmass white paper contribution : Physics with the
 2666 phase-2 atlas and cms detectors, 2012. ATL-PHYS-PUB-2022-018,CMS PAS FTR-22-001.
- 2667 [22] Fabrice Balli. Copying new empflow r22 run2+run3 nnjvt/fjvt config files. <https://its.cern.ch/jira/browse/ATLASG-2711>, 2024. JIRA ticket.
- 2669 [23] Benedikt Biedermann, Ansgar Denner, and Mathieu Pellen. Complete nlo corrections to
 2670 w+w+ scattering and its irreducible background at the lhc. *Journal of High Energy Physics*,
 2671 2017(10), 2017.
- 2672 [24] Matteo Cacciari, Gavin P Salam, and Gregory Soyez. The anti-ktjet clustering algorithm.
 2673 *Journal of High Energy Physics*, 2008(04) :063–063, April 2008.
- 2674 [25] N Cartiglia, R Arcidiacono, M Costa, M Ferrero, G Gioachin, M Mandurrino, L Menzio,
 2675 F Siviero, V Sola, and M Tornago. 4d tracking : present status and perspectives. *Nuclear
 2676 Instruments and Methods in Physics Research Section A : Accelerators, Spectrometers, Detec-
 2677 tors and Associated Equipment*, 1040 :167228, 2022.
- 2678 [26] ATLAS collaboration. Public atlas luminosity results for run-2 of the lhc. <https://twiki.cern.ch/twiki/bin/view/AtlasPublic/LuminosityPublicResultsRun2>. Twiki.
- 2680 [27] ATLAS collaboration. Public atlas luminosity results for run-3 of the lhc. <https://twiki.cern.ch/twiki/bin/view/AtlasPublic/LuminosityPublicResultsRun3>. Twiki.
- 2682 [28] ATLAS collaboration. Standard model summary plots june 2024. <https://atlas.web.cern.ch/Atlas/GROUPS/PHYSICS/PUBNOTES/ATL-PHYS-PUB-2024-011/>.
- 2684 [29] ATLAS Collaboration. Observation of a new particle in the search for the standard model
 2685 higgs boson with the atlas detector at the lhc. <https://doi.org/10.1016/j.physletb.2012.08.020>, 2012.
- 2687 [30] ATLAS collaboration. Event displays from upgrade physics simulated data. <https://cds.cern.ch/record/1604492/files/ATL-UPGRADE-PUB-2013-014.pdf>, 2013. ATLAS+CMS
 2688 NOTE.
- 2690 [31] ATLAS Collaboration. Fiducial and differential cross-section measurements of electroweak
 2691 $w\gamma jj$ production in pp collisions at $\sqrt{s} = 13$ tev with the atlas detector, 2024.
- 2692 [32] CMS Collaboration. Observation of a new boson at a mass of 125 gev with the cms experiment
 2693 at the lhc. <https://doi.org/10.1016/j.physletb.2012.08.021>, 2012.
- 2694 [33] The ATLAS collaboration. Atlas liquid argon calorimeter phase-ii upgrade :
 2695 Technical design report. <https://cds.cern.ch/record/2285582?ln=en>, 2017.
 2696 10.17181/CERN.6QIO.YGHO.
- 2697 [34] The ATLAS collaboration. Identification and rejection of pile-up jets at high pseudorapidity
 2698 with the atlas detector. <https://doi.org/10.1140/epjc/s10052-017-5081-5>, 2017.

- 2699 [35] The ATLAS Collaboration. Measurement of $W^\pm W^\pm$ vector-boson scattering and limits on
 2700 anomalous quartic gauge couplings with the atlas detector. *Physical Review D*, 96(1), July
 2701 2017.
- 2702 [36] The ATLAS Collaboration. Studies of $z\gamma$ production in association with a high-mass dijet
 2703 system in pp collisions at $\sqrt{s} = 8$ tev with the atlas detector. *Journal of High Energy Physics*,
 2704 2017(7), July 2017.
- 2705 [37] The ATLAS collaboration. Technical design report for the atlas inner tracker pixel detector.
 2706 <https://cds.cern.ch/record/2285585?ln=en>, 2017. 10.17181/CERN.FOZZ.ZP3Q.
- 2707 [38] The ATLAS collaboration. Technical design report for the phase-ii upgrade of the atlas muon
 2708 spectrometer. <https://cds.cern.ch/record/2285580?ln=en>, 2017.
- 2709 [39] The ATLAS collaboration. Technical design report for the phase-ii upgrade
 2710 of the atlas tdaq system. <https://cds.cern.ch/record/2285584?ln=fr>, 2017.
 2711 10.17181/CERN.2LBB.4IAL.
- 2712 [40] The ATLAS collaboration. Technical design report for the phase-ii upgrade of the atlas tile
 2713 calorimeter. <https://cds.cern.ch/record/2285583?ln=en>, 2017.
- 2714 [41] The ATLAS collaboration. Prospect study of electroweak production of a z boson pair plus
 2715 two jets at the hl-lhc. <http://cds.cern.ch/record/2647219>, 2018. ATL-PHYS-PUB-2018-
 2716 029.
- 2717 [42] The ATLAS collaboration. Prospective study of vector boson scattering in wz fully leptonic
 2718 final state at hl-lhc. <http://cds.cern.ch/record/2645271>, 2018. ATL-PHYS-PUB-2018-
 2719 023.
- 2720 [43] The ATLAS collaboration. Prospects for the measurement of the $W^\pm W^\pm$ scattering cross
 2721 section and extraction of the longitudinal scattering component in pp collisions at the high-
 2722 luminosity lhc with the atlas experiment. <https://cds.cern.ch/record/2652447>, 2018.
 2723 ATL-PHYS-PUB-2018-052.
- 2724 [44] The ATLAS collaboration. Forward jet vertex tagging using the particle flow algorithm.
 2725 ATL-PHYS-PUB-2019-026, 2019.
- 2726 [45] The ATLAS collaboration. Atlas hl-lhc computing conceptual design report. <http://cds.cern.ch/record/2729668>, 2020.
- 2728 [46] The ATLAS collaboration. Technical design report : A high-granularity timing detector for
 2729 the atlas phase-ii upgrade. <https://cds.cern.ch/record/2719855?ln=en>, 2020.
- 2730 [47] The ATLAS Collaboration. Muon reconstruction and identification efficiency in atlas using
 2731 the full run 2 pp collision data set at $\sqrt{s} = 13$ tev. <https://doi.org/10.1140/epjc/s10052-021-09233-2>, 2021.
- 2733 [48] The ATLAS Collaboration. Measurement of electroweak $z(\nu\bar{\nu})\gamma jj$ production and limits on
 2734 anomalous quartic gauge couplings in pp collisions at $\sqrt{s} = 13$ tev with the atlas detector.
 2735 *Journal of High Energy Physics*, 2023(6), jun 2023.
- 2736 [49] The ATLAS Collaboration. Measurement of the cross-sections of the electroweak and total
 2737 production of a $z\gamma$ pair in association with two jets in pp collisions at $\sqrt{s} = 13$ tev with the
 2738 atlas detector, 2023.
- 2739 [50] The ATLAS collaboration. Observation of electroweak production of two jets and a z-boson
 2740 pair. <https://doi.org/10.1038/s41567-022-01757-y>, 2023.
- 2741 [51] The ATLAS Collaboration. The atlas experiment at the cern large hadron collider : a de-
 2742 scription of the detector configuration for run-3. *Journal of Instrumentation*, 19(05) :P05063,
 2743 may 2024.

- [52] The ATLAS Collaboration. Differential cross-section measurements of the production of four charged leptons in association with two jets using the atlas detector. *Journal of High Energy Physics*, 2024(1), jan 2024.
- [53] The ATLAS Collaboration. Electron and photon energy calibration with the atlas detector using lhc run 2 data. <https://doi.org/10.1088/1748-0221/19/02/P02009>, 2024.
- [54] The ATLAS collaboration. Improving topological cluster reconstruction using calorimeter cell timing in atlas. <https://doi.org/10.1140/epjc/s10052-024-12657-1>, 2024.
- [55] The ATLAS collaboration. Measurement and interpretation of same-sign w boson pair production in association with two jets in pp collisions at $\sqrt{s} = 13$ tev with the atlas detector. [https://doi.org/10.1007/JHEP04\(2024\)026](https://doi.org/10.1007/JHEP04(2024)026), 2024.
- [56] The ATLAS collaboration. Measurements of electroweak $W^\pm Z$ boson pair production in association with two jets in pp collisions at $\sqrt{s} = 13$ tev with the atlas detector. [https://doi.org/10.1007/JHEP06\(2024\)192](https://doi.org/10.1007/JHEP06(2024)192), 2024.
- [57] The CMS collaboration. Measurement of electroweak wz production and search for new physics in pp collisions at $\sqrt{s} = 13$ tev. <http://cds.cern.ch/record/2629457>, 2018. ATL-PAS-SMP-18-001.
- [58] The CMS collaboration. Vector boson scattering prospective studies in the zz fully leptonic decay channel for the high-luminosity and high-energy lhc upgrades. <http://cds.cern.ch/record/2650915>, 2018. CMS-PAS-FTR-18-014.
- [59] TOTEM Collaboration. *Luminosity-Independent Measurement of the Proton-Proton Total Cross Section at $\sqrt{s}=8$ TeV*. American Physical Society, 2013. PRL 111, 012001 (2013).
- [60] D. Cussans. Description of the jra1 trigger logic unit (tlu), v0.2c. <https://www.eudet.org/e26/e28/e42441/e57298/EUDET-MEMO-2009-04.pdf>, 2009. Accessed : 2023-14-08.
- [61] L. CASTILLO GARCÍA D. BOUMEDIENE. Overview of october sps test beam. <https://indico.cern.ch/event/968948/contributions/4608807/attachments/2343653/3995967/SPS-TB-HGTD-10-2021-overview.pdf>, 2021. Accessed : 2023-14-08.
- [62] Eduardo da Silva Almeida and O. J. P. Éboli. Unitarity constraints on anomalous quartic couplings. PHYSICAL REVIEW D 101, 113003 (2020), 2020.
- [63] A. Denner and T. Hahn. Radiative corrections to $w^+w^- \rightarrow w^+w^-$ in the electroweak standard model. *Nuclear Physics B*, 525(1–2) :27–50, aug 1998.
- [64] eds. O. Brüning and L. Rossi. The high luminosity large hadron collider - new machine for illuminating the mysteries of the universe, second edition, <https://cds.cern.ch/record/2690118?ln=en>. ADVANCED SERIES ON DIRECTIONS IN HIGH ENERGY PHYSICS, Vol.31.
- [65] S. Farry et al. eds. P. Azzi. Standard model physics at the hl-lhc and he-lhc. report from working group 1 on the physics of the hl-lhc, and perspectives at the he-lhc, 2018. CERN-LPCC-2018-03.
- [66] C.J. Baker et al. E.K. Anderson. Observation of the effect of gravity on the motion of antimatter. <https://doi.org/10.1038/s41586-023-06527-1>, 2023.
- [67] A. Bocci et al. Recommendations from the anomalous gauge coupling taskforce. <https://cds.cern.ch/record/2261444/files/ATL-COM-PHYS-2017-433.pdf>, 2017.
- [68] G. Arnison et al. Experimental observation of lepton pairs of invariant mass around 95 gev/c2 at the cern sps collider. [https://doi.org/10.1016/0370-2693\(83\)90188-0](https://doi.org/10.1016/0370-2693(83)90188-0), 1983.

- 2787 [69] G. Durieux et al. Lhc eft wg note : Basis for anomalous quartic gauge couplings.
 2788 https://indico.cern.ch/event/1433939/contributions/6032971/attachments/2888812/5063744/aQGCs_2024-06-19.pdf, 2024.
- 2790 [70] M. Banner et al. Observation of single isolated electrons of high transverse momentum in
 2791 events with missing transverse energy at the cern pp collider. [https://doi.org/10.1016/0370-2693\(83\)91605-2](https://doi.org/10.1016/0370-2693(83)91605-2), 1983.
- 2793 [71] O. Arbele et al. High-luminosity large hadron collider (hl-lhc) technical design report. <https://cds.cern.ch/record/2749422>. CERN-2020-010.
- 2795 [72] R. Casanova et al. Altiroc2 datasheet. https://twiki.cern.ch/twiki/pub/Atlas/Altiroc2Board/ALTIROC2_DATASHEET_15March2022.pdf, 2022.
- 2797 [73] Marco Ferrero, Roberta Arcidiacono, Marco Mandurrino, Valentina Sola, and Nicolò Cartiglia. *An Introduction to Ultra-Fast Silicon Detectors*. CRC Press, 2021.
- 2799 [74] European Strategy for Particle Physics Preparatory Group. Strategy brochure 2006. <https://cds.cern.ch/record/2690118?ln=en>. CERN-ESU-001.
- 2801 [75] Christian Gumpert. Measurement of electroweak gauge boson scattering in the channel
 2802 $pp \rightarrow w^\pm w^\pm jj$ with the atlas detector at the large hadron collider, 2014. Presented 27 Feb
 2803 2015.
- 2804 [76] Salah El Dine HAMMOUD. Toa lsb – fitting different ranges of toa bins –
 2805 boards 15 - 47 : Delay scan vs rpg. <https://indico.cern.ch/event/1360548/#2-updates-from-omegaijclab>, 2024.
- 2807 [77] Michael Holzbock. fjvt performance. <https://indico.cern.ch/event/1223581/contributions/5147742/attachments/2555453/4403422/ETmissPU-2022-11-28-R22-fJvt-Study.pdf>, 2023. slides from ETmiss + PU sub-group meeting.
- 2811 [78] Michael Holzbock. fjvt.jvt in r22 recommendation software update. https://gitlab.cern.ch/atlas/athena/-/merge_requests/70961, 2024. GitLab Merge Request.
- 2813 [79] Hendrik Jansen, Simon Spannagel, Jörg Behr, Antonio Bulgheroni, Gilles Claus, Emlyn Corrin, David Cussans, Jan Dreyling-Eschweiler, Doris Eckstein, Thomas Eichhorn, et al. Performance of the euDET-type beam telescopes. *EPJ Techniques and Instrumentation*, 3 :1–20, 2016.
- 2817 [80] Peter Jenni. EAGLE : Experiment for Accurate Gamma, Lepton and Energy measurements :
 2818 expression of interest. 1992. Conference : Towards the LHC experimental programme :
 2819 General Meeting on LHC Physics and Detectors, Evian-les-Bains, France, 5 - 8 Mar 1992.
- 2820 [81] L. Moneta et al” K. Cranmer, G. Lewis. HistFactory : A tool for creating statistical models
 2821 for use with RooFit and RooStats. Technical report, New York U., New York, 2012.
- 2822 [82] R. U. Koetz. User manual : Atlas fe-i4a pixel module as a trigger plane for the beam telescope.
 2823 <https://www.desy.de/f/students/2013/reports/bisanz.pdf.gz>, 2013. Accessed :
 2824 2023-14-08.
- 2825 [83] Anastasia KOTSOKECHAGIA. Fvjt pflow algorithm. https://gitlab.cern.ch:8443/atlas/athena/-/blob/main/Reconstruction/Jet/JetMomentTools/JetMomentTools/JetForwardPFlowJvtTool.h?ref_type=heads. ATLAS Athena.
- 2828 [84] Anastasia KOTSOKECHAGIA. Search for vector boson scattering in semi-leptonic final
 2829 states with the atlas detector. contribution to the inner tracker upgrade in view of the high-
 2830 luminosity lhc. Thèse de doctorat, 2022.

- 2831 [85] Oleksii Kurdysh. fjvt in r22. [https://gitlab.cern.ch/atлас/athena/-/merge_requests/](https://gitlab.cern.ch/atлас/athena/-/merge_requests/64339)
2832 64339, 2023. GitLab Merge Request.
- 2833 [86] Mathieu Markovitch. Full run-2 aqgc combination status. [https://indico.cern.ch/event/](https://indico.cern.ch/event/1353688/contributions/5699756/attachments/2768423/4822783/Mathieu_081223.pdf)
2834 1353688/contributions/5699756/attachments/2768423/4822783/Mathieu_081223.pdf, 2023.
- 2835 [87] Mathieu Markovitch. Fit updates. [https://indico.cern.ch/event/1448186/](https://indico.cern.ch/event/1448186/contributions/6097771/attachments/2914320/5114021/Mathieu_220824.pdf)
2836 contributions/6097771/attachments/2914320/5114021/Mathieu_220824.pdf, 2024.
- 2837 [88] Mathieu Markovitch. Fit updates. [https://indico.cern.ch/event/1448186/](https://indico.cern.ch/event/1448186/contributions/6097771/attachments/2914320/5114021/Mathieu_220824.pdf)
2838 contributions/6097771/attachments/2914320/5114021/Mathieu_220824.pdf, 2024.
- 2839 [89] Mathieu Markovitch. Sm closure : Semi-leptonic vbs. [https://indico.cern.ch/event/](https://indico.cern.ch/event/1423251/contributions/5986144/attachments/2872111/5028695/Mathieu_SM.pdf)
2840 1423251/contributions/5986144/attachments/2872111/5028695/Mathieu_SM.pdf, 2024. slides from Standard Model Plenary Meeting.
- 2841 [90] Esma Mobs. The CERN accelerator complex - August 2018. Complexe des accélérateurs du
2842 CERN - Août 2018. 2018. General Photo.
- 2843 [91] Peter R Norton. The ASCOT detector at the LHC : expression of interest. 1992. Conference :
2844 Towards the LHC experimental programme : General Meeting on LHC Physics and Detectors,
2845 Evian-les-Bains, France, 5 - 8 Mar 1992.
- 2846 [92] Aleksandr Petukhov. Zzllvv editorial board request follow-up. [https://indico.cern.ch/](https://indico.cern.ch/event/1342027/contributions/5649518/attachments/2745972/4778036/2023.11.03%20ZZ%2020212v%20Status%20Report.pdf)
2847 event/1342027/contributions/5649518/attachments/2745972/4778036/2023.11.03%
2848 20ZZ%2020212v%20Status%20Report.pdf, 2023. slides from SM Electroweak group meeting.
- 2849 [93] Louis PORTALES. Observation of electroweak wzjj production, and studies on pile-up miti-
2850 gation with the atlas detector. Thèse de doctorat, 2020.
- 2851 [94] DILIA MARÍA PORTILLO QUINTERO. Introduction : jet inputs and mc calibration. 2024.
2852 slides from HCW2024.
- 2853 [95] H.Arnold et al. S. Ali. Performance in beam tests of carbon-enriched irradiated low gain
2854 avalanche detectors for the atlas high granularity timing detector. *JINST*, 18, 2023.
- 2855 [96] Gavin Salam. Jet reconstruction theory. [https://indico.cern.ch/event/817757/](https://indico.cern.ch/event/817757/contributions/3712514/attachments/1999205/3336281/hamburg-jets-1.pdf)
2856 contributions/3712514/attachments/1999205/3336281/hamburg-jets-1.pdf, 2020.
2857 slides from PREFIT school.
- 2858 [97] Federico Siviero, Roberta Arcidiacono, Giacomo Borghi, Maurizio Boscardin, Nicolo Carti-
2859 glia, M Centis Vignali, Marco Costa, G-F Dalla Betta, Marco Ferrero, Francesco Ficarella,
2860 et al. Optimization of the gain layer design of ultra-fast silicon detectors. *Nuclear Instru-
2861 ments and Methods in Physics Research Section A : Accelerators, Spectrometers, Detectors
2862 and Associated Equipment*, 1033 :166739, 2022.
- 2863 [98] Stefanie Todt. The $W^\pm W^\pm$ Scattering Process – Theoretical Studies, Observation, Cross-
2864 section Measurement, and EFT Reinterpretation at $\sqrt{s} = 13$ TeV with the ATLAS Detector,
2865 2022. Presented 02 Dec 2022.
- 2866 [99] Georges Trad. The cern accelerator complex. <https://indico.cern.ch/event/1418290/>,
2867 2024.
- 2868 [100] Corentin Allaire et al. Xiaocong Ai. A common tracking software project. <https://doi.org/10.1007/s41781-021-00078-8>, 2022.
- 2869 [101] Antonino Zichichi. ECFA-LEP working group : 1979 progress report. The LEP-White Book,
2870 1980. Repr. 2004.
- 2871 [102] O.J.P. Éboli and M.C. Gonzalez-Garcia. Classifying the bosonic quartic couplings. *Phys.
2872 Rev. D* 93, 093013, 2016.